



University
of Glasgow

Ashraf, Ehsan Ellahi (2011) *Advected bioconvection and the hydrodynamics of bounded biflagellate locomotion*.
PhD thesis.

<http://theses.gla.ac.uk/2826/>

Copyright and moral rights for this thesis are retained by the author

A copy can be downloaded for personal non-commercial research or study, without prior permission or charge

This thesis cannot be reproduced or quoted extensively from without first obtaining permission in writing from the Author

The content must not be changed in any way or sold commercially in any format or medium without the formal permission of the Author

When referring to this work, full bibliographic details including the author, title, awarding institution and date of the thesis must be given

Advected bioconvection and the hydrodynamics of bounded biflagellate locomotion

by

Ehsan Ellahi Ashraf

A thesis submitted to the
School of Mathematics and Statistics
College of Science and Engineering
at the University of Glasgow
for the degree of
Doctor of Philosophy

December 2010

© E E Ashraf 2010

To my late father

Muhammad Ashraf Qureshi

Abstract

The recent developments in using micro-organisms effectively for biofuels is the main motivation to carry out this research work. In this thesis, we have investigated two main aspects related micro-organisms: swimming behavior and bioconvection pattern formation. In the first aspect, we have discussed the swimming of a biflagellated green algae named as *Chlamydomonas augustae* in a Stokes flow in the absence and presence of the no-slip stationary plane boundary. For a micro-organism with similarly sized spherical cell body and flagella we have used Resistive Force Theory (RFT) for modelling the idealized flagellar beat pattern. The unbounded swimming analysis was used to calculate the organism's swimming velocity and angular velocity by balancing the forces and torques acting on the organism at every instant, and is a revision and improvement of the work carried out by Jones *et al.* [76]. The model was developed in general terms for uniplanar locomotion of the micro-organism. To facilitate analytical calculation a code in the software Maple was developed, which produced results consistent with the results in [76] as discussed in chapter 2. The model predicts a realistic swimming speed and showed that viscous torque acting on the flagellum has significant contribution to the angular velocity of the organism. The trajectories of swimming for one beat and for multiple beats were also plotted. In chapter 3 we have extended the same swimming model for the case of the presence of a no-slip stationary plane boundary. In order to satisfy conditions at the no-slip plane boundary we have incorporated the image system singularities solution. Again using RFT and the software Maple, we have calculated the micro-organism's swimming velocity and angular velocity for the different geometries such as swimming away/towards, angled and parallel to the no-slip stationary plane boundary. The results were further compared with the unbounded swimming case and found that the micro-organism's swimming velocity regressed close to the boundary and approaches the unbounded values, whereas angular velocity approaches to zero, as it swims far from the plane boundary.

For nutrient uptake and to optimize light for photosynthesis these micro-organisms swim in directions biased by environmental cues, termed taxes. These taxes inevitably lead to accumulations of micro-organisms that induce hydrodynamic instabilities due to their density difference. The large scale fluid flow and intricate patterns formed are called bioconvection. In chapter 4, we have for the first time, experimentally investigated pattern formation in thin, long, horizontal tubes with and without imposed flow. With no flow, the dependence of the dominant pattern wavelength at pattern onset on cell concentration is established for the three different tubes of variable diameter. The vertical plumes of micro-organisms are observed merely to bow in the direction of flow for the case of weak imposed flow. However, for sufficiently large flow rates, the plumes progressively fragment into piecewise linear diagonal plumes, inclined at constant angle and translating at fixed speeds. The pattern wavelength generally grows with flow rate, with transitions at critical rates that depend on concentration. The bioconvection is not wholly suppressed and perturbs the flow field, even at large imposed flow rates. The contents of this chapter have already been published in *Physical Biology* international journal with co authors Dr Ottavio A Croze and Dr Martin A Bees.

In chapter 5, we have attempted for the first time to theoretically examine bioconvection in horizontal tubes in the presence of imposed flow to compare and verify the results of the experimental investigations discussed in chapter 4. To avoid the cumbersome calculation, we modelled the situation by considering the suspension flow between two plates instead of tube. The aim is to predict a particular most unstable mode from equilibrium solution and average inclination, speed of the plumes and flow transitions observed. The investigation is still not finished as modelling of the problem is complete but numerical analysis for the solution of the problem need to be done at this stage.

Acknowledgements

All praise to almighty *Allah*, the most benevolent and merciful, the creator of the universe, who gave me potential and insight that enabled me to accomplish this research work.

First of all it indeed a great pleasure and honor for me to express my sincerest gratitude to my learned supervisor, *Dr Martin Alan Bees* (EPSRC fellow), under whose dynamic supervision, propitious guidance, illustrative advice, the research work presented in this thesis became possible. His caring attitude, suggestions, motivation and encouragement have proved invaluable for me for the past four years.

I am indebted to *Dr Ottavio A Croze* for his expertise and co-operation throughout the biolab project and research paper. I am also grateful to all Mathbio group members specially *Rosie* and *Stephen* for group discussions and suggestions. I also thanks other members of the faculty, in particular *Professor Nick*, *Dr Watson*, and *Dr Chris Athorne* for guidance and discussions.

I would like to thank Pakistan Air Force (PAF), Ministry of Defence, Government of Pakistan for financial assistance and providing me an opportunity to carry out this research work. Additionally, i am greatly indebted to Department of Mathematics, University of Glasgow for providing me conducive atmosphere for research, teaching opportunities, and financial support for conferences and third year University tuition fee.

I also acknowledge the support and able company of my office mates *Susan*, *Marjory*, *Monica*, *Robert* and *Yunfei*. I am really thankful to all my family friends at Glasgow specially *Imran*, *Muzahir*, *Amir*, *Jabbar bhai* and *Dr Asim* who guided and helped us for settling down in entirely new environment.

Words are wane in expressing my veneration for my parents, brothers, sister and brother-in-law who prayed for my edification, endeavored for my betterment and cheerfully took the burden of my studies throughout. Special thanks to my mother who always been

source of inspiration and encouraged me even underwent through stress after losing my father meanwhile.

Last but by no means least, many thanks go to my wife *Saba* for being constant source of support and encouragements and with understanding shared the burden throughout this research work.

Ehsan E. Ashraf

December - 2010

Statement

This thesis is submitted in accordance with the regulations for the degree of Doctor of Philosophy at the University of Glasgow UK. Chapter 1 includes the preliminaries and introduction of the subject used throughout the thesis. Chapter 2 is the revision and refinement of the unbounded swimming model of Jones *et al.* [76] by employing the simplified flagellar beat model and use of software Maple. Chapter 3, 4, 5 and 6 are authors original and novel work conducted under the supervision of Dr. Martin Alan Bees (EPSRC fellow), except where explicitly credited to others. The contents of chapter 4 have already been published in *Physical Biology* international journal with co authors Dr Ottavio A Croze and Dr Martin A Bees.

No part of this thesis has previously been submitted by me for a degree at this or any other University.

Contents

Abstract	ii
Acknowledgements	iv
Statement	vi
1 Preliminaries	1
1.1 Introduction	1
1.2 Hydrodynamics of swimming unicellular micro-organism	2
1.3 Orientation mechanism of swimming unicellular micro-organisms	5
1.4 Stokes Equations	8
1.5 Singularity solution for spheres	13
1.5.1 Translating motion	14
1.5.2 Rotating motion	14
1.6 Flagellar hydrodynamics	15
1.6.1 Resistive Force Theory	16
1.6.2 Slender Body Theory	19
1.6.3 Comparison of RFT and SBT	20
1.7 Bioconvection	21
1.7.1 Mathematical models of bioconvection	24
1.7.2 Stochastic gyrotactic bioconvection model	27
1.7.3 Recent development in bioconvection modelling	29
1.8 Applications and motivation of the study of biflagellate	30
1.9 Review of the thesis	32
2 Biflagellate swimming in an unbounded domain	34
2.1 Synopsis	34

2.2	Introduction	34
2.3	Resistive Force Theory	35
2.4	Force and torque balance for gyrotactic biflagellates	37
2.5	Flagellar Beat Pattern	42
2.6	The Jones <i>et al.</i> flagellar beat model	43
2.7	Modified implementation of the uniplanar flagellar beat model	48
2.7.1	Computation of viscous force and viscous torque acting on one flagellum	50
2.7.2	Force-Torque balance equations	58
2.8	Uniplanar vertical upward swimming	61
2.9	General unbounded uniplanar swimming	65
2.9.1	Calculation of effective gyrotactic re-orientation time	69
2.10	Tracking of the swimming cell	71
2.11	Conclusion	73
3	Bounded biflagellate swimming	75
3.1	Synopsis	75
3.2	Introduction	76
3.3	Swimming near the plane boundary	77
3.3.1	Image singularities system	77
3.3.2	Solution for the translating motion of a sphere near a stationary plane boundary	79
3.3.3	Solution for the rotational motion of a sphere near a stationary plane boundary	83
3.4	Force-Torque balance for bounded biflagellate swimming	88
3.4.1	Computation of viscous force and viscous torque acting on one flagellum	91
3.4.2	Force-Torque balance equations	99
3.4.3	Force-Torque balance equations without flagella contributions	102
3.5	Results	105
3.5.1	Uniplanar upward cell swimming away/towards the no-slip plane boundary	105
3.5.2	Comparison of swimming away and towards the no-slip stationary plane boundary	110

3.5.3	Biflagellate cell swimming in the vicinity of the no-slip stationary plane boundary	114
3.5.4	Biflagellate swimming parallel to the plane boundary	119
3.6	Conclusion	127
4	Experimental analysis of bioconvection	130
4.1	Synopsis	130
4.2	Introduction	131
4.3	Breeding and concentration of green algae cells	133
4.3.1	Culturing of cells	133
4.3.2	Concentration of cells	136
4.3.3	Transfer of suspension of cells	138
4.3.4	Measuring concentration of cells in suspension	138
4.4	Environmental control and Methods	140
4.4.1	Light source control	140
4.4.2	Mixing of suspension	140
4.4.3	Image recordings	141
4.4.4	Variation of cell concentration of suspension	142
4.4.5	Variation of tube diameter	143
4.4.6	Variation of Flow rate	144
4.4.7	Statistical Investigations	144
4.5	Experimental setup	144
4.6	Cleaning and processing of images	146
4.6.1	Fast Fourier Transform	147
4.6.2	Dominant wavenumber	148
4.6.3	Error Analysis	148
4.6.4	Dominant wavenumber analysis	151
4.7	Experimental results for no flow problems	155
4.7.1	Investigating the initial instability wavelength pattern	156
4.7.2	Investigating the final stable pattern wavelength	158
4.7.3	Investigating the dependence on variation of depth	160
4.7.4	Investigating the dependence on variations of concentration	162
4.7.5	Investigating the time for initiation of pattern formation	162
4.8	Experimental results for imposed flow experiments	166

4.8.1	Experiment protocol	167
4.8.2	Investigating the trends of wavelength	168
4.8.3	Investigating the first peak of wavelength	168
4.8.4	Investigating the average angle and average drift speed	172
4.9	Discussion	172
4.10	Conclusion	178
5	Modelling of advected bioconvection in tube	180
5.1	Synopsis	180
5.2	Introduction	181
5.3	Solution of the Fokker-Planck equation	181
5.4	Modelling the linear bioconvection equations	184
5.4.1	Stability analysis	188
5.5	Numerical analysis	193
5.6	Discussion	194
6	Conclusions and future work	196
6.1	Concluding remarks	196
6.2	Future work	199
A		201
A.1	Time dependent beat coefficients α_{ij}	201
A.2	Time dependent beat coefficients h_{ij}	202
A.3	Core integrals involved in beat coefficients α_{ij}	203
A.4	Core integrals involved in beat coefficients α_{ij}	205
A.4.1	Special integrals when point Q lies on the flagellum	207
B		209
B.1	Maple11 programming	209
B.1.1	Instruction flow and code details	209
B.1.2	Programming code	211
	References	220

List of Figures

1.1	A schematic diagram of unicellular biflagellate green algae <i>Chlamydomonas augustae</i> cell structure and inner structure of cross section of the flagellum. The length of the cell body and both flagella is approximately equal to 10 μm	3
1.2	A schematic diagram of forces acting on the swimming biflagellate green algae <i>Chlamydomonas augustae</i> cell. The Gravitational torque arise due to the centre-of-gravity offset and viscous torque is caused due to the strain and vorticity in the fluid. \mathbf{V}	5
1.3	A schematic diagram of U-tube experiment for gyrotaxis in Poiseuille flow. Cells swim towards relatively downwards flowing fluid to form plume structure on right-hand side whereas swim away from upward flowing fluid and gather close to the wall shown on the left hand side of the U-tube.	6
1.4	Vector plot of Stokeslet singularity solution	9
1.5	Vector plot of Dipole (source doublet) singularity solution	10
1.6	Vector plot of stresslet singularity solution	11
1.7	Vector plot of rotlet (couplet) singularity solution	12
1.8	Schematic diagram of the flagellar propulsion of monoflagellate sea urchin spermatozoon.	16
1.9	A sample of images of bioconvection pattern formation by suspension of <i>C. augustae</i> recorded in a thin long horizontal tube while focusing on the centre of the tube.	22
1.10	A schematic diagram of an overturning Rayleigh-Taylor instability from side. Cells which are denser than the fluid swim upward on average and gather at the top to form a suspension of greater density (dark region) than that of the fluid below.	23

1.11	A schematic diagram of a gyrotactic instability without the upper boundary. Cells swim towards the down welling fluid and this addition of mass make the fluid more denser (dark region) resulting sink faster and form a plume structure.	24
1.12	A design of tubular helical alga photobioreactor of 1000 L capacity at Murdoch University. Courtesy of Professor Michael Borowitzka, Murdoch University, Australia.	31
2.1	(a) A schematic diagram of uniplanar swimming of <i>C. augustae</i> cell: (\mathbf{i}, \mathbf{k}) are fixed space and (\mathbf{p}, \mathbf{q}) are body coordinates respectively, H is centre-of-gravity G offset from geometric centre C , θ is the Euler angle between \mathbf{k} in fixed space and primary axis of swimming \mathbf{p} in body coordinate system, \mathbf{g} is the force due to gravity, \mathbf{L}_{grv} and \mathbf{L}_{vis} represents torque due to gravity and viscosity respectively. (b) Swimming cell motion calculated by its velocity \mathbf{v} and angular velocity $\mathbf{\Omega}$ when embedded in the flow, with strain rate \mathbf{E} and vorticity $\boldsymbol{\omega}$, and Θ is the Euler angle between principal axes of the rate-of-strain and \mathbf{k} in fixed space coordinate system.	39
2.2	Tracing of one beat cycle of both flagella of <i>C. reinhardtii</i> mutant 622E. Reproduced from Ruffer and Nultsch [128].	43
2.3	A schematic diagram of step by step positions and height gained/lost by vertical upward swimming of <i>C. augustae</i> cell during effective and recovery stroke of one flagella beat.	44
2.4	The idealized model by Jones <i>et al.</i> [76] for flagellar beat pattern of <i>C. augustae</i> for different positions of the flagellum during (a) effective stroke and (b) recovery stroke.	47
2.5	Generalized Jones <i>et al.</i> flagellar beat pattern during effective and recovery stroke.	49
2.6	Addition and subtraction of forces acting on the flagellar section due to swimming in the (a) primary velocity direction \mathbf{p} and (b) transverse velocity direction \mathbf{q} respectively.	60

2.7	Variation in uniplanar upward swimming velocity during one flagellar beat. A discontinuity occurs at the changeover from effective to recovery stroke. The dashed line represents the graph for constant angular velocity and solid line zero moment recovery stroke case. (a) Reproduced from Jones <i>et al.</i> [76], (b) Using generalized expressions and Maple code simulations.	63
2.8	Uniplanar upward swimming speed plotted against ratio of resistance coefficients K_n/K_t for varying flagella length ($l = 2a, 3a, 4a$, from bottom to top), where a is the radius of the cell's body.	65
2.9	Variation in uniplanar instantaneous swimming velocity in transverse direction during one flagellar beat. The dashed line represents the graph for constant angular velocity and solid line zero moment recovery stroke case. With initial angle (a) $\theta = 40^\circ$ i.e. angled swimming, (b) $\theta = 90^\circ$ i.e. horizontal swimming.	67
2.10	Variation of angle θ from the initial angle θ_0 during one flagella beat due to the effect of gravitational torque only. With initial angle (a) $\theta = 40^\circ$ i.e. angled swimming, (b) $\theta = 90^\circ$ i.e. horizontal swimming.	68
2.11	Variation of the angle θ during one flagella beat when organism swims horizontally i.e. $\theta = 90^\circ$. The dashed line represents swimming organism without flagella and solid line indicates with the flagella.	69
2.12	Trajectory of the unbounded swimming cell in scales of the X and Z axes with initial angle $\theta_0 = 90^\circ, 80^\circ, 70^\circ$ from bottom to top respectively. The arrows represent the position of the cell after the flagella beat (effective and recovery stroke) at any time t.	72
3.1	The position of sphere and image sphere due to Stokeslet and potential dipole singularities and no-slip stationary plane boundary at $x_3 = 0$. The distance h is measured from the centre of the sphere to the plane boundary, whereas \mathbf{r} and \mathbf{R} represents the position vectors at any point P from the centre of sphere and image sphere, respectively.	78
3.2	Streamlines for a sphere and an image sphere translating away from the no-slip stationary plane boundary lies at the centre, $x_3 = 0$. (a) Unbounded sphere translating upwards. (b) Bounded sphere translating upwards away from the plane boundary.	81

- 3.3 Streamlines plot when sphere translating towards the no-slip plane boundary lies at the centre at $x_3 = 0$. (a) Unbounded sphere translating upwards. (b) Bounded sphere translating upwards towards the plane boundary. 84
- 3.4 Streamlines plot when sphere translating parallel to the no-slip plane boundary lies at the centre at $x_3 = 0$. (a) Unbounded sphere translating horizontally. (b) Bounded sphere translating horizontally parallel to the plane boundary. 85
- 3.5 Streamlines plot of the sphere and image sphere when rotating parallel to the stationary no-slip plane boundary lies at the centre at $x_3 = 0$. (a) Unbounded sphere rotating horizontally. (b) Bounded sphere rotating horizontally parallel to the plane boundary. 87
- 3.6 A schematic diagram of uniplanar swimming of *C. augustae* cell in the vicinity of the stationary no-slip plane boundary: (\mathbf{i}, \mathbf{k}) are fixed space and (\mathbf{p}, \mathbf{q}) are body coordinates respectively, H is centre-of-gravity G offset from geometric centre C, θ is the Euler angle between \mathbf{k} in fixed space and primary axis of swimming \mathbf{p} in body coordinate system, χ is the angle which flagella makes with the \mathbf{p} , \mathbf{g} is the force due to gravity and h is the distance of boundary from the centre of the cell body. 90
- 3.7 Addition and subtraction of forces acting on the flagellar section due to swimming in the (a) primary velocity direction \mathbf{p} and (b) transverse velocity direction \mathbf{q} respectively. 101
- 3.8 Swimming cell in the vicinity of no-slip stationary plane boundary. (a) Upward swimming away/towards the plane boundary, (b) Angled/parallel swimming near the plane boundary. 104
- 3.9 Upward swimming of a biflagellate cell away from the stationary no-slip plane boundary, where h is the distance of plane boundary from the centre of the cell body, \mathbf{r} and \mathbf{R} are the position vectors at an element of flagellum from the centre of sphere and image sphere, respectively. 106
- 3.10 Variations of primary swimming speed v_p with the increase of h ((a)-(f), $h = 2, 5, 10, 20, 50, h = 100$) for one flagella beat, when cell is swimming away from the no-slip plane boundary. The dashed line represents the graph for the unbounded case whereas the solid line is for a bounded swimming cell. 107

3.11 Variations of a biflagellate cell’s change in position for one flagellar beat with increasing of h when the cell is swimming away from the no-slip plane boundary. The dashed line represents the graph for the unbounded case whereas the solid line is for a bounded cell swimming away from the boundary. 108

3.12 Upward swimming of a biflagellate cell towards the stationary no-slip plane boundary, where h is the distance of plane boundary from the centre of the cell body, \mathbf{r} and \mathbf{R} are the position vectors at an element of flagellum from the centre of sphere and image sphere, respectively. 109

3.13 Variations of primary swimming speed v_p with the decrease of h ((a)-(f), $h = 100, 50, 20, 10, 5, h = 2$) for one flagella beat, when the cell is swimming towards the no-slip plane boundary. The dashed line represents the graph for the unbounded swimming case whereas solid line is for a bounded cell swimming towards the plane boundary. 111

3.14 Variations of transverse swimming speed v_q with the decrease of h , (a) $h = 5$, and (b) $h = 2$ for one flagella beat, when cell swimming towards the no-slip plane boundary. 112

3.15 Variations of biflagellate cell’s change in position for one flagella beat with the increase of h distance of the plane boundary from the centre of the cell body, as cell swimming towards the no-slip plane boundary. The dashed line represents the graph for unbounded case whereas solid line for bounded cell swimming towards the boundary. 113

3.16 Variations of primary swimming speed v_p with the increase of h ((a)-(f), $h = 2, 5, 10, 20, 50, h = 100$) for one flagella beat, when cell swimming away at an angle $\theta = 40^\circ$ from the no-slip plane boundary. The dashed line represents the graph for the unbounded case whereas the solid line is for a bounded cell swimming. 115

3.17 Variations of transverse swimming speed v_q with the increase of h ((a)-(f), $h = 2, 5, 10, 20, 50, h = 100$) for one flagella beat, when cell swimming away at an angle $\theta = 40^\circ$ from the no-slip plane boundary. The dashed line represents the graph for the unbounded case whereas the solid line is for a bounded cell swimming. 116

3.18 Variations of angle θ with the increase of h ((a)-(f), $h = 2, 5, 10, 20, 50, h = 100$) for one flagella beat, when cell swimming away at an angle $\theta = 40^\circ$ from the no-slip plane boundary. The dashed line represents the graph for the unbounded case whereas the solid line is for a bounded cell swimming. . 117

3.19 Variations of biflagellate cell's change in position and change in angle for one flagella beat with the increase of h , as cell swimming away at an angle of $\theta = 40^\circ$ from the boundary. The dashed line represents the graph for the unbounded case whereas solid line is for a bounded cell swimming towards the boundary. 118

3.20 Swimming of biflagellate cell parallel to the stationary no-slip plane boundary, where h is the distance of plane boundary from the centre of the cell body, \mathbf{r} and \mathbf{R} are the position vectors at an element of flagellum from the centre of the sphere and image sphere, respectively. 120

3.21 Variations of primary swimming speed v_p with the increase of h ((a)-(f), $h = 2, 5, 10, 20, 50, h = 100$) for one flagellar beat, when the cell is swimming parallel to the no-slip plane boundary. The dashed line represents the graph for unbounded case, dotted line for without Faxen's correction terms, dashdot line for without Faxen's correction and gravity contribution and solid line for bounded cell swimming. 122

3.22 Variations of transverse swimming speed v_q with the increase of h ((a)-(f), $h = 2, 5, 10, 20, 50, h = 100$) for one flagellar beat, when the cell is swimming parallel to the no-slip plane boundary. The dashed line represents the graph for unbounded case, dotted line for without Faxen's correction terms, dashdot line for without Faxen's correction and gravity contribution and solid line for bounded cell swimming. 123

3.23 Variations of change in angle θ of biflagellate cell for one flagellar beat with the increase of h ((a)-(f), $h = 2, 5, 10, 20, 50, h = 100$), when the cell is swimming parallel to the boundary. The dashed line represents the graph for unbounded case, dotted line for without Faxen's correction terms, dashdot line for without Faxen's correction and gravity contribution, longdashed line for without flagella and solid line for bounded cell swimming. 124

3.24	Variations of position and angle with the increase of h as the cell is swimming parallel to the no-slip plane boundary. The dashed line represents the graph for unbounded case whereas solid line for bounded cell swimming parallel to the boundary.	126
4.1	Cultures of green algae <i>Chlamydomonas augustae</i> in conical flasks.	134
4.2	Snap shot of algae cells concentration procedure captured at our biofluids laboratory.	137
4.3	Calibration of A the absorbance measurement from the spectrophotometer readings with C cell concentration found using cell counting with hemocytometer reproduced from Williams [147].	139
4.4	Illustration of the formation of the bioconvection pattern formation in a thin horizontal cylindrical tube as viewed from side.	142
4.5	A schematic diagram of the experimental setup for recording images of bioconvection in a thin horizontal cylindrical tube. The tube is clumped at horizontal position and held fixed with two stands. The red LED light source was fixed behind the centre of the tube and camera was mounted on stand so that images could be recorded from the side of the cylindrical tube. Suspensions were loaded via a plastic tube affixed to the left of the bioconvection tube and flow was imposed using a syringe pump shown schematically on the right of the tube.	145
4.6	A sample of cropped image from experiments recorded in tube A, where $c = 1.84 \times 10^6$ cells cm^{-3} . The mixing of cells suspension was performed outside the tube.	147
4.7	Sample of processed images from B0.42 experiment recorded in tube B where $c = 3.75 \times 10^6$ cells cm^{-3} . The images are captured every 2 seconds, where mixing was performed outside the tube.	149
4.8	A sample fourier spectra from B0.42 experiment recorded in tube B where $c = 3.75 \times 10^6$ cells cm^{-3} . The images are captured every 2 seconds, where mixing was performed outside the tube. The horizontal axis is wavenumber and vertical axis is Fourier density. The logarithmic fitting function was used to fit the data.	150

4.9 Snap shots of the processed image sequence (a-g) of a representative bioconvection pattern formation in tube A with varying time for cell concentration $1.84 \times 10^6 \text{ cells cm}^{-3}$ when mixing was performed outside of the tube. . . . 152

4.10 A sample 3d plot from experiment recorded in tube A, where $c = 1.84 \times 10^6 \text{ cells cm}^{-3}$. The images are captured every 2 seconds, where mixing was performed outside the tube. 153

4.11 A sample contour plot from experiment recorded in tube A, where $c = 1.84 \times 10^6 \text{ cells cm}^{-3}$. The images are captured every 2 seconds, where mixing was performed outside the tube. 154

4.12 Experimental data for the initial dominant wavelength λ_i as function of concentration of tubes A, B and tube C (top three panels, as indicted) for the cases of (a) mixing outside, and (b) mixing inside the tube. Straight line fits to the data are shown (for tube C we only fitted for $c > 1.45 \times 10^6 \text{ cell cm}^{-3}$). The last panel shows the fits without the data to allow a comparison of magnitudes. The error bars are standard deviations over a sample or the standard error in the mean over repeated experiments. 157

4.13 Experimental data for the final dominant wavelengths λ_f as function of concentration of tubes A, B and tube C (top three panels, as indicated) for the cases of (a) mixing outside, and (b) mixing inside the tube. Straight line fits to the data are shown. The last panel shows the fits without the data to allow a comparison of magnitudes. The error bars are standard deviations over a sample or the standard error in the mean over repeated experiments. 159

4.14 Experimental data plotted for mean pattern wavelength λ_m and gradient m for the three different diameter tubes for the initial instability and final pattern wavelength. 161

4.15 Experimental data for the variation of time to establish the initial instability for different cell concentrations for tubes A, B and C and bottom panel shows the comparison of linear fits to this variation. 163

4.16 Variations of pattern wavenumber with respect to time for different cell concentrations recorded in tube B. The images were captured every two seconds, where mixing was performed outside the tube. 164

- 4.17 Variations of pattern wavenumber with respect to time for different cell concentrations. The images were captured every two seconds, where mixing was performed outside the tube. 165
- 4.18 Snap shot of the experimental apparatus used for recording bioconvection pattern formation in a horizontal cylindrical tube with an imposed flow. . . 167
- 4.19 Bioconvection patterns recorded in tube B in the presence of imposed flow in the range $U_p = 0 - 16.6 \text{ cm s}^{-1}$ ($F = 0 - 35 \text{ ml h}^{-1}$) for cell concentrations (a) $c = 1.26 \times 10^6 \text{ cells cm}^{-3}$ and (c) $c = 5.18 \times 10^6 \text{ cells cm}^{-3}$. (As indicated, the second frame in (a) shows a frame for 3.4 cm s^{-1} rather than 2.8 cm s^{-1} .) (d) For $U_p = 13.8 \text{ cm s}^{-1}$ and concentration as in (b), we show three 5 s interval snapshots of the dynamics of a bowed plume (indicated by arrows). The figure to the right shows tracings of the plume with scale bar is 0.2 cm. 169
- 4.20 Variations of pattern wavenumber with respect to time for different flow rates, experiment recorded in tube B. The images were captured every second, where mixing was performed outside the tube. 170
- 4.21 Plots of (a) final pattern wavelength and (b) average top (positive) and bottom (negative) plume angles to the vertical as a function of the flow rate F for concentrations in the range $0.59 \times 10^6 - 5.18 \times 10^6 \text{ cells cm}^{-3}$, as indicated. The peaks in the wavelength around certain critical flow rates could be the signature of dynamic transitions in plume arrangement. The error bars indicates standard deviations. 171
- 4.22 Plot of (a) the average angles and (b) average plume drift speed as functions of the mean flow speed for all concentrations. Neither of these measures appears to depend strongly on concentration. Linear fits to data for all concentrations are also shown, and in the case of (b) the plume drift speed, the fit (solid line) is compared with the prediction for the mean (dot-dashed) and maximum (dashed) flow speeds for the Poiseuille flow. 174
- 4.23 Evolution of cell positions for (a) Plug and (c) Poiseuille flows, according to the simplified description, a line of cells (thin lines) released at equally spaced positions across the tube collapses and deforms while advected for (c), while it collapses vertically in (a). The stages in evolution are 20 s apart. The upper envelope (thick line) is the trajectory of cells released at the top of the tube, for the above defined two flow situations. 176

5.1 Linear bioconvection subject to weak poiseuille flow between two plates. . . 184

A.1 Difference in length of r during angled section of recovery stroke. 207

Chapter 1

Preliminaries

1.1 Introduction

Unicellular micro-organisms are one of the oldest organisms found on earth. They can not be seen by the human naked eye due to the smallness of the length scale. They play an important role in the development of the earth's atmosphere by photosynthesizing and acting as a sink for carbon dioxide. There is diverse range of species of micro-organism like bacteria found in our stomach causing health issues, algae and plankton affecting the global weather by photosynthesizing in rivers and oceans worldwide. They are estimated to make up more than half of the earth's biomass and variation in their number could have positive or negative effects in global warming or climate change (see Goodess and Palutikof [50]). They are mostly ocean dwelling phytoplankton and form a strong link in the food chain (see, Madigan *et al.* [100]). The study of these micro-organisms and their swimming behavior, which may lead to aggregations of cells can give insight of the lifecycle of these cells and we can further explore how they mate/die, regulate nutrients, control light for photosynthesis and reproduce themselves to form colonies. In addition to that investigations of motion in groups due to cell swimming, may reveal the details of phenomena like self ordering or migration of groups of cells and results of these investigations can be utilized to discuss other problems related to different species and organisms.

Many of these micro-organisms have lucrative industrial and commercial applications. Some species of micro-organism produce ethanol as a byproduct during intracellular photosynthesis and respiration and other applications include fertilizers, waste water treatment plants, plastics, and solid fuels. Recently different species of micro-organisms used to produce hydrogen gas and biodiesel, and act as an efficient source of biofuels or biodiesel

industry. Hence they can act as a potential source of renewable energy which reduces our dependence on the running out fossil fuel reservoirs and biofuels extracted from the edible crops like maize, corn, coconut, palm etc.

This thesis includes the hydrodynamics of the bounded unicellular biflagellate swimming micro-organism and investigations of pattern formation observed in suspension of these motile cells. The results of these investigations may lead to improved designs and enhanced production of renewable green energy through the production of hydrogen gas, and biodiesel from alga photo bioreactors.

1.2 Hydrodynamics of swimming unicellular micro-organism

In this thesis, we will be investigating the swimming of unicellular micro-organisms only. Generally micro-organisms can be classified into two broad categories: prokaryotic cells, which do not have a cell nucleus, like cyanobacteria, and eukaryotic cells, which include a nucleus and chloroplast, like green algae (see Madigan *et al.* [100]). The majority of these micro-organisms are motile and propel or swim by employing either flagella, having whip like projections, or cilia, having many smaller projections which beat synchronously to cause the swimming of the organism. The length scales for these micro-organisms are generally, of order $1 - 10 \mu\text{m}$. There is a wide range of their body shapes, size, position of flagella insertion, flagellar size and flagellar beat patterns depending upon the type of the micro-organism (see, Lighthill [94]).

Different species of micro-organism have variable cell morphology and swimming styles. As an example of small scale micro-organisms, the rod-like shaped bacterium *Bacillus subtilis* has body length of $4 \mu\text{m}$. The cell swims at a speed of $40 \mu\text{ms}^{-1}$ by using the flagella attached uniformly over the entire cell body, which come together to form a helical bundle (see Hill and Pedley [63]). *Euglena gracilis* swims using its only flagellum which passes a helical wave to power its swimming and shows up swimming tendencies (see Wager [144]). The genus *Tetrahymena* has elongated cell body of body diameter approximately $35 \mu\text{m}$. The cell swims with the swimming speed of $500 \mu\text{ms}^{-1}$ by using the cilia attached along the cell body (see Pedley and Kessler [114]).

Even with different cell morphology and swimming style, most of these micro-organisms swim at low Reynolds number due to the relative size of the cell in comparison with the surrounding fluid medium. Childress [27] compared the low Reynolds number swimming

of micro-organisms to humans swimming through a vat of warm pitch. In this case, viscous forces are dominant as compared to the inertial forces. This prevents the sustained directional movement due to the reversible fluid flow, if a time-symmetric, ‘reciprocal’ swimming stroke is employed by the cell (see Purcell [121]). Hence unicellular micro-organisms have established non-time-symmetric swimming strokes which ensure the locomotion of the cell in the desired direction.

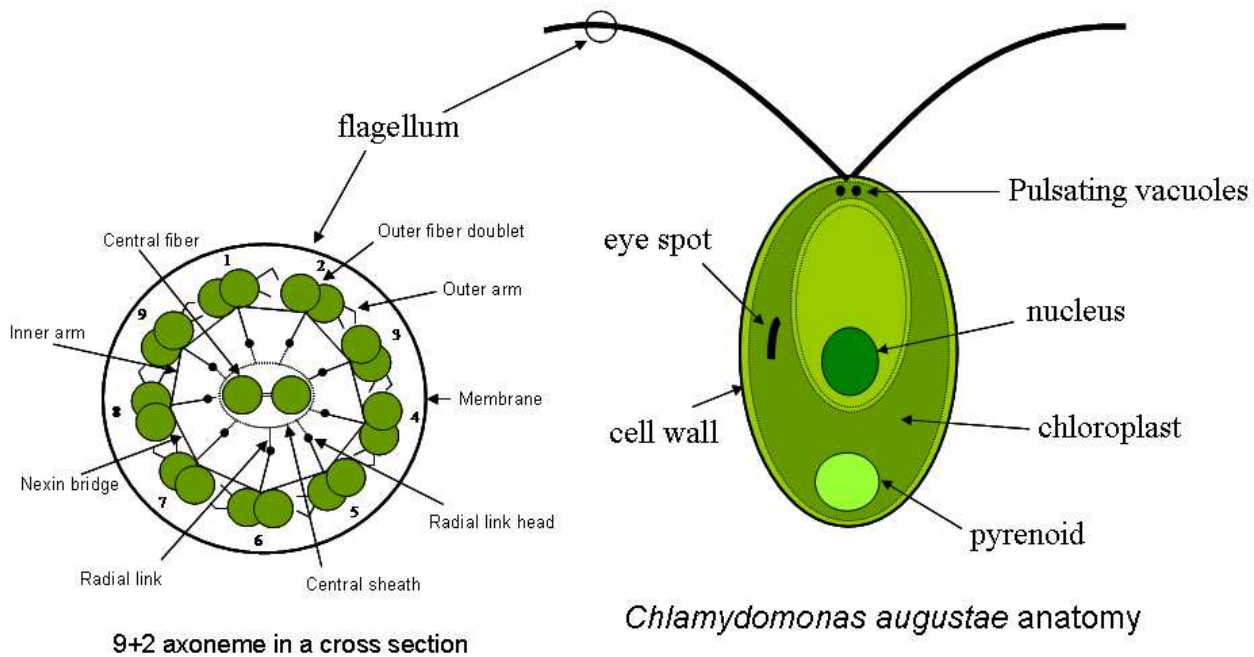


Figure 1.1: A schematic diagram of unicellular biflagellate green algae *Chlamydomonas augustae* cell structure and inner structure of cross section of the flagellum. The length of the cell body and both flagella is approximately equal to $10\ \mu\text{m}$.

The type of unicellular micro-organism that will be discussed in this thesis is a biflagellated green algae termed as *Chlamydomonas augustae*. It is found in aqueous environments (ice, fresh and sea water). A schematic diagram of the *C. augustae* cell is shown in Figure 1.1, showing the different parts and location of chloroplast and the pyrenoid, which stores starch, located at the posterior end of the cell. It has a roughly prolate spheroidal body shape and length of the cell body is approximately $10\ \mu\text{m}$. An eye-spot for light detection is located at the cell equator close to the surface of the cell. It has two long thin flagella attached at the anterior end of the cell body and are approximately $10\ \mu\text{m}$ long as well. The *trans*-flagellum is located away from the eye-spot as compared to the

cis-flagellum. The two flagella beat in a non-time-reversible breast stroke like motion to cause the swimming of the organism. *C. augustae* is said to swim in a manner similar to the human breast stroke with an effective-recovery stroke style, approximately in the direction of its axis of symmetry. During the effective stroke, the cell starts its swimming with both flagella directed vertically upward in the direction of cell swimming as shown in the Figure 1.1. The cell gain some ground by pushing the flagella back towards the cell body during the effective stroke. On the other hand ground is lost during the recovery stroke where a bend travels from base to tip of both flagella, resulting in a pull of the both flagella towards the cell body and re-positioned themselves to the starting position to undergo effective stroke again. However the latest research shows that this is not exactly the swimming style, actually the above defined two phases of beat overlap with each other (see, Ruffer and Nultsch [128], [129], [130], [131], [132]). As more ground is gained during the effective stroke as compared to ground lost during the recovery stroke, the net result is the cell movement in desired direction after completion of one flagella beat. The cell's beat frequency is found to be approximately 45-50 Hz and swimming speed is calculated as $55\text{-}67 \mu\text{ms}^{-1}$ on average (see Hill and Hader [58]). The typical cell is bottom heavy because the centre-of-mass is displaced towards the rear from the geometrical centre and cell contents are distributed asymmetrically within the cell.

The experimental investigations of Ruffer and Nultsch [128] for biflagellate green algae *C. reinhardtii* reveals that the flagella beat outside of the flagella plane and observed unequal beating pattern for both flagella. They observed that the *cis*-flagellum beat closer to the cell body in comparison to the *trans*-flagellum. This shows that the flagellar beat is not symmetric, but found synchronous, due to the fact that both flagella usually beat with approximately the same frequency. Recently, Polin *et al.* [118] investigated the stochastic relationship between the synchronous and asynchronous flagella beating of the cell.

Generally flagella and cilia have similar internal structure, Figure 1.1 shows different parts of the inner structure of a cross-section of a *C. augustae* flagellum. The basic structure comprise of micro-tubules running the length of the flagellum termed as axoneme and most of the time they occur in doublet pairs '9+2' format, 9 in a ring around 2 central micro-tubules. However tip and basal section of the flagellum may have different internal structure. A single bend usually occurs in a plane perpendicular to the plane formed by the central pair of micro-tubules as shown in the Figure 1.1. Since we are interested only in

the fluid flows around the swimming of the micro-organisms, consequently do not require the details of the internal structure and bending mechanism of the flagellum.

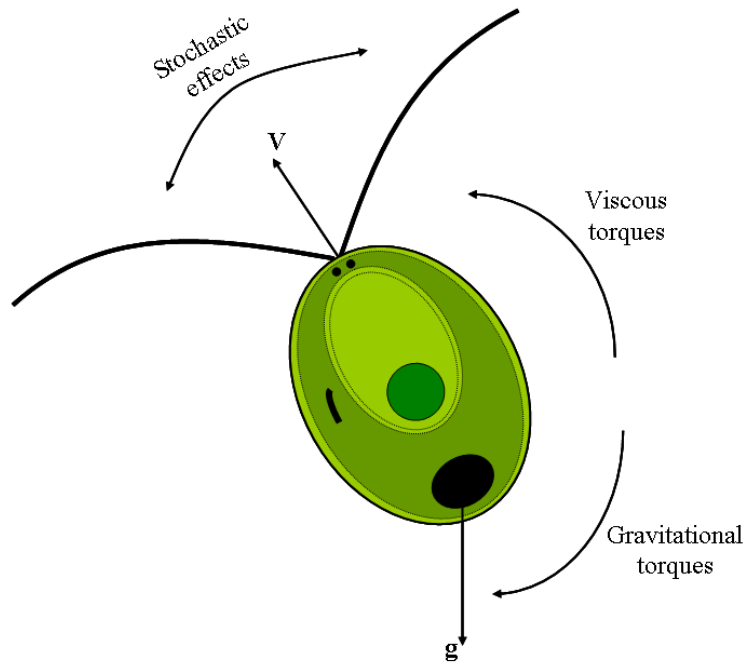


Figure 1.2: A schematic diagram of forces acting on the swimming biflagellate green algae *Chlamydomonas augustae* cell. The Gravitational torque arise due to the centre-of-gravity offset and viscous torque is caused due to the strain and vorticity in the fluid. \mathbf{V} is the cell's swimming velocity and \mathbf{g} represents the force due to gravity.

1.3 Orientation mechanism of swimming unicellular micro-organisms

The orientation of swimming green algae is not solely random as discussed by Wagner [144] and more recently by Kessler and his collaborators [80], [87], [78], [86]. The genus *Chlamydomonas* respond to the ‘taxes’ which bias the orientation of the swimming cell. Taxes are the simple rules for biasing the direction in which organism swim and defined as an innate behavioral response by a swimming organism away or towards a directional stimulus or termed as ‘an orientation behavior due to directional stimulus’ (see Holmes [66]). Taxes represent both the measurement of the surrounding environment and the physical mechanism by which organism responses to the stimulus. Thus majority of organisms have

evolved to use a combination of random movement and taxes (biased swimming directions) in order to attain the optimal conditions to improve their status and living. The examples of taxes include gravitaxis or geotaxis, a bias in direction of movement due to the gravity, chemotaxis which is a directional to gradients in chemical concentrations, and phototaxis which is a bias in direction of swimming away and towards the light.

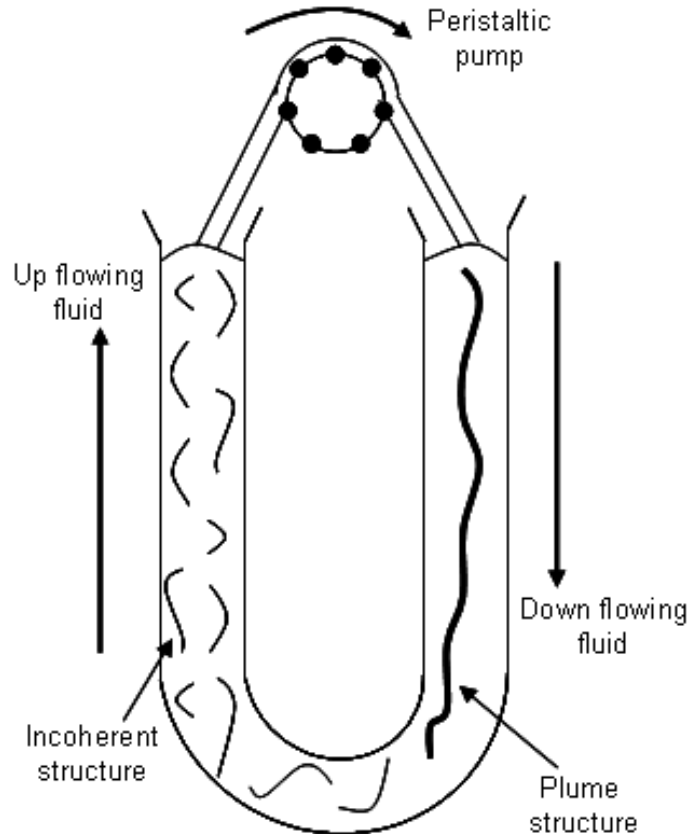


Figure 1.3: A schematic diagram of U-tube experiment for gyrotaxis in Poiseuille flow. Cells swim towards relatively downwards flowing fluid to form plume structure on right-hand side whereas swim away from upward flowing fluid and gather close to the wall shown on the left hand side of the U-tube.

Biflagellated green algae *Chlamydomonas* were found to be negatively gravitactic by Kessler [80]. Due to the bottom heaviness which resulted from the anisotropic mass distribution, they have tendency to swim upwards on average. They are phototactic as they swim towards weak light and away from strong light to evolve photosynthesis (see Foster and Smyth [40], Kessler [82], Vincent [143]). In addition to that these cells are ‘gyrotaxis’ a term defined by Kessler [79] to describe the phenomenon in which a balance between vis-

cous and gravitational torques occurs due to the cell geometry and centre-of-gravity offset as shown in the Figure 1.2. The gyrotaxis organisms swim vertically upwards on average due to the gravitaxis in the absence of fluid flow, whereas in the presence of fluid flow with the horizontal component of vorticity, they are tipped away from the vertical due to the viscous torque. Thus the gyrotactic organisms preferably swim away from the locally up flowing fluid and towards regions of locally down flowing fluid. Kessler demonstrated this phenomenon by setting up an experiment in vertical U-tube as shown in the Figure 1.3. He employed *C. nivalis* cells in a Poiseuille flow using a peristaltic pump and found that cells swam towards the edge of the tube and formed incoherent structure when fluid flowed upwards as shown on the left hand side of the tube. On the right-hand side where fluid flowed downwards, cells focused into a thin ‘plume’ structure in the centre away from the wall of the tube, which is called gyrotactic focusing as shown in the Figure 1.3.

Now to model the gravitaxis, we need to calculate the sedimentation speed of the non-swimming cells and the rotational torque caused by the this sedimentation. Following the work by Pedley and Kessler [114], we calculated the sedimentation speed of a non-swimming cell of spherical body shape as approximately $3 \mu\text{m}\cdot\text{s}^{-1}$. This is much smaller than the biflagellated swimming speed $60 \mu\text{m}\cdot\text{s}^{-1}$, thus we can ignore the aspect of sedimentation in comparison with the cells swimming. Roberts [125] proposed that viscous drag of the flagella on the cell body causes rotational orientation during the sedimentation because heavy cell body sediments faster than the flagella even for the case of uniform mass distribution of the cell. This mechanism as calculated by Roberts [126] also is of order of magnitude less than that due to bottom heaviness of the cell. Thus following the theoretical developments by Pedley and Kessler [114], we modelled gravitaxis in this thesis as due to the centre-of-gravity offset that causes the cell to be bottom heavy and neglect any rotational torque due to sedimentation.

It is also observed that *Chlamydomonas* cells swim away from the strong light termed as negative phototaxis and swim towards the weak light called as positive phototaxis, being a mechanical effect it involves complex detection and response phenomena (see Witman [148]). In this thesis, we do not consider phototactic effects and performed experiments in dark with room temperature of $24 \pm 1^\circ\text{C}$ and under the perfect laboratory conditions to avoid any bias in swimming due to light effects.

Hill and Hader [58] observed that the orientation of the swimming *Chlamydomonas* cells has a random component, using the swimming trajectories data of the tracking *C.*

nivalis cells. They found that the cells swim upwards on average and recorded some noise in results causing a spread in the trajectories. The results were further improved and investigated using laser velocimetry apparatus by Vladimirov *et al.* [142] to track hundreds of cells at a time. It is also observed that cells swimming direction is random which may be due to the unsynchronized growth of the cells which resulted in a population of variable size, shape and behavior as investigated by Vladimirov *et al.* [142]. Another reason can be the hydrodynamic interactions of the wall of the container and with each other in the concentrated suspensions of the cells. In addition to that even minor random changes in the flagella beating can cause the rotational variations, which can be due to the noise in biochemical reactions within the cell itself. Thus the combination of above defined factors may cause a stochastic effect to the orientation of cell swimming as mentioned in Figure 1.3 and may be employed for gyrotactic modelling.

Since Navier-Stokes equations describes the conservation of momentum in a continuum fluid. After defining the characteristic quantities as velocity (U), length (L), time (L/U) and denoting dimensionless quantities by bars we can write Navier-Stokes equations without body force in a non-dimensional form as

$$\text{Re} \left(\frac{\partial \bar{\mathbf{u}}}{\partial \bar{t}} + \bar{\mathbf{u}} \dot{\nabla} \bar{\mathbf{u}} \right) = -\nabla \bar{p} + \nabla^2 \bar{\mathbf{u}},$$

where

$$\bar{p} = \frac{pL}{\mu U} \quad \text{and} \quad \text{Re} = \frac{\rho U L}{\mu}.$$

The dimensionless Reynolds number (Re) is the relationship between the inertial forces and viscous forces.

1.4 Stokes Equations

In many problems in colloid science, microhydrodynamics, and nano scale fluid problems, the Reynolds number mostly assumed very small. This implies that viscous forces are dominant as compared to negligible inertial forces. Under such circumstances, to a good approximation, the flow is governed by the Stokes equation, where the inertial terms are neglected and the governing Navier-Stokes equations and equation of continuity for the fluid flow motion reduce to Stokes equations as

$$\begin{aligned} \nabla p &= \mu \nabla^2 \mathbf{u} + \mathbf{b}, \\ \nabla \cdot \mathbf{u} &= 0, \end{aligned} \tag{1.1}$$

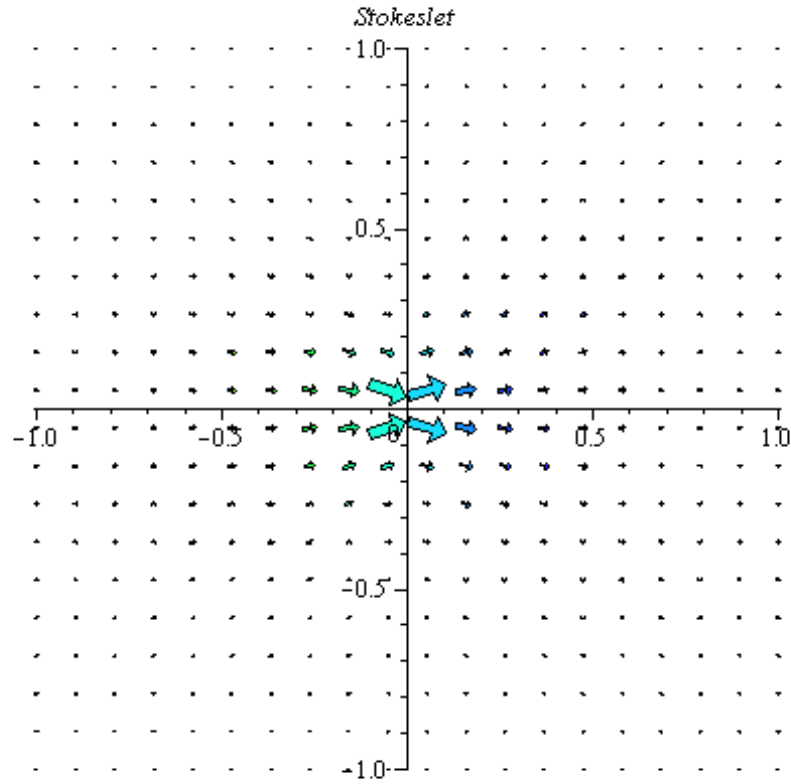


Figure 1.4: Vector plot of Stokeslet singularity solution

where p is the pressure, \mathbf{u} the velocity vector field, μ is the dynamic viscosity of the fluid and \mathbf{b} is the applied body force. The Stokes equations are linear and easy to solve as compared to Navier-Stokes equations. Due to linearity of the system of equations a solution to a complicated problem can be derived by the superposition of solutions to simpler problems.

The motion of a spherical body in a Newtonian fluid at low Reynolds number can be described by the Stokes equations. The velocity at a point on the surface of the sphere \mathbf{u} , the force on the sphere \mathbf{F} , and the torque about the centre of the sphere \mathbf{L} , can be calculated from the equations (1.1) as

$$\begin{aligned}
 \mathbf{u} &= \mathbf{u}_0 + \boldsymbol{\Omega} \times \mathbf{r}, \\
 \mathbf{F} &= \int_S (\boldsymbol{\sigma} \cdot \mathbf{n}) dS, \\
 \mathbf{L} &= \int_S \mathbf{r} \times (\boldsymbol{\sigma} \cdot \mathbf{n}) dS.
 \end{aligned} \tag{1.2}$$

Here $\boldsymbol{\Omega}$ is the angular velocity of the sphere about its centre, $\boldsymbol{\sigma}$ is the stress tensor, S is the surface of the sphere and \mathbf{n} is the outward drawn unit normal vector. The problem of calculating the velocity \mathbf{u} , given the forces and torques, is called the mobility problem, whereas the problem of solving for the forces and torques given the motion of the sphere is called the resistance problem.

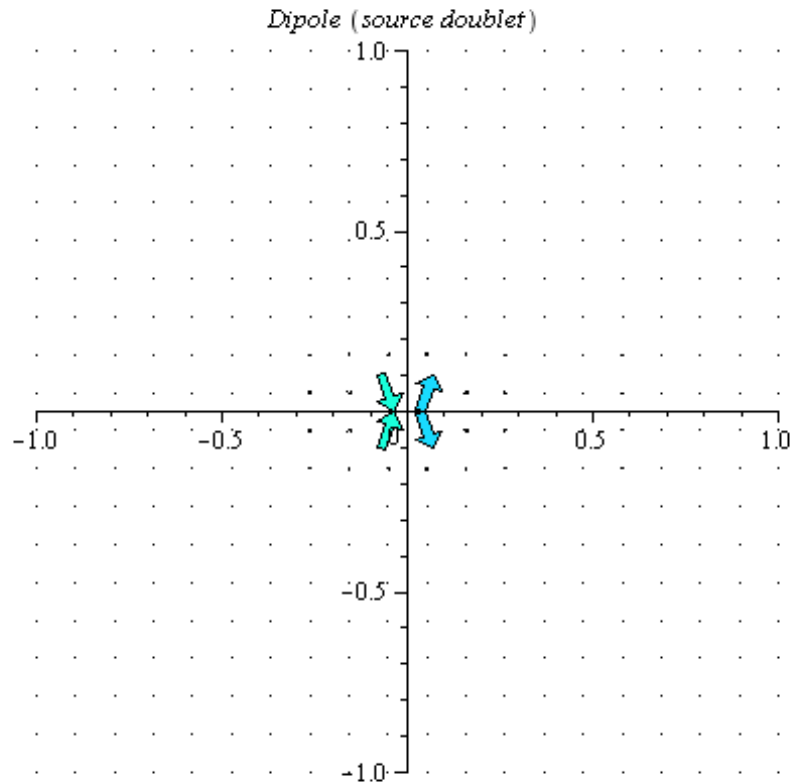


Figure 1.5: Vector plot of Dipole (source doublet) singularity solution

There are many different methods to solve the Stokes equations for the motion of sphere of radius a in a Newtonian fluid. Out of these, separation of variables leads to general solution in which the velocity and pressure fields are represented by spherical harmonics. Another simple approach is to use the solutions of Stokes equations generated by a point force, a source dipole and higher order singularities. These solutions are known as fundamental or singular solutions. As these solutions are linear in nature so they can be combined so as to satisfy the boundary conditions of the problem of different situations. This analytic approach is straight forward and easy to use that's why widely used in

microhydrodynamics and is adopted in the Stokesian dynamics method.

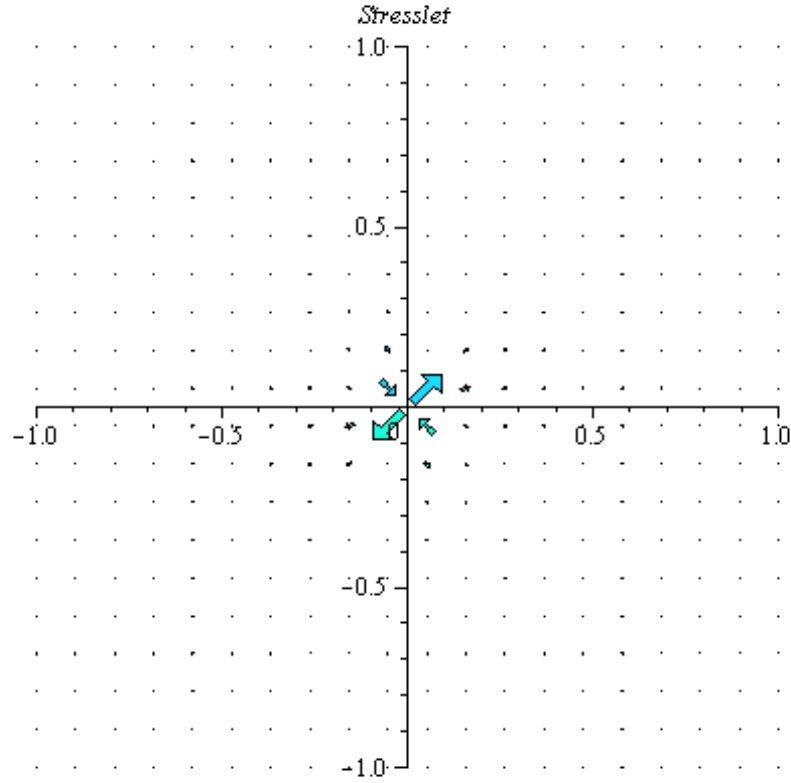


Figure 1.6: Vector plot of stresslet singularity solution

The Oseen tensor or Stokeslet singularity (see Oseen [107]) is defined as

$$S_{ij} = \frac{\delta_{ij}}{r} + \frac{r_i r_j}{r^3} \sim \frac{1}{r}, \quad \text{for large } r,$$

which is of order $\frac{1}{r}$. The derivative of the Stokeslet takes the form as

$$S_{ij,k} = \frac{\partial S_{ij}}{\partial r_k} = -\frac{r_k \delta_{ij}}{r^3} + \frac{r_j \delta_{ik}}{r^3} + \frac{r_i \delta_{jk}}{r^3} - \frac{3r_i r_j r_k}{r^5} \sim \frac{1}{r^2},$$

which is of order $\frac{1}{r^2}$, and known as Stokes doublet can be further rearrange as

$$S_{ij,k} = \frac{\partial S_{ij}}{\partial r_k} = \left(\frac{r_i \delta_{jk}}{r^3} - \frac{3r_i r_j r_k}{r^5} \right) + \left(\frac{r_j \delta_{ik} - r_k \delta_{ij}}{r^3} \right),$$

where the first term in brackets is symmetric term and is defined by Batchelor [4], a stresslet, whereas the second term which is antisymmetric is called as couplet. Additionally the antisymmetric term also named as rotlet in the literature (see Blake [14]).

Differentiating again using $\partial_i \delta_{ii} = 3$ gives the higher order singularities as

$$\nabla^2 S_{ij} = S_{ij,kk} = \frac{\partial^2 S_{ij}}{\partial r_k \partial r_k} = \frac{2\delta_{ij}}{r^3} - \frac{6r_i r_j}{r^5} \sim \frac{1}{r^3},$$

which is known as source dipole singularity or source doublet and is of order $\frac{1}{r^3}$.

Further differentiation leads to

$$\nabla^2 S_{ij,k} = \frac{\partial^2 S_{ij,k}}{\partial r_k \partial r_k} = -\frac{6r_k \delta_{ij}}{r^5} - \frac{6r_j \delta_{ik}}{r^5} - \frac{6r_i \delta_{jk}}{r^5} + \frac{30r_i r_j r_k}{r^7} \sim \frac{1}{r^4},$$

which is of order $\frac{1}{r^4}$, more complicated and called quadrapole singularity solutions.

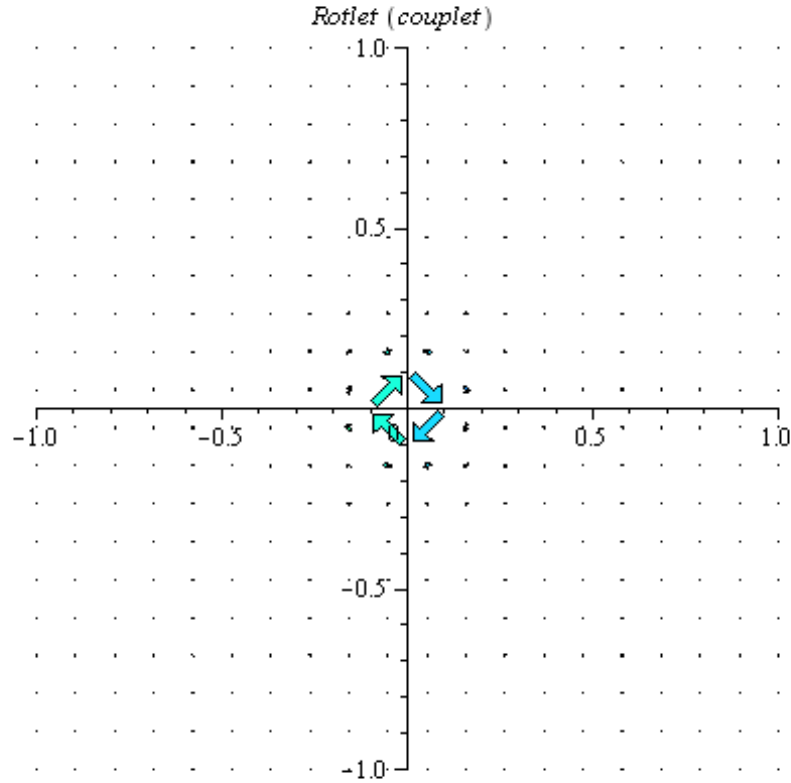


Figure 1.7: Vector plot of rotlet (couplet) singularity solution

Out of different possible solutions, one of the most useful solutions to the Stokes equation is that which describes the flow caused by a sphere of radius a propagating due to an applied force \mathbf{f} through an unbounded Newtonian fluid. If the sphere is far away from the source, the velocity and pressure fields are similar to that due to a point force of equal magnitude. This implies that the point-force solution gives a good far-field approximation and constitutes the basis of the solutions to the Stokes equations.

Now using the Dirac delta function δ to represent the point force \mathbf{f} , the singularly forced Stokes equations takes the form as

$$\begin{aligned}\nabla \cdot \mathbf{u} &= 0, \\ \nabla p &= \mu \nabla^2 \mathbf{u} + \delta(\mathbf{x}) \mathbf{F}.\end{aligned}\tag{1.3}$$

Oseen [107] found the solution of the above Stokes equations using the Green's function. Another approach is by taking the advantage of the relation between the Dirac delta function and Fourier transform. So by finding the Fourier representation of the Dirac delta function and solving the singular equations, the solution to the Stokes point-force problem can be calculated as

$$\mathbf{u}_j(\mathbf{x}) = \frac{F_k}{8\pi\mu} \left(\frac{\delta_{jk}}{r} + \frac{r_j r_k}{r^3} \right) = F_k S_{jk}(\mathbf{x}, \mathbf{y})\tag{1.4}$$

where \mathbf{y} is the location of the singularity and \mathbf{x} is the general position of a particle within the fluid. Here the multiple of \mathbf{F} i.e. S_{jk} is the solution to the singularly forced Stokes equation named as *Stokeslet*, *Oseen tensor*, *Green's function*, *fundamental solution* and *propagator function* (see Oseen [107], Blake [14]).

Due to the linearity of the Stokes equations the derivatives of the Stokeslet are also fundamental solutions to the Stokes equations. For the tensorial strength σ_{kl} , the velocity at the point \mathbf{x} due to Stokes doublet acting at the point \mathbf{y} will be

$$\mathbf{u}_j(\mathbf{x}) = \frac{\sigma_{kl}}{8\pi\mu} \left[\left(\frac{-\delta_{kl}}{r^3} + \frac{3r_k r_l}{r^5} \right) + \left(\frac{r_l \delta_{jk} - r_k \delta_{jl}}{r^3} \right) \right] = \sigma_{kl} S_{jkl}^D(\mathbf{x}, \mathbf{y}),\tag{1.5}$$

where the multiple of σ_{kl} i.e. S_{jkl}^D is the derivative of the Stokeslet known as Stokes-doublet. Here the first part in brackets is symmetric and known as stresslet singularity which corresponds to the straining motion of the fluid. The second term in the brackets is antisymmetric and named as rotlet or couplet singularity which is due to the torque acting on the fluid flow.

1.5 Singularity solution for spheres

Using the singularities as defined in section 1.4, we can construct the singularity solutions for the velocity of the sphere of radius a either translating or rotating in the Newtonian fluid (see Chwang and Wu [32], [33]).

1.5.1 Translating motion

The velocity disturbance \mathbf{u} caused by a translating sphere moving through an unbounded, Newtonian fluid under the influence of an applied force \mathbf{F} can be calculated as (see Binous and Philips [13])

$$\mathbf{u}_i(\mathbf{x}) = \frac{F_j}{8\pi\mu} \left[\left(1 + \frac{a^2}{6} \nabla_y^2 \right) S_{ij}(x, y) \right], \quad (1.6)$$

which can be further simplified as

$$\mathbf{u}_i(\mathbf{x}) = \frac{F_j}{8\pi\mu} \left(S_{ij}(x, y) + \frac{a^2}{6} \nabla_y^2 S_{ij}(x, y) \right), \quad (1.7)$$

now using the above values of the Stokeslet and Laplacian of Stokeslet i.e. source doublet as defined in section 1.4, we can rewrite as

$$\mathbf{u}_i(\mathbf{x}) = \frac{F_j}{8\pi\mu} \left[\frac{\delta_{ij}}{r} + \frac{r_i r_j}{r^3} + \frac{a^2}{6} \left(\frac{2\delta_{ij}}{r^3} - \frac{6r_i r_j}{r^5} \right) \right]. \quad (1.8)$$

Now on the surface of the sphere of radius a , we calculate the combination using Stokeslet and its Laplacian (source doublet) as (see Kim and Karrila [87])

$$\left(1 + \frac{a^2}{6} \nabla_y^2 \right) S_{ij}(x, y) = \frac{4}{3a} \delta_{ij}$$

Using above calculations we can find the approximate singular solution for the motion of the sphere translating with the steady velocity \mathbf{U} as

$$\mathbf{u}_i(\mathbf{x}) = \frac{U_j}{8\pi\mu} \left[\frac{\delta_{ij}}{r} + \frac{r_i r_j}{r^3} + \frac{a^2}{6} \left(\frac{2\delta_{ij}}{r^3} - \frac{6r_i r_j}{r^5} \right) \right] 6\pi\mu a, \quad (1.9)$$

which can further simplified as

$$\mathbf{u}_i(\mathbf{x}) = \frac{3a}{4} U_j \left(\frac{\delta_{ij}}{r} + \frac{r_i r_j}{r^3} \right) + \frac{a}{4} U_j \left(\frac{\delta_{ij}}{r^3} - \frac{3r_i r_j}{r^5} \right), \quad (1.10)$$

which is exactly the same solution as obtained by Oseen [107] for the translating motion of the sphere of radius a in an unbounded fluid flow as

$$\mathbf{u}_i(\mathbf{x}) = \frac{3a}{2} U_i \left(\frac{1}{r} \right) - \frac{a}{4} U_j \frac{\partial^2}{\partial r_i \partial r_j} \left(3r + \frac{a^2}{r} \right), \quad (1.11)$$

1.5.2 Rotating motion

The velocity disturbance \mathbf{u} caused by rotation due to torque applied to a sphere in an unbounded, Newtonian fluid at small Reynolds number can be written as

$$\mathbf{u}_i(\mathbf{x}) = \frac{1}{8\pi\mu} R_{ij} \Omega_j = \frac{1}{8\pi\mu} \left(\frac{r_j \delta_{ik} - r_k \delta_{ij}}{r^3} \right) \Omega_j = \frac{1}{8\pi\mu} \left(\frac{\epsilon_{ijk} r_k}{r^3} \right) \Omega_j, \quad (1.12)$$

where R_{ij} is the rotlet singularity and $\boldsymbol{\Omega}$ is the applied torque.

Now again following Kim and Karrila [87], on the surface of the sphere of radius a , the antisymmetric part of Stokes doublet i.e. rotlet as discussed in section 1.4 satisfies

$$R_{ij} = \frac{1}{r^3} (r_j \delta_{ik} - r_k \delta_{ij}) = \frac{1}{a^3} (r_j \delta_{ik} - r_k \delta_{ij}).$$

Hence the singular solution for the velocity of the sphere of radius a rotating with angular velocity $\boldsymbol{\Omega}$ takes the form as

$$\mathbf{u}_i(\mathbf{x}) = \frac{1}{8\pi\mu} \left[\left(\frac{\epsilon_{ijk} r_k}{r^3} \right) \Omega_j \right] 8\pi\mu a^3, \quad (1.13)$$

which further simplified as

$$\mathbf{u}_i(\mathbf{x}) = a^3 \left(\frac{\epsilon_{ijk} r_k}{r^3} \right) \Omega_j = (\boldsymbol{\Omega} \times \mathbf{r}) \frac{a^3}{r^3}, \quad (1.14)$$

which is exactly the same expression as calculated by Blake [15], the velocity field due to the rotlet singularity for a unit sphere

$$\mathbf{u}_i(\mathbf{x}) = \left(\frac{\epsilon_{ijk} r_k}{r^3} \right) \Omega_j = \frac{\boldsymbol{\Omega} \times \mathbf{r}}{r^3}. \quad (1.15)$$

1.6 Flagellar hydrodynamics

The study of hydrodynamics of flagellar locomotion mostly involved swimming analysis of monoflagellates micro-organisms like spermatozoa (see Taylor [138], Ramia [123], Smith *et al.* [136]). These investigations mostly focused on the computations of forces and torques produced by the beating flagellum and subsequently computing the velocity and angular velocity of the micro-organism.

The first landmark model was proposed by Taylor [138] in 1951, who gave the mathematical model of the propulsion of a flagellum like object (two dimensional thin sheet) due to traveling bending waves. He produced the first approximation to the velocity, the stress and rate of working in the sheet. He advanced the main principle underlying self-propulsion in a viscous flow that the resultant force which the fluid exerts on the body must be zero. He further investigated the helical flagellar waves for the case when the amplitude of the waves was small as compared to the radius of the flagellum. Due to this condition, experimental analysis was therefore not consistent with the theory.

In 1953 Hancock [56] improved Taylor's work and modelled the flagellum by distributions of Stokeslet and potential source doublets chosen to satisfy the no-slip boundary

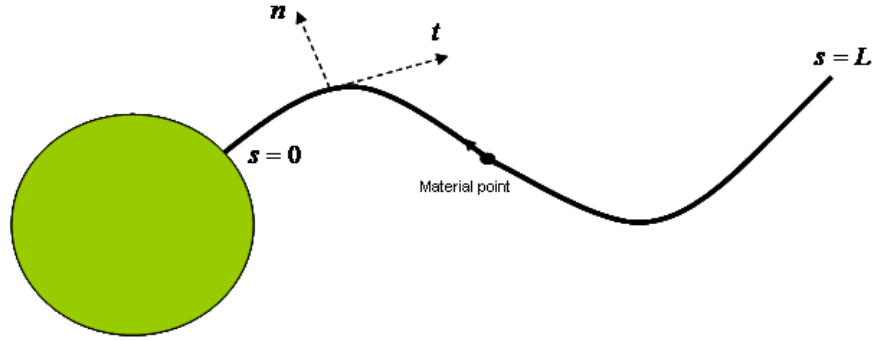


Figure 1.8: Schematic diagram of the flagellar propulsion of monoflagellate sea urchin spermatozoon.

condition on the flagellum. He showed that the approximation of a finite length flagellum by an infinite length flagellum is most accurate for a zero radius flagellum. Hancock was also able to show mathematically how an object translating tangential to its axis is subject to approximately half of the drag compared with if it translates normal to its axis, a conclusion which is important to low Reynolds number fluid dynamics and the propulsion of flagella and cilia. This forms the basis for an approximation for the hydrodynamical modelling of a swimming micro-organisms known as Resistive Force Theory.

1.6.1 Resistive Force Theory

Resistive Force Theory (RFT) was developed by Gray and Hancock [51] in 1955. They investigated an infinite flagellum of the spermatozoon and modelled a circular cross-section of the flagellum by a Stokeslet and a Stokes' dipole located at the centre. The theory states that a reasonable approximation can be obtained by assuming that the force per length, \mathbf{f} , exerted on the fluid by the flagellum at a point s (arc length along a flagellum) is proportional to the relative local centre line velocity, $\mathbf{V}(s, t)$ (in a coordinate frame in which fluid is at rest at infinity). Hence, the tangential and normal components of force per length take the form

$$f_t = \mu K_t V_t, \quad f_n = \mu K_n V_n, \quad (1.16)$$

where, μ is the fluid viscosity and the values of force per length coefficients proposed by Gray and Hancock [51] for computing flagellar motions are

$$K_t = \frac{2\pi}{\ln\left(\frac{2\lambda}{b}\right) - \frac{1}{2}}, \quad \gamma = \frac{K_n}{K_t} = 2, \quad (1.17)$$

where b is the cross-sectional radius of the flagellum and λ the wavelength. The ratio $\gamma = 2$, is only valid for the limiting case of a vanishingly thin flagellum. Johnson and Brokaw [75] rectify the problem and using Cox's [36] result, they derived the value of K_n as

$$K_n = \frac{4\pi}{\ln\left(\frac{2\lambda}{b}\right) + \frac{1}{2}}, \quad \gamma = 1.7. \quad (1.18)$$

However, experimental measurements were obtained for a sea urchin spermatozoon of $\gamma = 1.8$. So finally, Lighthill [94] considered the case of flagellum performing planar bending waves of small amplitude and derived the force per length coefficients, which were found to be consistent with experiments as

$$K_t = \frac{2\pi}{\ln\left(\frac{2q}{b}\right)}, \quad K_n = \frac{4\pi}{\ln\left(\frac{2q}{b}\right) + \frac{1}{2}}, \quad q = 0.09\lambda. \quad (1.19)$$

In the above two cases, they assumed infinite length of the flagellum and zero thrust during the calculation of the resistance coefficients for spermatozoa. As spermatozoa has large flagellar length in comparison with the cell's body diameter so that they could assume negligible drag caused by head. Later, Johnson and Brokaw [75] verified that Lighthill's resistance coefficients were valid even for organisms other than spermatozoa whose flagellar lengths approximately equal their body diameter.

RFT has been used for a variety of problems related to hydrodynamics of swimming micro-organisms. Shack *et al.* [133] calculated the resistance coefficients for helical wave form and found the results consistent with Lighthill [95]. Holwill and Sleigh [69] employed RFT to a flagellum with mastigonemes (increases the surface area of the flagellum) and found that organisms can propagate in the opposite direction to the direction of the propagation of bending wave if the length of the mastigonemes exceeds the flagellar length. Using RFT again Holwill [67] showed that the major production of thrust generated from the flagellum and the cell body oscillate to balance the torque produced by the flagellum. Blake [14] however investigated the flagellum locomotion near a plane surface and recalculated the resistance coefficients when flagella propel parallel and normal to the wall. He concluded that organisms swim more rapidly near but not exactly at the plane boundary. He also applied RFT for ciliated micro-organisms using methods to include the influence of each cilium upon every other by computing the fluid velocity of one cilium relative to mean fluid flow within the ciliate envelope. Chwang and Wu [31] approximated the viscous torque by a flagellar element rotating around its own axis again using RFT and assumed

the viscous torque $d\mathbf{M}_{flg}$ produced by an element of the flagellum as

$$d\mathbf{M}_{flg} = K_M \boldsymbol{\Omega}_{rel} ds, \quad (1.20)$$

where K_M and $\boldsymbol{\Omega}_{rel}$ are the resistance coefficient and relative angular velocity of the flagellum about its axis respectively.

Pironneau and Katz [115] used RFT to present insights into optimally energy efficient flagella beating by investigating the small amplitude only. Brokaw [21], [22] investigated using RFT to couple internal mechanics and fluid mechanics to realize the emergence of oscillatory propulsive waves. Jones *et al.* [76] investigated the swimming of biflagellate using RFT. Brokaw [23] analyzed beat pattern emergence in combination with detailed modelling of flagellar internal mechanics. Kinukawa *et al.* [88] used RFT in finding new interpretations of flagellar beat data and recently, Lauga *et al.* [89] investigated the trapping of bacteria near surfaces using RFT.

There are certain limitations found in the RFT proposed by Gray and Hancock [51]. In the first observation, they applied RFT to sinusoidal waveforms only. This issue was further investigated by Brokaw [20] who applied RFT to non-sinusoidal waves: arcs connected by straight lines. Holwill and Miles [68] further applied RFT to exponentially damped sinusoidal wave. They found good agreement with Gray and Hancock coefficients in the absence of cell body or in the presence of inert cell body. Chwang and Wu [31] investigated the helical wave form using RFT and found good agreement with the results. Silvester and Holwill [137] concluded the independence of RFT to the shape of the wave form for a small degree of accuracy. Secondly Gray and Hancock [51] assumed that each element produced the same amount of force for given relative velocity and angular velocity. They assumed flagellum as an infinitely long cylinder without considering the effects of the free end of the flagellum and the cell body. Johnson and Brokaw [75] showed that due to the end effect, the force produced by each element was not the same. Gray and Hancock [51] also assumed the hydrodynamic effect of one element of the flagellum on the other known as neighborhood effect, however Lighthill [94] found error in the weighting effect. Later, Jones [77] investigated the interactions between non-neighboring elements during the swimming biflagellates.

1.6.2 Slender Body Theory

Slender Body Theory (SBT) is applicable to various problems where a slender body micro-organism propels fluid or itself in a low Reynolds number Newtonian flow field. This allows the micro-organism movement and surrounding fluid flow in a three dimensional domain to be computed much more efficiently than by directly calculating the Stokes flow equations. In SBT flagellum is modelled using Stokeslet and Stokes dipole singularities as defined in section 1.4, as a series of small straight cylinders of length $2\delta s$. The velocity of the flagellar section as defined by Higdon [61] at any position \mathbf{x}^c can be written in the form of an integral equation as

$$u_i^c(\mathbf{x}^c) = \int_{|X^c| < \delta s} \left[\frac{1}{8\pi\mu} S_{jk}(\mathbf{x}^c, \mathbf{X}^c) f_k^c(\mathbf{X}^c) + \frac{1}{4\pi} D_{jk}(\mathbf{x}^c, \mathbf{X}^c) d_k^c(\mathbf{X}^c) \right] dX^c, \quad (1.21)$$

where \mathbf{X}^c is the local coordinate system of the section of the flagellum, \mathbf{f}^c is the force tangential and normal to the flagellar section and \mathbf{d}^c is the dipole strength normal to the flagellar section. Since the velocity at any point along the flagellum has contribution from all flagellar sections, so we assumed the flagellar sections small so that the Stokeslet and dipole strength become constant in each section. Now to find the velocity anywhere along the flagellum, we divide the flagellum into N circular cylinders and sum the contributions from each one of them as

$$\mathbf{u}(\mathbf{x}) = \sum_{n=1}^N \frac{\mathbf{f}(s)}{8\pi\mu} \int_{s_n-\delta s_n}^{s_n+\delta s_n} \mathbf{S}(\mathbf{x}, \mathbf{X}(s)) ds + \sum_{n=1}^N \frac{\mathbf{d}(s_n)}{4\pi} \int_{s_n-\delta s_n}^{s_n+\delta s_n} \mathbf{D}(\mathbf{x}, \mathbf{X}(s)) ds, \quad (1.22)$$

using the above boundary velocity $\mathbf{u}(\mathbf{x})$, we can construct the force and torque balance equations and subsequently find the micro-organism's swimming velocity \mathbf{U} and angular velocity $\mathbf{\Omega}$.

In the mid-1970s, researchers turned their attention to incorporating boundary effects for swimming micro-organisms which is of great importance for the case of mammalian sperm locomotion near the uterus wall. At the same time it was possible to calculate numerical solutions of the SBT integral equation for the force distribution on the flagellum. Batchelor [4] and Cox [36] investigated the Stokes flow past the slender bodies using SBT which was further investigated by Lighthill [94] who reduced the error by formulating his famous theorem. The Lighthill [94] study was found more accurate for the case of zero-thrust whereas for the case when flagellum is either finite or the organism is pushing a large inert body, Batchelor [4] and Cox [36] results are more accurate. In general there are two approaches that have been used while using SBT numerical calculations. In

the first approach researchers applied surface-velocity collocation directly to Hancock's SBT as used by Higdon [61], Smith *et al.* [135], and Clarke *et al.* [34]. In the second approach researchers worked out an approximation of Hancock's representation based on 'integrating out' the local Stokeslet/dipole contributions as initially calculated by Lighthill [94]. Further examples include Johnson [74], Gueron and Liron [55], Fulford *et al.* [41], and Gueron and Levit-Gurevich [54].

1.6.3 Comparison of RFT and SBT

For modelling of the swimming micro-organisms both RFT and SBT are extensively used. In general SBT is similar to the RFT, as in RFT force is directly proportional to the velocity at each flagellar section, but it differs with each flagellar section for the case of SBT. In RFT neighboring components of the flagella are not hydrocoupled as they are in SBT. After summation, the Stokeslet and dipoles have a contribution from every flagellar section to the flagellar velocity for SBT, which is termed as the neighborhood effect. Gray and Hancock [51] ignored this neighborhood effect while computing RFT coefficients, whereas Lighthill [94] recalculated these coefficients to improve the accuracy. SBT is also better choice for investigating the end effects of the flagellum. Tillett [140] found SBT a good first approximation at the free flagellar end in comparison to RFT. Johnson and Brokaw [75] found Lighthill's RFT resistance coefficients better than the Gray and Hancock coefficients even in the case of non-zero thrust in the presence of a cell body attached to the flagellum providing non-zero drag.

Since the SBT formulation involved an integral equation which further requires extensive numerical methods for the solution. Additionally, in SBT accurate representation of an organism's cell body is cumbersome as well. Additionally, Stokeslet and source dipoles singularities require respective image singularities inside the cell body to satisfy the no-slip boundary condition (see Blake [14]). Higdon [61] modelled the mono-flagellated micro-organism, both free swimming and near the plane boundary, using the image singularities numerically. He compared RFT and SBT and concluded that SBT should be employed to obtain accurate output. He also found that RFT with Lighthill's coefficients under-estimated the power output by the flagellum whereas Gray and Hancock coefficients under estimated in the zero-thrust case and over-estimated the non-zero thrust case.

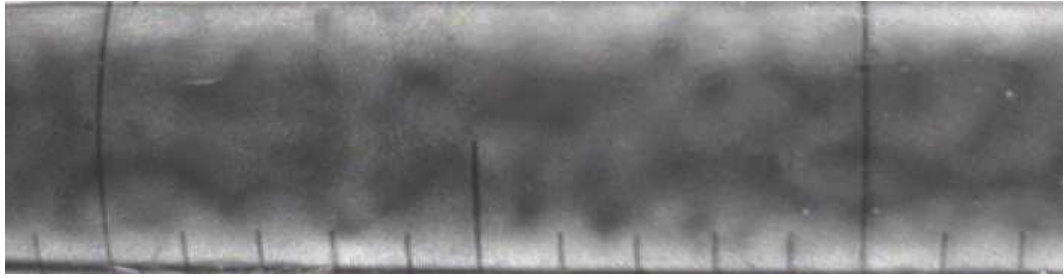
In 1994 Jones *et al.* [76] used RFT for the first time to model an external flow field acting upon the swimming biflagellate, which made a radical revision of the RFT without any

additional requirement. They assumed that neither flagellum of the biflagellate interacts with the other hydrodynamically. To avoid the cumbersome numerical calculation, they also assumed that there is no interaction of flagella with the body and the interaction occurs only near the slowly moving section of the flagella which are areas of minimal force production. This implies that they have negligible effect due to this interaction and can be ignored for modelling. Using these assumptions Jones *et al.* [76] found RFT a reasonable approximation for the analytical investigation of the locomotion of biflagellate in a flow field. This provides motivation and guidance to employ RFT for further analytical investigation of swimming biflagellates to different situations, like near the no-slip plane boundary as discussed in chapter 3 of this thesis. Thus by not using the SBT here we also not compromising the quality of results as by avoiding computing numerical methods for the solutions.

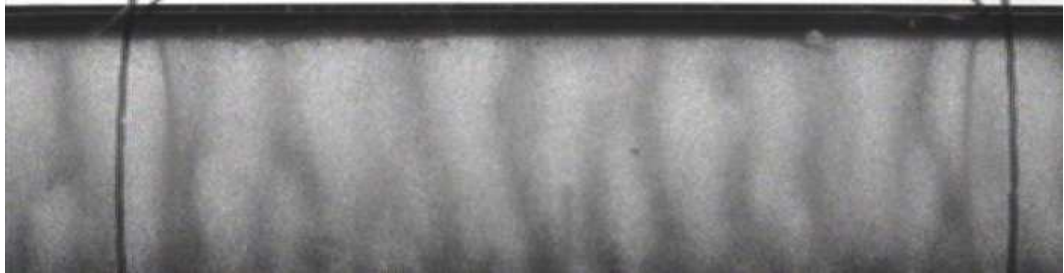
1.7 Bioconvection

Pattern formation in a suspension of motile swimming cells such as *C. nivalis*, *C. cohnii*, *Euglena gracilis*, *E. viridis* and *Tetrahymena pyriformis* was observed from long time ago. These patterns resulted from the instabilities of suspensions of cells which were denser than the surrounding fluid and appear as visually striking alternations of dark (high cell concentration) and light (low cell concentration) arrays of falling strips or spots when viewed from the top. This pattern formation may facilitate swimming micro-organisms in different forms ranging from better oxygen or nutrient mixing, enhanced reproduction, limited competition, optimize swimming speeds through hydrodynamic interaction.

In 1961 the term ‘bioconvection’ was first coined by Platt [116] to explain the process of pattern formation in shallow suspensions of motile swimming micro-organisms. However a literature survey reveals that the first ever experimental investigation of pattern formation was done by Wager [144] back in 1911 and other investigations recorded later by Loeffler and Mefferd [98], Nultsch and Hoff [106], Plesset and Winet [117], Kessler [80], Bees and Hill [7], [9]. Initial investigations of bioconvection were mainly focused on studies of pattern formations and effects by light, temperature, depth, concentration, and pH by different species of micro-organisms in perfect laboratory conditions. However Kessler in a series of papers [79], [80], [82], [84], has investigated pattern formation by *C. nivalis* and aspects of gyrotactic focusing or plume structure, such as the U-tube experiment as



(a) Image captured from top.



(b) Image captured from side.

Figure 1.9: A sample of images of bioconvection pattern formation by suspension of *C. augustae* recorded in a thin long horizontal tube while focusing on the centre of the tube.

discussed in section 1.3. Blip or pulse instabilities which resulted into localized regions of high concentration formed during down flowing plumes were also analyzed. They tend to establish when the initial cell concentration is large or when the velocity of the stream centreline is small.

Bioconvection results from the overturning and gyrotactic instabilities of suspensions of cells denser than the surrounding fluid. Overturning instabilities occur when upswimming cells accumulate at the top of the fluid in which they reside, forming a dense, unstable layer which is similar to the Rayleigh-Bernard convection [26]. A schematic diagram of the overturning instabilities by motile swimming micro-organism is shown in Figure 1.10. Gyrotactic instabilities arise from concentration fluctuations of sinking blobs of cells driving flows which bias cells to swim towards the blob. This accumulation of cells causes the blob to sink faster and leading to the formation of plumes structure anywhere in the suspension of cells as shown in the Figure 1.11.

Bees and Hill [7] investigated the quantitative analysis of the aspects of bioconvection pattern formations in suspension of *C. nivalis*. They used computational image analysis to extract the wavelength of the initial pattern formed before any non-linear affects arose

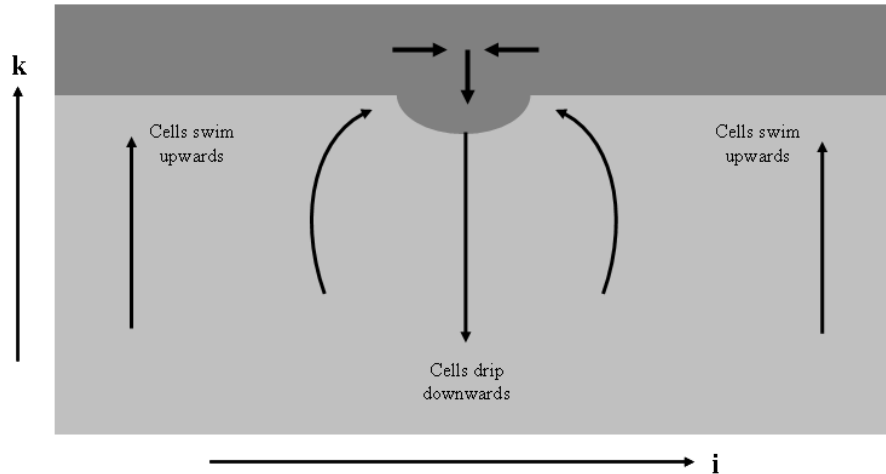


Figure 1.10: A schematic diagram of an overturning Rayleigh-Taylor instability from side. Cells which are denser than the fluid swim upward on average and gather at the top to form a suspension of greater density (dark region) than that of the fluid below.

and long term pattern wavelength establishes approximately 5 minutes after mixing of the suspension for different suspension concentration and depths. They found the initial pattern wavelength to be predominantly determined by depth of the suspension instead of cell concentration. However Cziráková *et al.* [37] using the bacteria *Bacillus subtilis* found the results other way around in respect of suspension depth and cell concentration. This may be because of the two different species ascribed particular taxes like gravity affects gyrotactic cells throughout the layer whereas aerotactic bacteria accumulate in thin layers where oxygen gradients exist. Taylor *et al.* [139] derived novel statistical measures for the regularity of patterns, Yamamoto *et al.* [149] investigated the critical depth and cell concentration required for pattern formation in the suspension of *C. reinhardtii*. Recently, Williams [147] investigated the initial pattern formations as a function of concentration and light intensity. The techniques presented in [7] and [37] are incorporated to analyze the initial and stable/final pattern wavelength in horizontal cylindrical tubes as a function of cell concentration, tube diameter, and flow rate in chapter 4 of this thesis.

Literature survey indicates that with the exception of few species of *biflagellates* and *dinoflagellate* blooms found in sea of Galilee (see Kessler [83]), there is little evidence of pattern formation found in real world environment. Thus majority of the micro-organisms forms bioconvection patterns under the conducive laboratory conditions, which include

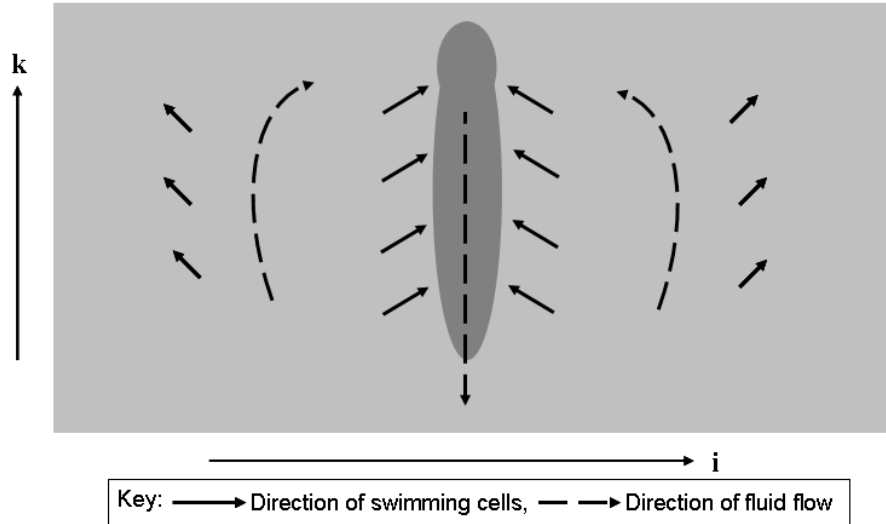


Figure 1.11: A schematic diagram of a gyrotactic instability without the upper boundary. Cells swim towards the down welling fluid and this addition of mass make the fluid more denser (dark region) resulting sink faster and form a plume structure.

good optical and temperature conditions, high cell concentrations and still fluid which is not very common in natural environment.

1.7.1 Mathematical models of bioconvection

Literature survey reveals that, there are many similarities between the bioconvection patterns formed by motile micro-organisms and thermal convection, so we can employ the techniques used in thermal convection problems in bioconvection analysis. Childress *et al.* [29] and Levandowsky *et al.* [91] established the first self-consistent theory for the onset of bioconvection. They incorporated purely upward swimming cells in a suspension with stress free and rigid upper boundary. They assumed the continuous density distribution and modelled cells as denser than the surrounding incompressible fluid. The sides of the container were assumed far apart so that the layer effectively has an infinite width and cell to cell interaction was negligible as suspension was modelled dilute. The cell's velocity was assumed to consist of random motion and steady upward drift in comparison to the media. The effects of non-Newtonian stresses and flow around the single cell was negligible because of the assumption that the length scale of the bulk motions were large in comparison with cell size and cell spacing. They used the Boussinesq approximation which implies that the cells affect the fluid flow through the change in density between the cells and the fluid.

Thus the governing equations for the motion of the fluid and cells were found as

$$\nabla \cdot \mathbf{u} = 0, \quad (1.23)$$

and

$$\rho \frac{D\mathbf{u}}{Dt} = -\nabla p + \mu \nabla^2 \mathbf{u} - \rho(1 + \alpha_e c)g\mathbf{k}, \quad (1.24)$$

which are equation for the conservation of fluid and conservation of momentum or Navier-Stokes equations respectively. Here $\frac{D}{Dt}$ represents the convective derivative, \mathbf{u} is fluid velocity, p is pressure, ρ and μ are the density and viscosity of the fluid respectively, $-g\mathbf{k}$ is acceleration due to gravity, and $\rho\alpha_e c$ is the extra density due to micro-organisms of cell concentration c at a point. Similarly Childress *et al.* [29] modelled the cell conservation equation as

$$\frac{\partial c}{\partial t} = -\nabla \cdot \mathbf{J}, \quad (1.25)$$

where \mathbf{J} is the net flux of cells through the fluid and consist of flux due to random motions and flux due to negatively gravitactic drift and can be defined as

$$\mathbf{J} = cU(c, z)\mathbf{k} - \mathbf{D} \cdot \nabla c, \quad (1.26)$$

where $U(c, z)$ is the cell swimming speed and \mathbf{D} is the orthotropic diffusion tensor introduced by Childress *et al.* [29] by taking account of random motions as

$$\mathbf{D} = \begin{bmatrix} D_h & 0 & 0 \\ 0 & D_h & 0 \\ 0 & 0 & D_v \end{bmatrix}. \quad (1.27)$$

It is also interesting to note that these equations are similar to the Rayleigh-Bénard equations for thermal convection problem (see Chandrasekar [26]). Childress [29] investigated an equilibrium solution for the case of no flow and found critical wavenumber zero corresponding to an infinite wavelength using linear analysis of the model. They have used *Tetrahymena* cells and found good agreement between model predictions and experimental results. The next worthy improvement in bioconvection modelling was done by Pedley and Kessler [111], who assumed the orientation of the spheroidal micro-organisms in a flow field and calculated the total torque as

$$\mathbf{L}_T = \mathbf{L}_v + \mathbf{L}_g, \quad (1.28)$$

where \mathbf{L}_v the viscous torque and \mathbf{L}_g is the gravitational torque. For gyrotactic bottom heavy micro-organism like *Chlamydomonas nivalis*, the gravitational torque using the summation convention takes the form as

$$L_{gx} = hmg\epsilon_{xyi}p_yk_i, \quad (1.29)$$

where h represents the centre-of-gravity offset from the geometric centre, m is the mass of the cell, g is the magnitude of the acceleration due to the gravity, \mathbf{k} is the unit vector in the vertical direction and ϵ_{xyi} is the Levi-Civita symbol. The expression for the viscous torque on a solitary body with zero Reynolds number (see Rallison [122]) takes the form as

$$L_{vx} = -\mu v [P_{xy}(v_y - u_y) + Y_{xy}(\omega_y^c - \frac{1}{2}\Omega_y) + R_{xyi}E_{yi}], \quad (1.30)$$

where μ is the fluid viscosity, \mathbf{v} and v are the cell's velocity and volume respectively, ω^c is the angular velocity of the cell, Ω is the vorticity and \mathbf{E} is the rate-of-strain tensor. \mathbf{P} , \mathbf{Y} and \mathbf{R} are tensors depending on the surface geometry and orientation of the cell only and for rigid prolate spheroid geometry can be defined as (see Batchelor [4])

$$P_{xy} = 0, \quad (1.31)$$

$$Y_{xy} = \alpha_{\parallel}p_xp_y + \alpha_{\perp}(q_xq_y + r_xr_y), \quad (1.32)$$

and

$$R_{xyz} = -\alpha_0Y_{xi}(r_ip_yq_z - q_ip_zr_y), \quad (1.33)$$

where \mathbf{p} , \mathbf{q} and \mathbf{r} form an orthonormal right-hand set of coordinates, α_{\parallel} , α_{\perp} and α_0 are shape parameters. The eccentricity α_0 for the prolate spheroid shaped cell is given by

$$\alpha_0 = \frac{a^2 - b^2}{a^2 + b^2}, \quad (1.34)$$

where a and b are the length and breadth of the cell. Since E_{yz} is symmetric, the equation (1.30) for viscous torque takes the form as

$$L_{vx} = -\mu v [Y_{xy}(\omega_y^c - \frac{1}{2}\Omega_y) - \alpha_0Y_{xi}\epsilon_{zij}p_jp_yE_{yz}]. \quad (1.35)$$

Using above equation and (1.29) and after substitution into equation (1.28) with setting $\mathbf{L}_T = \mathbf{0}$ implies

$$hmg\epsilon_{xyi}p_yk_i - \mu v [(\alpha_{\parallel}p_xp_y + \alpha_{\perp}(q_xq_y + r_xr_y))(\omega_y^c - \frac{1}{2}\Omega_y - \alpha_0\epsilon_{zyj}p_jp_yE_{iz})] = 0. \quad (1.36)$$

Now using the identity $\epsilon_{xyz}\epsilon_{ijk} = \delta_{xi}\delta_{yj} - \delta_{xj}\delta_{yi}$, and multiplying with $\epsilon_{xij}p_i$ transform equation (1.36) into

$$\dot{\mathbf{p}} = \frac{1}{2B} [\mathbf{k} - (\mathbf{k} \cdot \mathbf{p})\mathbf{p}] + \frac{1}{2}\boldsymbol{\Omega} \times \mathbf{p} + \alpha_0 [\mathbf{E} \cdot \mathbf{p} - \mathbf{p}\mathbf{p} \cdot \mathbf{E} \cdot \mathbf{p}], \quad (1.37)$$

where δ_{xy} is the Kronecker delta, $\dot{\mathbf{p}} = \boldsymbol{\omega}^c \times \mathbf{p}$ and gyrotaxis number

$$B = \frac{1}{2} \left(\frac{\mu\alpha_{\perp}}{h\rho g} \right), \quad (1.38)$$

as named by Pedley and Kessler [111] with units of seconds. The initial models for gyrotactic bioconvection by Pedley *et al.* [112] and Hill *et al.* [64] were based on the upswimming only and the cell swimming direction \mathbf{p} was found using Pedley and Kessler [111], as a function of vorticity and rate-of-strain tensor. The random motions were modelled by cell diffusion with constant isotropic tensor \mathbf{D} . Both models resulted in a finite, non-zero critical wavenumber for gyrotactic cells in comparison to a zero critical wavenumber for the earlier models [29], [91] of upswimming only.

1.7.2 Stochastic gyrotactic bioconvection model

In 1990, Pedley and Kessler [113] proposed a model, termed as new continuum model, using the strongly random isotropic diffusion tensor. They modelled the cell swimming direction in a probabilistic manner, using methods analogous to those of colloidal particles subject to Brownian motion (see Hinch and Leal [65]). They assumed a cell swimming direction probability density function $f(\mathbf{p})$, defined on a unit sphere, where \mathbf{p} is the cell swimming direction unit vector, given by

$$\mathbf{p} = (\sin \theta \cos \phi, \sin \theta \sin \phi, \cos \theta)^T, \quad (1.39)$$

where θ, ϕ are spherical polar angles termed as colatitude and cell orientation angle measured relative to \mathbf{k} and in the horizontal plane respectively. The probability density function $f(\mathbf{p})$ defined above in equation (1.39) in spherical polar coordinates, satisfies the Fokker-Plank equation which can be written as

$$\frac{\partial f}{\partial t} + \nabla \cdot (\dot{\mathbf{p}}f) = D_r \nabla^2 f, \quad (1.40)$$

where D_r is a constant rotational diffusivity associated with the rotational Brownian effects during the swimming of cells. The above equation (1.40) can be solved using equation

(1.39) for the rate of change of \mathbf{p} to calculate $f(\mathbf{p})$. Pedley and Kessler [113] defined the mean cell swimming velocity as

$$\mathbf{q} = \langle \mathbf{p} \rangle = \int_S \mathbf{p} f(\mathbf{p}) dS, \quad (1.41)$$

where S is the surface of the unit sphere and notation \mathbf{q} is used for simplification. The cell diffusivity tensor \mathbf{D} can be defined by following Pedley and Kessler [113] as

$$\mathbf{D}(t) = \int_0^\infty \langle \mathbf{V}_r(t) \mathbf{V}_r(t - t_1) \rangle dt_1. \quad (1.42)$$

Here \mathbf{V}_r is the cell velocity relative to its mean velocity. Using the assumption that the average cell's swimming speed V_s to be constant, Pedley and Kessler [113] removed the integral over time by further assumption that cell takes τ seconds to settled down to a preferred direction. This simplifies the equation (1.42) for diffusivity tensor to give

$$\mathbf{D} \approx V_s^2 \tau \langle (\mathbf{p} - \mathbf{q})(\mathbf{p} - \mathbf{q}) \rangle, \quad (1.43)$$

where τ is the direction correlation time scale. The basic equations and assumptions for the stochastic gyrotactic model developed by Pedley and Kessler [113] are based on the upswimming model proposed by Childress *et al.* [29]. Thus for the incompressible suspension, the equation of continuity and Navier-Stokes equation with an additional term due to the negative buoyancy of the cells takes the form as

$$\nabla \cdot \mathbf{u} = 0, \quad (1.44)$$

$$\rho \frac{D\mathbf{u}}{Dt} = \rho \left[\frac{\partial \mathbf{u}}{\partial t} + (\mathbf{u} \cdot \nabla) \mathbf{u} \right] = -\nabla P_e + nv\Delta\rho \mathbf{g} + \nabla \cdot \boldsymbol{\Sigma}, \quad (1.45)$$

where $\mathbf{u}(\mathbf{x})$ is the velocity of the suspension of swimming cells, $\boldsymbol{\Sigma}(\mathbf{x})$ the fluid stress tensor, $n(\mathbf{x})$ is the local cell concentration, μ is the fluid viscosity, $p_e(\mathbf{x})$ is the excess pressure over hydrostatic, v is the mean volume of cell and $\Delta\rho$ is the difference between the cell density and fluid density. The cell conservation equation can be defined by following Childress *et al.* [29] and Pedley *et al.* [113] as

$$\frac{\partial n}{\partial t} = -\nabla \cdot [n(\mathbf{u} + V_s \langle \mathbf{p} \rangle)] - \mathbf{D} \cdot \nabla n, \quad (1.46)$$

where $\langle \mathbf{p}(\mathbf{x}) \rangle$ is the mean cell swimming direction, V_s is the mean cell swimming speed and $\mathbf{D}(\mathbf{x})$ is the cell diffusion tensor. In addition to the negative buoyancy effect, Pedley and Kessler [113] considered all effects that cell may have on the bulk fluid motion and defined the fluid stress tensor as

$$\boldsymbol{\Sigma} = 2\mu\mathbf{E} + \boldsymbol{\Sigma}^{(d)} + \boldsymbol{\Sigma}^{(s)} + \boldsymbol{\Sigma}^{(p)}, \quad (1.47)$$

where $\Sigma^{(d)}$ are stresses associated with the effective particle rotation due to rotational diffusion, $\Sigma^{(s)}$ are stresslets due to the swimming motions of individual cells and $\Sigma^{(p)}$ are Batchelor stresses that are due to the fact that cells do not allow the fluid to deform in the same way as it would in the absence of rigid cells. Pedley and Kessler [113] found that in addition to basic Newtonian stress, stresslets makes notable contribution in comparison to other stresses in fluid stress tensor expression (1.47).

Pedley and Kessler [113] used this new model to investigate the linear stability and found good agreement with the Pedley *et al.* [112] gyrotaxis model. Bees and Hill [9] found an equilibrium solution and investigate a linear stability analysis for a finite layer depth with rigid boundary using Pedley and Kessler [113] model. They concluded from their investigations that the introduction of gyrotaxis creates a non-zero critical wavenumber associated with a finite wavelength and additionally, found that increasing gyrotaxis destabilizes the system for large wavenumbers. Bees and Hill [9] predicted wavelength ≈ 1 mm in comparison to experimental estimate of 4 – 7 mm (see Bees and Hill [7]) at the onset of bioconvection.

1.7.3 Recent development in bioconvection modelling

In 1998 Bees *et al.* [9] computed analytic solutions of the Fokker-Planck equation in terms of spherical harmonics for the orientation of dipolar particles in a steady shear flow with a uniform external field. Using Pedley and Kessler [113] model, Bees and Hill [10] performed a weekly non-linear analysis for a deep layer and found that the bifurcation to the gyrotactic instability is supercritical in comparison to the subcritical for gravitactic instability found by Childress and Spiegel [28]. This motivates to employ linear stability analysis to predict initial wavelengths of pattern formation in suspensions of gyrotactic swimming cells.

Hill and Bees [62] computed the first rational expression for the diffusion coefficients of gyrotactic cells in vertical shear flow, using generalized Taylor dispersion theory. They concluded that as vorticity approaches to infinity, consequently the effective diffusivity approaches to zero because of the cells tumbling in the shear plane, in contrast to earlier derived expressions for diffusivity by Bees *et al.* [8] and Pedley and Kessler [113]. This theory was further extended by Manela and Frankel [101] for axisymmetric micro-organisms which include local rate-of-strain and vorticity effects as well. Ghorai and Hill [45] numerically study gyrotactic bioconvection using a vorticity stream function formulation of the

Pedley *et al.* [112] model in 2D and 3D geometry. Ghorai and Hill [46] also computed the first computational examples of the bottom-standing plumes structures found in pattern formations and concluded that they are mostly transient, which implies the reason for the unavailability of the analytic solutions for these structures. Williams [147] in her PhD thesis extended the work of Bees and Hill [9] by including phototaxis using three physically diverse and novel methods. She performed linear stability analysis for each model and the most unstable wavenumber for a range of parameters values was predicted. She later performed experimental investigations and found good agreement with the theoretical results.

Bees and Croze [11] analyzed the dispersion of swimming cells in a flow in a vertical tube in the laminar regime and predicted the effective drift and diffusion in a gyrotactic algae in plumes. Recent developments in theoretical studies of bioconvection comprise of investigating thermo-bioconvection and bioconvection in the vicinity of the boundaries of various geometries, pattern formation in a porous media etc.

1.8 Applications and motivation of the study of biflagellate

Recently, micro-organisms have been used in establishing algal photo-bioreactors for biodiesel production and waste water treatment plants. Due to present price hikes of fossil fuels and biodiesel from food crops, they can be act as the most efficient source of feedstock for biofuels or biodiesel industry (see Chisti [30]). They can be also helpful to reduce accumulation of carbon dioxide from using fossil fuels in the environment. Durham *et al.* [38] showed that transient gyrotactic trapping of motile phytoplankton can generate thin, high cell concentrated layers in the ocean which implies consequences for the ecology of toxic algae and demonstrate the ecological importance of these micro-organisms.

Research in biotechnology applications has accelerated in recent years due to the possibility of using micro-organisms to produce hydrogen gas or biodiesel for the renewable energy sector (see Melis and Happe [104] and Chisti [30]). There are two main methods used for hydrogen production from micro-organisms as described by Williams [147]. The first one called as photobiological process which require, light as energy source, a substrate to donate electrons to the hydrogen production complex and a catalyst to combine protons and electrons to produce hydrogen gas (see Ghirardi *et al.* [43]). The second method is called as fermentative process in dark where anaerobic bacteria grow on carbohydrate

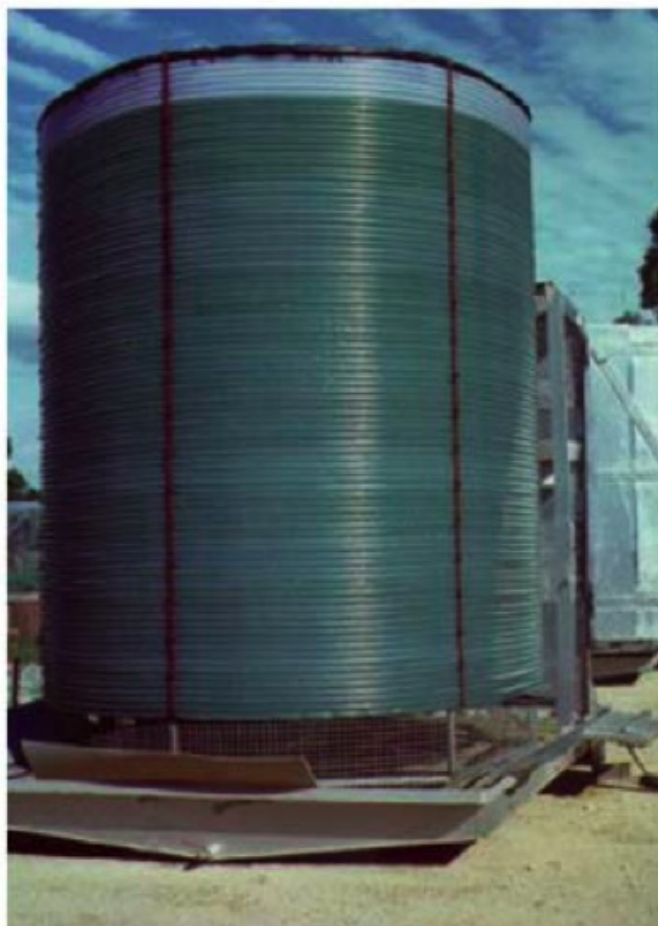


Figure 1.12: A design of tubular helical alga photobioreactor of 1000 L capacity at Murdoch University. Courtesy of Professor Michael Borowitzka, Murdoch University, Australia.

rich substrates and produce hydrogen gas and CO_2 as fermentation output (see Hawkes *et al.* [60]).

For the optimal and commercially competitive production of the renewable energy i.e. hydrogen gas or biodiesel from micro-organisms, existing bioreactors design require scrutiny. In the presently used closed bioreactors, algae are cultured in laminar or turbulent flows through arrangements of horizontal, inclined or vertical tubes, bubbled for gas exchange, and concentrated by flocculation, filtration or centrifugation in a manner of inert collides or mare chemicals (see Grima *et al.* [52], Chisti [30]). However, swimming biflagellate micro-organisms like *C. augustae* or *Dunaliella* used for biofuels production do not behave like inert chemicals or collides, their swimming trajectories close to boundaries of various geometries, peculiar collective motions and consequent transport properties need to be taken into account and investigated. The gyrotactic biflagellate motile cells form

patterns while swimming in various geometries and alter the flow even it was laminar or turbulent flow within that geometry.

There is a reasonable link between the bounded biflagellate swimming and bioconvection in a suspension of cells with renewable energy production. As most bioreactor design involves arrangements of thin tubes as shown in Figure 1.12 then this definitely require the study and understanding of the biflagellate swimming in the vicinity and away from the boundary. The plume formation during bioconvection creates an uneven distribution of the cells throughout the tubes of the bioreactors, which resulted in a non-uniform distribution of light and may optimize the output and efficiency of the bioreactors. Another area include the cell clogging phenomena within the tubes of the bioreactors could be investigated with this study of biflagellate swimming and bioconvection. Thus the investigations of the hydrodynamics of bounded cell swimming and pattern formation in thin tubes are the main areas of research in this thesis which are inherently linked and lead to the applications in renewable energy sector.

1.9 Review of the thesis

In this thesis we have investigated the bounded swimming using Resistive Force Theory (RFT), and experimental and theoretical techniques to study the mechanics involved in advected bioconvection in a suspension of gyrotactic swimming of unicellular biflagellated green algae named as *Chlamydomonas augustae*.

Chapter 2 describes the mathematical modelling and analysis of swimming biflagellate green algae in an unbounded domain using the Resistive Force Theory. The detailed analytic calculations and technique was used similar to the work by Jones *et al.* [76]. In order to simplify the tedious calculations we have simplified the implementation of the flagellar beat pattern and employed the use of the software Maple. These additional steps really worked well with verifying and improved the calculations done by Jones *et al.* [76] for unbounded biflagellate swimming.

Chapter 3 involves the mathematical modelling and analysis of the swimming biflagellate green algae in the vicinity of the no-slip stationary plane boundary using the Resistive Force Theory and image singularity solutions.

Chapter 4 investigates the experimental analysis of bioconvection in thin horizontal tubes to obtain quantitative data on the pattern wavelength. The dependence of pattern

formation on suspension concentration, time, tube diameter, and flow rate is discussed in detail. The contents of this chapter have already been published in *Physical Biology* international journal.

Chapter 5 details the modelling of the continuum model suggested by Kessler [85] with the addition of random cell swimming speed between the two horizontal plates in the presence of weak poiseuille flow for analytical linear analysis of the problem. The method used here is similar to the investigations done by Bees and Hill [9].

Chapter 6 includes the conclusions of the work done, limitations and future research directions in the projects involved in this thesis.

Chapter 2

Biflagellate swimming in an unbounded domain

2.1 Synopsis

In this chapter, we investigate the unbounded swimming of a unicellular biflagellated micro-organism. The swimming cell is modelled analytically using the Resistive Force Theory of Gray and Hancock [51]. Here, we first reproduce the detailed method and calculations of Jones *et al.* [76] for swimming biflagellates. This flagella beat pattern is then modified by redefining the position vector to ease the solution method involving cumbersome calculations. This arrangement results in a single position vector from the centre of the cell body that satisfies the three different parts of the flagella beat and become angle θ dependent when swimming in a plane. This modification also simplifies the recovery stroke integration calculations in comparison with the integrals involved in Jones *et al.* [76]. Later, we employ the software Maple to find analytical expressions for the swimming velocity and angular velocity of the swimming cell when swimming vertically upward and find good agreement with the Jones *et al.* [76] results. Additionally, using the same Maple code we investigate the swimming cell for different orientations.

2.2 Introduction

In 1994 M. S. Jones, L. Le Baron and T. J. Pedley published a paper [76] in which they presented a simplified mathematical model of the biflagellate *Chlamydomonas nivalis* at small Reynolds number. They employed an approximation called Resistive Force Theory

(RFT) to model and calculate the cell's swimming velocity and angular velocity relative to the ambient flow field as a function of the vorticity and strain rate in the vicinity of the cell. The cell body was assumed to be spherical and both flagella beat symmetrically in a vertical plane. For the simplified planar swimming model the ambient flow field lies in the same vertical plane. They showed that RFT was quite adequate to reproduce the experimentally observed swimming velocity and angular velocity of bottom-heavy biflagellated microorganisms.

By employing RFT Jones *et al.* [76] assumed no hydrodynamic interaction of flagella with the cell body and no interaction between neighboring elements of each flagellum. However, interactions might only take place at the slow moving sections of the flagella during the recovery stroke, which caused negligible force production effects (Ruffer and Nultsch [128]). Jones *et al.* [76] also assumed that the change in the body orientation and change in ambient flow field during one beat is negligible. They further assumed that one flagellar beat is equal to one traveling wave and approximately calculated the flagellar wavelength as equal to double the flagellar length. The earlier continuum models of cell suspensions by Pedley and Kessler [113] and [114] assumed that the viscous torque on a swimming cell same as the viscous torque on the spheroidal body, and cell swims with constant speed in the direction of the axis of symmetry. They improved these continuum models by considering the effects of the flagellum in addition to cell's body and conclude that the swimming speed and swimming direction of the organism could not remain constant and parallel to the axis of symmetry respectively as found by Pedley and Kessler [113]. The viscous torque was also found different in comparison with the Pedley and Kessler [113] due to the presence of the flagellum not solely because of the organism's cell body alone.

2.3 Resistive Force Theory

Resistive Force Theory (RFT) was developed by Gray and Hancock [51]. They investigated an infinite flagellum of a spermatozoon, and modelled its circular cross-section by Stokeslet and source doublet singularities located along the centre-line of the flagellum. The theory states that a reasonable approximation can be obtained by assuming that the force/length, \mathbf{f} , exerted on the fluid by the flagellum at a point s (arc length along a flagellum) is proportional to the relative local centre line velocity, $\mathbf{v}(s, t)$ (in a coordinate

frame in which fluid is at rest at infinity). In other words, the viscous force exerted upon an element of flagellum, $d\mathbf{F}_{flg}$, is linearly proportional to the velocity of fluid relative to the element, \mathbf{u}_{rel} :

$$d\mathbf{F}_{flg} = \mu [K_t(\mathbf{u}_{rel} \cdot \mathbf{t}) \mathbf{t} ds + K_n(\mathbf{u}_{rel} \cdot \mathbf{n}) \mathbf{n} ds], \quad (2.1)$$

where, μ is the fluid viscosity, $\mathbf{t} ds$ is an element of flagellum, \mathbf{t} and \mathbf{n} are unit vectors to the element acting in the tangential and normal direction. The dimensionless resistance coefficients K_t and K_n acting in the tangential and normal direction as proposed by Gray and Hancock [51] for computing flagellar motions are

$$K_t = \frac{2\pi}{\ln(\frac{2\lambda}{b}) - \frac{1}{2}}, \quad \gamma = \frac{K_n}{K_t} = 2, \quad (2.2)$$

where b is the cross-sectional radius of the flagellum and λ is the wavelength measured along the centre line of the flagellum. The ratio $\gamma = 2$ is only valid for the limiting case of a vanishingly thin flagellum. Johnson and Brokaw [75] rectify the problem of consistency of results with experiments and using Cox [36], they determine that

$$K_n = \frac{4\pi}{\ln(\frac{2\lambda}{b}) + \frac{1}{2}}, \quad (2.3)$$

such that $\gamma = 1.7$ for sea urchin spermatozoon. However, experimental measurements were obtained for a sea urchin spermatozoon giving $\gamma = 1.8$. Finally, Lighthill [94] considered the case of a flagellum performing planar bending waves of small amplitude and rederived the resistance coefficients

$$K_t = \frac{2\pi}{\ln(\frac{2q}{b})}, \quad K_n = \frac{4\pi}{\ln(\frac{2q}{b}) + \frac{1}{2}}, \quad q = 0.09\lambda, \quad (2.4)$$

where q is a characteristic length representing the range of influence exerted by a force acting on an element of the flagellum, which were found to be consistent with the experiments. The above two cases assumed that the flagellum was of infinite length and zero thrust, for the calculation of the resistance coefficients for spermatozoa. As spermatozoa have large flagellar length in comparison with the body diameter, so they have assumed negligible drag caused by spermatozoa's head. Later, Johnson and Brokaw [75] verified that Lighthill's resistance coefficients were valid even for organisms other than spermatozoa whose flagellar length is greater than their body diameter.

RFT is an approximation which is best suited for the case when flagellar length l is large as compared to the body radius a as in the case of spermatozoon and it takes no account

Name with dimensions	Dimensionless form
Distance - $[L]$	$\mathbf{x} = a \tilde{\mathbf{x}}$
Velocity - $[L S^{-1}]$	$\mathbf{v} = \left(\frac{a}{T}\right) \tilde{\mathbf{v}}$
Angular velocity - $[S^{-1}]$	$\boldsymbol{\omega} = \left(\frac{1}{T}\right) \tilde{\boldsymbol{\Omega}}$
Rate-of-strain - $[S^{-1}]$	$\mathbf{E} = \left(\frac{1}{T}\right) \tilde{\mathbf{E}}$
Vorticity - $[S^{-1}]$	$\boldsymbol{\omega} = \left(\frac{1}{T}\right) \tilde{\boldsymbol{\omega}}$
Function ξ - $[Kg^{-1}m^{-1}s]$	$\xi = \left(\frac{3\mu v}{4\pi}\right) \tilde{\xi}$

Table 2.1: Table of non-dimensionalisation.

of the coupling between neighboring elements of the flagella. The neighboring effect is dominant at the free ends of the flagella and close to the cell body. However, in our case, the cell under consideration (*Chlamydomonas*) has flagellar length approximately equal to body diameter. Johnson and Brokaw [75] suggested to employ slender-body theory for the case when cell body produced significant drag, but slender-body theory involves cumbersome calculations which require numerical methods for the solution. In order to obtain analytical solutions, we follow Jones *et al.* [76] and employ RFT, and have computed the results by using the two sets of resistance coefficients with (a) Gray and Hancock's and (b) Lighthill's to investigate the errors of these resistance coefficients.

2.4 Force and torque balance for gyrotactic biflagellates

To model the swimming of a biflagellated bottom heavy single cell of *C. nivalis* in a viscous fluid, consider C to be the geometric centre and G to be the centre-of-gravity, where both lie on the major axis \mathbf{p} of the cell. The unit vector \mathbf{p} represents the orientation of the cell. Let H be the displacement of the centre-of-gravity G from the geometric centre C as shown in Figure 2.1(a). Below we shall summaries the arguments of Jones *et al.* [76].

Here we have used *C. augustae* (previously, and possibly mistakenly, termed *C. nivalis* in the literature) as our model micro-organism for investigations of unbounded swimming. In general, for swimming micro-organisms inertia is negligible because the Reynolds numbers for the motion of the cell and its flagella are very small (see chapter 1). This means that the viscous forces in the fluid flow are dominant as compared to inertial forces. Thus the orientation and motion of the organism can be modelled, by setting to zero the total

force \mathbf{F}_{tot} and total torque \mathbf{L}_{tot} at any instant acting on the cell during the flagellar beat, which is the sum of cell body (*bdy*), gravitational (*grv*) and flagella contributions (*flg*):

$$\mathbf{F}_{tot} = \mathbf{F}_{bdy} + \mathbf{F}_{grv} + \mathbf{F}_{flg} = 0, \quad (2.5)$$

and

$$\mathbf{L}_{tot} = \mathbf{L}_{bdy} + \mathbf{L}_{grv} + \mathbf{L}_{flg} = 0. \quad (2.6)$$

To determine the contributions due to the spherical body of the cell, we neglect the presence of the flagella and assume only the hydrodynamic contributions on the body in the Stokes flow. The viscous body force and viscous body torque for a spherical body shape (e.g. see Kim and Karrila [87]) are

$$\mathbf{F}_{bdy} = -6\pi\mu a\mathbf{v}, \quad (2.7)$$

and

$$\mathbf{L}_{bdy} = -8\pi\mu a^3 \left(\boldsymbol{\Omega} - \frac{1}{2}\boldsymbol{\omega} \right), \quad (2.8)$$

where, \mathbf{v} and $\boldsymbol{\Omega}$ are the velocity and angular velocity of the body respectively, $\boldsymbol{\omega}$ is the vorticity of the ambient flow, a is the radius of the cell body and μ is the viscosity of the fluid.

Since for *Chlamydomonas* it is observed that the sedimentation speed ($2.2 \mu\text{m s}^{-1}$) is very low as compared to the swimming speed ($60\text{-}100 \mu\text{m s}^{-1}$), (see Yoshimura *et al.* [149] and Vladimirov *et al.* [142]) then as we know that sediment speed represents the gravitational force so we can take

$$\mathbf{F}_{grv} = \left(\frac{\rho - \rho_0}{v} \right) \mathbf{g} = 0, \quad (2.9)$$

where ρ and v are the density and volume of the cell respectively and \mathbf{g} is the gravitational acceleration. The gravitational torque due to the centre-of-gravity offset H , the displacement of G from C as mentioned in Figure 2.1(a), was investigated by Pedley and Kessler [111] and can be written in terms of the cell body co-ordinates system ($\mathbf{p}, \mathbf{q}, \bar{\mathbf{r}}$) as

$$\mathbf{L}_{grv} = H\mathbf{p} \times m\mathbf{g}\mathbf{k} = -mgH (\sin\theta \sin\psi \mathbf{q} + \sin\theta \cos\psi \bar{\mathbf{r}}), \quad (2.10)$$

where \mathbf{k} is the unit vector directed vertically upward and m is the mass of the cell. Also, θ and ψ are the Euler angles between fixed space coordinates ($\mathbf{i}, \mathbf{j}, \mathbf{k}$) and body coordinates

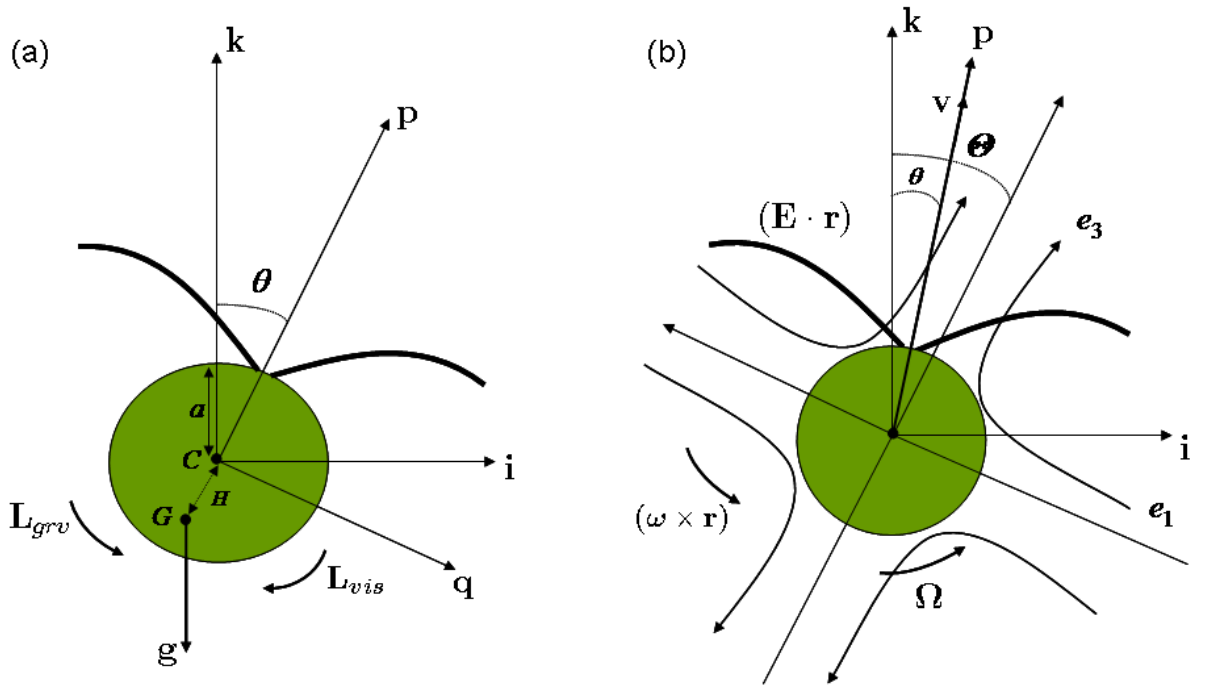


Figure 2.1: (a) A schematic diagram of uniplanar swimming of *C. augustae* cell: (\mathbf{i}, \mathbf{k}) are fixed space and (\mathbf{p}, \mathbf{q}) are body coordinates respectively, H is centre-of-gravity G offset from geometric centre C , θ is the Euler angle between \mathbf{k} in fixed space and primary axis of swimming \mathbf{p} in body coordinate system, \mathbf{g} is the force due to gravity, \mathbf{L}_{grv} and \mathbf{L}_{vis} represents torque due to gravity and viscosity respectively. (b) Swimming cell motion calculated by its velocity \mathbf{v} and angular velocity $\mathbf{\Omega}$ when embedded in the flow, with strain rate \mathbf{E} and vorticity $\boldsymbol{\omega}$, and Θ is the Euler angle between principal axes of the rate-of-strain and \mathbf{k} in fixed space coordinate system.

Name with symbol	Range for <i>Chlamydomonas</i>	Stand. value for <i>C. augustae</i>
Cell radius - a	2 - 10 μm	5 μm (0.0005 cm)
Cell density - ρ	1.01 - 1.10 gm cm $^{-3}$	1.05 gm cm $^{-3}$
Cell volume - v	$3 \times 10^{-11} - 3 \times 10^{-8}$ cm 3	5×10^{-10} cm 3
Cell mass - m	5.25×10^{-10} gm	5.25×10^{-10} gm
centre-of-gravity offset - H	0 - 0.01 a	0.1 μm (0.00001 cm)
Flagellar length - l	1 - 2 a	10 μm (0.001 cm)
Flagellar radius - b	0.02 - 0.04 a	0.2 μm (0.00002 cm)
Gravitational acceleration - g	1000 cm s $^{-2}$	1000 cm s $^{-2}$
Viscosity - μ	0.01 gm cm $^{-1}$ s $^{-1}$	0.01 gm cm $^{-1}$ s $^{-1}$
Beat frequency - f	40 - 60 Hz	50 Hz
Time for one beat - T	0.015 - 0.025 s	0.02 s
Time for effective stroke - Te	0.4 - 0.6 T	0.5 T

Table 2.2: Table of values taken from Jones *et al.* [76] and Pedley and Kessler [113].

($\mathbf{p}, \mathbf{q}, \bar{\mathbf{r}}$) (see Figure 2.1). Here we have used $\bar{\mathbf{r}}$ instead of \mathbf{r} just to avoid repetition of notation for position vector \mathbf{r} used frequently in later sections.

In order to calculate the viscous forces and torques on the flagellum attached to the cell body we use RFT. RFT states that the tangential, normal and binormal components of force and torque on an element of a flagellum is directly proportional to the tangential, normal and binormal components of the fluid velocity relative to that element of the flagellum. Hence,

$$d\mathbf{F}_{flg} = \mu [K_t(\mathbf{u}_{rel} \cdot \mathbf{t}) \mathbf{t} ds + K_n(\mathbf{u}_{rel} \cdot \mathbf{n}) \mathbf{n} ds + K_b(\mathbf{u}_{rel} \cdot \mathbf{b}) \mathbf{b} ds], \quad (2.11)$$

where ds is the flagellar element, and \mathbf{t} , \mathbf{n} and \mathbf{b} are unit vectors tangential, normal and binormal to the element of the flagellum respectively. Also K_t , K_n and K_b are dimensionless resistance coefficients in the tangential, normal and binormal directions.

Similarly the torque produced by an element of the flagellum can be calculated by computing the cross product of the position vector \mathbf{r} with the above calculated force $d\mathbf{F}$ as

$$d\mathbf{L}_{flg} = \mathbf{r} \times d\mathbf{F}_{flg}, \quad (2.12)$$

where \mathbf{r} is the position vector of an element of the flagellum from the centre of the cell body.

The velocity of fluid relative to the element of the flagellum, \mathbf{u}_{rel} , is then given by

$$\mathbf{u}_{rel} = \mathbf{u} - \mathbf{v}_{flg}, \quad (2.13)$$

where \mathbf{u} is the velocity of the fluid measured at the position of the element ds and \mathbf{v}_{flg} is the velocity of an element of the flagellum. Thus the flow past the spherical body in a general flow field \mathbf{u} , is the sum of three parts: flow due to translation of the body, due to vorticity of ambient flow relative to the rotation of the body and due to ambient straining motion (see Pasol *et al.* [110]). Hence,

$$\mathbf{u} = \mathbf{u}_{tr} + \mathbf{u}_{rt} + \mathbf{u}_{st}, \quad (2.14)$$

where the velocity of the fluid due to translational motion of the sphere is

$$\mathbf{u}_{tr} = -\mathbf{v} + \frac{3a}{4} \left[\frac{\mathbf{v}}{r} + \frac{(\mathbf{v} \cdot \mathbf{r})\mathbf{r}}{r^3} \right] - \frac{a}{4} \left[-\frac{\mathbf{v}}{r^3} + \frac{3(\mathbf{v} \cdot \mathbf{r})\mathbf{r}}{r^5} \right], \quad (2.15)$$

the velocity of the fluid due to the vorticity and rotational motion of the sphere is

$$\mathbf{u}_{rt} = \frac{1}{2}(\boldsymbol{\omega} \times \mathbf{r}) \left[1 - \frac{a^3}{r^3} \right] + (\boldsymbol{\Omega} \times \mathbf{r}) \frac{a^3}{r^3}, \quad (2.16)$$

and that due to straining motion of the sphere is

$$\mathbf{u}_{st} = \mathbf{E} \cdot \mathbf{r} \left(1 - \frac{a^5}{r^5} \right) - \mathbf{r}(\mathbf{r} \cdot \mathbf{E} \cdot \mathbf{r}) \left[\frac{5a^3}{2r^5} - \frac{5a^5}{2r^7} \right], \quad (2.17)$$

where a is the radius of the sphere (i.e. cell body of the organism).

The velocity of an element of flagellum relative to the spherical cell body, \mathbf{v}_{flg} , is given by

$$\mathbf{v}_{flg} = \boldsymbol{\Omega} \times \mathbf{r} + \dot{\mathbf{r}}, \quad (2.18)$$

where \mathbf{r} is the position vector of an element of the flagellum relative to the centre of the cell's body, and $\dot{\mathbf{r}}$ is the velocity of the flagellar element relative to body coordinates fixed in the body.

Thus after calculations of the above equations using the RFT and substituting in force torque balance equations (2.5) and (2.6), the total force produced by the fluid on one flagellum and total viscous torque exerted on one flagellum can be obtained as

$$\mathbf{F}_{flg} = \int_{s=0}^l d\mathbf{F}_{flg}, \quad (2.19)$$

and

$$\mathbf{L}_{flg} = \int_{s=0}^l \mathbf{r} \times d\mathbf{F}_{flg}, \quad (2.20)$$

where l is the total length of the flagellum. Similarly, the above integrals are calculated for the second flagellum and added to the first to get the total force and total torque produced due to both flagella (i.e. *cis* and *trans* flagella) during one flagellar beat. The flagellar coordinates in terms of $(\mathbf{n}, \mathbf{t}, \mathbf{b})$, position vector \mathbf{r} and velocity vector $\dot{\mathbf{r}}$ of an element of the flagellum will be obtained from a specific description of the flagellar beat pattern.

Finally, for one flagellar beat of the organism the force-torque balance equations (2.5) and (2.6) reduce to six equations in six unknowns: three equations for components of force and three for components of torque. In the body coordinates \mathbf{p}, \mathbf{q} and $\bar{\mathbf{r}}$ directions, we can write the system of equations as

$$\begin{bmatrix} \mathbf{F} \\ \mathbf{L} \end{bmatrix} = \begin{bmatrix} \mathbf{A} & \mathbf{B} \\ \mathbf{B}^T & \mathbf{C} \end{bmatrix} \cdot \begin{bmatrix} \mathbf{v} \\ \boldsymbol{\Omega} \end{bmatrix}, \quad (2.21)$$

where the above square matrix is symmetric and is termed as the resistance matrix. The inverse form of the above matrix equation can be written as

$$\begin{bmatrix} \mathbf{v} \\ \boldsymbol{\Omega} \end{bmatrix} = \begin{bmatrix} \mathbf{X} & \mathbf{Y} \\ \mathbf{Y}^T & \mathbf{Z} \end{bmatrix} \cdot \begin{bmatrix} \mathbf{F} \\ \mathbf{L} \end{bmatrix}, \quad (2.22)$$

where the square matrix is also symmetric and is called a mobility matrix. The components of these matrices involve unknown beat coefficients α_{ij} , which will depend upon the flagellar beat pattern as defined by Jones *et al.* [76]. Finally after substitution of α_{ij} , the unknowns in the above system of equations are the components of the instantaneous velocity \mathbf{v} and the instantaneous angular velocity $\boldsymbol{\Omega}$ of the organism.

2.5 Flagellar Beat Pattern

To explore the low Reynolds number swimming of micro-organisms, many authors including Ringo [124] and Hyams and Borissy [70], investigated the flagellar beat patterns of *Chlamydomonas* in detail. They classified the breast stroke like swimming into two phases, the effective stroke and the recovery stroke. However, many observations reveal that these phases overlap significantly and are not distinct. The typical cell swims forward during the effective stroke and backward during the recovery stroke. In general the cell swims forward after one beat because the contribution from the effective stroke exceeds that from the recovery stroke, essentially due to increase of resistance coefficient K_n from K_t . The two phases of cell swimming for one flagella beat are shown in the Figure 2.3.

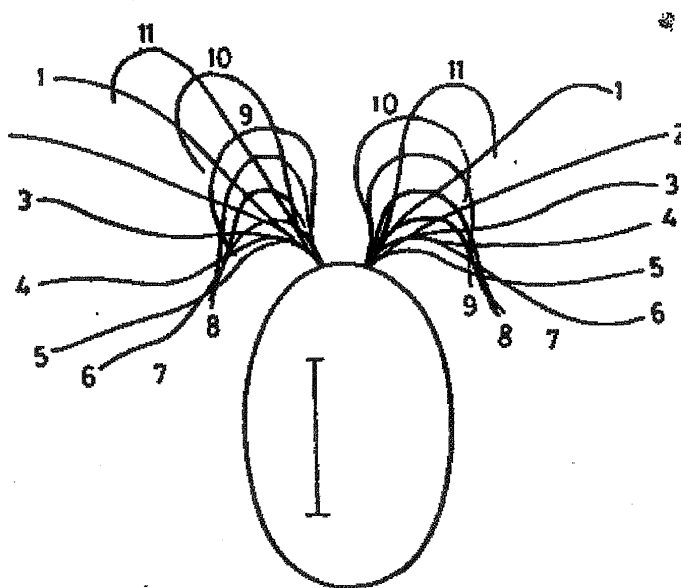


Figure 2.2: Tracing of one beat cycle of both flagella of *C. reinhardtii* mutant 622E. Reproduced from Ruffer and Nultsch [128].

Ruffer and Nultsch [128] studied the swimming of biflagellate cell in detail using the high speed digital microcinematography (100-500 f/s) and did frame-by-frame analysis as shown in Figure (2.2). They also observed that the two phases of the one beat cause net up-swimming and take place slightly out of the plane. The consequence is an anti-clockwise rotation during the effective stroke. A typical cell swims in a helical path, and experiences a change in the frequency in beat of the two flagellum for a short period of time. This may cause an asymmetry in the beat pattern.

Finally, Ruffer and Nultsch [128] found experimentally that the flagellar beat frequencies were approximately 40 – 60 Hz, the swimming speed of the cell was $100 - 150 \mu\text{m s}^{-1}$, the rotation rate about the \mathbf{p} -axis was 1.4 – 2.5 Hz and asymmetries occurred approximately once per 20 beats.

2.6 The Jones *et al.* flagellar beat model

To simplify the calculations, Jones *et al.* [76] formulated and used an idealized model of the flagellar beat of the bottom heavy, biflagellated *C. nivalis* swimming cell. They

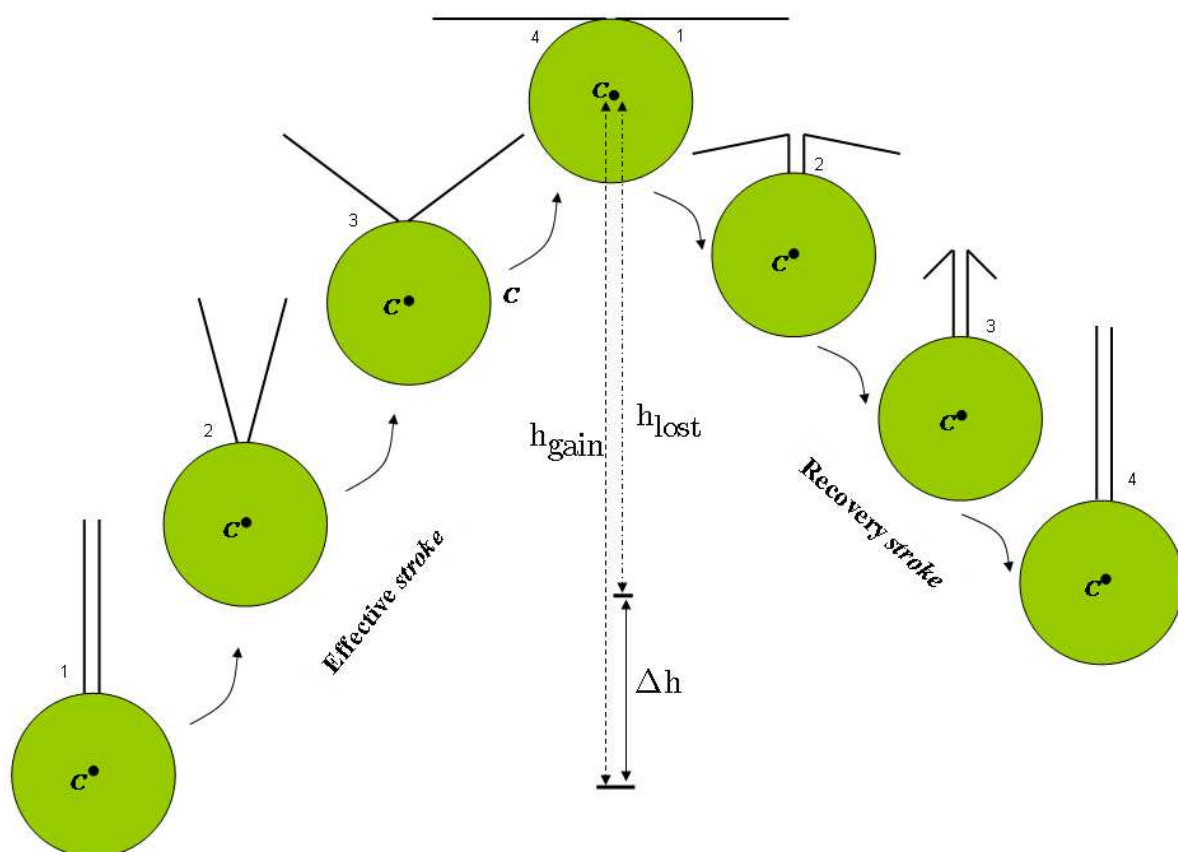


Figure 2.3: A schematic diagram of step by step positions and height gained/lost by vertical upward swimming of *C. augustae* cell during effective and recovery stroke of one flagella beat.

assumed a spherical cell body and that both flagella beat symmetrically in a plane containing the longitudinal body axis. Thus they did not allow any rotation about this body axis nor did they model the helical swimming path. They assumed that the effective and recovery strokes are distinct and the beat pattern is unchanged by any variations in the ambient flow. They also assumed that the change in body orientation during one beat and interaction between the flagella are both negligible.

They assumed for simplification that the flagella beat within a single plane, so vorticity is perpendicular to the rate-of-strain plane within the ambient flow field. Thus the rate-of-strain plane coincide with the flagellar beat plane. The gravity also lies within the same plane whereas torques will act perpendicular to the plane as shown in the Figure 2.1. The time for one beat is $T = \frac{1}{f}$ where f is the flagellar beat frequency.

The transformation matrices \mathbf{R}_{SB} , from the fixed space (represented by S) coordinate system $(\mathbf{i}, \mathbf{j}, \mathbf{k})$ to the body (termed as B) coordinates system $(\mathbf{p}, \mathbf{q}, \bar{\mathbf{r}})$ and \mathbf{R}_{BF} , from body coordinates $(\mathbf{p}, \mathbf{q}, \bar{\mathbf{r}})$ to flagellar (represented by F) coordinates system $(\mathbf{n}, \mathbf{t}, \mathbf{b})$ defined for the single plane flagellar beat are

$$\mathbf{R}_{SB} = \begin{bmatrix} \sin \theta & 0 & \cos \theta \\ \cos \theta & 0 & -\sin \theta \\ 0 & 1 & 0 \end{bmatrix} \quad \text{and} \quad \mathbf{R}_{BF} = \begin{bmatrix} \cos \chi & \sin \chi & 0 \\ \sin \chi & -\cos \chi & 0 \\ 0 & 0 & 1 \end{bmatrix},$$

where θ is the angle between principle swimming axis \mathbf{p} and vertical axis \mathbf{k} and χ is the angle the flagellum makes with the principle swimming axis \mathbf{p} . Similarly, from flagellar coordinates $(\mathbf{n}, \mathbf{t}, \mathbf{b})$ back to the cell's body coordinate system $(\mathbf{p}, \mathbf{q}, \bar{\mathbf{r}})$, the transformation matrix takes the form

$$\mathbf{R}_{FB} = \begin{bmatrix} \sin \chi & \cos \chi & 0 \\ -\cos \chi & \sin \chi & 0 \\ 0 & 0 & 1 \end{bmatrix},$$

and the rotation matrix from the rate-of-strain coordinates $(\mathbf{e}_1, \mathbf{e}_2, \mathbf{e}_3)$ to fixed space coordinate system $(\mathbf{i}, \mathbf{j}, \mathbf{k})$ is

$$\mathbf{R}_{PS} = \begin{bmatrix} \cos \Theta & 0 & \sin \Theta \\ 0 & 1 & 0 \\ -\sin \Theta & 0 & \cos \Theta \end{bmatrix},$$

where Θ is the Euler angle between the principal axes of the rate-of-strain and the fixed space coordinate system. The rate-of-strain tensor in the body coordinate system using

the above transformation matrices, takes the form as

$$\mathbf{E} = \begin{bmatrix} -e \cos 2\gamma & e \sin 2\gamma & 0 \\ e \sin 2\gamma & e \cos 2\gamma & 0 \\ 0 & 0 & 0 \end{bmatrix},$$

where $\gamma = \theta - \Theta$. The vorticity and gravity vector for the single plane using the above transformation matrices in body coordinates system $(\mathbf{p}, \mathbf{q}, \bar{\mathbf{r}})$ become

$$\boldsymbol{\omega} = \begin{bmatrix} 0 \\ \boldsymbol{\omega} \\ 0 \end{bmatrix} \quad \text{and} \quad \mathbf{g} = \begin{bmatrix} 0 \\ 0 \\ -g \sin \theta \end{bmatrix}.$$

The body coordinate axes for the single plane situation can be written as

$$\mathbf{p} = \begin{bmatrix} \sin \theta \\ 0 \\ \cos \theta \end{bmatrix}, \quad \mathbf{q} = \begin{bmatrix} \cos \theta \\ 0 \\ -\sin \theta \end{bmatrix} \quad \text{and} \quad \bar{\mathbf{r}} = \begin{bmatrix} 0 \\ 1 \\ 0 \end{bmatrix}.$$

As define by Jones *et al.* [76], for the case of planar swimming, the simplified model beat begins with the flagella fully extended parallel to body axis \mathbf{p} as shown in Figure 2.4. The two phases of the beat are as follows.

(a) Effective Stroke

For an effective stroke swimming, the flagella rotate rigidly about their base O until perpendicular to the body axis \mathbf{p} as shown in Figure (2.4(a)). The angular velocity of each flagellum about O is taken to be constant throughout the motion. The angle between the flagellum and body axis \mathbf{p} at any stage is denoted by χ . The other flagellum beats symmetrically. The position vector and angular velocity of an element of the flagellum relative to the centre of the cell in various coordinate systems are

$$\begin{aligned} \mathbf{r}_{ef}^S(s, t) &= a\mathbf{p} + s\mathbf{t}, \\ \mathbf{r}_{ef}^B(s, t) &= (a + s \cos \chi)\mathbf{p} + (s \sin \chi)\mathbf{q}, \\ \mathbf{r}_{ef}^F(s, t) &= (a \sin \chi)\mathbf{n} + (a \cos \chi + s)\mathbf{t}, \end{aligned} \tag{2.23}$$

where $0 \leq \chi \leq \frac{\pi}{2}$, s is the variable along the length of the flagellum and the subscript ef represents effective stroke and the superscript shows the respective coordinate system. The element of flagellum moves through a right angle during the effective stroke. The angular velocity of the flagellum is modelled as

$$\chi = \frac{\pi t}{2 T_e} \quad \text{and} \quad \dot{\chi} = \frac{\pi}{2 T_e}, \tag{2.24}$$

where T_e is the time to completion of the effective stroke. Also the velocity of an element of the flagellum relative to $(\mathbf{p}, \mathbf{q}, \bar{\mathbf{r}})$ coordinates can be calculated by differentiating (2.23) w.r.t χ . Using the transformation matrix R_{BF} , the velocity of an element of flagellum during the effective stroke takes the form

$$\dot{\mathbf{r}}_{ef}^F = -s\dot{\chi} \mathbf{n}. \quad (2.25)$$

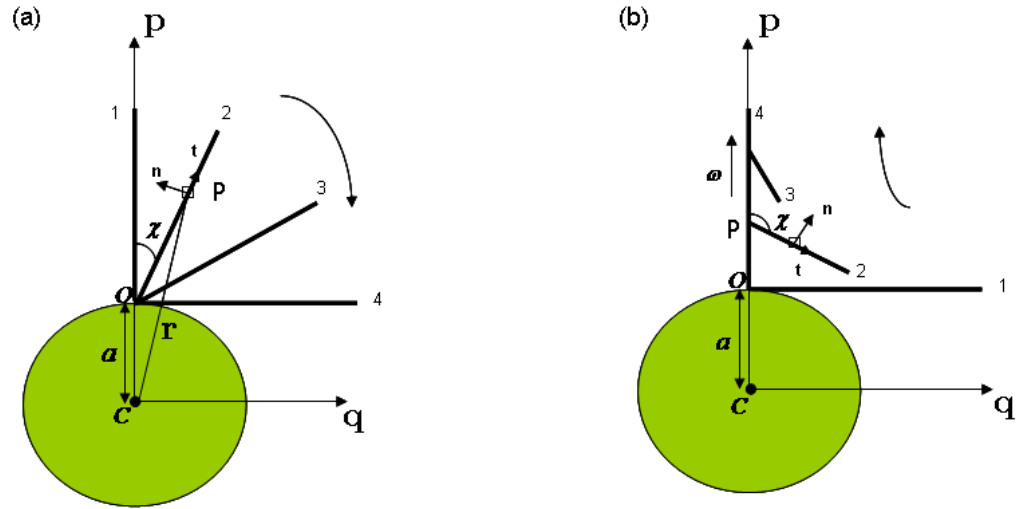


Figure 2.4: The idealized model by Jones *et al.* [76] for flagellar beat pattern of *C. augustae* for different positions of the flagellum during (a) effective stroke and (b) recovery stroke.

(b) Recovery Stroke

During the recovery stroke a bending waves propagates up the flagellum from base to tip. The propagation point P is moved in the direction of the body axis \mathbf{p} , so that the flagellum reaches the initial location as shown in Figure 2.4(b). The bend moves with constant speed w . Thus the Jones *et al.* [76] model for the recovery stroke has two sections: a stationary straight section and an angled section, as follows.

Stationary section: This section is parallel to the body axis and is stationary with respect to the centre of the cell having length wt , where $wt < l$, as shown in Figure 2.4(b). The position of an element of the flagellum in the stationary section is taken as

$$\mathbf{r}_{st}^S(s, t) = (a + s) \mathbf{p}, \quad \Rightarrow \quad \mathbf{r}_{st}^F(s, t) = (a + s) \mathbf{t}, \quad (2.26)$$

where subscript st indicates stationary section of the recovery stroke and superscript represent the respective coordinate system.

Angled section: The position and angular velocity of an element of the flagellum in the angled section of the right-hand flagellum is

$$\begin{aligned}\mathbf{r}_{ag}^S(s, t) &= (a + wt) \mathbf{p} + (s - wt) \mathbf{t}, \\ \mathbf{r}_{ag}^B(s, t) &= [(a + wt) + (s - wt) \cos\chi] \mathbf{p} + [(s - wt) \sin\chi] \mathbf{q}, \\ \mathbf{r}_{ag}^F(s, t) &= [(a + wt) \sin\chi] \mathbf{n} + [(a + wt) \cos\chi + (s - wt)] \mathbf{t},\end{aligned}\quad (2.27)$$

where $\frac{\pi}{2} \leq \chi \leq \pi$, ag represents angled section of the recovery stroke and superscript indicates the respective coordinate system.

Jones *et al.* [76] modelled angular velocity in two different forms. In the first scheme they assumed that the angle increases with constant angular velocity w and bends through a right angle during the recovery stroke. This will be termed as the constant angular velocity case and gives the angular velocity of the flagellum as

$$\chi = \frac{\pi}{2} + \frac{\pi wt}{2l}, \quad \text{and} \quad \dot{\chi} = \frac{\pi w}{2l}, \quad (2.28)$$

whereas, in the second case they calculated the moment of viscous forces about the bending point P as shown in the Figure 2.4(b) using RFT and neglecting cell body. The angular velocity is found by setting the moment equal to zero and is called the zero moment angular velocity case, which gives

$$\chi = 2 \tan^{-1} \left[\left(1 - \frac{wt}{l} \right)^{-\frac{3}{2}} \right], \quad \text{and} \quad \dot{\chi} = \frac{3}{2} \frac{w \sin\chi}{(l - wt)}. \quad (2.29)$$

Note that Jones *et al.* [76] and Jones [77] contain a few typos and a simple qualitative mistake in the calculation of the velocity of the flagellum during the recovery stroke. They have

$$\dot{\mathbf{r}}_{re}^F = [w \sin\chi - (s - wt)\dot{\chi}] \mathbf{n} + [w \cos\chi(\cos\chi - 1)] \mathbf{t}, \quad (2.30)$$

rather than the correct form

$$\dot{\mathbf{r}}_{re}^F = [w \sin\chi - (s - wt)\dot{\chi}] \mathbf{n} + [w(\cos\chi - 1)] \mathbf{t}. \quad (2.31)$$

2.7 Modified implementation of the uniplanar flagellar beat model

By repeating the detailed calculations of Jones *et al.* [76], we found some misprints which we have corrected at first step as one mentioned in the section 2.6. Secondly,

Using the transformation matrices we can write this in flagellar coordinates such that

$$\begin{aligned}\mathbf{r}^B(s, t) &= [b + (s - b) \cos \chi] \mathbf{p} + [(s - b) \sin \chi] \mathbf{q}, \\ \mathbf{r}^F(s, t) &= [b \sin \chi] \mathbf{n} + [(s - b) + b \cos \chi] \mathbf{t}.\end{aligned}\quad (2.33)$$

This generalized position vector of flagellum element eases the calculations as we incorporate general expression for a single section instead of the three different sections of the beat defined by Jones *et al.* [76]. We shall also avoid splitting the integrals about the point of closest approach to the centre of the body (as described in appendix A) by employing Maple. This is particularly relevant for the bounded problem in chapter 3 where we require many more troublesome integrals. The details of the different parts of the flagella beat during effective and recovery stroke are shown in Figure 2.4.

2.7.1 Computation of viscous force and viscous torque acting on one flagellum

Here, we will calculate the viscous force and torque acting on the flagellum and substitute into the force-torque balance equations. There are several methods for calculation of viscous forces and torques on the cell that compute solutions of the Stokes equations at every instant as the surface of the body and flagella change shape. The methods include boundary integral/element method, immersed boundary method, slender body theory and resistive force theory. Here, we follow Jones *et al.* [76] and employ Resistive Force Theory (RFT) due to the relative analytical simplicity and clarity of the method. The velocity \mathbf{v} and angular velocity $\mathbf{\Omega}$ of the organism in the flagellar coordinate system can be written as

$$\mathbf{v} = \begin{bmatrix} v_n \\ v_t \\ v_b \end{bmatrix} = \begin{bmatrix} v_p(\mathbf{p} \cdot \mathbf{n}) + v_q(\mathbf{q} \cdot \mathbf{n}) + v_r(\bar{\mathbf{r}} \cdot \mathbf{n}) \\ v_p(\mathbf{p} \cdot \mathbf{t}) + v_q(\mathbf{q} \cdot \mathbf{t}) + v_r(\bar{\mathbf{r}} \cdot \mathbf{t}) \\ v_p(\mathbf{p} \cdot \mathbf{b}) + v_q(\mathbf{q} \cdot \mathbf{b}) + v_r(\bar{\mathbf{r}} \cdot \mathbf{b}) \end{bmatrix}$$

and

$$\mathbf{\Omega} = \begin{bmatrix} \Omega_n \\ \Omega_t \\ \Omega_b \end{bmatrix} = \begin{bmatrix} \Omega_p(\mathbf{p} \cdot \mathbf{n}) + \Omega_q(\mathbf{n} \cdot \mathbf{t}) + \Omega_r(\bar{\mathbf{r}} \cdot \mathbf{n}) \\ \Omega_p(\mathbf{p} \cdot \mathbf{t}) + \Omega_q(\mathbf{t} \cdot \mathbf{n}) + \Omega_r(\bar{\mathbf{r}} \cdot \mathbf{t}) \\ \Omega_p(\mathbf{p} \cdot \mathbf{b}) + \Omega_q(\mathbf{q} \cdot \mathbf{b}) + \Omega_r(\bar{\mathbf{r}} \cdot \mathbf{b}) \end{bmatrix}, \quad (2.34)$$

respectively. The position vector, velocity and angular velocity of an element of flagellum in flagellar coordinate system for the uniplanar case become

$$\mathbf{r} = \begin{bmatrix} r_n \\ r_t \\ 0 \end{bmatrix}, \quad \mathbf{v} = \begin{bmatrix} v_n \\ v_t \\ 0 \end{bmatrix} \quad \text{and} \quad \boldsymbol{\Omega} = \begin{bmatrix} 0 \\ 0 \\ \Omega_b \end{bmatrix}, \quad (2.35)$$

respectively.

Contribution of the translation of the spherical body

The velocity of the fluid due to the translation of a spherical body of radius a in a low Reynolds number fluid flow is given by

$$\mathbf{u}_{tr} = -\mathbf{v} + \left(\frac{3a}{4r} + \frac{a^3}{4r^3} \right) + (\mathbf{v} \cdot \mathbf{r}) \mathbf{r} \left[\frac{3a}{4r^3} - \frac{3a^3}{4r^5} \right]. \quad (2.36)$$

Now, using RFT, the force produced by an element of a flagellum within this flow with $a = 1$ is given by

$$\begin{aligned} d\mathbf{F}_{tr}^F &= K_n \left[-v_n \left(1 - \frac{3}{4r} - \frac{1}{4r^3} \right) + (v_n r_n^2 + v_t r_n r_t) \left(\frac{3}{4r^3} - \frac{3}{4r^5} \right) \right] \mathbf{n} ds \\ &+ K_t \left[-v_t \left(1 - \frac{3}{4r} - \frac{1}{4r^3} \right) + (v_t r_t^2 + v_n r_n r_t) \left(\frac{3}{4r^3} - \frac{3}{4r^5} \right) \right] \mathbf{t} ds. \end{aligned} \quad (2.37)$$

The total force from the flagellum can thus be calculated by integrating along the length of the flagellum to yield

$$\begin{aligned} \mathbf{F}_{tr}^F &= K_n \left[-v_n \left(I_1 - \frac{3}{4} I_2 - \frac{1}{4} I_3 \right) + v_n r_n^2 \left(\frac{3I_3}{4} - \frac{3I_4}{4} \right) + v_t r_n \left(\frac{3J_3}{4} - \frac{3J_4}{4} \right) \right] \mathbf{n} \\ &+ K_t \left[-v_t \left(I_1 - \frac{3}{4} I_2 - \frac{1}{4} I_3 \right) + v_n r_n \left(\frac{3J_3}{4} - \frac{3J_4}{4} \right) + v_t \left(\frac{3I_7}{4} - \frac{3I_8}{4} \right) \right] \mathbf{t}, \end{aligned} \quad (2.38)$$

where I_i and J_i are specific integrals and will be defined in detail below and in appendix A as calculated by Jones *et al.* [77]. Now using our generalized position vector these integrals will be integrated w.r.t s (the distance along the flagellum) instead of r (the distance from the geometric centre of the cell body), which will simplify the calculations here and later on (see chapter 3). The integrals we now define here as

$$\begin{aligned} I_1 &= \int ds, & I_2 &= \int \frac{ds}{r}, & I_3 &= \int \frac{ds}{r^3}, & I_4 &= \int \frac{ds}{r^5}, \\ I_5 &= \int \frac{ds}{r^7}, & I_6 &= \int r_t^2 ds, & J_1 &= \int r_t ds, & J_2 &= \int \frac{r_t}{r} ds, \\ J_3 &= \int \frac{r_t}{r^3} ds & J_4 &= \int \frac{r_t}{r^5} ds, & J_5 &= \int \frac{r_t}{r^7} ds, \end{aligned}$$

$$I_7 = \int \frac{r_t^2}{r^3} ds = I_2 - r_n^2 I_3, \quad I_8 = \int \frac{r_t^2}{r^5} ds = I_3 - r_n^2 I_5,$$

and

$$J_6 = \int \frac{r_t^3}{r^5} ds = J_3 - r_n^2 J_4, \quad J_7 = \int \frac{r_t^3}{r^7} ds = J_4 - r_n^2 J_5. \quad (2.39)$$

Therefore, the total force from one flagellum in the body coordinates system for uniplanar locomotion, becomes

$$\begin{aligned} \mathbf{F}_{tr}^F \cdot \mathbf{p} &= \bar{\alpha}_{11} v_p + \alpha_{12} v_q, \\ \mathbf{F}_{tr}^F \cdot \mathbf{q} &= \alpha_{21} v_p + \bar{\alpha}_{22} v_q, \end{aligned} \quad (2.40)$$

where α_{ij} are the time dependent beat coefficients involving integrals I_i and J_i . The beat coefficients $\bar{\alpha}_{ij}$ additionally incorporate the viscous forces and viscous torques contribution and are defined in section 2.7.2. The detailed expressions for α_{ij} are listed in appendix A.

The viscous torque due to translating motion of the unit sphere with fluid velocity (2.36) on an element of flagellum is given by

$$d\mathbf{L}_{tr}^F = \mathbf{r} \times d\mathbf{F}_{tr}^F.$$

Using equation (2.35) for \mathbf{r} and equation (2.37) for $d\mathbf{F}_{tr}^F$, the above equation becomes

$$\begin{aligned} d\mathbf{L}_{tr}^F &= \left[K_t \left\{ -v_t \left(1 - \frac{3}{4r} - \frac{1}{4r^3} \right) + (v_t r_t^2 + v_n r_n r_t) \left(\frac{3}{4r^3} - \frac{3}{4r^5} \right) \right\} r_n \right. \\ &\quad \left. - K_n \left\{ -v_n \left(1 - \frac{3}{4r} - \frac{1}{4r^3} \right) + (v_n r_n^2 + v_t r_n r_t) \left(\frac{3}{4r^3} - \frac{3}{4r^5} \right) \right\} r_t \right] \mathbf{b} ds. \end{aligned}$$

The total viscous torque for the single flagellum can be calculated by integrating along the length of the flagellum, giving

$$\begin{aligned} \mathbf{L}_{tr}^F &= \left[K_t \left\{ -v_t r_n \left(I_1 - \frac{3}{4} I_2 - \frac{1}{4} I_3 \right) + v_n r_n^2 \left(\frac{3J_3}{4} - \frac{3J_4}{4} \right) + v_t r_n \left(\frac{3I_7}{4} - \frac{3I_8}{4} \right) \right\} \right. \\ &\quad \left. - K_n \left\{ -v_n \left(J_1 - \frac{3}{4} J_2 - \frac{1}{4} J_3 \right) + v_n r_n^2 \left(\frac{3J_3}{4} - \frac{3J_4}{4} \right) + v_t r_n \left(\frac{3I_7}{4} - \frac{3I_8}{4} \right) \right\} \right] \mathbf{b}. \end{aligned} \quad (2.41)$$

Now finally, the total torque due to translational motion of the sphere on one flagellum for the uniplanar case in body coordinates can be written as

$$\mathbf{L}_{tr}^F \cdot \bar{\mathbf{r}} = \alpha_{61} v_p + \alpha_{62} v_q. \quad (2.42)$$

Contribution of the rotation of the spherical body

In general, the velocity of the fluid due to ambient vorticity $\boldsymbol{\omega}$, and rotational motion of the spherical body of radius a in body coordinates is

$$\mathbf{u}_{rt} = \frac{1}{2} (\boldsymbol{\omega} \times \mathbf{r}) \left[1 - \frac{a^3}{r^3} \right] + (\boldsymbol{\Omega} \times \mathbf{r}) \frac{a^3}{r^3}. \quad (2.43)$$

For simplicity in later chapters, the viscous force and torque due to rotational motion were only calculated in terms of the angular velocity of the body $\boldsymbol{\Omega}$ (i.e. with zero ambient vorticity). Thus for $\boldsymbol{\omega} = 0$, we can rewrite (2.43) in body coordinates as

$$\mathbf{u}_{rt} = -(\boldsymbol{\Omega} \times \mathbf{r}) \left[1 - \frac{a^3}{r^3} \right]. \quad (2.44)$$

Now, using RFT, the force on an element of a flagellum due to rotational motion of the unit sphere is given by

$$d\mathbf{F}_{rt}^F = K_n \left[\Omega_b r_t \left(1 - \frac{1}{r^3} \right) \right] \mathbf{n} ds - K_t \left[\Omega_b r_n \left(1 - \frac{1}{r^3} \right) \right] \mathbf{t} ds. \quad (2.45)$$

The total force can be calculated by integrating along the length of the flagellum as

$$\mathbf{F}_{rt}^F = K_n [\Omega_b (J_1 - J_3)] \mathbf{n} - K_t [\Omega_b r_n (I_1 - I_3)] \mathbf{t}. \quad (2.46)$$

Therefore, the total force due to rotational motion of the sphere on one flagellum for the uniplanar case in body coordinates system becomes

$$\begin{aligned} \mathbf{F}_{rt}^F \cdot \mathbf{p} &= \alpha_{16} \Omega_r, \\ \mathbf{F}_{rt}^F \cdot \mathbf{q} &= \alpha_{26} \Omega_r. \end{aligned} \quad (2.47)$$

The viscous torque due to rotational motion of the unit sphere with rotational velocity (2.44) on an element of flagellum is given by

$$d\mathbf{L}_{rt}^F = \mathbf{r} \times d\mathbf{F}_{rt}^F.$$

Using equation (2.35) for \mathbf{r} and equation (2.45) for $d\mathbf{F}_{rt}^F$, the torque becomes

$$d\mathbf{L}_{rt}^F = \left[(K_n \Omega_b r_t^2) + K_t \Omega_b r_n^2 \left(1 - \frac{1}{r^3} \right) \right] \mathbf{b} ds.$$

Hence, the total viscous torque can be calculated by integrating along the length of the flagellum, to give

$$\mathbf{L}_{rt}^F = [K_n \Omega_b (I_6 - I_7) + K_t \Omega_b r_n^2 (I_1 - I_3)] \mathbf{b}. \quad (2.48)$$

Now, finally, the total torque due to rotational motion of the sphere for uniplanar locomotion on one flagellum in body coordinates can be written as

$$\mathbf{L}_{rt}^F \cdot \bar{\mathbf{r}} = \bar{\alpha}_{66} \Omega_r. \quad (2.49)$$

Contribution due to the straining flow around the spherical body

The velocity of the fluid due to an ambient straining motion about a spherical body of radius a in a low Reynolds number fluid flow is given by

$$\mathbf{u}_{st} = \mathbf{E} \cdot \mathbf{r} \left(1 - \frac{a^5}{r^5} \right) - \mathbf{r}(\mathbf{r} \cdot \mathbf{E} \cdot \mathbf{r}) \left[\frac{5a^3}{2r^5} - \frac{5a^5}{2r^7} \right], \quad (2.50)$$

where the rate-of-strain tensor for uniplanar case has been rotated into flagellar coordinate system using

$$\mathbf{E}^F = \mathbf{R}_{BF} \mathbf{E} \mathbf{R}_{BF}^T = \begin{bmatrix} e_{11} & e_{12} & 0 \\ e_{21} & e_{22} & 0 \\ 0 & 0 & 0 \end{bmatrix}, \quad (2.51)$$

where e_{jk} are the individual components of the rate-of-strain tensor.

The viscous force due to the straining motion of the unit sphere from an element of a flagellum using RFT is given by

$$\begin{aligned} d\mathbf{F}_{st}^F = & K_n \left[(e_{11}r_n + e_{12}r_t) \left(1 - \frac{1}{r^5} \right) - (e_{11}r_n^3 + 2e_{12}r_n^2r_t + e_{22}r_nr_t^2) \left(\frac{5}{2r^5} - \frac{5}{2r^7} \right) \right] \mathbf{n} ds \\ & + K_t \left[(e_{12}r_n + e_{22}r_t) \left(1 - \frac{1}{r^5} \right) - (e_{11}r_n^2r_t + 2e_{12}r_t^2r_n + e_{22}r_t^3) \left(\frac{5}{2r^5} - \frac{5}{2r^7} \right) \right] \mathbf{t} ds. \end{aligned} \quad (2.52)$$

The total force on one flagellum is obtained by integrating along the length of the flagellum i.e.

$$\begin{aligned} \mathbf{F}_{st}^F = & K_t \left[e_{12}r_n(I_1 - I_4) + e_{22}(J_1 - J_4) - \frac{5}{2} \left\{ e_{11}r_n^2(J_4 - J_5) + 2e_{12}r_n(I_8 - I_9) \right. \right. \\ & \left. \left. + e_{22}(J_6 - J_7) \right\} \right] \mathbf{t} + K_n \left[e_{11}r_n(I_1 - I_4) + e_{12}r_n(J_1 - J_4) \right. \\ & \left. - \frac{5}{2} \left\{ e_{11}r_n^3(I_4 - I_5) + 2e_{12}r_n^2(J_4 - J_5) + e_{22}r_n(I_8 - I_9) \right\} \right] \mathbf{n}. \end{aligned} \quad (2.53)$$

Therefore, the total force due to straining motion of sphere from one flagellum for uniplanar case in body coordinates system becomes

$$\begin{aligned} \mathbf{F}_{st}^F \cdot \mathbf{p} &= h_{11}e_{11} + h_{12}e_{12} + h_{13}e_{22}, \\ \mathbf{F}_{st}^F \cdot \mathbf{q} &= h_{21}e_{11} + h_{22}e_{12} + h_{23}e_{22}, \end{aligned} \quad (2.54)$$

where h_{ij} are the time dependent beat coefficients involving integrals I_i and J_i defined in Appendix A.

The viscous torque due to straining motion of the unit sphere with velocity (2.50) on an element of flagellum is given by

$$d\mathbf{L}_{st}^F = \mathbf{r} \times d\mathbf{F}_{st}^F,$$

Using equation (2.35) for \mathbf{r} and equation (2.52) for $d\mathbf{F}_{st}^F$, the above equation becomes

$$\begin{aligned} d\mathbf{L}_{st}^F = & \left[K_t \left\{ (e_{12}r_n^2 + e_{22}r_t r_n) \left(1 - \frac{1}{r^5} \right) \right\} - K_n \left\{ (e_{11}r_n r_t + e_{12}r_t^2) \left(1 - \frac{1}{r^5} \right) \right\} \right. \\ & \left. - \frac{5}{2} (K_t - K_n) \left\{ e_{11}r_n^3 r_t + 2e_{12}r_n^2 r_t^2 + e_{22}r_n r_t^3 \right\} \left(\frac{1}{r^5} - \frac{1}{r^7} \right) \right] \mathbf{b} ds. \end{aligned}$$

The total torque for one flagellum is obtained by integrating along the length of the flagellum i.e.

$$\begin{aligned} \mathbf{L}_{st}^F = & \left[K_t \left\{ e_{12}r_n^2 (I_1 - I_4) + e_{22}r_n (J_1 - J_4) \right\} - K_n \left\{ (e_{11}r_n (J_1 - J_4) + e_{12} (I_6 - I_8)) \right\} \right. \\ & \left. - \frac{5}{2} (K_t - K_n) \left\{ e_{11}r_n^3 (J_4 - J_5) + 2e_{12}r_n^2 (I_8 - I_9) + e_{22}r_n (J_6 - J_7) \right\} \right] \mathbf{b}. \quad (2.55) \end{aligned}$$

Therefore, the total torque due to straining motion of sphere for uniplanar case on one flagellum in body coordinates system becomes

$$\mathbf{L}_{st}^F \cdot \bar{\mathbf{r}} = h_{61}e_{11} + h_{62}e_{12} + h_{63}e_{22}. \quad (2.56)$$

Flagellar beating contribution

Following Jones *et al.* [76], we shall calculate the viscous force and torque due to the imposed velocity of the flagella $\dot{\mathbf{r}}$, beating relative to the cell body. For the effective stroke, the velocity of an element of flagellum for the planar case can be rewritten from (2.25) as

$$\dot{\mathbf{r}} = -s\dot{\chi} \mathbf{n}.$$

Using RFT, the force produced during effective stroke due to the velocity of flagella relative to cell body becomes

$$d\mathbf{F}_{fl}^F = -K_n (s\dot{\chi}) \mathbf{n} ds.$$

The total force from the flagellum can be calculated by integrating along its length to give

$$\mathbf{F}_{fl}^F = -K_n \left(\frac{l^2}{2} \dot{\chi} \right) \mathbf{n}. \quad (2.57)$$

Therefore, the total force due to the velocity of the flagellum during the effective stroke for the uniplanar case in body coordinates system becomes

$$\mathbf{F}_{fl}^F \cdot \mathbf{p} = -K_n \left(\frac{l^2}{2} \dot{\chi} \right) (\mathbf{n} \cdot \mathbf{p}) = -K_n \left(\frac{l^2}{2} \dot{\chi} \right) \sin\chi. \quad (2.58)$$

The recovery stroke consists of two parts stationary, the straight section and the moving angled section. The velocity of an element of flagellum during recovery stroke for the planar case as defined earlier in (2.31) is

$$\dot{\mathbf{r}} = [w \sin\chi - (s - wt)\dot{\chi}] \mathbf{n} + [w(\cos\chi - 1)] \mathbf{t}.$$

Using RFT, the force produced by the angled section during the recovery stroke due to the velocity of the flagellum relative to the cell body is

$$d\mathbf{F}_{fl}^F = K_n [w \sin\chi - (s - wt)\dot{\chi}] \mathbf{n} ds + K_t [w(\cos\chi - 1)] \mathbf{t} ds, \quad (2.59)$$

The total force from the flagellum can thus be calculated by integrating, giving

$$\mathbf{F}_{fl}^F = K_n \left[w \sin\chi(l - wt) - \frac{1}{2}(l - wt)^2 \dot{\chi} \right] \mathbf{n} + K_t [w(\cos\chi - 1)(l - wt)] \mathbf{t}. \quad (2.60)$$

Thus, the total force due to velocity of the flagellum during the recovery stroke for the uniplanar case in body coordinates system becomes

$$\mathbf{F}_{fl}^F \cdot \mathbf{p} = K_n \left[w \sin\chi(l - wt) - \frac{1}{2}(l - wt)^2 \dot{\chi} \right] \sin\chi + K_t [w(\cos\chi - 1)(l - wt)] \cos\chi.$$

The total force due to flagellar beating for the planar case in body coordinates can be written as

$$\mathbf{F}_{fl}^F = f_1 \mathbf{p} + f_2 \mathbf{q}, \quad (2.61)$$

where for the effective stroke we have derived

$$f_1 = -K_n \left(\frac{l^2}{2} \dot{\chi} \right) \sin\chi, \quad \text{and} \quad f_2 = K_n \left(\frac{l^2}{2} \dot{\chi} \right) \cos\chi, \quad (2.62)$$

and similarly for recovery stroke we have found

$$\begin{aligned} f_1 &= K_n \left[w \sin\chi(l - wt) - \frac{1}{2}(l - wt)^2 \dot{\chi} \right] \sin\chi + K_t [w(\cos\chi - 1)(l - wt)] \cos\chi \\ f_2 &= -K_n \left[w \sin\chi(l - wt) - \frac{1}{2}(l - wt)^2 \dot{\chi} \right] \cos\chi + K_t [w(\cos\chi - 1)(l - wt)] \sin\chi. \end{aligned} \quad (2.63)$$

The viscous torque due to the velocity of the flagellum is given by

$$d\mathbf{L}_{fl}^F = \mathbf{r} \times d\mathbf{F}_{fl}^F,$$

Using equation (2.35) for \mathbf{r} and equation (3.54) for $d\mathbf{F}_{fl}^F$, above equation for effective stroke becomes

$$d\mathbf{L}_{fl}^F = K_n [s\dot{\chi}(s + \cos\chi)] \mathbf{b} ds$$

The total torque from the flagellum can be calculated by integrating as

$$\mathbf{L}_{fl}^F = K_n \left[\dot{\chi} \left(\frac{l^3}{3} + \frac{l^2}{2} \cos\chi \right) \right] \mathbf{b}. \quad (2.64)$$

Therefore, the total torque due to the velocity of the flagellum during the effective stroke for the uniplanar case in body coordinates system becomes

$$\mathbf{L}_{fl}^F \cdot \bar{\mathbf{r}} = K_n \left[\dot{\chi} \left(\frac{l^3}{3} + \frac{l^2}{2} \cos\chi \right) \right] (\mathbf{b} \cdot \bar{\mathbf{r}}) = K_n \left[\dot{\chi} \left(\frac{l^3}{3} + \frac{l^2}{2} \cos\chi \right) \right]. \quad (2.65)$$

Similarly, for the recovery stroke using equation (2.35) for \mathbf{r} and equation (2.59) for $d\mathbf{F}_{fl}^F$, the viscous torque becomes

$$d\mathbf{L}_{fl}^F = \left[K_t\{(1+wt)w(\cos\chi-1)\} - K_n\{(1+wt)\cos\chi(s-wt)\} \right. \\ \left. w \sin\chi - (s-wt)\dot{\chi} \right] \mathbf{b}ds.$$

The total force from the flagellum can be calculated by integrating as

$$\mathbf{L}_{fl}^F = \left[K_t\{(1+wt)w(\cos\chi-1)\} - K_n\{(1+wt)\cos\chi(s-wt)\} \right. \\ \left. w \sin\chi - (s-wt)\dot{\chi} \right] \mathbf{b}. \quad (2.66)$$

Thus, the total torque due to the velocity of the flagellum during the recovery stroke for the uniplanar case in body coordinates system becomes

$$\mathbf{L}_{fl}^F \cdot \bar{\mathbf{r}} = \left[K_t\{(1+wt)w(\cos\chi-1)\} - K_n\{(1+wt)\cos\chi(s-wt)\} \right. \\ \left. w \sin\chi - (s-wt)\dot{\chi} \right]. \quad (2.67)$$

The total torque due to flagellar beating for the uniplanar case in body coordinates system becomes

$$\mathbf{L}_{fl}^F = f_6 \bar{\mathbf{r}}, \quad (2.68)$$

where for the effective stroke we found

$$f_6 = K_n \left[\dot{\chi} \left(\frac{l^3}{3} + \frac{l^2}{2} \cos\chi \right) \right], \quad (2.69)$$

and for recovery stroke it takes the form

$$f_6 = \left[K_t\{(1+wt)w(\cos\chi-1)\} - K_n\{(1+wt)\cos\chi(s-wt)\} w \sin\chi - (s-wt)\dot{\chi} \right]. \quad (2.70)$$

Thus, the total viscous force and viscous torque produced by both flagella can be calculated by substitution of the above equations in

$$\mathbf{F}_{flg} = \mathbf{F}_{tr} + \mathbf{F}_{rt} + \mathbf{F}_{st} - \mathbf{F}_{fl}, \quad (2.71)$$

and

$$\mathbf{L}_{flg} = \mathbf{L}_{tr} + \mathbf{L}_{rt} + \mathbf{L}_{st} - \mathbf{L}_{fl}. \quad (2.72)$$

2.7.2 Force-Torque balance equations

For the uniplanar unbounded swimming case the vorticity is perpendicular to the plane of the straining motion within the ambient flow. The flagellar beat plane coincides with the plane of the straining motion and gravity. Both flagella beat symmetrically and the cell body is symmetric about the primary axis \mathbf{p} , which leads to simplification of the values of beat coefficients $\alpha_{12} = \alpha_{21} = 0$. Similarly, the fluid flow around the swimming cell is also symmetric with no torque effect which further simplifies the values of unknown beat coefficients as $\alpha_{16} = \alpha_{61} = 0$. So using the equation (2.9), the force-torque balance equations (2.5) and (2.6) takes the form

$$\mathbf{F}_{bdy} + \mathbf{F}_{flg} = 0,$$

$$\mathbf{L}_{bdy} + \mathbf{L}_{grv} + \mathbf{L}_{flg} = 0. \quad (2.73)$$

Now using the above defined assumptions for the uniplanar flagella beat pattern and equations (2.40), (2.47), (2.54) and (2.58) for forces and (2.42), (2.49), (2.56) and (2.65) for torques, the force-torque balance equations can be written in matrix form as

$$\begin{aligned} \begin{bmatrix} F_p \\ F_q \\ L_r \end{bmatrix} &= \begin{bmatrix} \bar{\alpha}_{11} & 0 & 0 \\ 0 & \bar{\alpha}_{22} & \alpha_{26} \\ 0 & \alpha_{62} & \bar{\alpha}_{66} \end{bmatrix} \begin{bmatrix} v_p \\ v_q \\ \Omega_r \end{bmatrix} + \begin{bmatrix} \bar{\alpha}_{11} & 0 & 0 \\ 0 & \bar{\alpha}_{22} & \alpha_{26} \\ 0 & \alpha_{62} & \bar{\alpha}_{66} \end{bmatrix} \begin{bmatrix} 0 \\ 0 \\ \omega/2 \end{bmatrix} + \begin{bmatrix} 0 \\ 0 \\ -mgH \sin \theta \end{bmatrix} \\ &+ \begin{bmatrix} h_{11} & 0 & h_{13} \\ 0 & h_{22} & 0 \\ 0 & h_{62} & 0 \end{bmatrix} \begin{bmatrix} e_{11} \\ e_{12} \\ -e_{11} \end{bmatrix} - \begin{bmatrix} f_1 \\ 0 \\ 0 \end{bmatrix} = 0, \end{aligned}$$

which can be further simplified after rearrangement as

$$\begin{aligned} \begin{bmatrix} \bar{\alpha}_{11} & 0 & 0 \\ 0 & \bar{\alpha}_{22} & \alpha_{26} \\ 0 & \alpha_{62} & \bar{\alpha}_{66} \end{bmatrix} \begin{bmatrix} v_p \\ v_q \\ \Omega_r \end{bmatrix} &= \begin{bmatrix} f_1 \\ 0 \\ 0 \end{bmatrix} - \begin{bmatrix} \bar{\alpha}_{11} & 0 & 0 \\ 0 & \bar{\alpha}_{22} & \alpha_{26} \\ 0 & \alpha_{62} & \bar{\alpha}_{66} \end{bmatrix} \begin{bmatrix} 0 \\ 0 \\ \omega/2 \end{bmatrix} - \begin{bmatrix} 0 \\ 0 \\ -mgH \sin \theta \end{bmatrix} \\ &- \begin{bmatrix} h_{11} & 0 & h_{13} \\ 0 & h_{22} & 0 \\ 0 & h_{62} & 0 \end{bmatrix} \begin{bmatrix} e_{11} \\ e_{12} \\ -e_{11} \end{bmatrix}. \end{aligned} \quad (2.74)$$

The coefficient matrix or resistance matrix from the above matrix equation can be defined as

$$A = \begin{bmatrix} \bar{\alpha}_{11} & 0 & 0 \\ 0 & \bar{\alpha}_{22} & \alpha_{26} \\ 0 & \alpha_{62} & \bar{\alpha}_{66} \end{bmatrix},$$

where the diagonal terms $\bar{\alpha}_{ij}$, incorporate viscous drag and viscous torque due to the spherical body. These diagonal terms have been modified using equations (2.7) for viscous drag and (2.8) for viscous torque as

$$\bar{\alpha}_{11} = \alpha_{11} - 6\pi, \quad \bar{\alpha}_{22} = \alpha_{22} - 6\pi,$$

and

$$\bar{\alpha}_{66} = \alpha_{66} - 8\pi.$$

The inverse of the above resistance matrix A , termed as the mobility matrix, can be evaluated as

$$B = A^{-1} = \begin{bmatrix} 1/\bar{\alpha}_{11} & 0 & 0 \\ 0 & -\bar{\alpha}_{66}/\Lambda & \alpha_{26}/\Lambda \\ 0 & \alpha_{62}/\Lambda & -\bar{\alpha}_{22}/\Lambda \end{bmatrix},$$

where

$$\Lambda = \alpha_{26}\alpha_{62} - \bar{\alpha}_{22}\bar{\alpha}_{66}.$$

After multiplication with the mobility matrix B , equation (2.74) takes the form

$$\begin{bmatrix} v_p \\ v_q \\ \dot{\theta} \end{bmatrix} = \begin{bmatrix} f_1/\bar{\alpha}_{11} \\ 0 \\ 0 \end{bmatrix} - \begin{bmatrix} 0 \\ 0 \\ \omega/2 \end{bmatrix} - \begin{bmatrix} 0 \\ -mgH \sin \theta \alpha_{26}/\Lambda \\ mgH \sin \theta \bar{\alpha}_{22}/\Lambda \end{bmatrix} - \begin{bmatrix} h_{11}/\bar{\alpha}_{11} & 0 & h_{13}/\bar{\alpha}_{11} \\ 0 & (h_{62}\alpha_{26} - h_{22}\bar{\alpha}_{66})/\Lambda & 0 \\ 0 & (h_{22}\alpha_{62} - h_{62}\bar{\alpha}_{22})/\Lambda & 0 \end{bmatrix} \begin{bmatrix} e_{11} \\ e_{12} \\ -e_{11} \end{bmatrix}, \quad (2.75)$$

where

$$\Omega_r = \dot{\theta}, \quad e_{11} = e \cos 2\gamma \quad \text{and} \quad e_{12} = e \sin 2\gamma,$$

and γ is the angle between the \mathbf{p}, \mathbf{q} plane and the plane containing \mathbf{p} and the flagellum. Also, α_{ij} and h_{ij} are the time dependent beat coefficients and e_{ij} are the components of the rate-of-strain tensor.

Finally, in component form, the total force and total torque are

$$\bar{\alpha}_{11}v_p + (h_{11} - h_{13})e \cos 2\gamma = f_1, \quad (2.76)$$

$$\bar{\alpha}_{22}v_q + \alpha_{26}\left(\dot{\theta} + \frac{\omega}{2}\right) + h_{22}e \sin 2\gamma = 0, \quad (2.77)$$

and

$$\alpha_{62}v_q + \bar{\alpha}_{66}\left(\dot{\theta} + \frac{\omega}{2}\right) + h_{66}e \sin 2\gamma = -mgH \sin \theta, \quad (2.78)$$

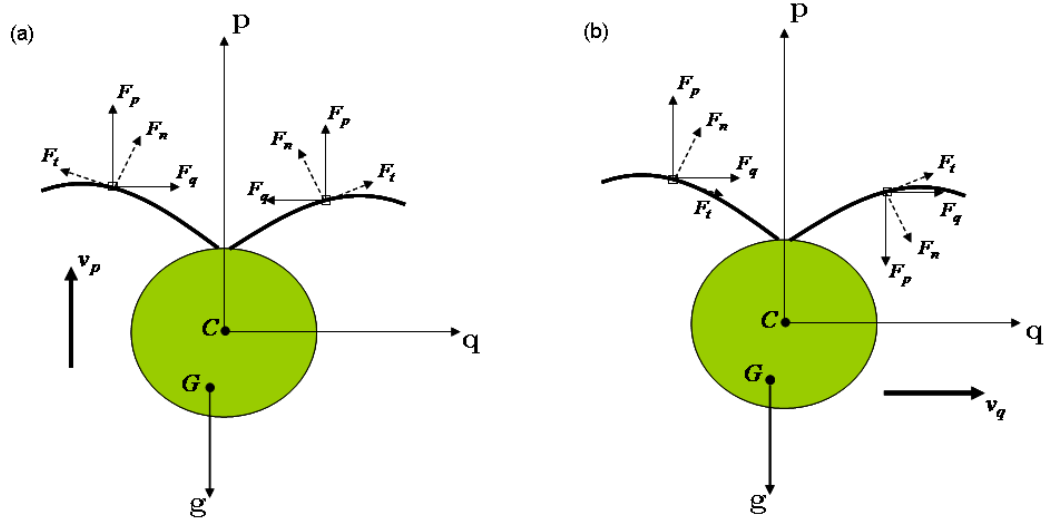


Figure 2.6: Addition and subtraction of forces acting on the flagellar section due to swimming in the (a) primary velocity direction \mathbf{p} and (b) transverse velocity direction \mathbf{q} respectively.

where, v_p and v_q are the components of the organism's tangential velocity parallel and perpendicular to the body axis \mathbf{p} , respectively. $\dot{\theta}$ is the angular velocity of the organism, whereas α_{ij} and h_{ij} are time dependent beat coefficients depending on the flagellar beat parameters. It is interesting to note that the velocity component v_p in the forward/primary direction is uncoupled from the other component v_q in the transverse direction, whereas v_q and the angular velocity $\dot{\theta}$ are coupled with each other.

The forces acting on the section of flagella while swimming in the primary direction \mathbf{p} are shown in the Figure 2.6(a). Since the flagella beat symmetrically so the forces in the \mathbf{q} direction cancel each other, while those in the \mathbf{p} direction will combine with each other. However, motion in the \mathbf{q} direction leads to the generation of torque due to the asymmetric arrangement of the flagella about \mathbf{q} . After rearrangement of terms we can write explicitly v_p and v_q as

$$v_p = \frac{f_1}{\bar{\alpha}_{11}} - \left(\frac{h_{11}}{\bar{\alpha}_{11}} \right) e \cos 2\gamma + \left(\frac{h_{13}}{\bar{\alpha}_{11}} \right) e \cos 2\gamma, \quad (2.79)$$

$$v_q = - \left(\frac{h_{62}\alpha_{26} - h_{22}\tilde{\alpha}_{66}}{\alpha_{26}\alpha_{62} - \bar{\alpha}_{22}\bar{\alpha}_{66}} \right) e \sin 2\gamma + \left(\frac{\alpha_{26}}{\alpha_{26}\alpha_{62} - \bar{\alpha}_{22}\bar{\alpha}_{66}} \right) mgH \sin \theta, \quad (2.80)$$

and $\dot{\theta}$ takes the form

$$\dot{\theta} = -\frac{\omega}{2} + \left(\frac{h_{62}\bar{\alpha}_{22} - h_{22}\alpha_{62}}{\alpha_{26}\alpha_{62} - \bar{\alpha}_{22}\bar{\alpha}_{66}} \right) e \sin 2\gamma - \left(\frac{\bar{\alpha}_{22}}{\alpha_{26}\alpha_{62} - \bar{\alpha}_{22}\bar{\alpha}_{66}} \right) mgH \sin \theta. \quad (2.81)$$

The unknown variables v_p, v_q and $\dot{\theta}$ can be solved at any time t throughout the beat. Finally, we can obtain the average velocity \mathbf{v} and average angular velocity $\mathbf{\Omega}$ of the organism by integrating v_p, v_q and $\dot{\theta}$ with respect to time over one beat and dividing by the beat time.

2.8 Uniplanar vertical upward swimming

Now as a first step, consider the simple case of uniplanar vertical upward swimming in a stationary flow field. In the present flagella beat model, this implies that there is no gravitational torque and no contribution of vorticity and strain rate. Thus inserting the corresponding values $\theta = 0$ and $\omega = e = 0$ into equations (2.79) to (2.81) gives the force-torque balance for pure uniplanar vertical upward swimming as

$$v_p = \frac{f_1}{\bar{\alpha}_{11}}, \quad (2.82)$$

$$v_q = 0, \quad (2.83)$$

and

$$\dot{\theta}_r = 0. \quad (2.84)$$

The beat coefficients can be calculated using the modified beat pattern and integrals I_i, J_i explained in Appendix A. For the effective stroke

$$f_1 = -K_n \left(\frac{l^2}{2} \dot{\chi} \right) \sin \chi, \quad (2.85)$$

and

$$\begin{aligned}
\alpha_{11} = & K_t \left[-l \cos^2 \chi + \frac{3}{2} \cos^2 \chi \ln \left| [(l + \cos \chi)^2 + \sin^2 \chi]^{\frac{1}{2}} + (l + \cos \chi)^2 \right| + \frac{\cos^5 \chi}{4 \sin^2 \chi} \right. \\
& - \frac{3}{2} \cos^2 \chi \ln |1 + \cos \chi| + \frac{\{(l + \cos \chi)^2 + \sin^2 \chi\} \cos^2 \chi}{4 \sin^2 \chi \{(l + \cos \chi)^2 + \sin^2 \chi\}^{\frac{1}{2}}} + \frac{3 \cos^3 \chi}{4} \\
& - \frac{3\{(l + \cos \chi)^2 + \sin^2 \chi\} \cos^2 \chi}{4\{(l + \cos \chi)^2 + \sin^2 \chi\}^{\frac{1}{2}}} + \frac{\sin^2 \chi \cos \chi}{4\{(l + \cos \chi)^2 + \sin^2 \chi\}^{\frac{3}{2}}} + \frac{\sin^2 \chi \cos \chi}{2} \\
& \left. - \frac{\{(l + \cos \chi)^2 + \sin^2 \chi\}^3 \cos^2 \chi}{4 \sin^2 \chi \{(l + \cos \chi)^2 + \sin^2 \chi\}^{\frac{3}{2}}} - \frac{\cos^3 \chi}{4 \sin^2 \chi} - \frac{3 \sin^2 \chi \cos \chi}{4\{(l + \cos \chi)^2 + \sin^2 \chi\}^{\frac{1}{2}}} \right] \\
& + K_n \left[-l \sin^2 \chi + \frac{3}{4} \sin^2 \chi \ln \left| [(l + \cos \chi)^2 + \sin^2 \chi]^{\frac{1}{2}} + (l + \cos \chi)^2 \right| - \frac{\cos^3 \chi}{4} \right. \\
& - \frac{3}{4} \sin^2 \chi \ln |1 + \cos \chi| - \frac{\{(l + \cos \chi)^2 + \sin^2 \chi\}}{2\{(l + \cos \chi)^2 + \sin^2 \chi\}^{\frac{1}{2}}} - \frac{\sin^2 \chi \cos \chi}{4} \\
& - \frac{3 \sin^2 \chi \cos \chi}{4\{(l + \cos \chi)^2 + \sin^2 \chi\}^{\frac{1}{2}}} + \frac{\{(l + \cos \chi)^2 + \sin^2 \chi\}^3}{4\{(l + \cos \chi)^2 + \sin^2 \chi\}^{\frac{3}{2}}} + \frac{\cos \chi}{2} \\
& \left. + \frac{\sin^2 \chi \cos \chi}{4\{(l + \cos \chi)^2 + \sin^2 \chi\}^{\frac{3}{2}}} + \frac{3\{(l + \cos \chi)^2 + \sin^2 \chi\} \sin^2 \chi}{4\{(l + \cos \chi)^2 + \sin^2 \chi\}^{\frac{1}{2}}} \right] - 6\pi. \quad (2.86)
\end{aligned}$$

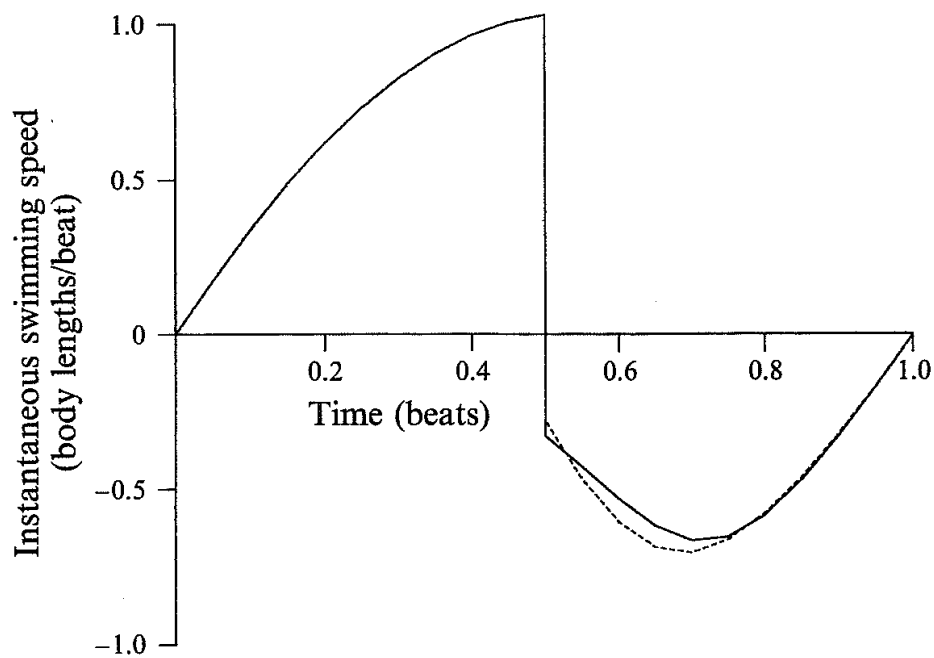
For the recovery stroke we can calculate

$$f_1 = K_t [w(\cos \chi - 1)(l - wt)] \cos \chi + K_n [w \sin \chi (l - wt) - \frac{1}{2}(l - wt)^2 \dot{\chi}] \sin \chi, \quad (2.87)$$

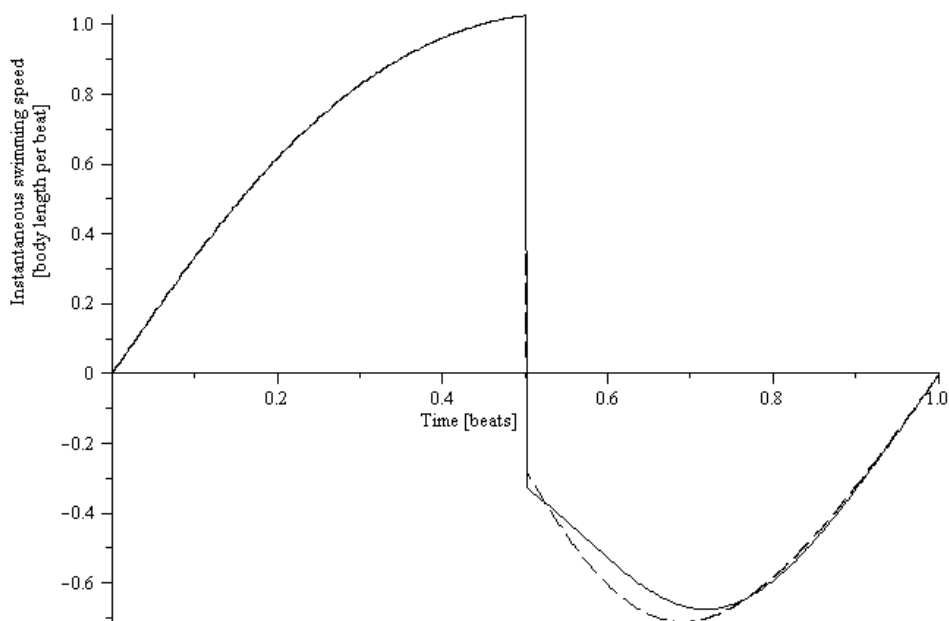
$$\begin{aligned}
\alpha_{11} = & K_t \left[-wt - \frac{1}{4} + \frac{1}{4(1 + wt)^2} + \frac{3}{2} \ln |1 + wt| - 2A \cos^2 \chi - (l - wt) \cos^2 \chi \right. \\
& + \frac{3}{2} \cos^2 \chi \ln \left| \frac{C + D}{B} \right| + \frac{3}{2} \cos^2 \chi \ln \left| \frac{E}{B} \right| + \frac{D \cos^2 \chi}{4CB^2} - \frac{3D \cos^2 \chi}{4C} - \frac{D^3 \cos^2 \chi}{4B^2 C^3} \\
& + \frac{\cos^2 \chi}{4B^2} - \frac{3 \cos^3 \chi}{4} - \frac{\cos^5 \chi}{4B^2} - \frac{3B \sin \chi \cos \chi}{4(1 + wt)} - \frac{3B \sin \chi \cos \chi}{4C} \\
& \left. + \frac{3 \sin \chi \cos \chi}{2} + \frac{B \sin \chi \cos \chi}{4(1 + wt)^3} + \frac{B \sin \chi \cos \chi}{4C^3} - \frac{\sin \chi \cos \chi}{2B^2} \right] \\
& + K_n \left[-2A \sin^2 \chi - (l - wt) \sin^2 \chi + \frac{3}{4} \sin^2 \chi \ln \left| \frac{C + D}{B} \right| + \frac{3}{4} \sin^2 \chi \ln \left| \frac{E}{B} \right| \right. \\
& - \frac{\sin^2 \chi \cos \chi}{2B^2} + \frac{3D \sin^2 \chi}{4C} + \frac{D^3 \sin^2 \chi}{4B^2 C^3} + \frac{3 \sin^2 \chi \cos \chi}{4} + \frac{\sin^2 \chi \cos^3 \chi}{4B^2} \\
& - \frac{3B \sin \chi \cos \chi}{4(1 + wt)} - \frac{3B \sin \chi \cos \chi}{4C} + \frac{3 \sin \chi \cos \chi}{2} + \frac{B \sin \chi \cos \chi}{4(1 + wt)^3} \\
& \left. - \frac{D \sin^2 \chi}{2CB^2} + \frac{B \sin \chi \cos \chi}{4C^3} - \frac{\sin \chi \cos \chi}{2B^2} \right] - 6\pi, \quad (2.88)
\end{aligned}$$

where

$$\begin{aligned}
A &= (1 + wt) \cos \chi, & B &= (1 + wt) \sin \chi, & C &= [(A + (l - wt))^2 + B^2]^{\frac{1}{2}}, \\
D &= A + l - wt, & \text{and} & & E &= A + 1 + wt.
\end{aligned}$$



(a)



(b)

Figure 2.7: Variation in uniplanar upward swimming velocity during one flagellar beat. A discontinuity occurs at the changeover from effective to recovery stroke. The dashed line represents the graph for constant angular velocity and solid line zero moment recovery stroke case. (a) Reproduced from Jones *et al.* [76], (b) Using generalized expressions and Maple code simulations.

Substituting the above beat coefficients into equation (2.82) we can calculate the instantaneous upward swimming speed v_p of the cell during the effective and recovery strokes. Figure 2.7 shows results of calculations for the organism's velocity for one complete flagellar beat. The first graph (a) is reproduced from Jones *et al.* [76], whereas, graph (b) was obtained using the generalized expressions and Maple code simulations.

In the above results for swimming velocity, the organism performs the effective stroke during the first portion of the beat, which causes upward swimming with increasing velocity. There is then discontinuity in the instantaneous velocity, and the organism swims backwards during the recovery stroke. It is clear from Figure 2.7 that the integral of this curve for one beat is positive resulting in upward swimming. The velocities during the recovery stroke have been modelled in two different ways, zero-moment and constant angular velocity cases. The Figure 2.7 indicates that backward velocity during the recovery stroke for the case of zero moment angular velocity case is slightly less than the constant angular velocity case. Jones *et al.* [76] computed average swimming velocity of 0.20 body radius for zero moment case and 0.18 body radius per beat for constant angular velocity case. For clarity, we will use zero-moment angular velocity model for future calculations.

Since resistance coefficients, K_t and K_n as mentioned in Section 2.3 depend upon the ratio of the length l and radius b of the flagellum. So the ratio K_n/K_t , is a function of l/b which is plotted against the upward swimming speed for Gray and Hancock's resistance coefficients [51] and Lighthill's resistance coefficients [94] as shown in the Figure 2.8. Using the values from Table 2.2 and Gray and Hancock's resistance coefficients [51] i.e. $K_n = 2.17$ and $K_t = 1.31$, we have computed the organism's swimming speed as 0.128 body radii per beat or $32 \mu\text{m s}^{-1}$. On the other hand using Lighthill's resistance coefficients [94] i.e. $K_n = 3.7$ and $K_t = 2.2$, we found 0.197 body radii per beat or $49.3 \mu\text{m s}^{-1}$. The above values show consistency with Jones *et al.* [76] as they found 0.6 body length or $31 \mu\text{m s}^{-1}$ and 0.1 body length or $50 \mu\text{m s}^{-1}$ respectively. Clearly Lighthill's coefficients [94] gave swimming speed closer to the experimental observations (see Ruffer and Nultsch [128]), so for the further investigations we will use Lighthill's resistance coefficients [94] i.e. $K_n = 3.7$ and $K_t = 2.2$. Jones *et al.* [76] found that during effective stroke organism swims upwards a distance of 0.33 body diameters and during recovery stroke regress 0.23 body diameters. So this combines to give an average instantaneous swimming speed of organism of 0.10 body diameters per beat. For cell body diameter $10 \mu\text{m}$ and with beat frequency of 50 s^{-1} , this provides a swimming velocity as $50 \mu\text{m s}^{-1}$. With many more time steps and using

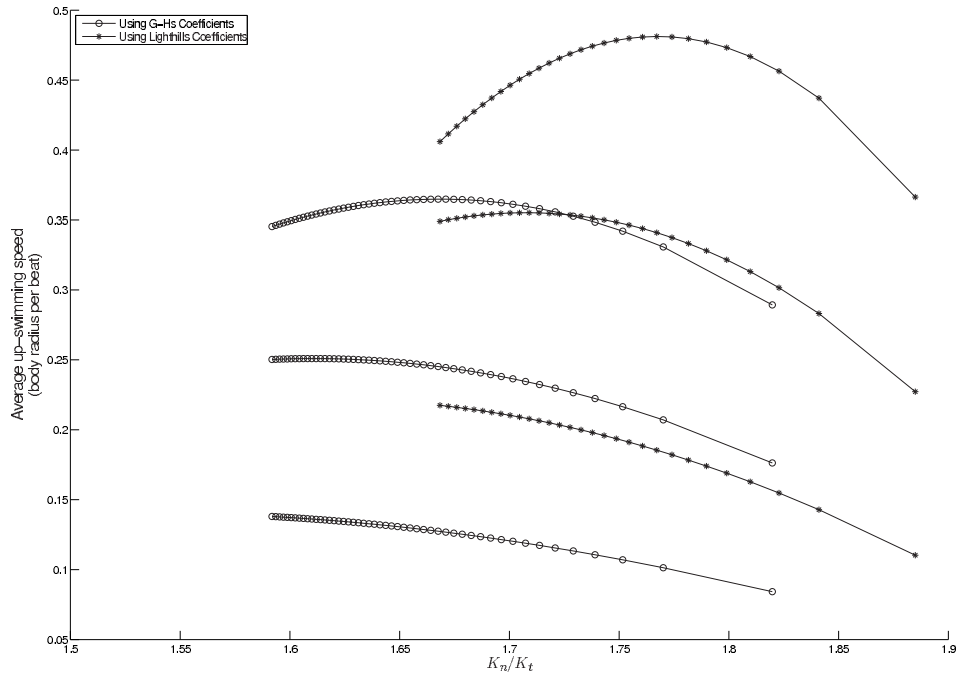


Figure 2.8: Uniplanar upward swimming speed plotted against ratio of resistance coefficients K_n/K_t for varying flagella length ($l = 2a, 3a, 4a$, from bottom to top), where a is the radius of the cell's body.

our Maple code, the organism's upward swimming speed is calculated as 0.1967 body radii per beat or 0.098 body diameter per beat providing excellent agreement with the upward swimming speed of 0.10 body diameter calculated by Jones *et al.* [76] analytically.

2.9 General unbounded uniplanar swimming

Consider the force torque balance equations (2.79) to (2.81), and the assumptions for the simplified symmetric flagellar beat in an unbounded domain. For simplicity, as we have the bounded case in mind, we also assume no rate-of-strain and no vorticity. The organism's translational velocity parallel, v_p and perpendicular, v_q to the body axis \mathbf{p} is

$$v_p = \frac{f_1}{\bar{\alpha}_{11}}, \quad (2.89)$$

and

$$v_q = \left(\frac{\alpha_{26}}{\alpha_{26}\alpha_{62} - \bar{\alpha}_{22}\bar{\alpha}_{66}} \right) mgH \sin \theta. \quad (2.90)$$

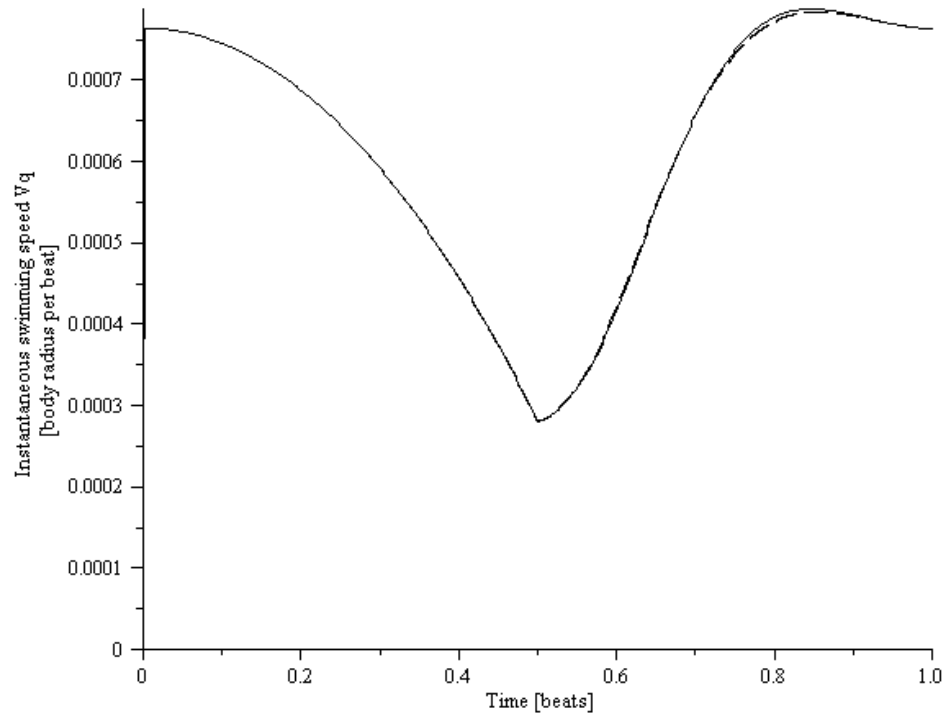
Similarly the organism's angular velocity is

$$\dot{\theta} = - \left(\frac{\bar{\alpha}_{22}}{\alpha_{26}\alpha_{62} - \bar{\alpha}_{22}\bar{\alpha}_{66}} \right) mgH \sin \theta. \quad (2.91)$$

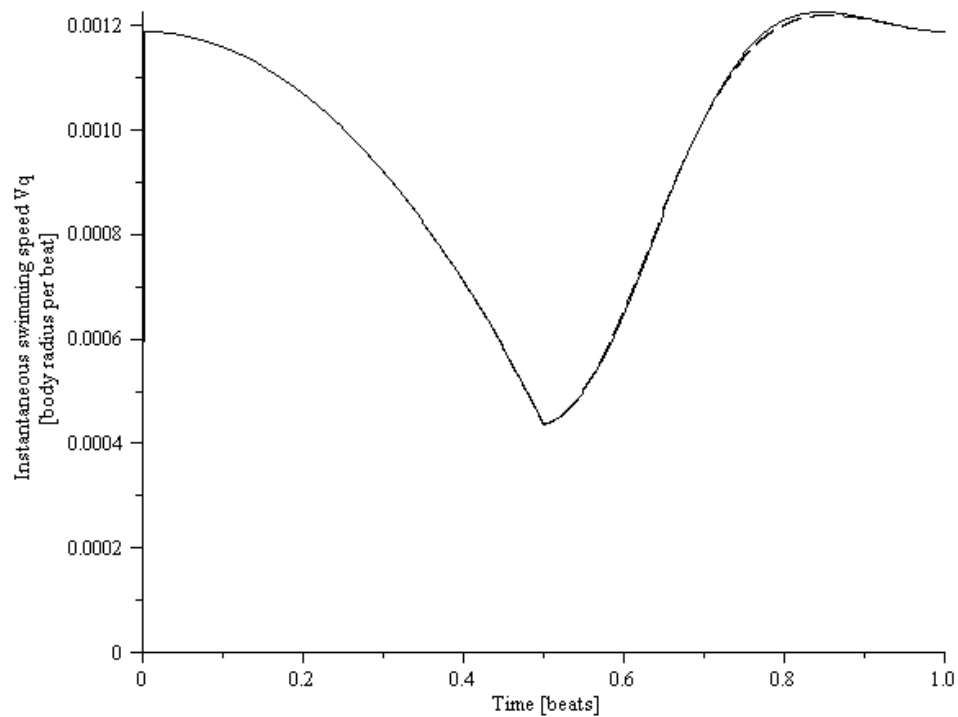
Using these equations, we shall investigate the swimming velocity and angular velocity of the organism. We will explore the two initial values $\theta = 40^\circ$ and $\theta = 90^\circ$ (i.e. swimming horizontally). As v_p is uncoupled from θ , it remains the same as in Figure 2.7 even for the two different initial values of θ . But this is not the complete picture as for the general case the transverse swimming speed component v_q is non-zero. The graphs for the transverse component of the swimming velocity are shown in the Figure 2.9. For the case of cell swimming horizontally initially i.e. $\theta = 90^\circ$, we have computed that organism swims a distance of 0.00046 body radii in the direction during effective stroke and 0.00049 body radii during recovery stroke. This will sum up to give 0.00096 body radii per beat in the \mathbf{q} or transverse swimming direction. Interestingly here the values for v_q are positive and decreased to zero as θ tends to zero for one flagella beat. It is also observed that swimming speed v_q increases with the increase of the centre-of-gravity offset H .

The most interesting application of the unbounded swimming flagellar beat model is the computation of angular velocity to provide estimates for the effective centre-of-gravity offset and cell eccentricity over one flagella beat. The graphs for the variation of θ for two different values of initial θ are shown below in Figure 2.10. Again for the case of horizontal swimming i.e. $\theta = 90^\circ$, we have found the change in the organism's orientation angle from $\theta = 90^\circ$ to $\theta = 89.91^\circ$. In both cases the value of θ decreases after the completion of the beat, and curves are qualitatively are the same. This is because the swimming organism is bottom heavy and cell tends to swim upwards on average. The angular velocity $\dot{\theta}$ again increases by increasing the value of centre-of-gravity offset H .

In this uniplanar locomotion, viscous torque on the body and flagella will balance the gravitational torque opposing the organism's angular velocity $\dot{\theta}$ as shown in Figure 2.1. In order to investigate the contribution of the flagella on the magnitude of the viscous torque we have calculated the angular velocity and found the change in the angle θ of the organism for one beat without the inclusion of flagella. After one beat the variation was found from $\theta = 90^\circ$ to $\theta = 89.8^\circ$, which is approximately 50 % greater than the value with the inclusion of the flagella as shown in Figure 2.11. This shows that flagella torque plays a significant role for the calculation of the angular velocity of the organism.

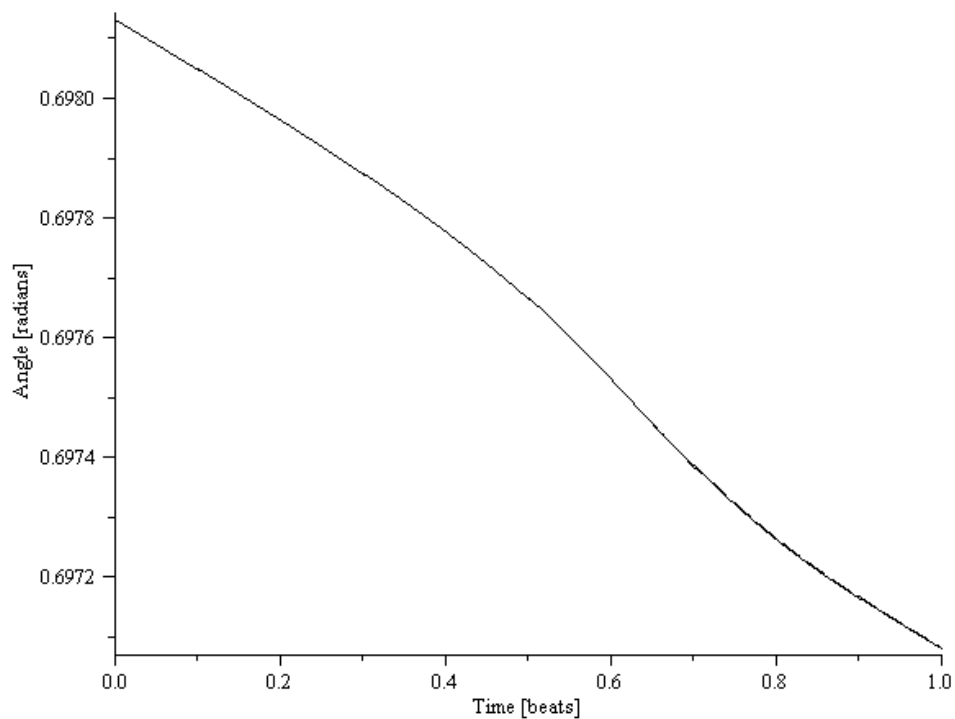


(a)

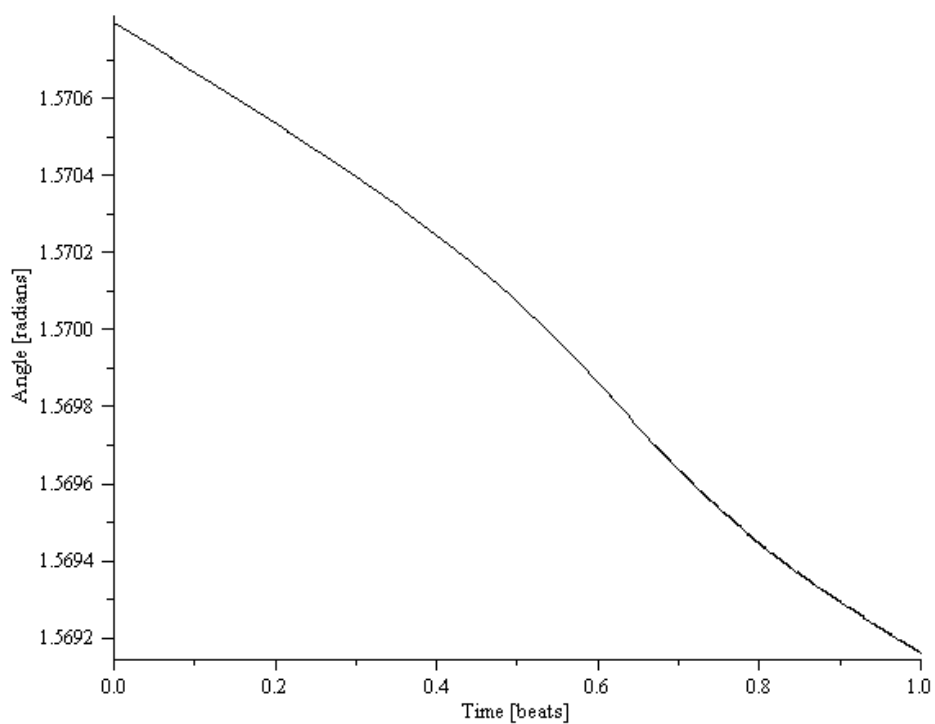


(b)

Figure 2.9: Variation in uniplanar instantaneous swimming velocity in transverse direction during one flagellar beat. The dashed line represents the graph for constant angular velocity and solid line zero moment recovery stroke case. With initial angle (a) $\theta = 40^\circ$ i.e. angled swimming, (b) $\theta = 90^\circ$ i.e. horizontal swimming.



(a)



(b)

Figure 2.10: Variation of angle θ from the initial angle θ_0 during one flagella beat due to the effect of gravitational torque only. With initial angle (a) $\theta = 40^\circ$ i.e. angled swimming, (b) $\theta = 90^\circ$ i.e. horizontal swimming.

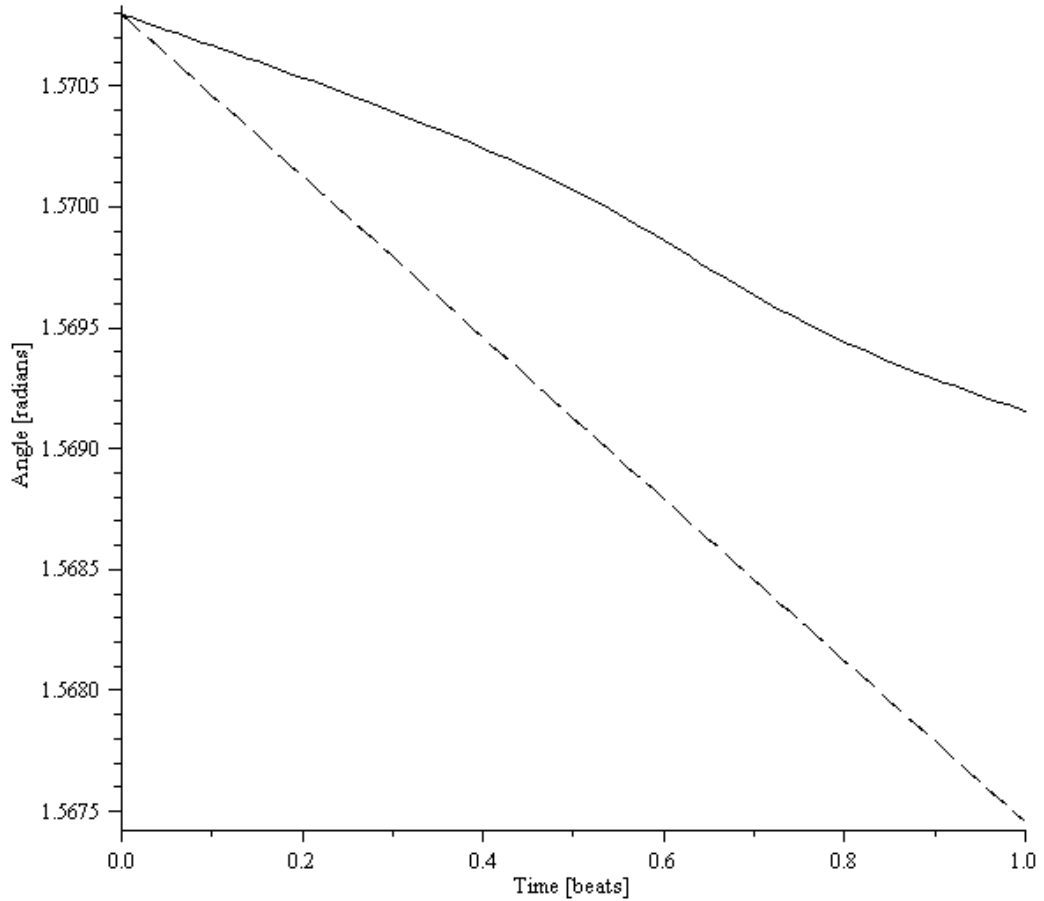


Figure 2.11: Variation of the angle θ during one flagella beat when organism swims horizontally i.e. $\theta = 90^\circ$. The dashed line represents swimming organism without flagella and solid line indicates with the flagella.

2.9.1 Calculation of effective gyrotactic re-orientation time

Pedley and Kessler [114] in the analysis of gyrotaxis, found the rate of change of the swimming direction as

$$\dot{\mathbf{p}} = \frac{1}{2B} [\mathbf{k} - (\mathbf{k} \cdot \mathbf{p})\mathbf{p}] + \frac{1}{2}\boldsymbol{\omega} \times \mathbf{p} + \alpha_0 \mathbf{p} \cdot \mathbf{E} \cdot [\mathbf{I} - \mathbf{p}\mathbf{p}^T], \quad (2.92)$$

where \mathbf{p} and \mathbf{k} are the unit vectors directed along the major axis of the swimming cell and vertically upwards respectively, $\boldsymbol{\omega}$, \mathbf{E} are the vorticity and the rate-of-strain of the ambient flow, respectively, α_0 is cell's eccentricity, \mathbf{I} is the identity tensor and B is the gyrotactic reorientation time. The above equation was derived by ignoring the viscous flagellar torque contribution in the force-torque balance equations. This equation is similar to equation (2.81) which includes the contribution due to the flagellar torque for the

Name with symbol	Values by Pedley <i>et al.</i>	Values by Jones <i>et al.</i>
Swimming speed - v_p	$5 - 10 \times 10^{-3} \text{ cm s}^{-1}$	$5 \times 10^{-3} \text{ cm s}^{-1}$
Cell eccentricity - α_0	0.31	0.08
Sedimentation speed - v_s	$3 \times 10^{-4} \text{ cm s}^{-1}$	$2.5 \times 10^{-4} \text{ cm s}^{-1}$
Viscous torque parameter - α_{\perp}	6.8	12.6
Gyrotactic re-orientation time - B	3.4 s	6.3 s

Table 2.3: Table of values taken from Jones *et al.* [76].

uniplanar locomotion and can be rewritten as

$$\dot{\theta} = -\frac{\omega}{2} + \eta e \sin 2\gamma - \xi mgH \sin \theta, \quad (2.93)$$

where

$$\eta = \left(\frac{h_{62}\bar{\alpha}_{22} - h_{22}\alpha_{62}}{\alpha_{26}\alpha_{62} - \bar{\alpha}_{22}\bar{\alpha}_{66}} \right), \quad \text{and} \quad \xi = \left(\frac{\bar{\alpha}_{22}}{\alpha_{26}\alpha_{62} - \bar{\alpha}_{22}\bar{\alpha}_{66}} \right).$$

Note that the dimensions of ξ are $\text{kg}^{-1}\text{m}^{-1}\text{s}$, whereas η is non-dimensional and both are positive valued functions. Now comparing the two analogous equations (2.92) and (2.93) gives

$$\alpha_0 = \eta, \quad \text{and} \quad B = \frac{1}{2\tilde{\xi}mgH}, \quad (2.94)$$

where $\tilde{\xi}$ is the dimensional form of ξ . Now using the non-dimensional form of ξ from Table 2.1, the gravitational re-orientation time takes the form as

$$B = \frac{3\mu v}{8\pi\xi mgH} = \frac{\mu\alpha_{\perp}}{2H\rho g}, \quad (2.95)$$

where α_{\perp} is a non-dimensional parameter, termed the viscous torque parameter by Pedley and Kessler *et al.* [111] and can be defined here as

$$\alpha_{\perp} = \frac{3}{4\pi\xi}. \quad (2.96)$$

Using the idealized flagella beat pattern with the dimensions for *C. nivalis* in Table 2.2, the average values of the function are

$$\eta = \alpha_0 = 0.09 \quad \text{and} \quad \xi = 0.019, \quad (2.97)$$

as in Jones *et al.* [76]. Using these values one may calculate the new values of the quantities discussed above to improve the existing Pedley and Kessler [113] continuum model (see Table 2.3).

2.10 Tracking of the swimming cell

Using the equations (2.89) to (2.91), we can track the motion of the swimming micro-organism in a flow field performing more than one beat. In the fixed space coordinates system (using the transformation matrix R_{SB}^T) we can write as

$$\begin{bmatrix} v_1 \\ \Omega_2 \\ v_3 \end{bmatrix} = \begin{bmatrix} \sin \theta & \cos \theta & 0 \\ 0 & 0 & 1 \\ \cos \theta & -\sin \theta & 0 \end{bmatrix} \begin{bmatrix} v_p \\ v_q \\ \dot{\theta} \end{bmatrix}, \quad (2.98)$$

where v_1 , v_3 are velocities in the x and z direction and Ω_2 is the angular velocity. We can write the differential equations for the position and angle of cell at any time t during the flagella beat as

$$\begin{aligned} \frac{dx_1}{dt} &= v_1(t), \\ \frac{dx_3}{dt} &= v_3(t), \\ \frac{d\Omega_2}{dt} &= \dot{\theta}(t). \end{aligned} \quad (2.99)$$

We can use the Euler method to solve these first order ordinary differential equations numerically, such that

$$\begin{aligned} x_1^{i+1} &= x_1^i + dt(v_1(t)) \\ x_3^{i+1} &= x_3^i + dt(v_3(t)) \\ \theta^{i+1} &= \theta^i + dt(\dot{\theta}(t)). \end{aligned} \quad (2.100)$$

Thus at every time step v_p , v_q and $\dot{\theta}$ are calculated for the old position and orientation in the body coordinate system and then converted into the fixed space coordinate system v_1 , v_3 and Ω_2 . These equations produce the a new position and orientation x_1 , x_3 and θ of the cell. It is also interesting to note that here we can use a higher order numerical scheme like Runge-Kutta method but our analysis shows that Euler's scheme is adequate and works well in this case.

Using the above defined method we have plotted the trajectory of the swimming cell for three different initial angles i.e. when $\theta = 70^\circ$, $\theta = 80^\circ$ and $\theta = 90^\circ$ as shown in the Figure 2.12. The tendency for the cells to swim upwards on average is clearly observed.

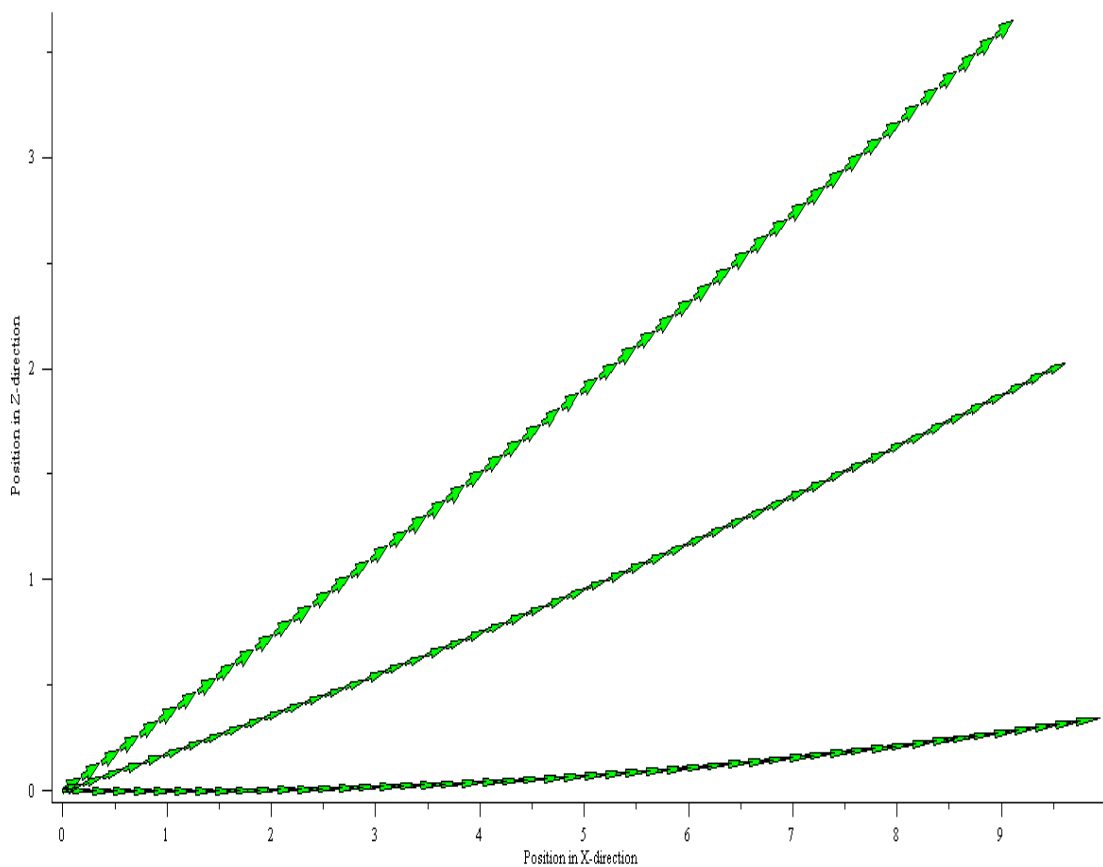


Figure 2.12: Trajectory of the unbounded swimming cell in scales of the X and Z axes with initial angle $\theta_0 = 90^\circ, 80^\circ, 70^\circ$ from bottom to top respectively. The arrows represent the position of the cell after the flagella beat (effective and recovery stroke) at any time t .

2.11 Conclusion

After reviewing the detailed calculations Jones *et al.* [76] and the PhD thesis of Jones [77], we have found certain misprints. So as a first step we have revised and performed all the calculations again for the uniplanar case to identify and rectify all misprints and errors. Later we have generalized the Jones *et al.* [76] flagellar beat model to make it simple to employ. Additionally this modification makes the model θ dependent which enables computation of the trajectory of the swimming cell. To avoid lengthy and tedious calculations we employed the software Maple for the verification of the swimming of cell in an unbounded fluid flow problem. Our method showed good agreement with the results found in Jones *et al.* [76].

The above idealized model using the RFT approximation, which is considered as a compromised choice in comparison to the slender-body theory shows handsome qualitative agreement with experimental observations for the cell swimming velocity in an unbounded domain. It also reveals that the torque due to the flagella has a prominent role in the calculations of the cell's angular velocity, which was ignored in the previous continuum models (see Pedley and Kessler [113]). After comparison with the Pedley and Kessler [113] angular velocity equation, Jones *et al.* [76] found interesting results as shown in Table 2.3. Our generalization of the beat pattern and Maple code procedure also showed good agreement with the Jones *et al.* [76] results listed in Table 2.3. They conclude that the interestingly the increased values of gyrotactic re-orientation time scale B and cell's eccentricity α_0 are due to the flagellar torque which slows down the angular velocity of the micro-organism. The lower angular velocity of the micro-organism ultimately implies a lower angular deviation from the organism's swimming path.

The comparison of the two different resistance coefficients used while employing the Resistive Force Theory shows that Lighthill's [94] resistance coefficients gave better results in comparison to the experimental observations, as expected. Secondly the two procedures for modelling the angular velocity during the recovery stroke of the flagella beat shows that the zero moment angular velocity case results gave good agreement with the experimental results.

To avoid cumbersome calculations Jones *et al.* [76] in their later computations have used averaged values of the time dependent beat coefficients instead of instantaneous values, which somehow compromises the accuracy and consistency of the results. However our generalized procedure based on modified position vector and Maple code can easily

be used to simulate different results for extended time periods for the cell's locomotion in an unbounded domain. This also motivates the author to extend the procedure and apply the same idealized model with generalization procedure adopted here and the RFT approximation to further complex situations like swimming of the cell in the proximity of a rigid no-slip plane boundary.

The main result of this chapter is that the method of Jones *et al.* [76] for the single cell locomotion in an unbounded domain, can be generalized and implemented on the algebraic manipulation software Maple, yielding good agreement with the already published results.

Chapter 3

Biflagellate swimming in the vicinity of a plane boundary

3.1 Synopsis

In this chapter, we have studied the swimming motion of the bottom heavy micro-organism in the vicinity of the no-slip stationary plane boundary. Here we have modelled the bounded cell swimming problems using the method as discussed in chapter 2 and image system singularities defined by Blake and Chwang [16] to satisfy the no-slip plane boundary condition. Using Resistive Force Theory (RFT), an analytical modified method for a biflagellated swimming cell which beats its flagella within a single plane near the no-slip plane boundary was established. The cumbersome analytical calculations of the problem were incorporated using the software Maple. The detailed analysis of the different bounded swimming situations of a biflagellate that is swimming away, towards, angled and parallel to the plane boundary was discussed. This analysis will help to understand the swimming dynamics of the cell under the influence of the boundaries such as micro slides, tubes and pipes etc. This will also help to improve the existing continuum model for suspensions of gyrotactic biflagellate micro-organism. The analysis will assist in better understanding of laboratory experiments of the trajectories of the bounded swimming cells and improve the investigations of the collective behavior of the biflagellate cells.

3.2 Introduction

The interaction of a wall and a particle depend upon the particle geometry, position, and orientation, and shape, and geometry of the wall. We experience that most of the laboratory experiments of swimming micro-organisms involve microscopic or macroscopic study of suspensions on micro slides, petri dishes, thin cylindrical tubes etc. Due to the smallness of the dimensions of the micro-organisms, typically a *Chlamydomonas* cell is of radius 2-10 μm , we can expect some indisputable effect in the swimming cell locomotion in the vicinity of the boundaries. Since the presence of the boundaries modify the hydrodynamic stresses acting on the swimming micro-organisms, this changes the motility both physically and biologically from bulk motility near the boundaries (see Lauga and Powers [90]). The applications of biological locomotion near the boundaries involve spermatozoa accumulation near uterus (Smith *et al.* [136]), biofilm formation (Ishikawa and Pedley [71]), surface associated bacterial infections (Harkes *et al.* [57]), etc. Here, we are interested in the fluid mechanics of the spherical shape biflagellate cell locomotion near the plane boundary.

The modelling of the motion of slender bodies or spheres close to the boundary in a viscous fluid in different situations were studied by Katz *et al.* [78], Barta and Liron [2], [3], Pasol *et al.* [109], Binous and Phillips [13]. These involve mostly slender-body theory and numerical techniques for the solutions of the different problems near the boundary. Recently, Smith *et al.* [135] and [136] used a hybrid algorithm of boundary integral/slender-body theory to model cilia and human sperms accumulation close to a boundary. The inclusion of boundaries can modify the cell locomotion in different ways. In the first case they can effect the cell swimming speed near the boundary and secondly boundaries can influence some micro-organism's swimming kinematics by modifying their trajectories (see Lauga and Powers [90]). The inclusion of boundaries also influence cell-cell interactions but here we are only interested in single cell locomotion and will investigate only aspects of swimming speed and angular velocity changes due to the presence of the no-slip plane boundaries.

In this chapter we extend the generalized analytical Jones *et al.* [76] flagella beat model problem discussed in chapter 2 from unbounded to bounded problems. Here we discuss the problems of swimming of a biflagellated *C. augustae* cell in a viscous flow field in the vicinity of the no-slip plane boundary. We use again the approximation Resistive Force Theory (RFT) to model and calculate the biflagellate cell's swimming velocity and angular

velocity relative to the ambient flow field in the proximity of the no-slip stationary plane boundaries. For the ease of calculations, we have assumed that the contributions from ambient vorticity and rate-of-strain are negligible.

To model the biflagellate bounded swimming problems we mostly follow the assumptions of the unbounded generalized flagella beat pattern problem discussed in chapter 2. we assume no hydrodynamic interaction of flagellum with the cell body and no interaction between neighboring elements of the flagellum. We also assume the no-slip plane boundary is at rest and lies at a distance h from the centre of the cell body.

3.3 Swimming near the plane boundary

As most of the laboratory experiments relating to swimming of micro-organisms involve swimming situations close to the plane boundary, thus we will investigate the swimming of *C. augustae* cell in the vicinity of the rigid stationary no-slip plane boundary. To satisfy the no-slip conditions, we require the image system for the Stokeslet and potential doublet singular solutions. The image systems for the fundamental singularities of viscous flow near an infinite plane boundary were first discussed by Blake (see, Blake [14] and Blake and Chwang [15]). Since the micro-organism under consideration is assumed to be of spherical shape, so we first discuss and explain in detail about the image system for the motion of a sphere in the vicinity of a no-slip stationary plane boundary.

3.3.1 Image singularities system

In chapter 1 we have briefly defined the singularities like Stokeslet and their derivatives such as the Stokes doublet and source doublet, which we later used to establish the singular solutions for the motion of the sphere in the Stokes fluid flow. Here we require the singular solutions for motion of the sphere of radius a in the Stokes flow near the no-slip stationary plane boundary. Now as we know that the Oseen tensor or Stokeslet singularity is defined as

$$S_{ij}(x, y') = \frac{1}{8\pi\mu} \left(\frac{\delta_{ij}}{R} + \frac{R_i R_j}{R^3} \right) \sim \frac{1}{R}, \quad \text{for large } R,$$

where \mathbf{R} is the position vector at any point P from the centre of the image sperm as shown in the Figure 3.1 and its magnitude is defined as

$$R = [(x_1 - y_1)^2 + (x_2 - y_2)^2 + (x_3 + h)^2]^{\frac{1}{2}}.$$

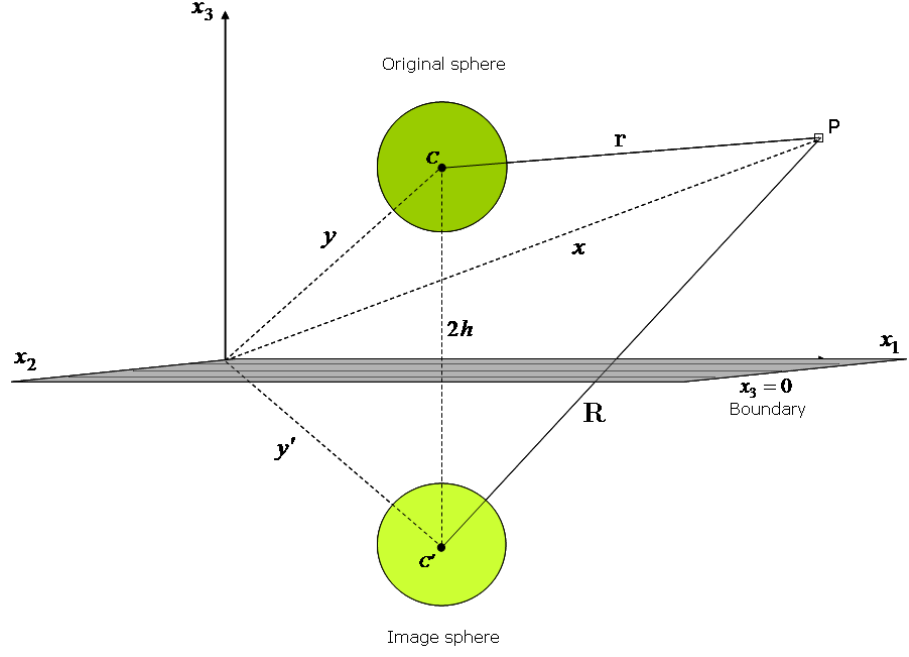


Figure 3.1: The position of sphere and image sphere due to Stokeslet and potential dipole singularities and no-slip stationary plane boundary at $x_3 = 0$. The distance h is measured from the centre of the sphere to the plane boundary, whereas \mathbf{r} and \mathbf{R} represents the position vectors at any point P from the centre of sphere and image sphere, respectively.

The differentiation of the above defined Stokeslet gives the Stokes doublet singularity

$$S_{ij,k}(x, y') = \frac{\partial S_{ij}}{\partial R_k} = \frac{1}{8\pi\mu} \left(-\frac{R_k \delta_{ij}}{R^3} + \frac{R_j \delta_{ik}}{R^3} + \frac{R_i \delta_{jk}}{R^3} - \frac{3R_i R_j R_k}{R^5} \right) \sim \frac{1}{R^2},$$

and further differentiation leads to source doublet singularity as

$$D_{ij}(x, y') = \nabla^2 S_{ij}(x, y') = S_{ij,kk} = \frac{\partial^2 S_{ij}}{\partial R_k \partial R_k} = \frac{1}{8\pi\mu} \left(\frac{2\delta_{ij}}{R^3} - \frac{6R_i R_j}{R^5} \right) \sim \frac{1}{R^3}.$$

Blake [14] first derived the solution for the Stokeslet in the presence of the stationary plane boundary and the exact solution for a force singularity in the presence of a no-slip plane boundary was defined as

$$u_i(x, y) = F_j \left[S_{ij}(x, y) + S_{ij}^{img}(x, y') \right], \quad (3.1)$$

where $S_{ij}^{img}(x, y')$ is the image Stokeslet and was found to be

$$S_{ij}^{img}(x, y') = \left[-S_{ij}(x, y') + h(\delta_{j\bar{\alpha}}\delta_{\bar{\alpha}k} - \delta_{j3}\delta_{3k}) \left(h\nabla^2 S_{ik}(x, y') - 2\frac{\partial}{\partial R_k} S_{i3}(x, y') \right) \right],$$

where $\tilde{\alpha} = 1, 2$, the tensor $(\delta_{j\tilde{\alpha}}\delta_{\tilde{\alpha}k} - \delta_{j3}\delta_{3k})$ is non-zero when $j = k$ and has values

$$(\delta_{j\tilde{\alpha}}\delta_{\tilde{\alpha}k} - \delta_{j3}\delta_{3k}) = \begin{cases} 1, & \text{for } j = 1, 2, \\ -1, & \text{for } j = 3, \end{cases}$$

which can be further simplified by substituting the differentials and can be rewritten as

$$\begin{aligned} S_{ij}^{img}(x, y') &= \frac{1}{8\pi\mu} \left[\left(-\frac{\delta_{ij}}{R} - \frac{R_i R_j}{R^3} \right) + 2h^2 (\delta_{j\tilde{\alpha}}\delta_{\tilde{\alpha}k} - \delta_{j3}\delta_{3k}) \left(\frac{\delta_{ik}}{R^3} - \frac{3R_i R_k}{R^5} \right) \right. \\ &\quad \left. - 2h (\delta_{j\tilde{\alpha}}\delta_{\tilde{\alpha}k} - \delta_{j3}\delta_{3k}) \left(-\frac{\delta_{i3}R_k}{R^3} + \frac{\delta_{3k}R_i}{R^3} + \frac{\delta_{ik}R_3}{R^3} - \frac{3R_i R_3 R_k}{R^5} \right) \right], \end{aligned} \quad (3.2)$$

where

$$\tilde{\alpha} = 1, 2, \quad R_l = x_l - y_l, \quad \text{and} \quad R_3 = x_3 + h.$$

Blake and Chwang [16], derived the solution for the source doublet (Laplacian of Stokeslet) in the presence of a stationary no-slip plane boundary, which can be written as

$$u_i(x, y) = D_j \left[D_{ij}(x, y) + D_{ij}^{img}(x, y') \right], \quad (3.3)$$

where $D_{ij}^{img}(x, y')$, is the image source doublet and was defined by taking the gradient of a source in the presence of the plane boundary and can be written after simplifications as

$$\begin{aligned} D_{ij}^{img}(x, y') &= -\frac{1}{8\pi\mu} \left(\frac{2\delta_{ij}}{R^3} - \frac{6R_i R_j}{R^5} \right) - \frac{3}{2\pi\mu} (\delta_{j3}\delta_{i\tilde{\alpha}} + \delta_{j\tilde{\alpha}}\delta_{i3}) \frac{R_{\tilde{\alpha}} R_3}{R^5} \\ &\quad + \frac{3\delta_{j3}\delta_{i\tilde{\alpha}}}{2\pi\mu} \left(-\frac{R_{\tilde{\alpha}} x_3}{R^5} + \frac{5R_{\tilde{\alpha}} R_3^2 x_3}{R^7} \right) - \frac{3\delta_{j\tilde{\alpha}}\delta_{i\tilde{\beta}}}{2\pi\mu} \left(-\frac{\delta_{\tilde{\alpha}\tilde{\beta}} R_3 x_3}{R^5} + \frac{5R_{\tilde{\alpha}} x_3 R_3 R_{\tilde{\beta}}}{R^7} \right) \\ &\quad + \frac{3\delta_{j3}\delta_{i3}}{2\pi\mu} \left(-\frac{3R_3 x_3}{R^5} + \frac{5R_3^3 x_3}{R^7} \right) - \frac{3\delta_{j\tilde{\alpha}}\delta_{i3}}{2\pi\mu} \left(-\frac{R_{\tilde{\alpha}} x_3}{R^5} + \frac{5R_{\tilde{\alpha}} R_3^2 x_3}{R^7} \right), \end{aligned} \quad (3.4)$$

where

$$\tilde{\alpha}, \tilde{\beta} = 1, 2, \quad R_l = x_l - y_l, \quad \text{and} \quad R_3 = x_3 + h.$$

3.3.2 Solution for the translating motion of a sphere near a stationary plane boundary

The velocity and pressure fields for the unbounded translating motion of a sphere in a Stokes flow obtained by Oseen [107] are

$$\begin{aligned} u_j(x, y) &= 6\pi\mu a U_i \left[\left(1 + \frac{a^2}{6} \nabla^2 \right) S_{ij}(x, y) \right] \\ &= 6\pi\mu a U_i \left[S_{ij}(x, y) + \frac{a^2}{6} D_{ij}(x, y) \right] \\ &= \frac{3a}{4} U_k \left(\frac{\delta_{jk}}{r} + \frac{r_j r_k}{r^3} \right) - \frac{a^3}{4} U_k \left(-\frac{\delta_{jk}}{r^3} + \frac{3r_j r_k}{r^5} \right), \end{aligned} \quad (3.5)$$

and

$$p = \frac{3}{2}\mu U_k \left(\frac{r_k}{r^3} \right), \quad (3.6)$$

where a is the radius and \mathbf{x} is the position of the sphere.

Similarly, the velocity disturbance \mathbf{u} caused by the image of a translating sphere of radius a moving through the Newtonian fluid in the presence of the no-slip stationary plane boundary under the influence of an applied force \mathbf{F} can be calculated as

$$\begin{aligned} u_j^{img}(x, y) &= F_i \left[\left(1 + \frac{a^2}{6} \nabla^2 \right) S_{ij}^{img}(x, y') \right] \\ &= F_i \left[S_{ij}^{img}(x, y') + \frac{a^2}{6} D_{ij}^{img}(x, y') \right]. \end{aligned} \quad (3.7)$$

As we know that on the surface of the sphere of radius a the above combination for Faxen's law (see Kim and Karrila [87]) takes the form as

$$\left(1 + \frac{a^2}{6} \nabla_y^2 \right) S_{ij}^{img}(x, y) = \frac{4}{3a} \delta_{ij}.$$

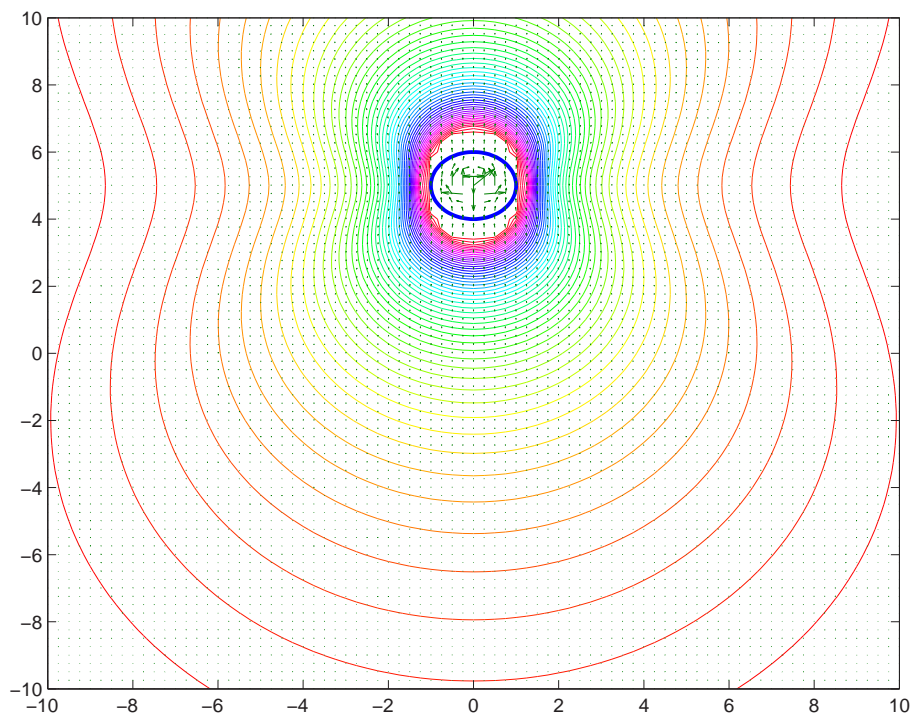
Therefore, the approximate singular solution for the motion of the image sphere translating with the velocity \mathbf{U} in the presence of the stationary plane boundary takes the form

$$u_j^{img}(x, y) = 6\pi\mu a U_i \left[S_{ij}^{img}(x, y') + \frac{a^2}{6} D_{ij}^{img}(x, y') \right], \quad (3.8)$$

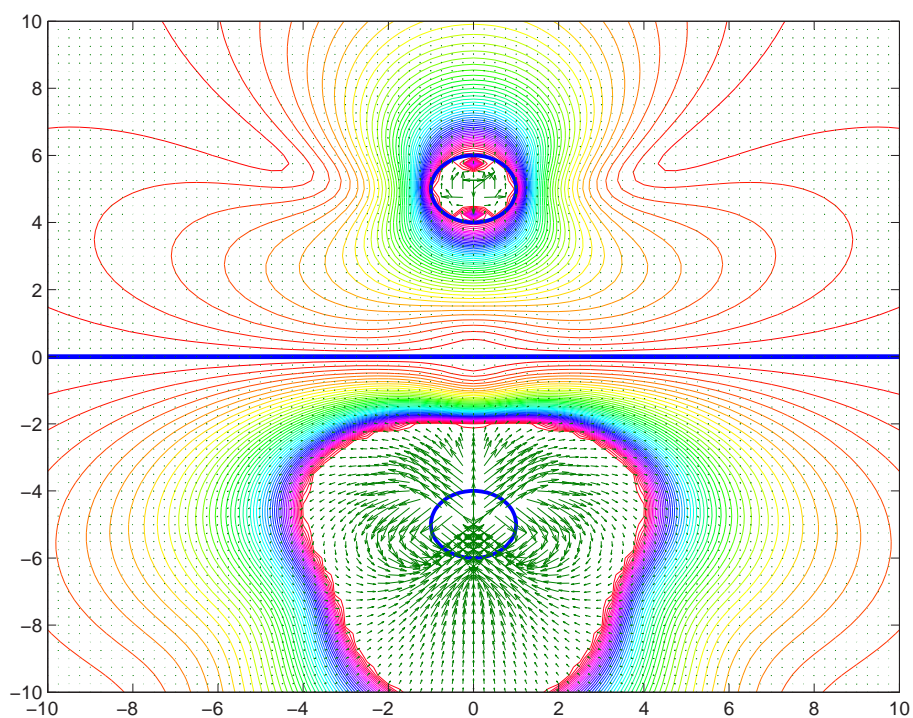
Now using the equations (3.2) and (3.4), for image Stokeslet and image source doublet respectively, we can rewrite after simplifications as

$$\begin{aligned} u_j^{img}(x, y) &= \frac{3a}{4} U_i \left[-\frac{\delta_{ij}}{R} - \frac{R_i R_j}{R^3} + 2h^2 (\delta_{j\tilde{\alpha}} \delta_{\tilde{\alpha}k} - \delta_{j3} \delta_{3k}) \left(\frac{\delta_{ik}}{R^3} - \frac{3R_i R_k}{R^5} \right) \right. \\ &\quad - 2h (\delta_{j\tilde{\alpha}} \delta_{\tilde{\alpha}k} - \delta_{j3} \delta_{3k}) \left(-\frac{\delta_{i3} R_k}{R^3} + \frac{\delta_{3k} R_i}{R^3} + \frac{\delta_{ik} R_3}{R^3} - \frac{3R_i R_3 R_k}{R^5} \right) \\ &\quad - \frac{a^2}{3} \left(\frac{\delta_{ij}}{R^3} - \frac{3R_i R_j}{R^5} \right) - 2a^2 (\delta_{j3} \delta_{i\tilde{\alpha}} + \delta_{j\tilde{\alpha}} \delta_{i3}) \frac{R_{\tilde{\alpha}} R_3}{R^5} \\ &\quad + 2a^2 \delta_{j3} \delta_{i\tilde{\alpha}} \left(-\frac{R_{\tilde{\alpha}} x_3}{R^5} + \frac{5R_{\tilde{\alpha}} R_3^2 x_3}{R^7} \right) - 2a^2 \delta_{j\tilde{\alpha}} \delta_{i\tilde{\beta}} \left(-\frac{\delta_{\tilde{\alpha}\tilde{\beta}} R_3 x_3}{R^5} + \frac{5R_{\tilde{\alpha}} x_3 R_3 R_{\tilde{\beta}}}{R^7} \right) \\ &\quad \left. + 2a^2 \delta_{j3} \delta_{i3} \left(-\frac{3R_3 x_3}{R^5} + \frac{5R_3^3 x_3}{R^7} \right) - 2a^2 \delta_{j\tilde{\alpha}} \delta_{i3} \left(-\frac{R_{\tilde{\alpha}} x_3}{R^5} + \frac{5R_{\tilde{\alpha}} R_3^2 x_3}{R^7} \right) \right], \\ &\text{where, } \tilde{\alpha}, \tilde{\beta} = 1, 2. \end{aligned} \quad (3.9)$$

Now for the uniplanar translational motion of the sphere, the velocity field due to the translating motion of the image sphere acting at any point within the fluid can be found after substitutions $U_1 = v_1$, $U_2 = 0$ and $U_3 = v_3$ and simplifications of above equation



(a)



(b)

Figure 3.2: Streamlines for a sphere and an image sphere translating away from the no-slip stationary plane boundary lies at the centre, $x_3 = 0$. (a) Unbounded sphere translating upwards. (b) Bounded sphere translating upwards away from the plane boundary.

gives velocity in components form as

$$u_1^*(x, y) = -\frac{3a}{4}v_1 \left[\frac{1}{R} + \frac{R_1^2}{R^3} + \frac{2hx_3}{R^3} - \frac{6hx_3R_1^2}{R^5} + a^2 \left(\frac{1}{3R^3} - \frac{R_1^2}{R^5} - \frac{2x_3R_3}{R^5} + \frac{10x_3R_1^2R_3}{R^7} \right) \right] \\ - \frac{3a}{4}v_3 \left[\frac{R_1R_3}{R^3} - \frac{2hR_1}{R^3} + \frac{6hx_3R_1R_3}{R^5} + a^2 \left(\frac{R_1R_3}{R^5} - \frac{2x_3R_1}{R^5} + \frac{10x_3R_1R_3^2}{R^7} \right) \right],$$

and

$$u_3^*(x, y) = -\frac{3a}{4}v_1 \left[\frac{R_1R_3}{R^3} - \frac{2hR_1}{R^3} + \frac{6hx_3R_1R_3}{R^5} + a^2 \left(\frac{R_1R_3}{R^5} + \frac{2x_3R_1}{R^5} - \frac{10x_3R_1R_3^2}{R^7} \right) \right] \\ - \frac{3a}{4}v_3 \left[\frac{1}{R} + \frac{R_3^2}{R^3} - \frac{2hx_3}{R^3} + \frac{6hx_3R_3^2}{R^5} + a^2 \left(\frac{1}{3R^3} - \frac{R_3^2}{R^5} + \frac{6x_3R_3}{R^5} - \frac{10x_3R_3^3}{R^7} \right) \right].$$

Therefore, the velocity field vector acting at any point within the fluid due to translating motion of unit sphere in fixed space coordinates system takes the form as

$$\bar{\mathbf{u}}_{tr}^S(x, y) = u_1^*(x, y) \mathbf{i} + u_3^*(x, y) \mathbf{k}, \quad (3.10)$$

$$\bar{\mathbf{u}}_{tr}^S(x, y) = \left[-\frac{3v_1}{4} \left(\frac{1}{R} + \frac{R_1^2}{R^3} + \frac{2hx_3}{R^3} - \frac{6hx_3R_1^2}{R^5} + \frac{1}{3R^3} - \frac{R_1^2}{R^5} - \frac{2x_3R_3}{R^5} + \frac{10x_3R_1^2R_3}{R^7} \right) \right. \\ \left. - \frac{3v_3}{4} \left(\frac{R_1R_3}{R^3} - \frac{2hR_1}{R^3} + \frac{6hx_3R_1R_3}{R^5} + \frac{R_1R_3}{R^5} - \frac{2x_3R_1}{R^5} + \frac{10x_3R_1R_3^2}{R^7} \right) \right] \mathbf{i} \\ + \left[-\frac{3v_1}{4} \left(\frac{R_1R_3}{R^3} - \frac{2hR_1}{R^3} + \frac{6hx_3R_1R_3}{R^5} + \frac{R_1R_3}{R^5} + \frac{2x_3R_1}{R^5} - \frac{10x_3R_1R_3^2}{R^7} \right) \right. \\ \left. - \frac{3v_3}{4} \left(\frac{1}{R} + \frac{R_3^2}{R^3} - \frac{2hx_3}{R^3} + \frac{6hx_3R_3^2}{R^5} + \frac{1}{3R^3} - \frac{R_3^2}{R^5} + \frac{6x_3R_3}{R^5} - \frac{10x_3R_3^3}{R^7} \right) \right] \mathbf{k},$$

where superscripts S represents fixed space coordinates. Also

$$R_1 = R_t \sin(\chi + \theta) - R_n \cos(\chi + \theta), \quad R_3 = R_n \sin(\chi + \theta) + R_t \cos(\chi + \theta),$$

$$\text{and } x_3 = R_n \sin(\chi + \theta) + R_t \cos(\chi + \theta) - h,$$

where h is the distance of the plane boundary from the centre of the sphere or image sphere as shown in the Figure 3.1.

Now using the transformation matrices R_{SB} and R_{BF} defined in chapter 2, we can finally write velocity due to the translating motion of the image sphere in flagellar coordinates system for uniplanar locomotion as

$$\bar{\mathbf{u}}_{tr}^F(x, y) = \left[-\frac{3}{4}v_n \left(-\frac{R_1R_3}{R^3} + \frac{R_1R_3}{R^5} + 2x_3 \frac{R_1}{R^3} + 2x_3 \frac{R_1}{R^5} + 6hx_3 \frac{R_1R_3}{R^5} - 10x_3 \frac{R_1R_3^2}{R^7} \right) \right. \\ \left. - \frac{3}{4}v_t \left(\frac{1}{R} + \frac{1}{3R^3} + \frac{R_3^2}{R^3} - \frac{R_3^2}{R^5} + 6x_3 \frac{R_3}{R^5} - \frac{2hx_3}{R^3} + 6hx_3 \frac{R_3^2}{R^5} - 10x_3 \frac{R_3^3}{R^7} \right) \right] \mathbf{t} \\ + \left[\frac{3}{4}v_t \left(-\frac{R_1R_3}{R^3} + \frac{R_1R_3}{R^5} + 2x_3 \frac{R_1}{R^3} + 2x_3 \frac{R_1}{R^5} + 6hx_3 \frac{R_1R_3}{R^5} - 10x_3 \frac{R_1R_3^2}{R^7} \right) \right. \\ \left. - \frac{3}{4}v_n \left(\frac{1}{R} + \frac{1}{3R^3} + \frac{R_3^2}{R^3} - \frac{R_3^2}{R^5} + 6x_3 \frac{R_3}{R^5} - \frac{2hx_3}{R^3} + 6hx_3 \frac{R_3^2}{R^5} - 10x_3 \frac{R_3^3}{R^7} \right) \right] \mathbf{n}, \quad (3.11)$$

where F represents flagellar coordinates system.

Similarly, the velocity due to the translating motion of the sphere in an unbounded domain in the flagella coordinates system using (3.5) can be calculated as

$$\begin{aligned} \mathbf{u}_{tr}^F(x, y) = & \left[-v_t \left(1 - \frac{3}{4r} - \frac{1}{4r^3} \right) + 3(v_n r_n r t + v_t r_t^2) \left(\frac{1}{4r^3} - \frac{1}{4r^5} \right) \right] \mathbf{t} \\ & + \left[-v_n \left(1 - \frac{3}{4r} - \frac{1}{4r^3} \right) + 3(v_t r_n r t + v_n r_n^2) \left(\frac{1}{4r^3} - \frac{1}{4r^5} \right) \right] \mathbf{n}, \end{aligned} \quad (3.12)$$

The Green's function or total velocity field acting on any point P within the fluid due to the translating motion of a unit sphere near a no-slip plane boundary becomes

$$\underline{\mathbf{u}}_{tr} = \mathbf{u}_{tr} + \bar{\mathbf{u}}_{tr}, \quad (3.13)$$

where \mathbf{u}_{tr} is the contribution from the sphere for uniplanar locomotion and found in equation (3.12) and $\bar{\mathbf{u}}_{tr}$ from the image sphere due to the presence of the plane boundary which is calculated as in equation (3.11).

3.3.3 Solution for the rotational motion of a sphere near a stationary plane boundary

The velocity and pressure fields for the unbounded rotational motion of a sphere of radius a in a Stokes flow using Faxen's law can be written as

$$\begin{aligned} u_i(x, y) &= 4\pi\mu a^3 \left[\frac{D_{jk}(r_k \delta_{ij} - r_j \delta_{ik})}{4\pi\mu r^3} \right] \\ &\equiv (\epsilon_{ijk} \Omega_j r_k) \frac{a^3}{r^3} \equiv (\mathbf{\Omega} \times \mathbf{r}) \frac{a^3}{r^3}, \end{aligned} \quad (3.14)$$

and

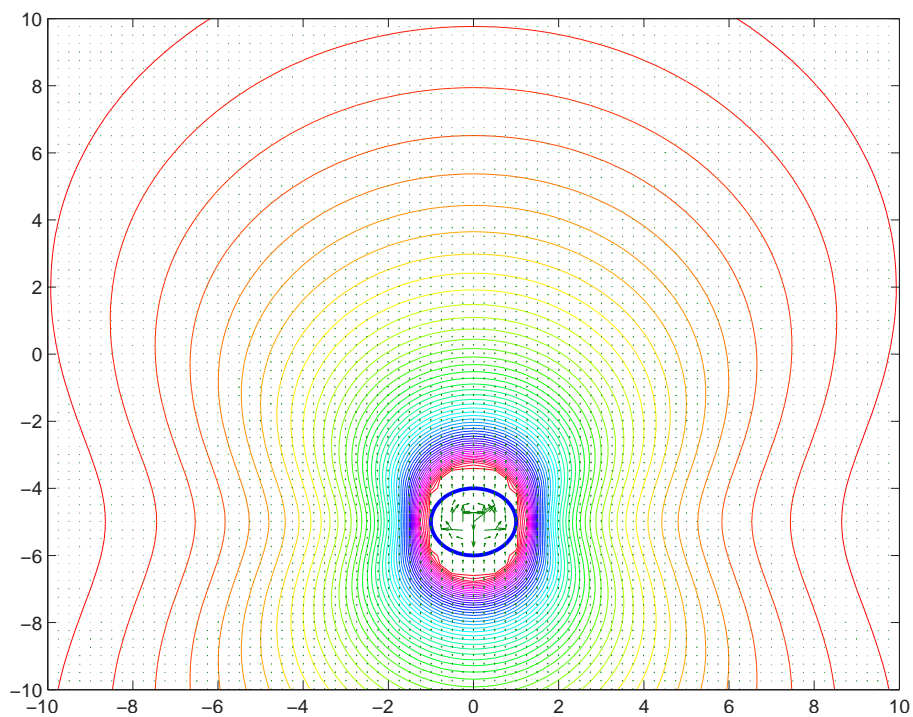
$$p = -\mu D_{jk} \left(\frac{\delta_{jk}}{r^3} \right). \quad (3.15)$$

The velocity and pressure fields for the solution of rotlet, characterized by the rotational vector $\mathbf{\Omega}$ in the vicinity of a stationary no-slip plane boundary was derived by Blake and Chwang [16] as

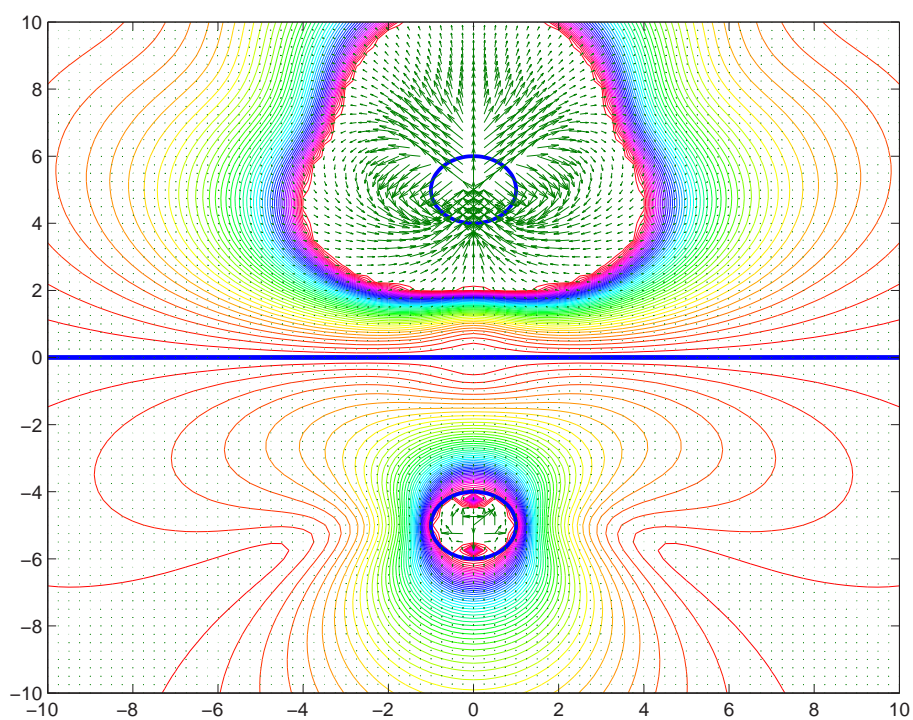
$$u_i^{img}(x, y) = -\frac{\epsilon_{ijk} \Omega_j R_k}{R^3} + 2h\epsilon_{kj3} \Omega_j \left(\frac{\delta_{ik}}{R^3} - \frac{3R_i R_k}{R^5} \right) + 6\epsilon_{kj3} \left(\frac{\Omega_j R_i R_k R_3}{R^5} \right), \quad (3.16)$$

and

$$p^* = -4\mu \frac{\partial}{\partial R_k} \left(\frac{\epsilon_{kj3} \Omega_j R_3}{R^3} \right), \quad (3.17)$$

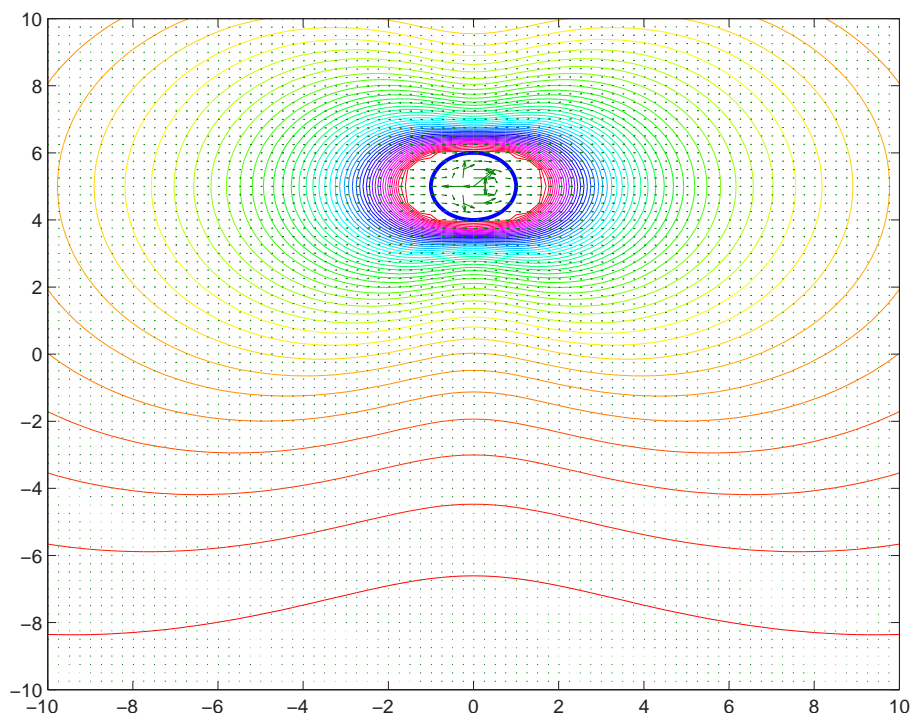


(a)

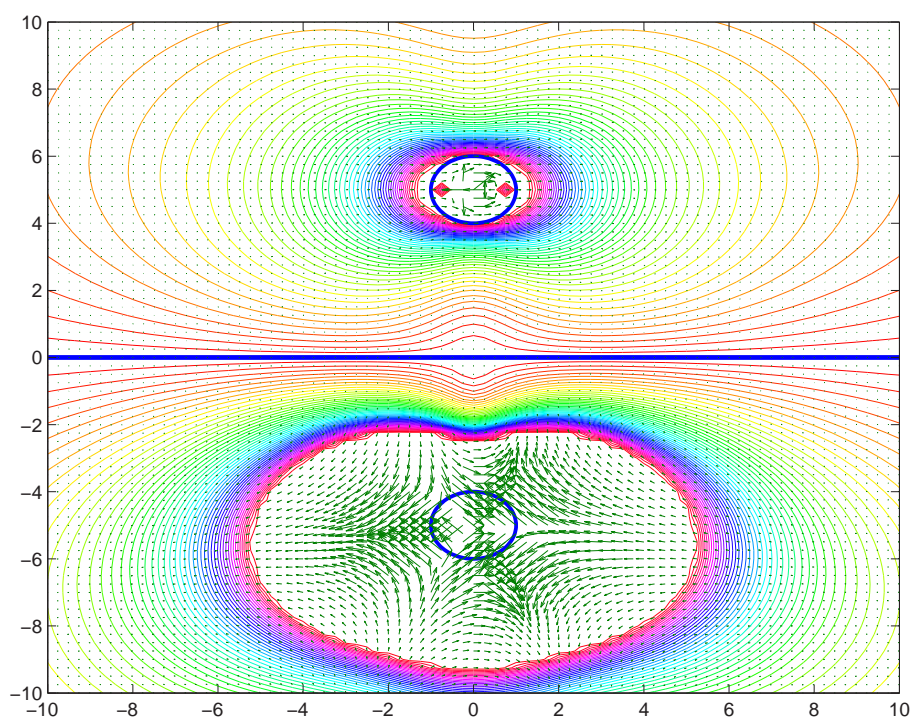


(b)

Figure 3.3: Streamlines plot when sphere translating towards the no-slip plane boundary lies at the centre at $x_3 = 0$. (a) Unbounded sphere translating upwards. (b) Bounded sphere translating upwards towards the plane boundary.



(a)



(b)

Figure 3.4: Streamlines plot when sphere translating parallel to the no-slip plane boundary lies at the centre at $x_3 = 0$. (a) Unbounded sphere translating horizontally. (b) Bounded sphere translating horizontally parallel to the plane boundary.

where

$$R = [(x_1 - y_1)^2 + (x_2 - y_2)^2 + (x_3 + h)^2]^{\frac{1}{2}}.$$

Now for the uniplanar rotational motion of the sphere, the velocity field for the rotational motion of the image sphere after substitution $\Omega_1 = \Omega_3 = 0$ and simplification of the above equation gives

$$u_1^*(x, y) = \Omega_2 \left(-\frac{R_3}{R^3} + \frac{2h}{R^3} - \frac{6hR_1^2}{R^5} + \frac{6R_1^2R_3}{R^5} \right), \quad (3.18)$$

and

$$u_3^*(x, y) = \Omega_2 \left(\frac{R_1}{R^3} - \frac{6hR_1R_3}{R^5} + \frac{6R_1R_3^2}{R^5} \right), \quad (3.19)$$

Therefore, the velocity field vector acting at any point P within the fluid due to the rotational motion of the sphere in fixed space coordinate system takes the form as

$$\bar{\mathbf{u}}_{rt}^S(x, y) = u_1^*(x, y) \mathbf{i} + u_3^*(x, y) \mathbf{k}, \quad (3.20)$$

$$\begin{aligned} \bar{\mathbf{u}}_{rt}^S(x, y) &= \left[\Omega_2 \left(-\frac{R_3}{R^3} + \frac{2h}{R^3} - \frac{6hR_1^2}{R^5} + \frac{6R_1^2R_3}{R^5} \right) \right] \mathbf{i} \\ &\quad + \left[\Omega_2 \left(\frac{R_1}{R^3} - \frac{6hR_1R_3}{R^5} + \frac{6R_1R_3^2}{R^5} \right) \right] \mathbf{k}. \end{aligned}$$

Now again using the transformation matrices R_{SB} and R_{BF} , we will derive the velocity due to the rotational motion of the unit sphere acting on an element of flagellum in flagellar coordinates system as

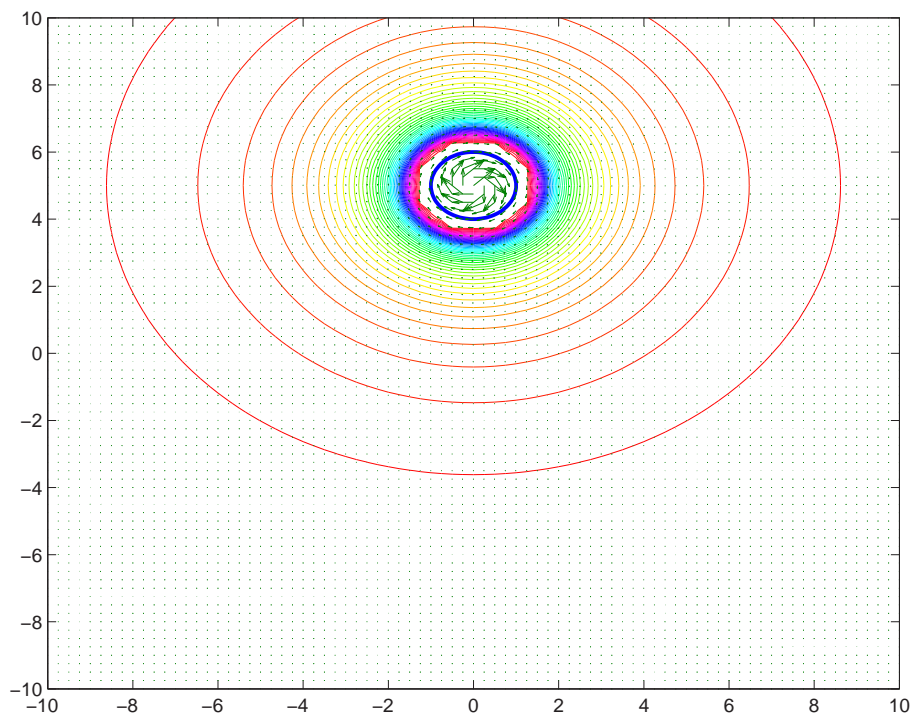
$$\begin{aligned} \bar{\mathbf{u}}_{rt}^F(x, y) &= \left[\Omega_b \sin(\chi + \theta) \left(-\frac{R_3}{R^3} + \frac{2h}{R^3} - \frac{6hR_1^2}{R^5} + \frac{6R_1^2R_3}{R^5} \right) + \Omega_b \cos(\chi + \theta) \right. \\ &\quad \left. \left(\frac{R_1}{R^3} - \frac{6hR_1R_3}{R^5} + \frac{6R_1R_3^2}{R^5} \right) \right] \mathbf{t} + \left[\Omega_b \sin(\chi + \theta) \left(\frac{R_1}{R^3} - \frac{6hR_1R_3}{R^5} + \frac{6R_1R_3^2}{R^5} \right) \right. \\ &\quad \left. + \Omega_b \cos(\chi + \theta) \left(-\frac{R_3}{R^3} + \frac{2h}{R^3} - \frac{6hR_1^2}{R^5} + \frac{6R_1^2R_3}{R^5} \right) \right] \mathbf{n}, \quad (3.21) \end{aligned}$$

where superscripts S represents fixed space coordinates. Also

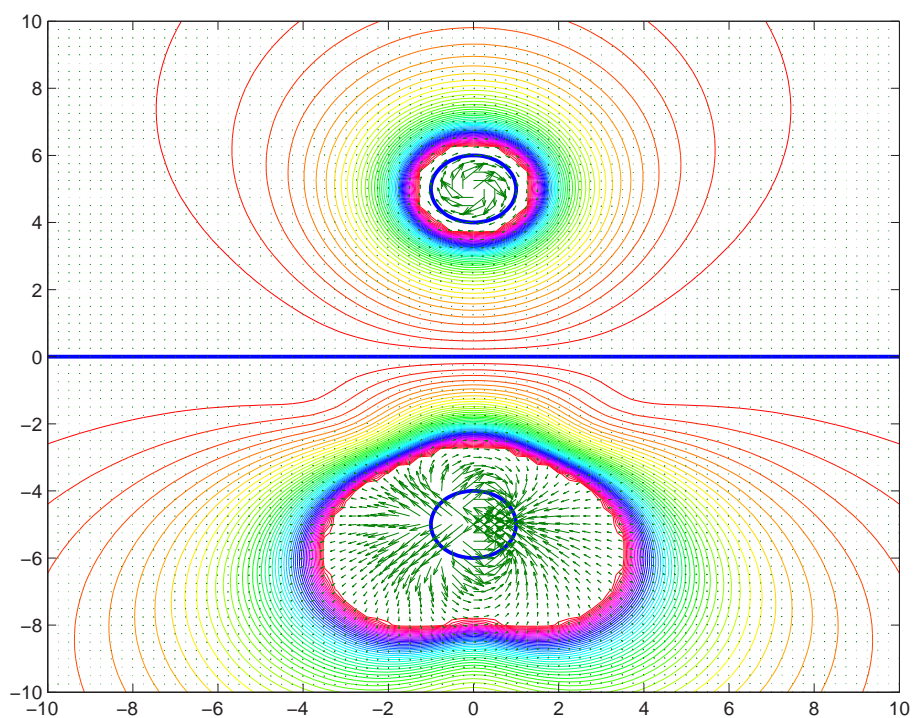
$$R_1 = R_t \sin(\chi + \theta) - R_n \cos(\chi + \theta), \quad R_3 = R_n \sin(\chi + \theta) + R_t \cos(\chi + \theta),$$

$$\Omega_2 = \Omega_b \quad \text{and} \quad x_3 = R_n \sin(\chi + \theta) + R_t \cos(\chi + \theta) - h,$$

where h is the distance of plane boundary from the centre of the sphere and image sphere.



(a)



(b)

Figure 3.5: Streamlines plot of the sphere and image sphere when rotating parallel to the stationary no-slip plane boundary lies at the centre at $x_3 = 0$. (a) Unbounded sphere rotating horizontally. (b) Bounded sphere rotating horizontally parallel to the plane boundary.

Following the same procedure and using equation (3.14), the velocity due to the rotational motion of the sphere in an unbounded domain in flagella coordinates system can be found as

$$\mathbf{u}_{rt}^F(x, y) = \left[-\Omega_b r_n \left(1 - \frac{1}{r^3} \right) \right] \mathbf{t} + \left[\Omega_b r_t \left(1 - \frac{1}{r^3} \right) \right] \mathbf{n}, \quad (3.22)$$

where F represents flagellar coordinates system.

The Green's function or total velocity field acting at any point P within the fluid due to the rotating motion of a unit sphere near a no-slip plane boundary becomes

$$\underline{\mathbf{u}}_{rt} = \mathbf{u}_{rt} + \bar{\mathbf{u}}_{rt}, \quad (3.23)$$

where \mathbf{u}_{rt} is the contribution from the sphere for uniplanar locomotion and found in equation (3.22) and $\bar{\mathbf{u}}_{rt}$ is the corresponding image system due to the presence of plane boundary which is calculated as in equation (3.21).

3.4 Force-Torque balance for bounded biflagellate swimming

To model the swimming of a biflagellated bottom heavy single cell of *C. augustae* in a viscous fluid in the vicinity of the no-slip plane boundary, consider C to be the geometric centre and G to be the centre-of-gravity, where both lie on the major axis \mathbf{p} of the cell. The unit vector \mathbf{p} represents the orientation of the cell. Let H be the displacement of the centre-of-gravity G from geometric centre C as shown in Figure 3.6. We also assume that the no-slip plane is stationary and lies at a distance h from the centre of the cell body, whereas cell body and flagella are moving with the change of time. For the ease of calculations, we neglect the $\boldsymbol{\omega}$ vorticity and \mathbf{e} rate-of-strain of the ambient flow. Below we shall follow the same steps for modelling the bounded swimming problems as mentioned in chapter 2 for the unbounded swimming.

Since for low Reynolds number swimming of micro-organisms inertia is negligible, the viscous forces in the fluid flow are dominant as compared to inertial forces. Thus the orientation and motion of the organism can be modelled by setting to zero the total force and total torque at any instant acting on the cell during the flagellar beat, which is the sum of gravitational, cell body and flagella contributions, i.e.

$$\underline{\mathbf{F}}_{bdy} + \underline{\mathbf{F}}_{grv} + \underline{\mathbf{F}}_{flg} = 0, \quad (3.24)$$

and

$$\underline{\mathbf{L}}_{bdy} + \underline{\mathbf{L}}_{grv} + \underline{\mathbf{L}}_{flg} = 0. \quad (3.25)$$

To determine the contributions due to the spherical body of the cell, we neglect the presence of the flagella and assume only the hydrodynamic contributions on the body in the Stokes flow. The viscous body force and viscous body torque for a spherical body shape translating and rotating simultaneously in the presence of the no-slip plane boundary (e.g. see Goldman *et al.* [48], [49]) are

$$\underline{\mathbf{F}}_{bdy} = 6\pi\mu a \left(\mathbf{v}F_{tr}^* + a\boldsymbol{\Omega}F_{rt}^* \right), \quad (3.26)$$

and

$$\underline{\mathbf{L}}_{bdy} = 8\pi\mu a^2 \left(\mathbf{v}T_{tr}^* + a\boldsymbol{\Omega}T_{rt}^* \right), \quad (3.27)$$

where \mathbf{v} and $\boldsymbol{\Omega}$ are the velocity and angular velocity of the body respectively, a is the radius of the cell body and μ is the viscosity of the fluid. The subscript tr corresponds to the translation and rt represents rotational motion of the sphere. The normalized non-dimensional scalar force and torque components, F_{tr}^* , F_{rt}^* and T_{tr}^* , T_{rt}^* may be positive or negative and are functions of $\left(\frac{a}{h}\right)$. The values of F_{tr}^* and T_{tr}^* for translational motion as defined by Goldman *et al.* [48] using the approximate solutions of Faxen [39], obtained by the method of reflections, are

$$F_{tr}^* = - \left[1 - \frac{9}{16} \left(\frac{a}{h}\right) + \frac{1}{8} \left(\frac{a}{h}\right)^3 - \frac{45}{256} \left(\frac{a}{h}\right)^4 - \frac{1}{16} \left(\frac{a}{h}\right)^5 \right]^{-1},$$

and

$$T_{tr}^* = \frac{3}{32} \left(\frac{a}{h}\right)^4 \left[1 - \frac{3}{8} \left(\frac{a}{h}\right) \right].$$

Similarly, the results for rotational motion of the sphere, F_{rt}^* and T_{rt}^* are defined as

$$F_{rt}^* = \frac{1}{8} \left[\left(\frac{a}{h}\right)^4 \left(1 - \frac{3a}{8h} \right) \right],$$

and

$$T_{rt}^* = - \left[1 + \frac{5}{16} \left(\frac{a}{h}\right)^3 \right].$$

Using the above values and ignoring the higher order terms, the viscous body force and viscous body torque for a spherical body translating and rotating simultaneously in the vicinity of the no-slip stationary plane boundary takes the form as

$$\underline{\mathbf{F}}_{bdy} = 6\pi\mu a \left[\left\{ -1 - \frac{9}{16} \left(\frac{a}{h}\right) \right\} \mathbf{v} + \frac{1}{8} \left(\frac{a}{h}\right)^4 a\boldsymbol{\Omega} \right], \quad (3.28)$$

and

$$\underline{\mathbf{L}}_{bdy} = 8\pi\mu a^2 \left[\frac{3}{32} \left(\frac{a}{h}\right)^4 \mathbf{v} + \left\{ -1 - \frac{5}{16} \left(\frac{a}{h}\right)^3 \right\} a\boldsymbol{\Omega} \right], \quad (3.29)$$

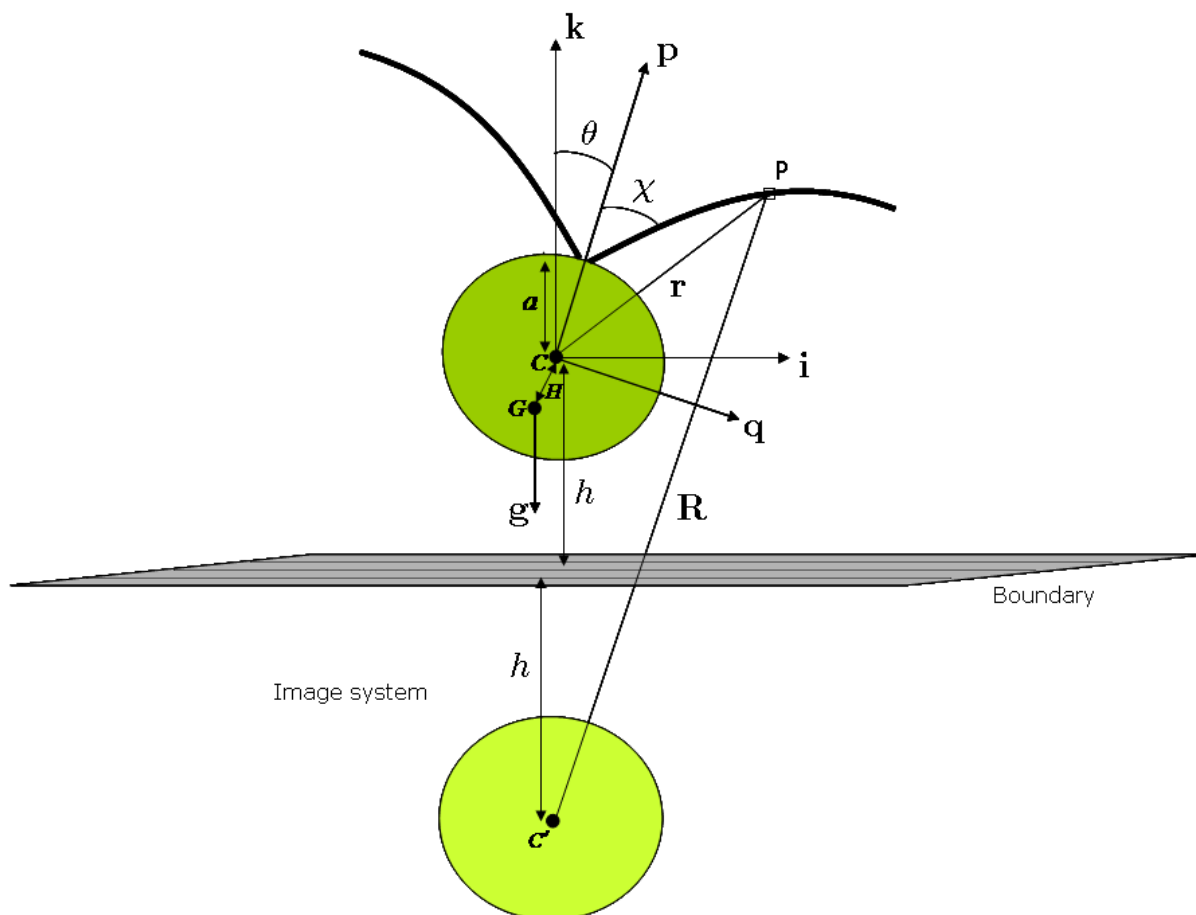


Figure 3.6: A schematic diagram of uniplanar swimming of *C. augustae* cell in the vicinity of the stationary no-slip plane boundary: (\mathbf{i}, \mathbf{k}) are fixed space and (\mathbf{p}, \mathbf{q}) are body coordinates respectively, H is centre-of-gravity G offset from geometric centre C , θ is the Euler angle between \mathbf{k} in fixed space and primary axis of swimming \mathbf{p} in body coordinate system, χ is the angle which flagella makes with the \mathbf{p} , \mathbf{g} is the force due to gravity and h is the distance of boundary from the centre of the cell body.

whereas, in the absence of the plane boundary or for the case of $h \rightarrow \infty$, i.e. cell body at a very large distance away from the plane boundary, the above equations for the forces and torques due to the spherical cell body reduce to equations (2.7) and (2.8) as discussed in chapter 2.

For *Chlamydomonas* it was observed by Yoshimura *et al.* [149] that the sedimentation speed ($2.2 \mu\text{m s}^{-1}$) is very low as compared to the swimming speed ($102 \mu\text{m s}^{-1}$, whereas other studies found it to be in the range of $40\text{-}70 \mu\text{m s}^{-1}$, see Vladimirov *et al.* [142]). Then, as we know that sedimentation speed represents the gravitational force, so we can take

$$\underline{\mathbf{F}}_{grv} = \left(\frac{\rho - \rho_0}{v} \right) \mathbf{g} = 0, \quad (3.30)$$

where ρ and v are the density and volume of the cell respectively and \mathbf{g} is the gravitational acceleration. The gravitational torque due to H centre-of-gravity offset, the displacement of G from C as described in Figure 3.6, was investigated by Pedley and Kessler [111] and can be written in terms of the cell body co-ordinate system $(\mathbf{p}, \mathbf{q}, \bar{\mathbf{r}})$ for uniplanar locomotion as

$$\underline{\mathbf{L}}_{grv} = H\mathbf{p} \times mg\mathbf{k} = -mgH \sin \theta \bar{\mathbf{r}}, \quad (3.31)$$

where \mathbf{k} is the unit vector directed vertically upward and m is the mass of the cell. Also, θ is the Euler angle between fixed space coordinates $(\mathbf{i}, \mathbf{j}, \mathbf{k})$ and body coordinates $(\mathbf{p}, \mathbf{q}, \bar{\mathbf{r}})$ (see Figure 3.6). Here, we have used $\bar{\mathbf{r}}$ instead of \mathbf{r} just to avoid repetition of notation for position vector \mathbf{r} used frequently in later sections.

3.4.1 Computation of viscous force and viscous torque acting on one flagellum

Now for the last part of the force-torque balance equations, $\underline{\mathbf{F}}_{flg}$ and $\underline{\mathbf{L}}_{flg}$, i.e. forces and torques on the flagella, we again apply the RFT as we did in chapter 2. Now the velocity of the fluid relative to the element of the flagellum in the presence of the plane boundary takes the form as

$$\underline{\mathbf{u}}_{rel} = \underline{\mathbf{u}} - \mathbf{v}_{flg}, \quad (3.32)$$

where $\underline{\mathbf{u}}$ is the velocity of the fluid measured at the position of the element ds and \mathbf{v}_{flg} is the velocity of an element of the flagellum in the presence of the plane boundary. Thus the flow past the bounded spherical body, in a general flow field $\underline{\mathbf{u}}$, is the sum of three parts: flow due to translation of the body, due to vorticity of ambient flow relative to the

rotation of the body and due to ambient straining motion (see Pasol *et al.* [110]). For the simplicity of calculations we ignore the contribution due to ambient straining motion. Therefore the velocity of the fluid for uniplanar locomotion in the vicinity of the plane boundary takes the form as

$$\underline{\mathbf{u}} = \underline{\mathbf{u}}_{tr} + \underline{\mathbf{u}}_{rt} = \mathbf{u}_{tr} + \bar{\mathbf{u}}_{tr} + \mathbf{u}_{rt} + \bar{\mathbf{u}}_{rt}, \quad (3.33)$$

where \mathbf{u}_{tr} and $\bar{\mathbf{u}}_{tr}$ calculated earlier in equations (3.12) and (3.11) are the velocity of the fluid due to translational motion of the sphere and image sphere respectively. The last two terms \mathbf{u}_{rt} and $\bar{\mathbf{u}}_{rt}$ can be found in equations (3.22) and (3.21) are the velocity of the fluid due to rotational motion of the sphere and image sphere, respectively.

The velocity of an element of flagellum relative to the spherical cell body, \mathbf{v}_{flg} , as discussed in chapter 2, is given by

$$\mathbf{v}_{flg} = \boldsymbol{\Omega} \times \mathbf{r} + \dot{\mathbf{r}}, \quad (3.34)$$

where \mathbf{r} is the position vector of an element of the flagellum relative to the centre of the cell's body, and $\dot{\mathbf{r}}$ is the velocity of the flagellar element relative to body coordinates fixed in the body.

Thus, the total viscous force and viscous torque produced by both the flagella in the presence of no-slip plane boundary can be calculated as

$$\underline{\mathbf{F}}_{flg} = \underline{\mathbf{F}}_{tr} + \underline{\mathbf{F}}_{rt} - \mathbf{F}_{fl}, \quad (3.35)$$

and

$$\underline{\mathbf{L}}_{flg} = \underline{\mathbf{L}}_{tr} + \underline{\mathbf{L}}_{rt} - \mathbf{L}_{fl}, \quad (3.36)$$

where the underline terms on the right-hand side $\underline{\mathbf{F}}_{tr}$, $\underline{\mathbf{F}}_{rt}$ and $\underline{\mathbf{L}}_{tr}$, $\underline{\mathbf{L}}_{rt}$ represents the forces and torques due to the translational and rotational motion of the sphere in the presence of plane boundary. To satisfy the no-slip boundary condition these terms include the contributions from the image sphere in addition to the original contribution as discussed in chapter 2.

The velocity \mathbf{v} and angular velocity $\boldsymbol{\Omega}$ of the organism in the flagellar coordinate system for uniplanar locomotion can be written as

$$\mathbf{v} = \begin{bmatrix} v_n \\ v_t \\ 0 \end{bmatrix} = \begin{bmatrix} v_p(\mathbf{p} \cdot \mathbf{n}) + v_q(\mathbf{q} \cdot \mathbf{n}) \\ v_p(\mathbf{p} \cdot \mathbf{t}) + v_q(\mathbf{q} \cdot \mathbf{t}) \\ 0 \end{bmatrix}$$

and

$$\boldsymbol{\Omega} = \begin{bmatrix} 0 \\ 0 \\ \Omega_b \end{bmatrix} = \begin{bmatrix} 0 \\ 0 \\ \Omega_r(\bar{\mathbf{r}} \cdot \mathbf{b}) \end{bmatrix}, \quad (3.37)$$

respectively.

The position vector of an element of flagellum from the centre of the sphere and image sphere in flagellar coordinate system for uniplanar case becomes

$$\mathbf{r} = \begin{bmatrix} r_n \\ r_t \\ 0 \end{bmatrix}, \quad \text{and} \quad \mathbf{R} = \begin{bmatrix} R_n \\ R_t \\ 0 \end{bmatrix}, \quad (3.38)$$

respectively.

The generalized position vector of an element of the flagellum relative to the centre of the cell body in fixed space coordinates is defined in chapter 2 as

$$\mathbf{r}^S(s, t) = [b \sin \theta + (s - b) \sin(\theta + \chi)] \mathbf{i} + [b \cos \theta + (s - b) \cos(\theta + \chi)] \mathbf{k}, \quad (3.39)$$

where χ is the angle of flagellum from the \mathbf{p} axis, θ is measured from the \mathbf{k} axis at any time t and

$$b \leq s \leq l, \quad a \leq b \leq l, \quad \text{and} \quad a \leq (s - b) \leq l.$$

Using the transformation matrices R_{SB} and R_{BF} discussed in chapter 2, we can write this in flagellar coordinates such that

$$\begin{aligned} \mathbf{r}^B(s, t) &= [b + (s - b) \cos \chi] \mathbf{p} + [(s - b) \sin \chi] \mathbf{q}, \\ \mathbf{r}^F(s, t) &= [b \sin \chi] \mathbf{n} + [(s - b) + b \cos \chi] \mathbf{t}. \end{aligned} \quad (3.40)$$

Using the same generalization, we now define the position vector of the same element of the flagellum from the centre of the image sphere as shown in Figure 3.6 as

$$\mathbf{R}^S(s, t) = [b \sin \theta + (s - b) \sin(\theta + \chi)] \mathbf{i} + [2h + b \cos \theta + (s - b) \cos(\theta + \chi)] \mathbf{k}, \quad (3.41)$$

where h is the distance of the plane boundary from the centre of the image sphere. Now using the transformation matrices R_{SB} and R_{BF} , we can write the position vector in the flagellar coordinates system such that

$$\begin{aligned} \mathbf{R}^B(s, t) &= [b + (s - b) \cos \chi - 2h \sin \theta] \mathbf{p} + [(s - b) \sin \chi - 2h \cos \theta] \mathbf{q}, \\ \mathbf{R}^F(s, t) &= [b \sin \chi + 2h \sin(\chi + \theta)] \mathbf{n} + [(s - b) + b \cos \chi + 2h \cos(\chi + \theta)] \mathbf{t}. \end{aligned} \quad (3.42)$$

Contribution of the translation of the bounded spherical body

The velocity of the fluid due to the uniplanar translation of a spherical body of radius a in the presence of no-slip plane boundary in a low Reynolds number fluid flow is given by

$$\begin{aligned}
\mathbf{u}_{tr} = & \left[-v_n \left(1 - \frac{3}{4r} - \frac{1}{4r^3} \right) + 3(v_t r_n r_t + v_n r_n^2) \left(\frac{1}{4r^3} - \frac{1}{4r^5} \right) + \frac{3}{4} v_t \right. \\
& \left(-\frac{R_1 R_3}{R^3} + \frac{R_1 R_3}{R^5} + 2x_3 \frac{R_1}{R^3} + 2x_3 \frac{R_1}{R^5} + 6hx_3 \frac{R_1 R_3}{R^5} - 10x_3 \frac{R_1 R_3^2}{R^7} \right) - \frac{3}{4} v_n \\
& \left(\frac{1}{R} + \frac{1}{3R^3} + \frac{R_3^2}{R^3} - \frac{R_3^2}{R^5} + 6x_3 \frac{R_3}{R^5} - \frac{2hx_3}{R^3} + 6hx_3 \frac{R_3^2}{R^5} - 10x_3 \frac{R_3^3}{R^7} \right) \Big] \mathbf{n} \\
& + \left[-v_t \left(1 - \frac{3}{4r} - \frac{1}{4r^3} \right) + 3(v_n r_n r_t + v_t r_t^2) \left(\frac{1}{4r^3} - \frac{1}{4r^5} \right) - \frac{3}{4} v_n \right. \\
& \left(-\frac{R_1 R_3}{R^3} + \frac{R_1 R_3}{R^5} + 2x_3 \frac{R_1}{R^3} + 2x_3 \frac{R_1}{R^5} + 6hx_3 \frac{R_1 R_3}{R^5} - 10x_3 \frac{R_1 R_3^2}{R^7} \right) - \frac{3}{4} v_t \\
& \left. \left(\frac{1}{R} + \frac{1}{3R^3} + \frac{R_3^2}{R^3} - \frac{R_3^2}{R^5} + 6x_3 \frac{R_3}{R^5} - \frac{2hx_3}{R^3} + 6hx_3 \frac{R_3^2}{R^5} - 10x_3 \frac{R_3^3}{R^7} \right) \Big] \mathbf{t}.
\end{aligned}$$

The above expression of the fluid velocity is the sum of the contributions from the translating sphere and corresponding image sphere as shown in Figure 3.6.

Now, using RFT the force produced by an element of a flagellum within this flow with $a = 1$ is given by

$$\begin{aligned}
d\mathbf{F}_{tr}^F = & K_n \left[-v_n \left(1 - \frac{3}{4r} - \frac{1}{4r^3} \right) + 3(v_t r_n r_t + v_n r_n^2) \left(\frac{1}{4r^3} - \frac{1}{4r^5} \right) + \frac{3}{4} v_t \right. \\
& \left(-\frac{R_1 R_3}{R^3} + \frac{R_1 R_3}{R^5} + 2x_3 \frac{R_1}{R^3} + 2x_3 \frac{R_1}{R^5} + 6hx_3 \frac{R_1 R_3}{R^5} - 10x_3 \frac{R_1 R_3^2}{R^7} \right) - \frac{3}{4} v_n \\
& \left(\frac{1}{R} + \frac{1}{3R^3} + \frac{R_3^2}{R^3} - \frac{R_3^2}{R^5} + 6x_3 \frac{R_3}{R^5} - \frac{2hx_3}{R^3} + 6hx_3 \frac{R_3^2}{R^5} - 10x_3 \frac{R_3^3}{R^7} \right) \Big] \mathbf{nds} \\
& + K_t \left[-v_t \left(1 - \frac{3}{4r} - \frac{1}{4r^3} \right) + 3(v_n r_n r_t + v_t r_t^2) \left(\frac{1}{4r^3} - \frac{1}{4r^5} \right) - \frac{3}{4} v_n \right. \\
& \left(-\frac{R_1 R_3}{R^3} + \frac{R_1 R_3}{R^5} + 2x_3 \frac{R_1}{R^3} + 2x_3 \frac{R_1}{R^5} + 6hx_3 \frac{R_1 R_3}{R^5} - 10x_3 \frac{R_1 R_3^2}{R^7} \right) - \frac{3}{4} v_t \\
& \left. \left(\frac{1}{R} + \frac{1}{3R^3} + \frac{R_3^2}{R^3} - \frac{R_3^2}{R^5} + 6x_3 \frac{R_3}{R^5} - \frac{2hx_3}{R^3} + 6hx_3 \frac{R_3^2}{R^5} - 10x_3 \frac{R_3^3}{R^7} \right) \Big] \mathbf{tds}. \quad (3.43)
\end{aligned}$$

The total force from the flagellum can thus be calculated by integrating along the length of the flagellum to yield

$$\begin{aligned}
\mathbf{F}_{tr}^F = & K_n \left[-v_n \left(I_1 - \frac{3}{4} I_2 - \frac{1}{4} I_3 \right) + v_n r_n^2 \left(\frac{3I_3}{4} - \frac{3I_4}{4} \right) + v_t r_n \left(\frac{3J_3}{4} - \frac{3J_4}{4} \right) \right. \\
& \left. + \text{terms involving } \tilde{I}_i \text{ and } \tilde{J}_i \right] \mathbf{n} \\
& + K_t \left[-v_t \left(I_1 - \frac{3}{4} I_2 - \frac{1}{4} I_3 \right) + v_n r_n \left(\frac{3J_3}{4} - \frac{3J_4}{4} \right) + v_t \left(\frac{3I_7}{4} - \frac{3I_8}{4} \right) \right. \\
& \left. + \text{terms involving } \tilde{I}_i \text{ and } \tilde{J}_i \right] \mathbf{t}, \quad (3.44)
\end{aligned}$$

where I_i and J_i are specific integrals used and defined in chapter 2 for unbounded sphere locomotion. The integrals \tilde{I}_i and \tilde{J}_i correspond to the image sphere contributions and are evaluated using Maple code and are defined as

$$\begin{aligned} \tilde{I}_1 &= \int ds, & \tilde{I}_2 &= \int \frac{ds}{R}, & \tilde{I}_3 &= \int \frac{ds}{R^3}, & \tilde{I}_4 &= \int \frac{ds}{R^5}, \\ \tilde{I}_5 &= \int \frac{ds}{R^7}, & \tilde{I}_6 &= \int R_t^2 ds, & \tilde{J}_1 &= \int R_t ds, & \tilde{J}_2 &= \int \frac{R_t}{R} ds, \end{aligned}$$

$$\tilde{J}_3 = \int \frac{R_t}{R^3} ds \quad \tilde{J}_4 = \int \frac{R_t}{R^5} ds, \quad \tilde{J}_5 = \int \frac{R_t}{R^7} ds,$$

$$\tilde{I}_7 = \int \frac{R_t^2}{R^3} ds = \tilde{I}_2 - R_n^2 \tilde{I}_3, \quad \tilde{I}_8 = \int \frac{R_t^2}{R^5} ds = \tilde{I}_3 - R_n^2 \tilde{I}_5,$$

and

$$\tilde{J}_6 = \int \frac{R_t^3}{R^5} ds = \tilde{J}_3 - R_n^2 \tilde{J}_4, \quad \tilde{J}_7 = \int \frac{R_t^3}{R^7} ds = \tilde{J}_4 - R_n^2 \tilde{J}_5. \quad (3.45)$$

Therefore, the total force from one flagellum in the body coordinates system for uniplanar locomotion, becomes

$$\underline{\mathbf{F}}_{tr}^F \cdot \mathbf{p} = (\bar{\alpha}_{11} + \underline{\alpha}_{11}) v_p + (\alpha_{12} + \underline{\alpha}_{12}) v_q = \bar{\beta}_{11} v_p + \beta_{12} v_q,$$

$$\underline{\mathbf{F}}_{tr}^F \cdot \mathbf{q} = (\alpha_{21} + \underline{\alpha}_{21}) v_p + (\bar{\alpha}_{22} + \underline{\alpha}_{22}) v_q = \beta_{21} v_p + \bar{\beta}_{22} v_q, \quad (3.46)$$

where α_{ij} are the time dependent beat coefficients involving integrals I_i and J_i , and corresponds to sphere locomotion. The beat coefficients $\underline{\alpha}_{ij}$ involve \tilde{I}_i and \tilde{J}_i and are due to the image sphere locomotion. The special term $\bar{\alpha}_{ij}$ incorporates the effect of viscous forces and drag. The detailed expressions of time dependent beat coefficients α_{ij} are defined in appendix A.

The viscous torque due to translating motion of the unit sphere in the presence of the plane boundary with fluid velocity (3.43) on an element of flagellum is given by

$$d\underline{\mathbf{L}}_{tr}^F = \mathbf{r} \times d\underline{\mathbf{F}}_{tr}^F.$$

Using equation (2.35) for \mathbf{r} and equation (3.43) for $d\mathbf{F}_{flg}^{tr}$, the above equation becomes

$$\begin{aligned} d\mathbf{L}_{tr}^F = & \left[-K_n \left\{ -v_n \left(1 - \frac{3}{4r} - \frac{1}{4r^3} \right) + 3(v_t r_n r t + v_n r_n^2) \left(\frac{1}{4r^3} - \frac{1}{4r^5} \right) + \frac{3}{4} v_t \right. \right. \\ & \left. \left(-\frac{R_1 R_3}{R^3} + \frac{R_1 R_3}{R^5} + 2x_3 \frac{R_1}{R^3} + 2x_3 \frac{R_1}{R^5} + 6hx_3 \frac{R_1 R_3}{R^5} - 10x_3 \frac{R_1 R_3^2}{R^7} \right) - \frac{3}{4} v_n \right. \\ & \left. \left(\frac{1}{R} + \frac{1}{3R^3} + \frac{R_3^2}{R^3} - \frac{R_3^2}{R^5} + 6x_3 \frac{R_3}{R^5} - \frac{2hx_3}{R^3} + 6hx_3 \frac{R_3^2}{R^5} - 10x_3 \frac{R_3^3}{R^7} \right) \right\} r_t \\ & + K_t \left\{ -v_t \left(1 - \frac{3}{4r} - \frac{1}{4r^3} \right) + 3(v_n r_n r t + v_t r_t^2) \left(\frac{1}{4r^3} - \frac{1}{4r^5} \right) - \frac{3}{4} v_n \right. \\ & \left. \left(-\frac{R_1 R_3}{R^3} + \frac{R_1 R_3}{R^5} + 2x_3 \frac{R_1}{R^3} + 2x_3 \frac{R_1}{R^5} + 6hx_3 \frac{R_1 R_3}{R^5} - 10x_3 \frac{R_1 R_3^2}{R^7} \right) - \frac{3}{4} v_t \right. \\ & \left. \left(\frac{1}{R} + \frac{1}{3R^3} + \frac{R_3^2}{R^3} - \frac{R_3^2}{R^5} + 6x_3 \frac{R_3}{R^5} - \frac{2hx_3}{R^3} + 6hx_3 \frac{R_3^2}{R^5} - 10x_3 \frac{R_3^3}{R^7} \right) \right\} r_n \right] \mathbf{b} \text{ds.} \end{aligned}$$

The total viscous torque for the single flagellum can be calculated by integrating along the length of the flagellum, giving

$$\begin{aligned} \mathbf{L}_{tr}^F = & \left[K_t \left\{ -v_t r_n \left(I_1 - \frac{3}{4} I_2 - \frac{1}{4} I_3 \right) + v_n r_n^2 \left(\frac{3J_3}{4} - \frac{3J_4}{4} \right) + v_t r_n \left(\frac{3I_7}{4} - \frac{3I_8}{4} \right) \right. \right. \\ & \left. \left. + \text{terms involving } \tilde{I}_i \text{ and } \tilde{J}_i \right\} \right. \\ & \left. - K_n \left\{ -v_n \left(J_1 - \frac{3}{4} J_2 - \frac{1}{4} J_3 \right) + v_n r_n^2 \left(\frac{3J_3}{4} - \frac{3J_4}{4} \right) + v_t r_n \left(\frac{3I_7}{4} - \frac{3I_8}{4} \right) \right. \right. \\ & \left. \left. + \text{terms involving } \tilde{I}_i \text{ and } \tilde{J}_i \right\} \right] \mathbf{b}. \end{aligned} \quad (3.47)$$

Now finally, the total torque due to translation motion of sphere on one flagellum for the uniplanar case in body coordinates can be written as

$$\mathbf{L}_{tr}^F \cdot \bar{\mathbf{r}} = (\bar{\alpha}_{61} + \bar{\alpha}_{61}) v_p + (\alpha_{62} + \alpha_{62}) v_q = \bar{\beta}_{61} v_p + \beta_{62} v_q. \quad (3.48)$$

Contribution of the rotation of the spherical body

The velocity of the fluid due to the uniplanar rotation of a spherical body of radius a in the presence of no-slip plane boundary in a low Reynolds number fluid flow is given by

$$\begin{aligned} \mathbf{u}_{rt} = & \left[\Omega_b r_t \left(1 - \frac{1}{r^3} \right) + \Omega_b \sin(\chi + \theta) \left(\frac{R_1}{R^3} - \frac{6hR_1 R_3}{R^5} + \frac{6R_1 R_3^2}{R^5} \right) \right. \\ & \left. + \Omega_b \cos(\chi + \theta) \left(-\frac{R_3}{R^3} + \frac{2h}{R^3} - \frac{6hR_1^2}{R^5} + \frac{6R_1^2 R_3}{R^5} \right) \right] \mathbf{n} \\ & + \left[-\Omega_b r_n \left(1 - \frac{1}{r^3} \right) + \Omega_b \sin(\chi + \theta) \left(-\frac{R_3}{R^3} + \frac{2h}{R^3} - \frac{6hR_1^2}{R^5} + \frac{6R_1^2 R_3}{R^5} \right) \right. \\ & \left. + \Omega_b \cos(\chi + \theta) \left(\frac{R_1}{R^3} - \frac{6hR_1 R_3}{R^5} + \frac{6R_1 R_3^2}{R^5} \right) \right] \mathbf{t}. \end{aligned}$$

The above expression of the fluid velocity is the sum of the contributions from the rotating sphere and corresponding image sphere as shown in the Figure 3.6.

Now, using RFT the force produced by an element of a flagellum within this flow with $a = 1$ is given by

$$\begin{aligned}
d\underline{\mathbf{F}}_{tr}^F &= K_n \left[\Omega_b r_t \left(1 - \frac{1}{r^3} \right) + \Omega_b \sin(\chi + \theta) \left(\frac{R_1}{R^3} - \frac{6hR_1R_3}{R^5} + \frac{6R_1R_3^2}{R^5} \right) \right. \\
&\quad \left. + \Omega_b \cos(\chi + \theta) \left(-\frac{R_3}{R^3} + \frac{2h}{R^3} - \frac{6hR_1^2}{R^5} + \frac{6R_1^2R_3}{R^5} \right) \right] \mathbf{n} ds \\
&\quad + K_t \left[-\Omega_b r_n \left(1 - \frac{1}{r^3} \right) + \Omega_b \sin(\chi + \theta) \left(-\frac{R_3}{R^3} + \frac{2h}{R^3} - \frac{6hR_1^2}{R^5} + \frac{6R_1^2R_3}{R^5} \right) \right. \\
&\quad \left. + \Omega_b \cos(\chi + \theta) \left(\frac{R_1}{R^3} - \frac{6hR_1R_3}{R^5} + \frac{6R_1R_3^2}{R^5} \right) \right] \mathbf{t} ds. \tag{3.49}
\end{aligned}$$

The total force can be calculated by integrating along the length of the flagellum as

$$\begin{aligned}
\underline{\mathbf{F}}_{rt}^F &= K_n \left[\Omega_b (J_1 - J_3) + \text{terms involving } \tilde{I}_i \text{ and } \tilde{J}_i \right] \mathbf{n} \\
&\quad - K_t \left[\Omega_b r_n (I_1 - I_3) + \text{terms involving } \tilde{I}_i \text{ and } \tilde{J}_i \right] \mathbf{t}. \tag{3.50}
\end{aligned}$$

Therefore, the total force due to rotational motion of sphere on one flagellum for the uniplanar case in the presence of plane boundary in body coordinates system becomes

$$\begin{aligned}
\underline{\mathbf{F}}_{rt}^F \cdot \mathbf{p} &= (\bar{\alpha}_{16} + \bar{\alpha}_{16}) \Omega_r = \bar{\beta}_{16} \Omega_r, \\
\underline{\mathbf{F}}_{rt}^F \cdot \mathbf{q} &= (\alpha_{26} + \alpha_{26}) \Omega_r = \beta_{26} \Omega_r. \tag{3.51}
\end{aligned}$$

The viscous torque due to rotational motion of the unit sphere with rotational velocity (2.44) on an element of flagellum is given by

$$d\underline{\mathbf{L}}_{rt}^F = \mathbf{r} \times d\underline{\mathbf{F}}_{rt}^F.$$

Using equation (2.35) for \mathbf{r} and equation (3.49) for $d\underline{\mathbf{F}}_{rt}^F$, the torque becomes

$$d\underline{\mathbf{L}}_{rt}^F = \left[(K_n \Omega_b r_t^2) + K_t \Omega_b r_n^2 \left(1 - \frac{1}{r^3} \right) \right] \mathbf{b} ds.$$

Hence, the total viscous torque can be calculated by integrating along the length of the flagellum, to give

$$\underline{\mathbf{L}}_{rt}^F = \left[K_n \Omega_b (I_6 - I_7) + K_t \Omega_b r_n^2 (I_1 - I_3) + \text{terms involving } \tilde{I}_i \text{ and } \tilde{J}_i \right] \mathbf{b}. \tag{3.52}$$

Now, finally, the total torque due to rotational motion of the sphere in the presence of plane boundary for uniplanar locomotion on one flagellum in body coordinates can be written as

$$\underline{\mathbf{L}}_{rt}^F \cdot \bar{\mathbf{r}} = (\bar{\alpha}_{66} + \bar{\alpha}_{66}) \Omega_r = \bar{\beta}_{66} \Omega_r. \tag{3.53}$$

Flagellar beating contribution

Following the unbounded biflagellate swimming discussed in chapter 2, we shall calculate the viscous force and torque due to the imposed velocity of the flagella $\dot{\mathbf{r}}$, beating relative to the cell body in the vicinity of the no-slip plane boundary. For the effective stroke, the velocity of an element of flagellum for the planar case can be rewritten from (2.25) as

$$\dot{\mathbf{r}} = -s\dot{\chi} \mathbf{n}.$$

Using RFT again, and to avoid the same steps discussed in chapter 2 we can directly rewrite the total force due to velocity of flagellum during effective stroke for uniplanar case in body coordinates system as

$$\mathbf{F}_{fl}^F \cdot \mathbf{p} = -K_n \left(\frac{l^2}{2} \dot{\chi} \right) \sin\chi. \quad (3.54)$$

Similarly, for the recovery stroke the total force due to velocity of flagellum for uniplanar case in body coordinates system becomes

$$\mathbf{F}_{fl}^F \cdot \mathbf{p} = K_n \left[w \sin\chi(l - wt) - \frac{1}{2}(l - wt)^2 \dot{\chi} \right] \sin\chi + K_t \left[w(\cos\chi - 1)(l - wt) \right] \cos\chi.$$

Therefore, the total force due to flagellar beating for the planar case in body coordinates can be written as

$$\mathbf{F}_{fl}^F = f_1 \mathbf{p} + f_2 \mathbf{q}, \quad (3.55)$$

where for the effective stroke we have derived

$$f_1 = -K_n \left(\frac{l^2}{2} \dot{\chi} \right) \sin\chi, \quad \text{and} \quad f_2 = K_n \left(\frac{l^2}{2} \dot{\chi} \right) \cos\chi, \quad (3.56)$$

and similarly for recovery stroke we have found

$$\begin{aligned} f_1 &= K_n \left[w \sin\chi(l - wt) - \frac{1}{2}(l - wt)^2 \dot{\chi} \right] \sin\chi + K_t \left[w(\cos\chi - 1)(l - wt) \right] \cos\chi \\ f_2 &= -K_n \left[w \sin\chi(l - wt) - \frac{1}{2}(l - wt)^2 \dot{\chi} \right] \cos\chi + K_t \left[w(\cos\chi - 1)(l - wt) \right] \sin\chi. \end{aligned} \quad (3.57)$$

Thus, the total viscous force and viscous torque produced by both flagella in the presence of a no-slip stationary plane boundary can be calculated by substitution of the equations (3.46), (3.51), (3.56) and (3.57) for forces and equations (3.48) and (3.53) for torques in

$$\underline{\mathbf{F}}_{flg} = \underline{\mathbf{F}}_{tr} + \underline{\mathbf{F}}_{rt} - \mathbf{F}_{fl}, \quad (3.58)$$

and

$$\underline{\mathbf{L}}_{flg} = \underline{\mathbf{L}}_{tr} + \underline{\mathbf{L}}_{rt} - \mathbf{L}_{fl}. \quad (3.59)$$

3.4.2 Force-Torque balance equations

Now following the unbounded swimming case discussed in chapter 2 we can constitute the force torque balance equations for the biflagellate cell swimming in the vicinity of the no-slip plane boundary. Both of the cell's flagella beat symmetrically but the flow around the cell body does not remain symmetric because of the presence of the plane boundary. Using equations (3.24) and (3.25), the force torque balance equations for the symmetric flagella beat and non-symmetric fluid flow problem in a uniplanar locomotion takes the form

$$\underline{\mathbf{F}}_{bdy} + \underline{\mathbf{F}}_{flg} = 0, \quad (3.60)$$

$$\underline{\mathbf{L}}_{bdy} + \underline{\mathbf{L}}_{grv} + \underline{\mathbf{L}}_{flg} = 0. \quad (3.61)$$

Now using the above defined assumptions for the uniplanar flagella beat pattern and equations (3.28) and (3.58) for forces and (3.29), (3.31) and (3.59) for torques (3.28), the force-torque balance equations for biflagellate swimming in the presence of plane boundary can be written in matrix form as

$$\begin{bmatrix} F_p \\ F_q \\ L_r \end{bmatrix} = \begin{bmatrix} \bar{\beta}_{11} & \beta_{12} & \bar{\beta}_{16} \\ \beta_{21} & \bar{\beta}_{22} & \beta_{26} \\ \bar{\beta}_{61} & \beta_{62} & \bar{\beta}_{66} \end{bmatrix} \begin{bmatrix} v_p \\ v_q \\ \Omega_r \end{bmatrix} + \begin{bmatrix} 0 \\ 0 \\ -mgH \sin \theta \end{bmatrix} - \begin{bmatrix} f_1 \\ 0 \\ 0 \end{bmatrix} = 0,$$

which can be further simplified in the absence of vorticity ω , and after rearrangement as

$$\begin{bmatrix} \bar{\beta}_{11} & \beta_{12} & \bar{\beta}_{16} \\ \beta_{21} & \bar{\beta}_{22} & \beta_{26} \\ \bar{\beta}_{61} & \beta_{62} & \bar{\beta}_{66} \end{bmatrix} \begin{bmatrix} v_p \\ v_q \\ \Omega_r \end{bmatrix} = \begin{bmatrix} f_1 \\ 0 \\ 0 \end{bmatrix} - \begin{bmatrix} 0 \\ 0 \\ -mgH \sin \theta \end{bmatrix}. \quad (3.62)$$

The coefficient matrix or resistance matrix from the above matrix equation can be defined as

$$C = \begin{bmatrix} \bar{\beta}_{11} & \beta_{12} & \bar{\beta}_{16} \\ \beta_{21} & \bar{\beta}_{22} & \beta_{26} \\ \bar{\beta}_{61} & \beta_{62} & \bar{\beta}_{66} \end{bmatrix},$$

where β_{ij} are the unknown beat coefficients, which are the sum of α_{ij} and $\underline{\alpha}_{ij}$, beat coefficients due to sphere and image sphere locomotion respectively. The terms $\bar{\beta}_{ij}$, incorporates viscous drag and viscous torque due to the translational and rotational motion of the spherical body in the presence of the plane boundary. The diagonal terms $\bar{\beta}_{ii}$ have been modified using equations (3.28) for viscous drag and (3.29) for viscous torque in the

presence of a plane boundary as

$$\bar{\beta}_{11} = \beta_{11} - 6\pi - \frac{27\pi}{8h}, \quad \bar{\beta}_{22} = \beta_{22} - 6\pi - \frac{27\pi}{8h}, \quad \text{and} \quad \bar{\beta}_{66} = \beta_{66} - 8\pi - \frac{5\pi}{2h^3},$$

whereas, off diagonal terms $\bar{\beta}_{ij}$, again using equations (3.28) and (3.29), take the form as

$$\bar{\beta}_{16} = \beta_{16} + \frac{3\pi}{4h^4}, \quad \text{and} \quad \bar{\beta}_{61} = \beta_{61} + \frac{3\pi}{4h^4}.$$

The inverse of the above resistance matrix C , termed a mobility matrix can be evaluated as

$$D = C^{-1} = \frac{1}{\Lambda^*} \begin{bmatrix} \Delta_{11} & \Delta_{12} & \Delta_{13} \\ \Delta_{21} & \Delta_{22} & \Delta_{23} \\ \Delta_{31} & \Delta_{32} & \Delta_{33} \end{bmatrix},$$

where

$$\begin{aligned} \Delta_{11} &= \bar{\beta}_{22}\bar{\beta}_{66} - \beta_{62}\beta_{26}, & \Delta_{12} &= \bar{\beta}_{16}\beta_{62} - \beta_{12}\bar{\beta}_{66}, & \Delta_{13} &= \beta_{12}\beta_{26} - \bar{\beta}_{16}\bar{\beta}_{22}, \\ \Delta_{21} &= \bar{\beta}_{61}\beta_{26} - \beta_{21}\bar{\beta}_{66}, & \Delta_{22} &= \bar{\beta}_{11}\bar{\beta}_{66} - \bar{\beta}_{16}\bar{\beta}_{61}, & \Delta_{23} &= \bar{\beta}_{16}\beta_{21} - \bar{\beta}_{11}\beta_{26}, \\ \Delta_{31} &= \beta_{21}\beta_{62} - \bar{\beta}_{61}\bar{\beta}_{22}, & \Delta_{32} &= \beta_{12}\bar{\beta}_{61} - \bar{\beta}_{11}\beta_{62}, & \Delta_{33} &= \bar{\beta}_{11}\bar{\beta}_{22} - \beta_{21}\beta_{12}, \end{aligned}$$

and

$$\Lambda^* = \bar{\beta}_{61}\beta_{12}\beta_{26} - \bar{\beta}_{61}\bar{\beta}_{16}\bar{\beta}_{22} - \beta_{21}\beta_{12}\bar{\beta}_{66} + \beta_{21}\bar{\beta}_{16}\beta_{62} + \bar{\beta}_{11}\bar{\beta}_{22}\bar{\beta}_{66} - \bar{\beta}_{11}\beta_{62}\beta_{26}.$$

After multiplication with the mobility matrix D , equation (3.62) takes the form

$$\begin{bmatrix} v_p \\ v_q \\ \dot{\theta} \end{bmatrix} = \frac{1}{\Lambda^*} \begin{bmatrix} \Delta_{11}f_1 \\ \Delta_{21}f_1 \\ \Delta_{31}f_1 \end{bmatrix} - \frac{1}{\Lambda^*} \begin{bmatrix} -\Delta_{13}\text{mgH} \sin \theta \\ -\Delta_{23}\text{mgH} \sin \theta \\ -\Delta_{33}\text{mgH} \sin \theta \end{bmatrix}, \quad (3.63)$$

where

$$\Omega_r = \dot{\theta}.$$

Thus for the symmetric flagella beat of a biflagellate cell in the presence of plane boundary in a uniplanar locomotion, v_p and v_q can be written in components form as

$$v_p = \left(\frac{\bar{\beta}_{22}\bar{\beta}_{66} - \beta_{62}\beta_{26}}{\Lambda^*} \right) f_1 + \left(\frac{\beta_{12}\beta_{26} - \bar{\beta}_{16}\bar{\beta}_{22}}{\Lambda^*} \right) \text{mgH} \sin \theta, \quad (3.64)$$

$$v_q = \left(\frac{\bar{\beta}_{61}\beta_{26} - \beta_{21}\bar{\beta}_{66}}{\Lambda^*} \right) f_1 + \left(\frac{\bar{\beta}_{16}\beta_{21} - \bar{\beta}_{11}\beta_{26}}{\Lambda^*} \right) \text{mgH} \sin \theta, \quad (3.65)$$

and angular velocity $\dot{\theta}$ can be found as

$$\dot{\theta} = \left(\frac{\beta_{21}\beta_{62} - \bar{\beta}_{61}\bar{\beta}_{22}}{\Lambda^*} \right) f_1 + \left(\frac{\bar{\beta}_{11}\bar{\beta}_{22} - \beta_{21}\beta_{12}}{\Lambda^*} \right) \text{mgH} \sin \theta. \quad (3.66)$$

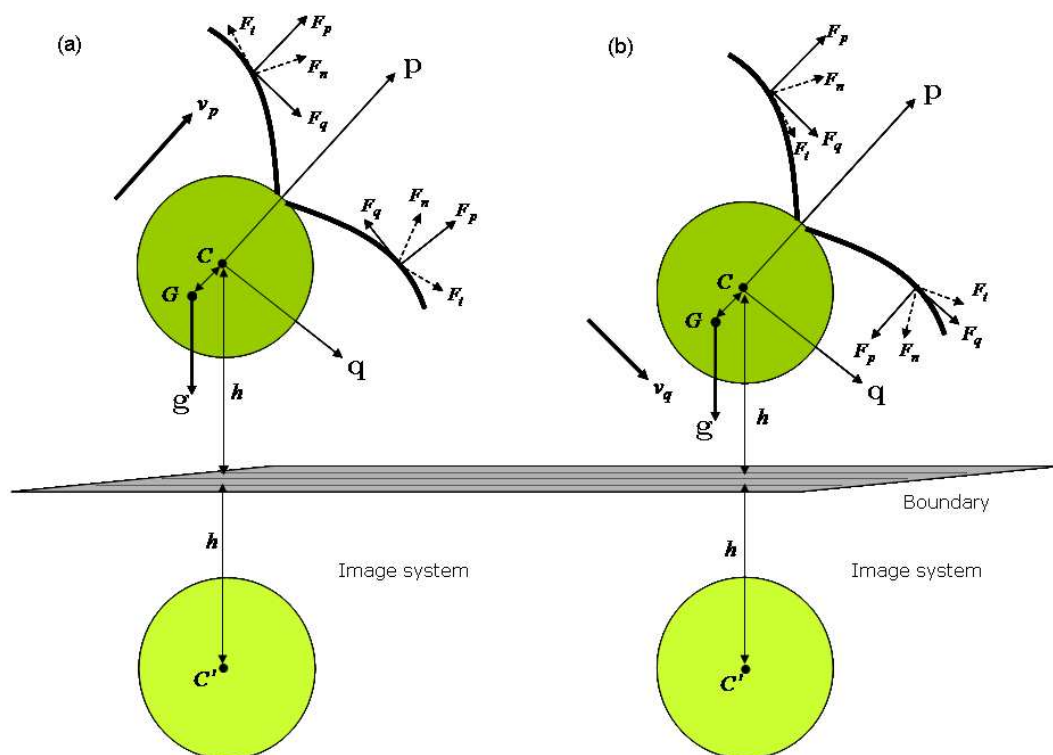


Figure 3.7: Addition and subtraction of forces acting on the flagellar section due to swimming in the (a) primary velocity direction \mathbf{p} and (b) transverse velocity direction \mathbf{q} respectively.

Since, due to the presence of the plane boundary the flow around the swimming cell is not symmetric, so we have observed that velocity component in the primary direction v_p and velocity component in transverse direction v_q depend upon h distance from the centre of cell to the boundary, angle θ and centre-of-gravity offset H . Similarly velocity component v_q also depend upon the h , θ and H respectively.

For the case of bounded cell swimming in the absence of gravitational forces and torques, the components of swimming velocity and angular velocity, (3.64) to (3.66), takes the form as

$$v_p = \left(\frac{\bar{\beta}_{22}\bar{\beta}_{66} - \beta_{62}\beta_{26}}{\bar{\beta}_{61}\beta_{12}\beta_{26} - \bar{\beta}_{61}\bar{\beta}_{16}\bar{\beta}_{22} - \beta_{21}\beta_{12}\bar{\beta}_{66} + \beta_{21}\bar{\beta}_{16}\beta_{62} + \bar{\beta}_{11}\bar{\beta}_{22}\bar{\beta}_{66} - \bar{\beta}_{11}\beta_{62}\beta_{26}} \right) f_1, \quad (3.67)$$

$$v_q = \left(\frac{\bar{\beta}_{61}\beta_{26} - \beta_{21}\bar{\beta}_{66}}{\bar{\beta}_{61}\beta_{12}\beta_{26} - \bar{\beta}_{61}\bar{\beta}_{16}\bar{\beta}_{22} - \beta_{21}\beta_{12}\bar{\beta}_{66} + \beta_{21}\bar{\beta}_{16}\beta_{62} + \bar{\beta}_{11}\bar{\beta}_{22}\bar{\beta}_{66} - \bar{\beta}_{11}\beta_{62}\beta_{26}} \right) f_1, \quad (3.68)$$

and angular velocity $\dot{\theta}$ can be found as

$$\dot{\theta} = \left(\frac{\beta_{21}\beta_{62} - \bar{\beta}_{61}\bar{\beta}_{22}}{\bar{\beta}_{61}\beta_{12}\beta_{26} - \bar{\beta}_{61}\bar{\beta}_{16}\bar{\beta}_{22} - \beta_{21}\beta_{12}\bar{\beta}_{66} + \beta_{21}\bar{\beta}_{16}\beta_{62} + \bar{\beta}_{11}\bar{\beta}_{22}\bar{\beta}_{66} - \bar{\beta}_{11}\beta_{62}\beta_{26}} \right) f_1, \quad (3.69)$$

where $\bar{\beta}_{ij}$ are special terms involving Faxen's corrections due to the biflagellate cell's body translation and rotation in the vicinity of the no-slip plane boundary.

Furthermore in the absence of the Faxen's correction terms as defined in equations (3.28) and (3.29), the equations for cell swimming velocity and angular velocity without the gravitational forces and torques further simplify to yield

$$v_p = \left(\frac{\beta_{22}\beta_{66} - \beta_{62}\beta_{26}}{\beta_{61}\beta_{12}\beta_{26} - \beta_{61}\beta_{16}\beta_{22} - \beta_{21}\beta_{12}\beta_{66} + \beta_{21}\beta_{16}\beta_{62} + \beta_{11}\beta_{22}\beta_{66} - \beta_{11}\beta_{62}\beta_{26}} \right) f_1, \quad (3.70)$$

$$v_q = \left(\frac{\beta_{61}\beta_{26} - \beta_{21}\beta_{66}}{\beta_{61}\beta_{12}\beta_{26} - \beta_{61}\beta_{16}\beta_{22} - \beta_{21}\beta_{12}\beta_{66} + \beta_{21}\beta_{16}\beta_{62} + \beta_{11}\beta_{22}\beta_{66} - \beta_{11}\beta_{62}\beta_{26}} \right) f_1, \quad (3.71)$$

and angular velocity $\dot{\theta}$ can be found as

$$\dot{\theta} = \left(\frac{\beta_{21}\beta_{62} - \beta_{61}\beta_{22}}{\beta_{61}\beta_{12}\beta_{26} - \beta_{61}\beta_{16}\beta_{22} - \beta_{21}\beta_{12}\beta_{66} + \beta_{21}\beta_{16}\beta_{62} + \beta_{11}\beta_{22}\beta_{66} - \beta_{11}\beta_{62}\beta_{26}} \right) f_1. \quad (3.72)$$

3.4.3 Force-Torque balance equations without flagella contributions

To investigate the contribution of the flagella during the cell swimming in the vicinity of a no-slip plane boundary, we derive again the equations of motion for cell swimming

using force-torque balance equations without the flagella contribution. Following the same assumptions discussed in section (3.4.2) and using equations (3.60) and (3.61), the force torque balance equations for bounded symmetric cell without the flagella in the presence of the no-slip plane boundary in a uniplanar locomotion takes the form as

$$\underline{\mathbf{F}}_{bdy} = 0, \quad (3.73)$$

$$\underline{\mathbf{L}}_{bdy} + \underline{\mathbf{L}}_{grv} = 0. \quad (3.74)$$

Now using the above defined assumptions for the uniplanar flagella beat pattern and equations (2.7), (2.8) and (2.10), the force-torque balance equations can be written in matrix form as

$$\begin{bmatrix} F_p \\ F_q \\ L_r \end{bmatrix} = \begin{bmatrix} -6\pi - \frac{27}{8h} & 0 & \frac{3\pi}{4h^4} \\ 0 & -6\pi - \frac{27}{8h} & 0 \\ \frac{3\pi}{4h^4} & 0 & -8\pi - \frac{5\pi}{2h^3} \end{bmatrix} \begin{bmatrix} v_p \\ v_q \\ \Omega_r \end{bmatrix} + \begin{bmatrix} 0 \\ 0 \\ -mgH \sin \theta \end{bmatrix} = 0,$$

which can be further simplified and after rearrangement as

$$\begin{bmatrix} -6\pi - \frac{27}{8h} & 0 & \frac{3\pi}{4h^4} \\ 0 & -6\pi - \frac{27}{8h} & 0 \\ \frac{3\pi}{4h^4} & 0 & -8\pi - \frac{5\pi}{2h^3} \end{bmatrix} \begin{bmatrix} v_p \\ v_q \\ \Omega_r \end{bmatrix} = - \begin{bmatrix} 0 \\ 0 \\ -mgH \sin \theta \end{bmatrix}. \quad (3.75)$$

The coefficient matrix or resistance matrix from the above matrix equation can be defined as

$$F = \begin{bmatrix} -6\pi - \frac{27}{8h} & 0 & \frac{3\pi}{4h^4} \\ 0 & -6\pi - \frac{27}{8h} & 0 \\ \frac{3\pi}{4h^4} & 0 & -8\pi - \frac{5\pi}{2h^3} \end{bmatrix},$$

the inverse of the above resistance matrix F , termed as mobility matrix can be evaluated as

$$G = F^{-1} = \frac{1}{\Lambda^{**}} \begin{bmatrix} -8\pi - \frac{5\pi}{2h^3} & 0 & -\frac{3\pi}{4h^4} \\ 0 & -8\pi - \frac{5\pi}{2h^3} & 0 \\ -\frac{3\pi}{4h^4} & 0 & -6\pi - \frac{27}{8h} \end{bmatrix},$$

where

$$\Lambda^{**} = \left(-6\pi - \frac{27}{8h}\right) \left(-8\pi - \frac{5\pi}{2h^3}\right) - \left(\frac{3\pi}{4h^4}\right)^2.$$

After multiplication with the mobility matrix G , equation (3.75) takes the form

$$\begin{bmatrix} v_p \\ v_q \\ \dot{\theta} \end{bmatrix} = \frac{1}{\Lambda^{**}} \begin{bmatrix} -\left(\frac{3\pi}{4h^4}\right) mgH \sin \theta \\ 0 \\ \left(-6\pi - \frac{27}{8h}\right) mgH \sin \theta \end{bmatrix}. \quad (3.76)$$

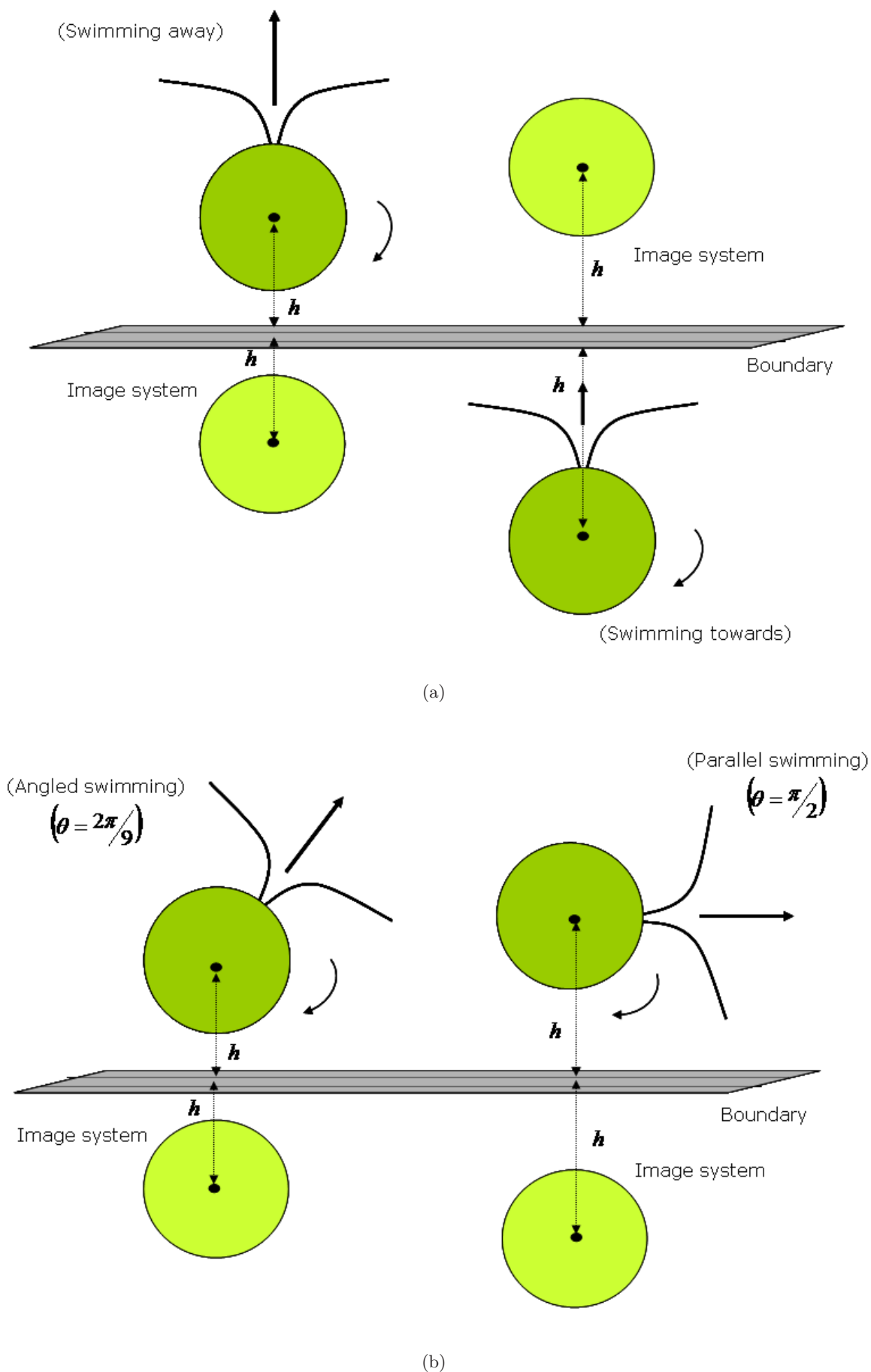


Figure 3.8: Swimming cell in the vicinity of no-slip stationary plane boundary. (a) Upward swimming away/towards the plane boundary, (b) Angled/parallel swimming near the plane boundary.

Thus for a biflagellate cell swimming without the flagella contribution in the presence of a plane boundary in a non-symmetric fluid flow problem for a uniplanar locomotion v_p and v_q takes the form as

$$v_p = \frac{1}{\Lambda^{**}} \left(-\frac{3\pi}{4h^4} \right) \text{mgH} \sin \theta, \quad (3.77)$$

$$v_q = 0, \quad (3.78)$$

and angular velocity $\dot{\theta}$ can be found as

$$\dot{\theta} = \frac{1}{\Lambda^{**}} \left(-6\pi - \frac{27}{8h} \right) \text{mgH} \sin \theta. \quad (3.79)$$

Here we have observed that velocity component in the primary direction v_p and angular velocity $\dot{\theta}$ are depending upon angle θ , distance of centre of cell from the boundary h and centre-of-gravity offset H . The swimming velocity in the transverse direction v_q is found to be zero which means no drift in the \mathbf{q} direction without the inclusion of flagella.

3.5 Results

Now we will discuss the different situations of the uniplanar biflagellate swimmer *C. augustae* in the vicinity of the stationary and rigid no-slip plane boundary, as shown in Figure 3.8 in detail.

3.5.1 Uniplanar upward cell swimming away/towards the no-slip plane boundary

In the first part of the bounded swimming problems we start with the most simple case when the biflagellate cell swims away/towards the stationary no-slip stationary plane boundary. It is clear from Figure 3.8(a) that for the uniplanar upward swimming case $\theta = 0^\circ$, which implies no contribution from the gravitational torque. Therefore, the above derived equations (3.64) to (3.66) for the organism's swimming velocity and angular velocity reduced to equations (3.67) to (3.69) as discussed earlier in section (3.4.2).

Now we will discuss the two cases of the uniplanar upward swimming of biflagellate cell in the vicinity of the stationary no-slip plane boundary in detail.

Case(a): Upward swimming away from the plane boundary

In the first case we will discuss the organism's uniplanar swimming vertically upward away from the rigid no-slip plane boundary, which lies at a distance h from the center of the body as shown in Figure 3.9.

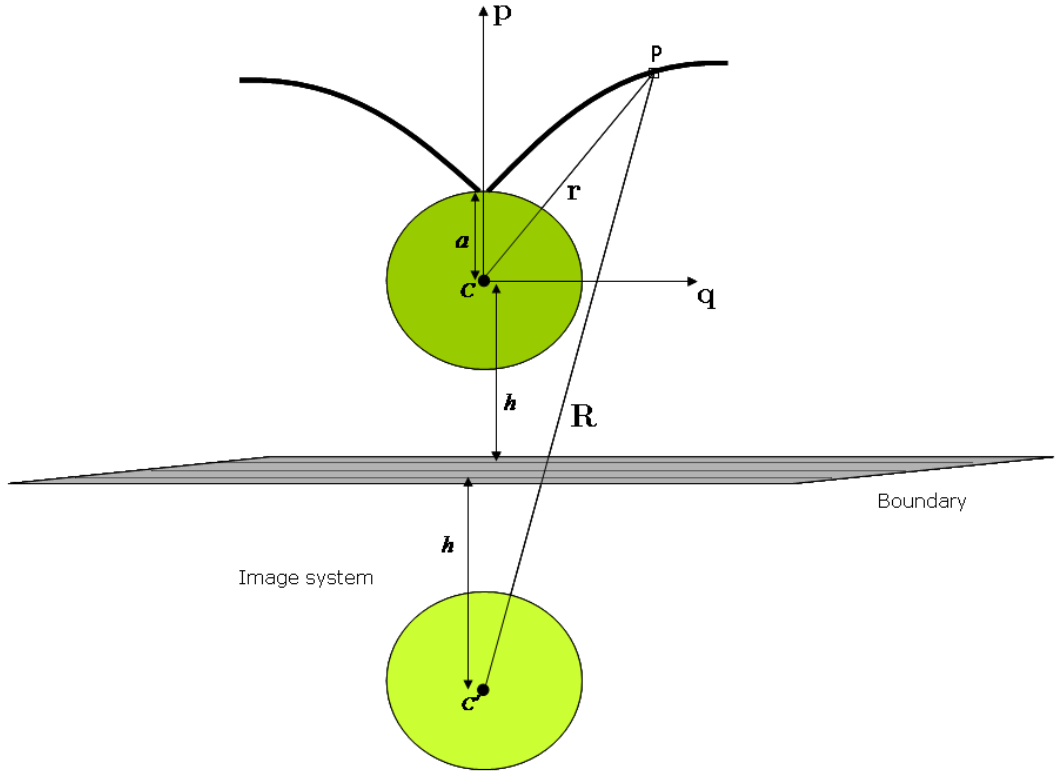


Figure 3.9: Upward swimming of a biflagellate cell away from the stationary no-slip plane boundary, where h is the distance of plane boundary from the centre of the cell body, \mathbf{r} and \mathbf{R} are the position vectors at an element of flagellum from the centre of sphere and image sphere, respectively.

The position vector and velocity vector from the centre of the image sphere at any point on the flagellum for uniplanar swimming case can be calculated by substituting $\theta = 0^\circ$ in the generalized expression of the position vector for the image sphere defined in equation (3.39) as

$$\begin{aligned}\mathbf{R}^S(s, t) &= [(s - b) \sin\chi] \mathbf{i} + [2h + b + (s - b) \cos\chi] \mathbf{k}, \\ \mathbf{R}^F(s, t) &= [(b + 2h) \sin\chi] \mathbf{n} + [(s - b) + (b + 2h) \cos\chi] \mathbf{t}.\end{aligned}\quad (3.80)$$

and

$$\dot{\mathbf{r}} = [w(\cos\chi - 1)] \mathbf{t} + [w \sin\chi - (s - wt)\dot{\chi}] \mathbf{n}.\quad (3.81)$$

Now using the above equations (3.67) to (3.69) and our Maple code, we have calculated the uniplanar upward swimming velocity and angular velocity of the cell away from the

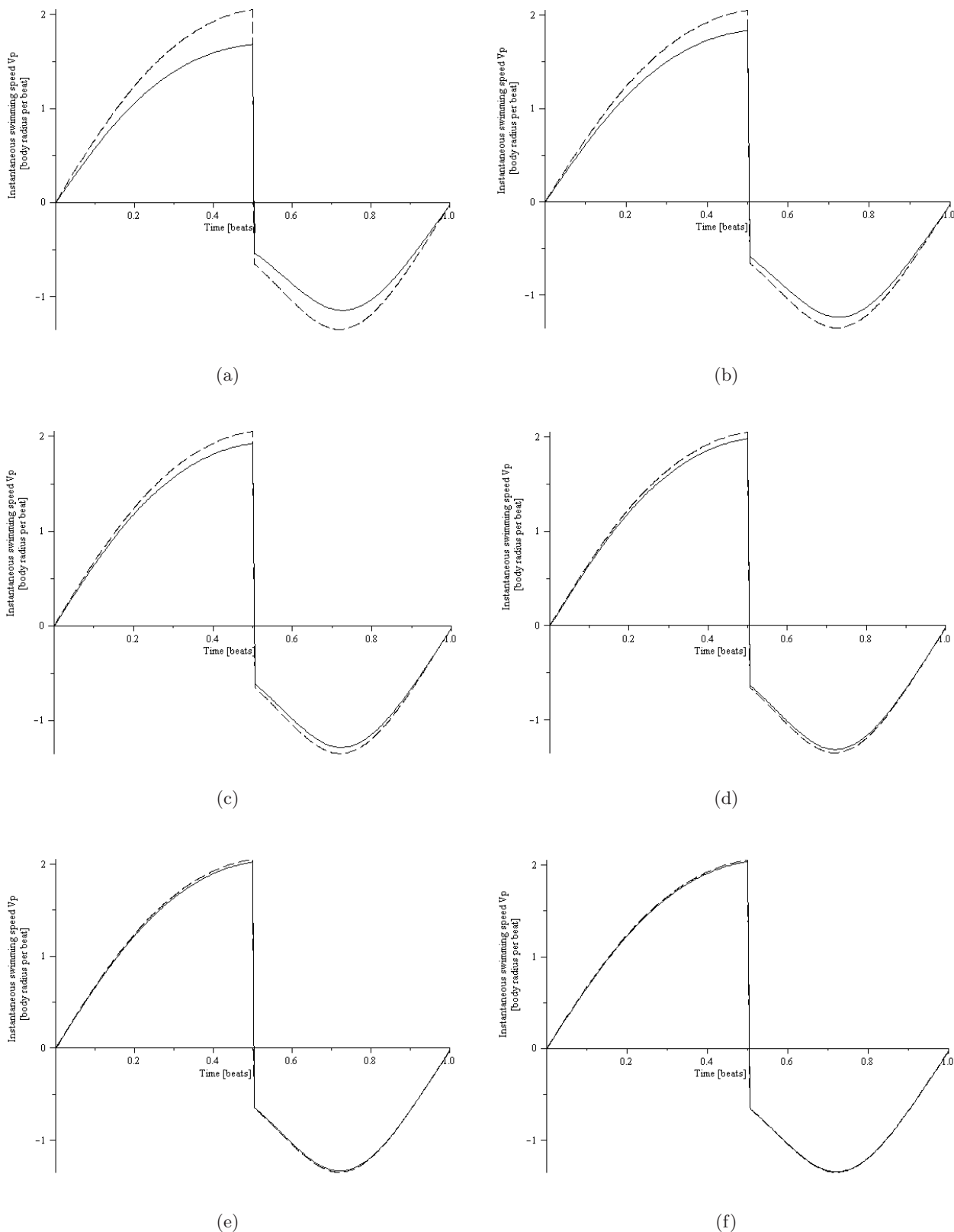


Figure 3.10: Variations of primary swimming speed v_p with the increase of h ((a)-(f), $h = 2, 5, 10, 20, 50, h = 100$) for one flagella beat, when cell is swimming away from the no-slip plane boundary. The dashed line represents the graph for the unbounded case whereas the solid line is for a bounded swimming cell.

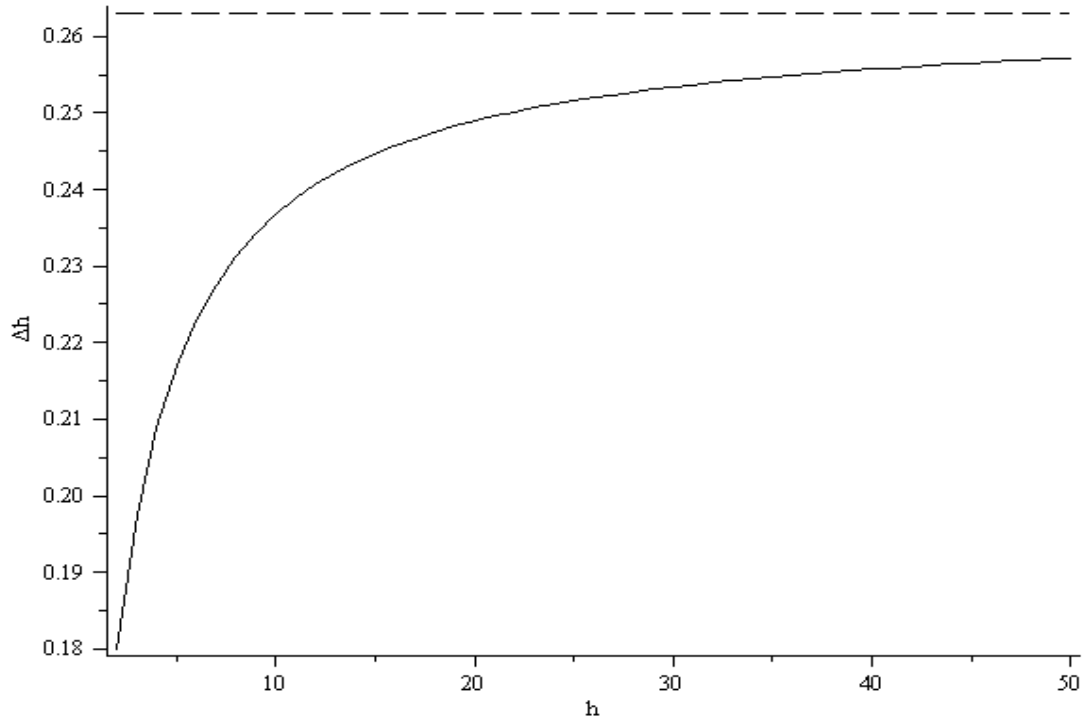


Figure 3.11: Variations of a biflagellate cell's change in position for one flagellar beat with increasing of h when the cell is swimming away from the no-slip plane boundary. The dashed line represents the graph for the unbounded case whereas the solid line is for a bounded cell swimming away from the boundary.

no-slip plane boundary. For comparison purpose and to test the convergence of the results we have compared the results for the bounded swimming with the unbounded swimming results explained in chapter 2. The detailed results are shown in the graphs plotted in Figures 3.10 and 3.11.

Now after analyzing the results we conclude that the swimming velocity in the primary swimming direction v_p is suppressed during effective stroke and more regressed during recovery stroke and with a slower swimming speed initially very close to the boundary due to the presence of the no-slip plane boundary. The typical value of v_p at a distance $h = 2$ from the plane boundary is calculated as 0.139 body radii per beat. After several beats, as cell swims upward away from the plane boundary, the swimming velocity increases in comparison with the previous velocity value due to the increased distance from the plane boundary. We have found the swimming velocity v_p at a distance $h = 100$ as 0.1945 body radii per beat. For unbounded swimming biflagellate we have calculated v_p as 0.1967 body radii per beat in chapter 2. Thus we conclude that for a large value of h , i.e. far

away from the plane boundary, the boundary effect diminishes and the bounded swimming speed approaches the unbounded swimming speed, as shown in the Figures 3.10 and 3.11.

The flagella beat is symmetric and $\theta = 0$ is for swimming away from the boundary case so the system is symmetric, so we expect component of velocity in the transverse direction v_q also equal to zero.

Case(b): Upward swimming towards the plane boundary

The second problem of uniplanar upward swimming is quite similar to the first problem with the only change is now organism swims towards the plane boundary which is at a distance h above the cell from the centre of the cell body. Here the distance h must be enough to enables the flagella to move freely as shown in the Figure 3.12.

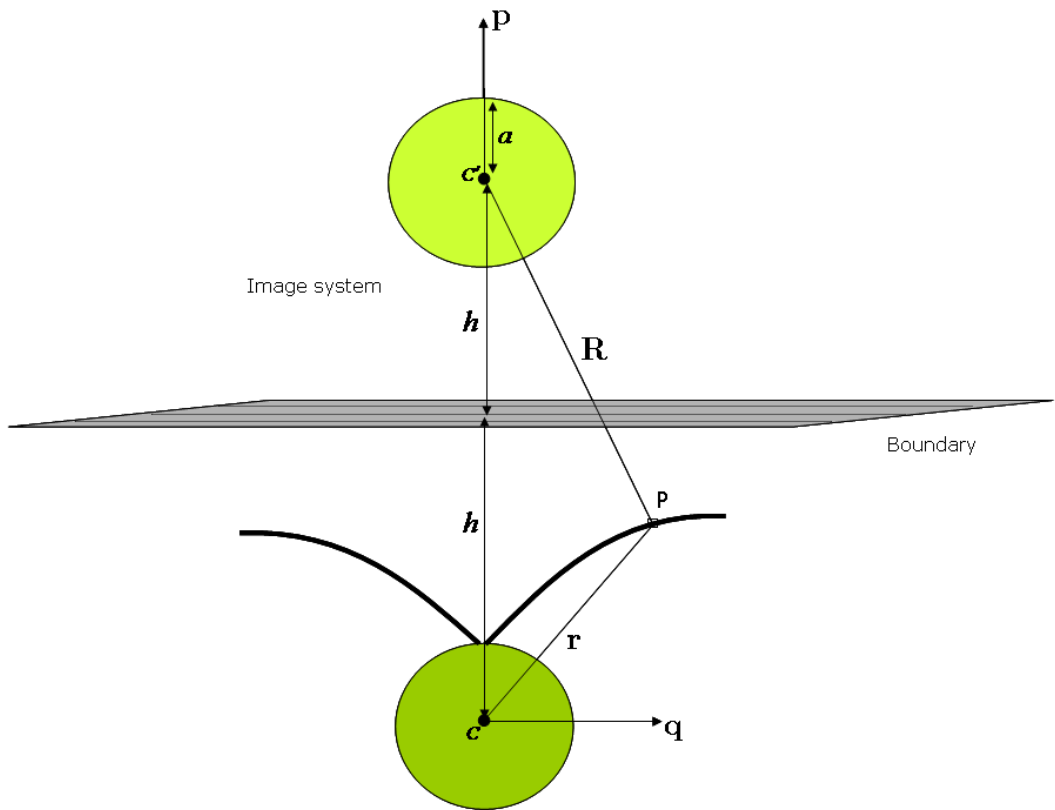


Figure 3.12: Upward swimming of a biflagellate cell towards the stationary no-slip plane boundary, where h is the distance of plane boundary from the centre of the cell body, \mathbf{r} and \mathbf{R} are the position vectors at an element of flagellum from the centre of sphere and image sphere, respectively.

The position vector and velocity vector from the centre of the image sphere at any

point on the flagellum for the uniplanar swimming case can be calculated by substituting $\theta = 0^\circ$ in the generalized expression of position vector for the image sphere defined in equation (3.38) as

$$\begin{aligned}\mathbf{R}^S(s, t) &= [(s - b) \sin\chi] \mathbf{i} + [-2h + b + (s - b) \cos\chi] \mathbf{k}, \\ \mathbf{R}^F(s, t) &= [(b - 2h) \sin\chi] \mathbf{n} + [(s - b) + (b - 2h) \cos\chi] \mathbf{t}.\end{aligned}\quad (3.82)$$

and

$$\dot{\mathbf{r}} = [w(\cos\chi - 1)] \mathbf{t} + [w \sin\chi - (s - wt)\dot{\chi}] \mathbf{n}.\quad (3.83)$$

Now using the above equations for the position vectors, the equations (3.67) to (3.69) and using our Maple code we have found the components of the swimming velocity and angular velocity of the biflagellate swimming cell towards the stationary no-slip plane boundary. The details of the results are shown in the graphs in Figures 3.13 to 3.15.

It is clear from the Figure 3.13 that at sufficiently far away from the plane boundary the value of the primary swimming velocity component v_p is consistent with the unbounded uniplanar swimming velocity discussed in chapter 2. As the biflagellate swimming cell approaches the plane boundary, the swimming velocity regressed gradually and reduced significantly very close to the plane boundary. For swimming close to the boundary at $h = 2$, we have calculated the swimming speed v_p as 0.2221 body radii per beat which gradually increases sufficiently at far away from the plane boundary.

The transverse velocity component v_q and angular velocity $\dot{\theta}$ both are zero at far away from the no-slip plane boundary which is also consistent with the results for unbounded cell swimming case. In this case, the geometry of the problem is different from the previous case, here biflagellate cell is facing towards the plane boundary. As $\theta = 0$, in this case as well so the system is symmetric again, but we have found some very small non-zero contribution for v_q swimming speed close to the boundary as shown in Figure 3.14. This may be due to the calculation error and can be investigated in future.

3.5.2 Comparison of swimming away and towards the no-slip stationary plane boundary

After analyzing the above two cases in detail and from Figures 3.11 and 3.15 we have found few similarities in the cell's locomotion. At Sufficiently far away from the no-slip plane boundary the above two cases behaves alike and cell's swimming speed approaches to the unbounded swimming cell speed for one flagella beat for the both cases. However,

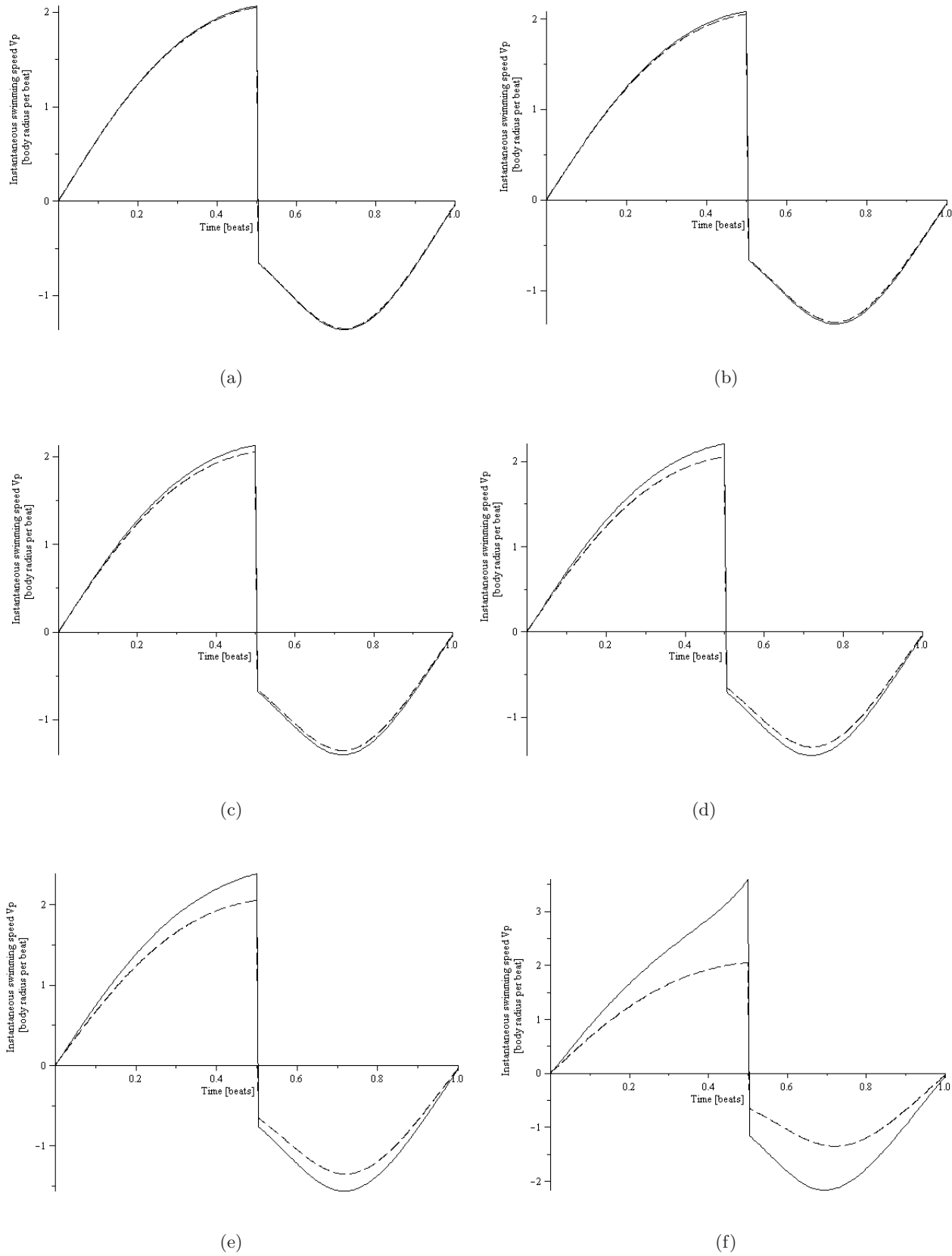
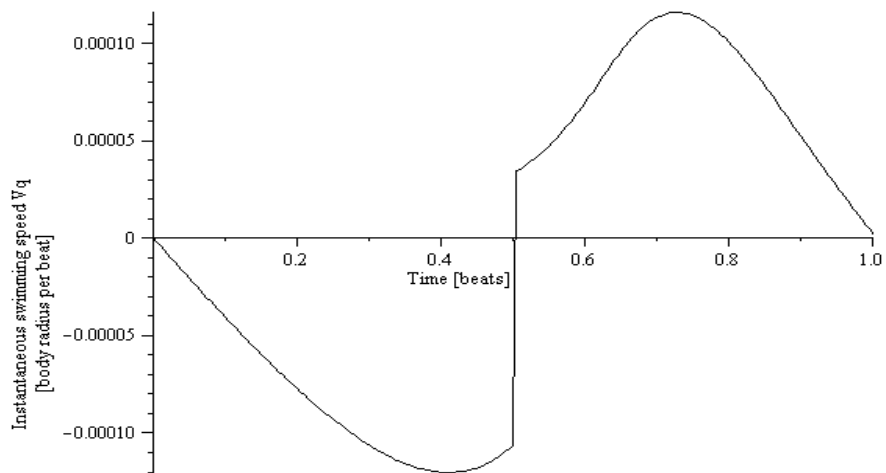
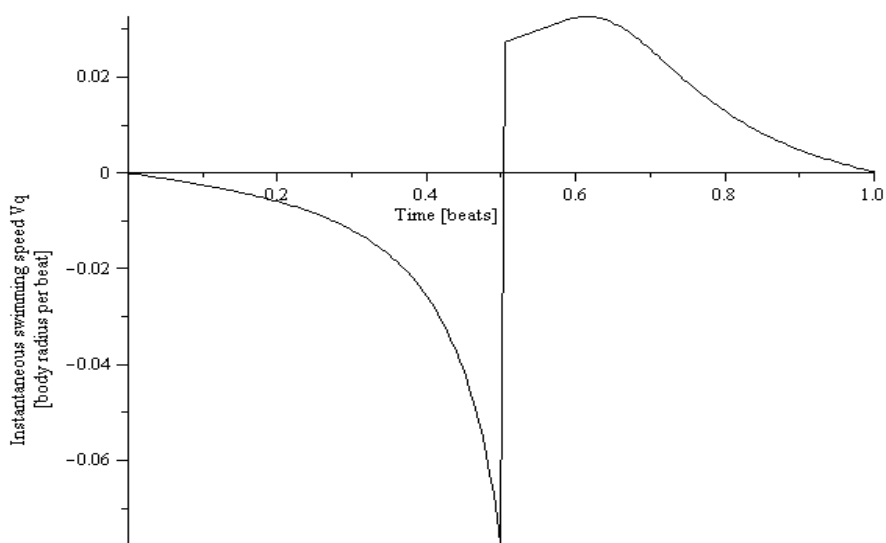


Figure 3.13: Variations of primary swimming speed v_p with the decrease of h ((a)-(f), $h = 100, 50, 20, 10, 5, h = 2$) for one flagella beat, when the cell is swimming towards the no-slip plane boundary. The dashed line represents the graph for the unbounded swimming case whereas solid line is for a bounded cell swimming towards the plane boundary.



(a)



(b)

Figure 3.14: Variations of transverse swimming speed v_q with the decrease of h , (a) $h = 5$, and (b) $h = 2$ for one flagella beat, when cell swimming towards the no-slip plane boundary.

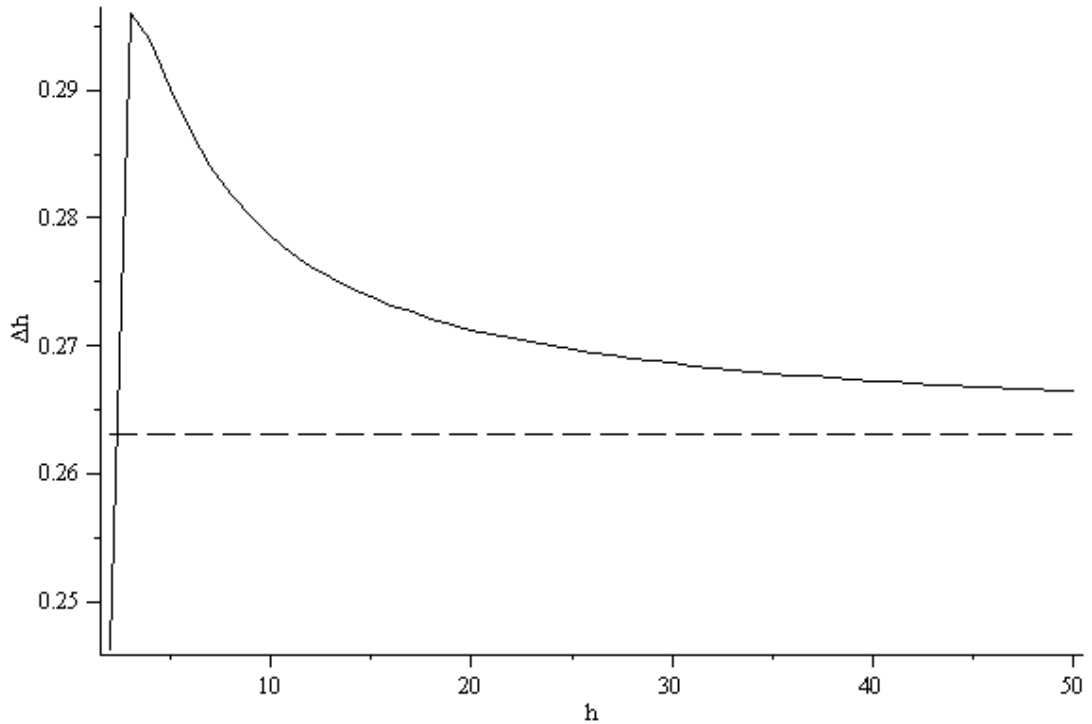


Figure 3.15: Variations of biflagellate cell's change in position for one flagella beat with the increase of h distance of the plane boundary from the centre of the cell body, as cell swimming towards the no-slip plane boundary. The dashed line represents the graph for unbounded case whereas solid line for bounded cell swimming towards the boundary.

very close to the plane boundary the above two cases are not similar. For the case of swimming away from the plane boundary, cell's swimming speed is much reduced due to the presence of the plane boundary in comparison with the unbounded case and gradually start increasing as cell moves away from the plane boundary as shown in Figure 3.11. On the other hand, when cell swimming towards and close to the plane boundary, cell's swimming speed gradually increases due to the presence of the plane boundary, position of the flagella and geometry of the problem as shown in Figure 3.15. A sudden drop in the swimming speed found as swimming cell approaches to the plane boundary and this may be due to the close proximity of the flagella with the boundary which may restricts the free flagella movement as clear from the Figure 3.12 and 3.15.

3.5.3 Biflagellate cell swimming in the vicinity of the no-slip stationary plane boundary

In the second part we now investigate the general problem of biflagellate cell swimming at any angle near the no-slip stationary plane boundary. This case can be analyzed by changing the orientation of the cell from the previous case, which leads to the change in force-torque balance equations with the involvement of gravity effects and we expect some healthy contributions from transverse swimming speed v_q and angular velocity $\dot{\theta}$. Thus to keep the axes same as discussed in the previous section we define the problem of swimming in the vicinity of the no-slip plane boundary as shown in Figure 3.6. Now the position vector from the image cell at any point on the flagellum of the swimming cell for the general case as defined earlier can be written as

$$\begin{aligned}\mathbf{R}^S(s, t) &= [b \sin \theta + (s - b) \sin(\theta + \chi)] \mathbf{i} + [2h + b \cos \theta + (s - b) \cos(\theta + \chi)] \mathbf{k}, \\ \mathbf{R}^F(s, t) &= [b \sin \chi + 2h \sin(\chi + \theta)] \mathbf{n} + [(s - b) + b \cos \chi + 2h \cos(\chi + \theta)] \mathbf{t},\end{aligned}$$

whereas the velocity of the any point of the flagellum as defined earlier in flagella coordinates system is

$$\dot{\mathbf{r}} = [w(\cos \chi - 1)] \mathbf{t} + [w \sin \chi - (s - wt)\dot{\chi}] \mathbf{n}.$$

Now as a general case we do the analysis of the biflagellate cell swimming at an angle of $\theta = 40^\circ$. Thus using the general force-torque balance equations (3.64) to (3.66) and our Maple code with the substitution of $\theta = 40^\circ$ we have calculated the components of the swimming velocity v_p , v_q and angular velocity. The results of the simulations with the variations of the distance h from the plane boundary from the centre of the biflagellate cell body are shown in Figures 3.16 to 3.19.

Since the biflagellate cell is bottom heavy because of its centre-of-gravity offset we have observed again more or less the same behavior as in the previous case for the case of primary swimming velocity v_p . The swimming velocity v_p is regressed close to the boundary and gradually increases as the cell moves further away from the plane boundary as shown in the graphs on Figure 3.16. It is also interesting to note that the swimming velocity v_p is more regressed close to the plane boundary: at $h = 2$ we found 0.1398 body radii per beat. This is due to the fact that even if the beat is symmetric but the right-hand flagellum is closer than the left-hand flagellum to the boundary in this position. This closeness of flagellum to the boundary causes non-symmetric thrust and moves the body at an angle to the vertical with rotation, inducing non-symmetric flow.

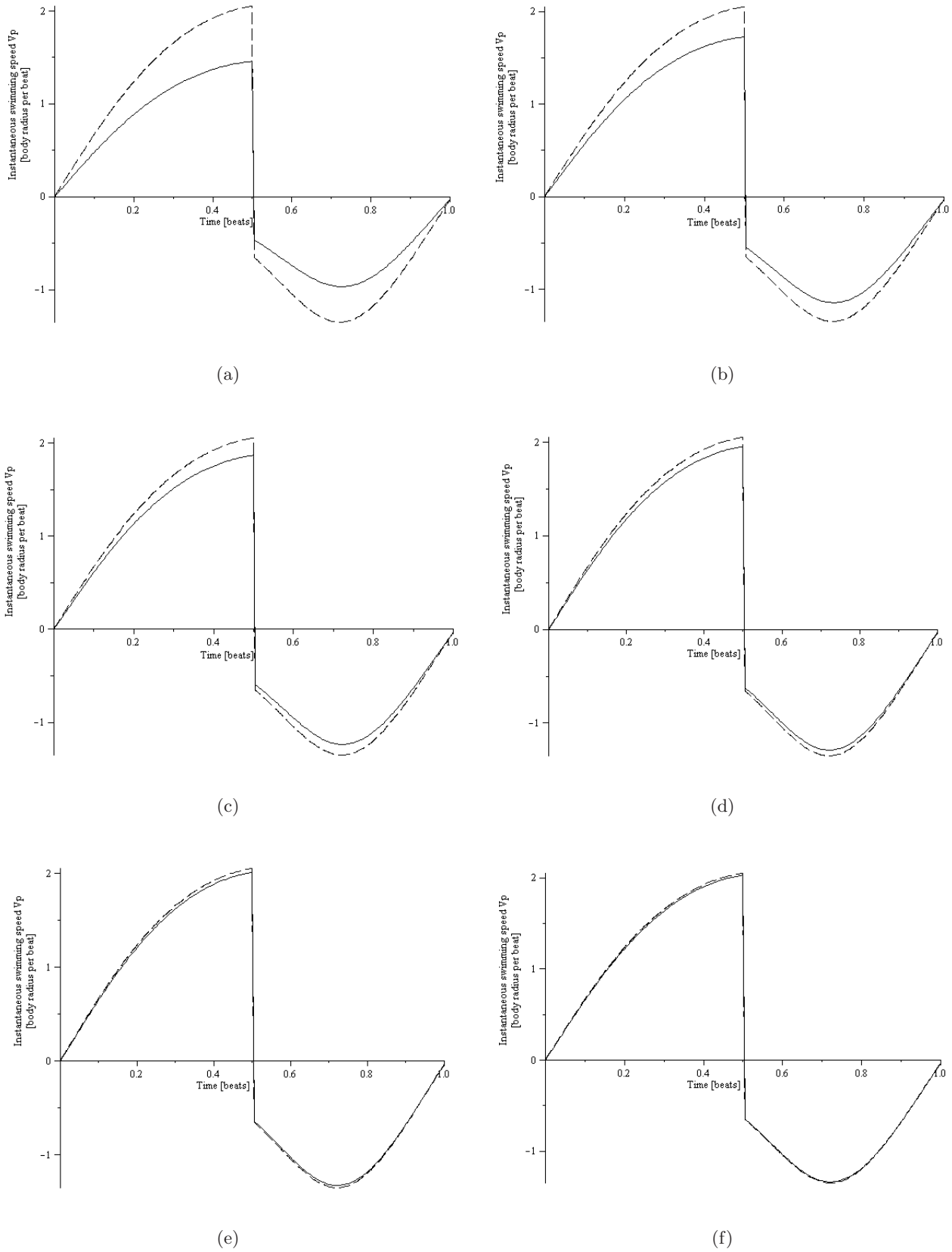
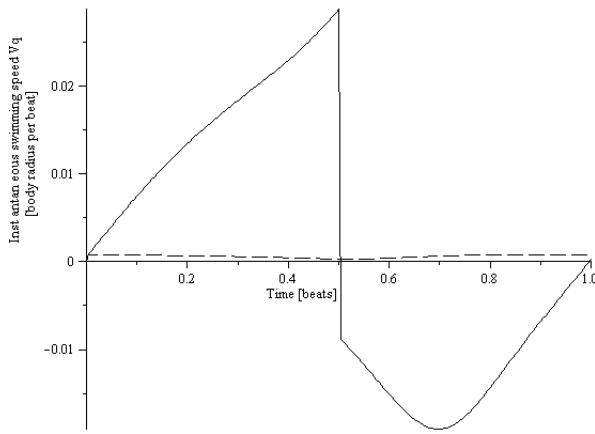
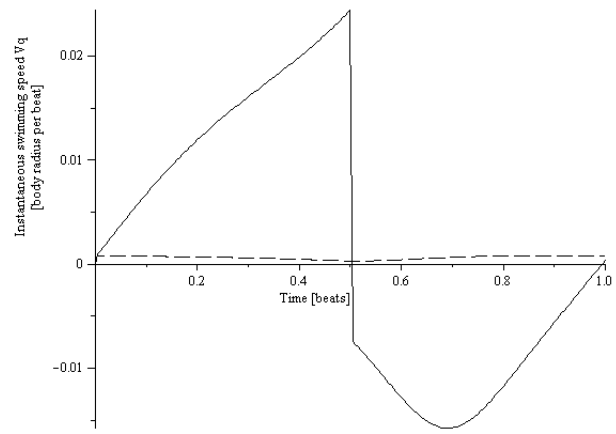


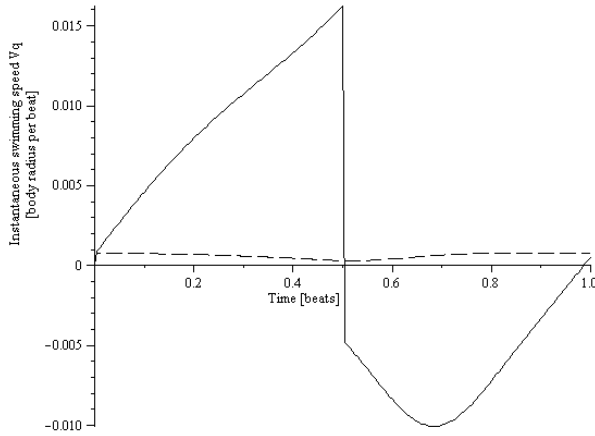
Figure 3.16: Variations of primary swimming speed v_p with the increase of h ((a)-(f), $h = 2, 5, 10, 20, 50, h = 100$) for one flagella beat, when cell swimming away at an angle $\theta = 40^\circ$ from the no-slip plane boundary. The dashed line represents the graph for the unbounded case whereas the solid line is for a bounded cell swimming.



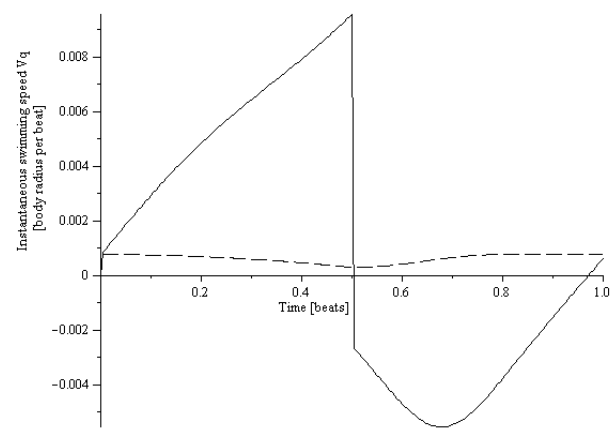
(a)



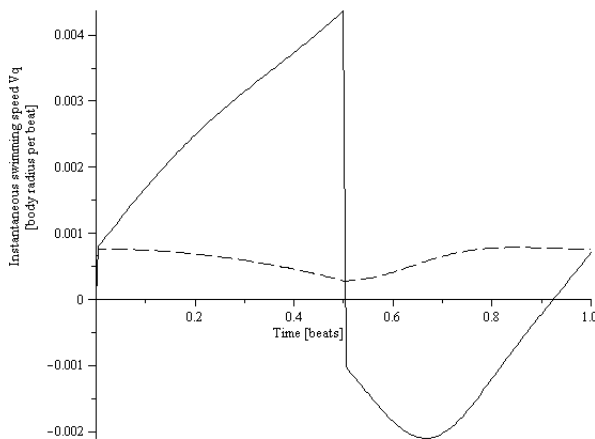
(b)



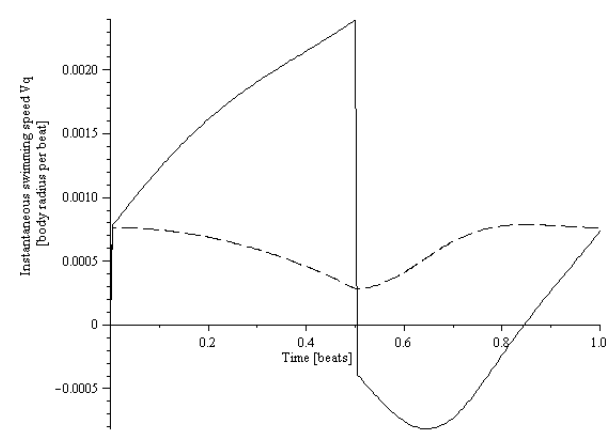
(c)



(d)

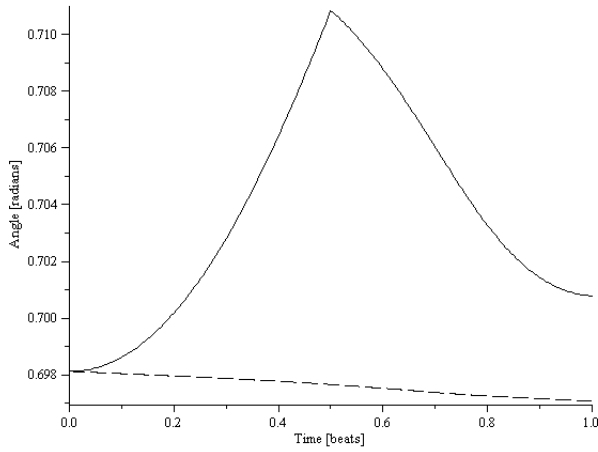


(e)

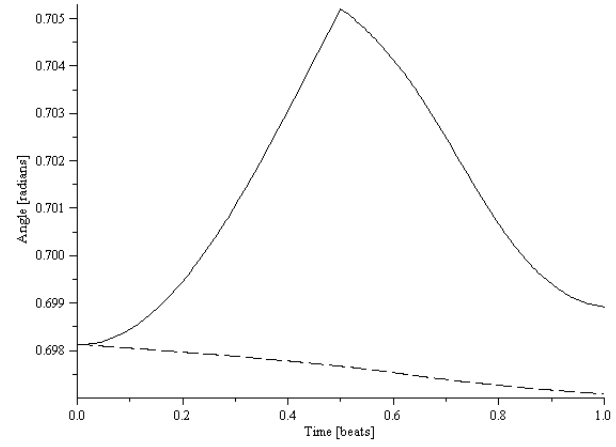


(f)

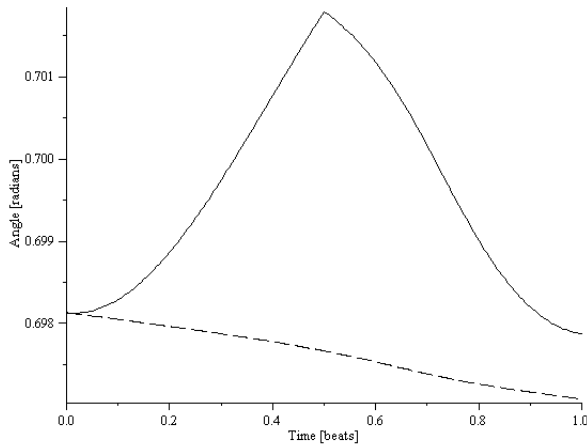
Figure 3.17: Variations of transverse swimming speed v_q with the increase of h ((a)-(f), $h = 2, 5, 10, 20, 50, h = 100$) for one flagella beat, when cell swimming away at an angle $\theta = 40^\circ$ from the no-slip plane boundary. The dashed line represents the graph for the unbounded case whereas the solid line is for a bounded cell swimming.



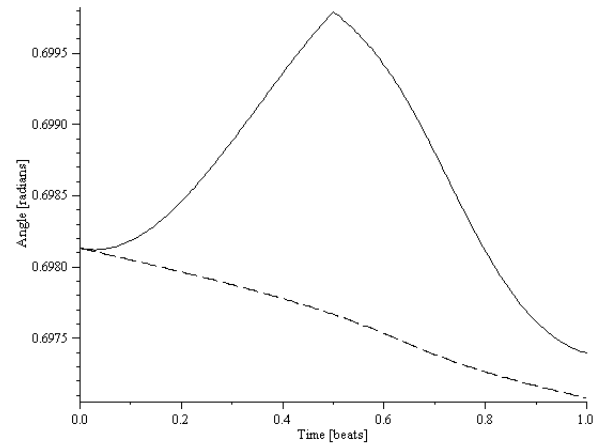
(a)



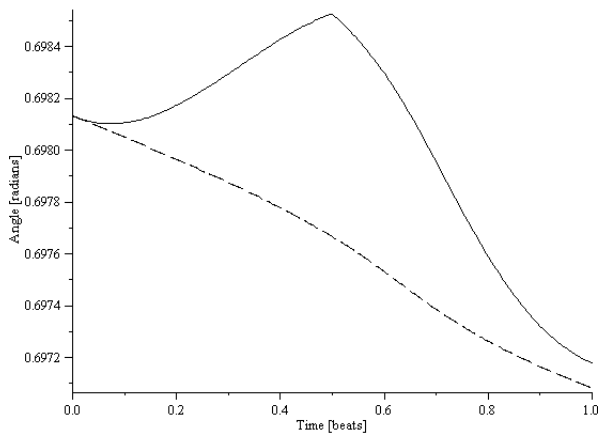
(b)



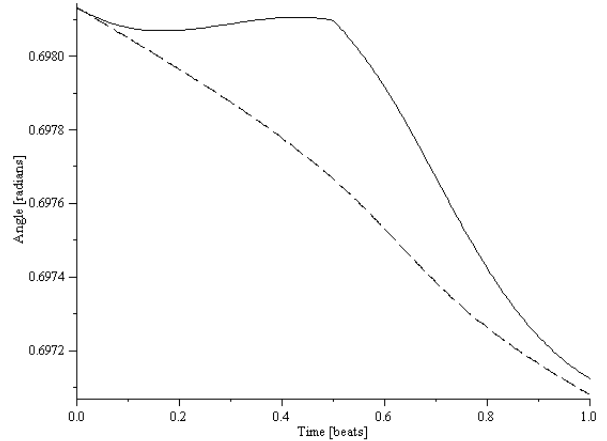
(c)



(d)



(e)



(f)

Figure 3.18: Variations of angle θ with the increase of h ((a)-(f), $h = 2, 5, 10, 20, 50, h = 100$) for one flagella beat, when cell swimming away at an angle $\theta = 40^\circ$ from the no-slip plane boundary. The dashed line represents the graph for the unbounded case whereas the solid line is for a bounded cell swimming.

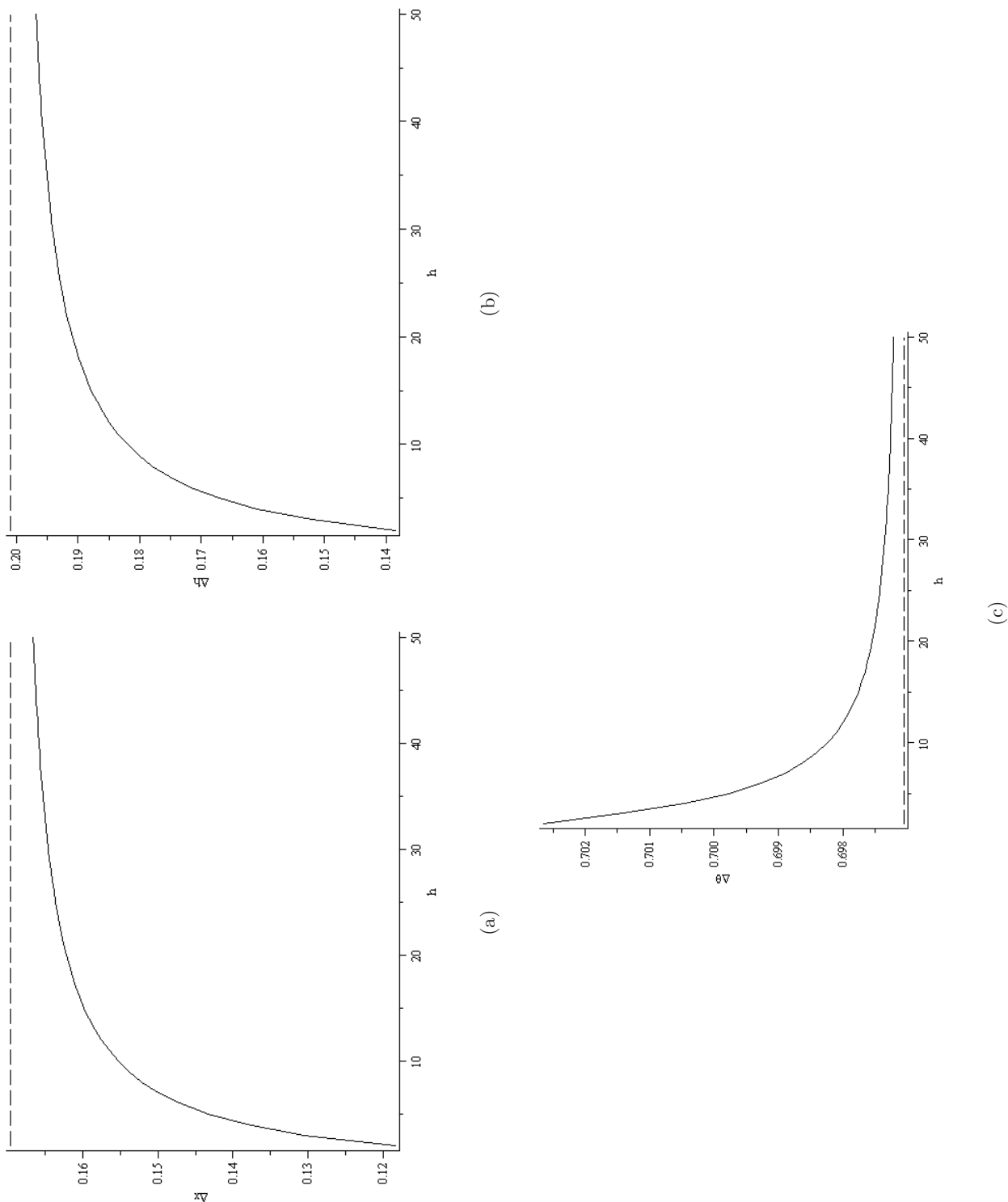


Figure 3.19: Variations of biflagellate cell's change in position and change in angle for one flagella beat with the increase of h , as cell swimming away at an angle of $\theta = 40^\circ$ from the boundary. The dashed line represents the graph for the unbounded case whereas solid line is for a bounded cell swimming towards the boundary.

Due to the geometry of the problem, the gravitational effect plays a significant role in the calculation of the transverse swimming velocity v_q and angular velocity $\dot{\theta}$. Here, we have observed some noticeable contribution for swimming velocity in the \mathbf{q} direction close to the boundary in comparison with the unbounded swimming. A typical value of 0.00177 body radii per beat for v_q was found when biflagellate swimming as a distance $h = 2$ from the plane boundary. Additionally, it is evident from the graphs in Figure 3.17, the values of v_q decays slowly even as after the cell moves away from the boundary, and converges to the unbounded swimming velocity at very far distances from the boundary. This shows that in this case the plane boundary has a significant effect on the swimming velocity v_q . On the other hand, angular velocity $\dot{\theta}$ is also effected enormously for one flagella beat in this setup due to the presence of the plane boundary, as shown in the graphs in Figure 3.18. Here, we have also noticed that at very close to the plane boundary the net change in the swimming cell's angle for one flagella beat is positive, i.e. 0.002743 body radii per beat at a distance $h = 2$, and at far from the plane boundary changes in angle became negative, i.e. -0.00101 per beat at a distance $h = 100$ from the plane boundary, for one flagella beat. This is consistent with the change in angle for an unbounded swimming cell for one flagella beat. The transition from positive change in angle for one flagella beat into negative change is observed again to slowly as the cell swims away from the plane boundary in this particular geometry, as shown in the graphs in Figure 3.18.

3.5.4 Biflagellate swimming parallel to the plane boundary

An important aspect of the swimming close to the boundary is to investigate the biflagellate cell swimming parallel to the no-slip plane boundary. As most of our laboratory experimental studies required investigation of cell suspensions in micro slides, thin tubes, or petri dishes, this involves cells mostly swimming parallel to the boundary. Here, for the ease of calculations, we have used a plane boundary which is stationary and lies at a distance h from the centre of the biflagellate cell body as shown in the Figure 3.20.

The position vector of an element of flagellum from the centre of the image cell body in generalized form again can be written as

$$\begin{aligned}\mathbf{R}^S(s, t) &= [b \sin \theta + (s - b) \sin(\theta + \chi)] \mathbf{i} + [2h + b \cos \theta + (s - b) \cos(\theta + \chi)] \mathbf{k}, \\ \mathbf{R}^F(s, t) &= [b \sin \chi + 2h \sin(\chi + \theta)] \mathbf{n} + [(s - b) + b \cos \chi + 2h \cos(\chi + \theta)] \mathbf{t},\end{aligned}$$

whereas the velocity of the any point of the flagellum as defined earlier in flagella coordi-

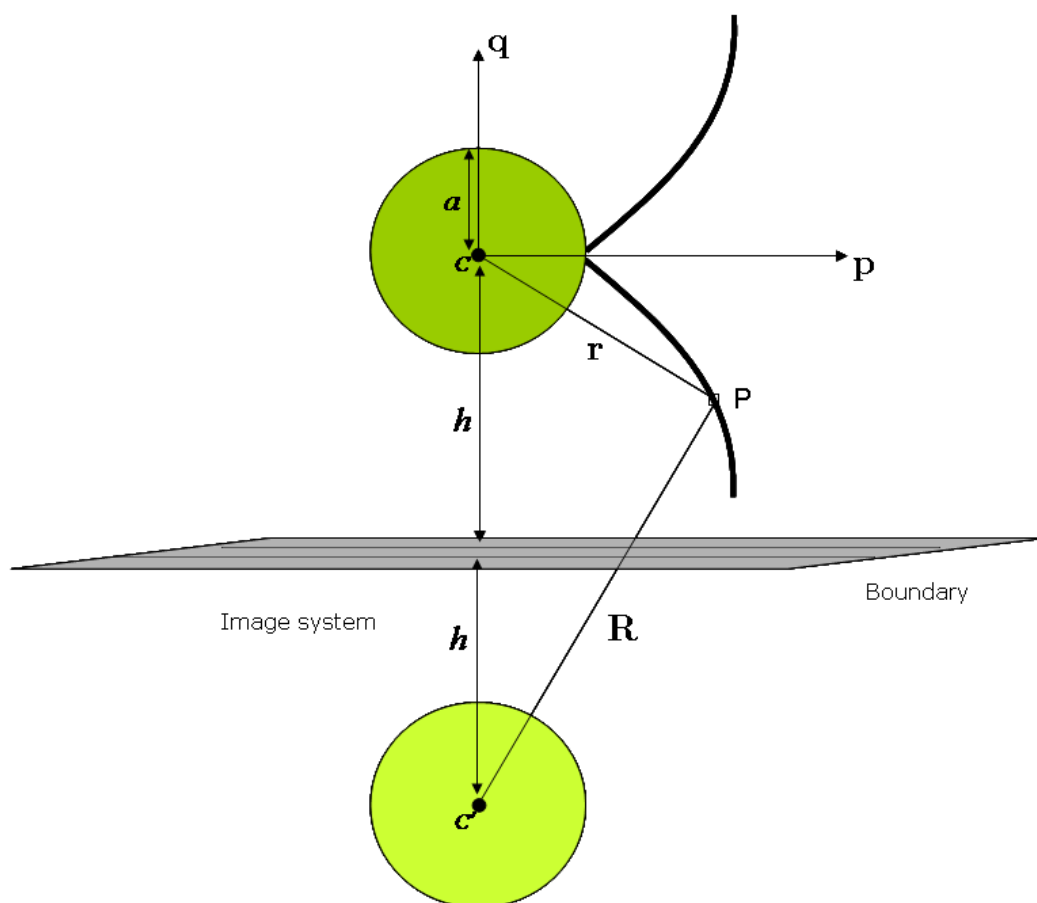


Figure 3.20: Swimming of biflagellate cell parallel to the stationary no-slip plane boundary, where h is the distance of plane boundary from the centre of the cell body, r and R are the position vectors at an element of flagellum from the centre of the sphere and image sphere, respectively.

nates system is

$$\dot{\mathbf{r}} = [w(\cos \chi - 1)] \mathbf{t} + [w \sin \chi - (s - wt)\dot{\chi}] \mathbf{n}.$$

Now to investigate the biflagellate swimming parallel to the plane boundary we substitute $\theta = 90^\circ$ in the generalized position vector as shown in the Figure 3.20. Using the force-torque balance equations for the general uniplanar locomotion of the cell swimming in the vicinity of the no-slip plane boundary, we have derived the equations for components of the swimming velocity v_p , v_q and angular velocity $\dot{\theta}$ in equations (3.64), (3.65) and (3.66). Thus using these equations and our generalized maple code we found the results for the biflagellate swimming velocity and angular velocity for one flagella beat. As swimming parallel to plane boundary is the most interesting case due to the geometry of the problem of our analysis of biflagellate swimming close to the plane boundary, so we investigate a few extra aspects of the biflagellate swimming.

To investigate the contribution of the Faxen's correction terms for the cell body translational and rotational motion defined in equations (3.28) and (3.29), we have calculated the components of swimming velocity and angular velocity without the Faxen's corrections and analyze the difference with results including them. Additionally, we also try to explore the effects of gravitational torques upon the biflagellate swimming near the plane boundary. For this purpose we have calculated the biflagellate swimming velocity and angular velocity using our Maple code and equations (3.70) to (3.72) derived earlier, which are without including the gravity and Faxen's correction terms. Finally, in order to investigate the contribution of flagella on the biflagellate cell swimming parallel to the plane boundary, we compute the swimming velocity and angular velocity of the cell without the flagella contribution using the equations (3.77) to (3.79) and our Maple code. The difference of the two results, one with the flagellar and other without the flagellar contribution, will reveal the desired information. The detailed graphs for the results of the above discussed aspects of the biflagellate swimming parallel to the no-slip plane boundary are shown in Figures 3.21 to 3.23.

The graphs in Figure 3.21 indicate that the swimming velocity in the primary direction v_p is regressed very close to the boundary and gradually increases as the biflagellate swims at a large distance from the plane boundary. A typical value of 0.1440 body radii per beat was found whereas without Faxen contribution we obtain 0.1677 body radii per beat at a distance $h = 2$ from the plane boundary was recorded when cell swimming parallel to the plane boundary. The swimming speed v_p without the gravitational contribution was found

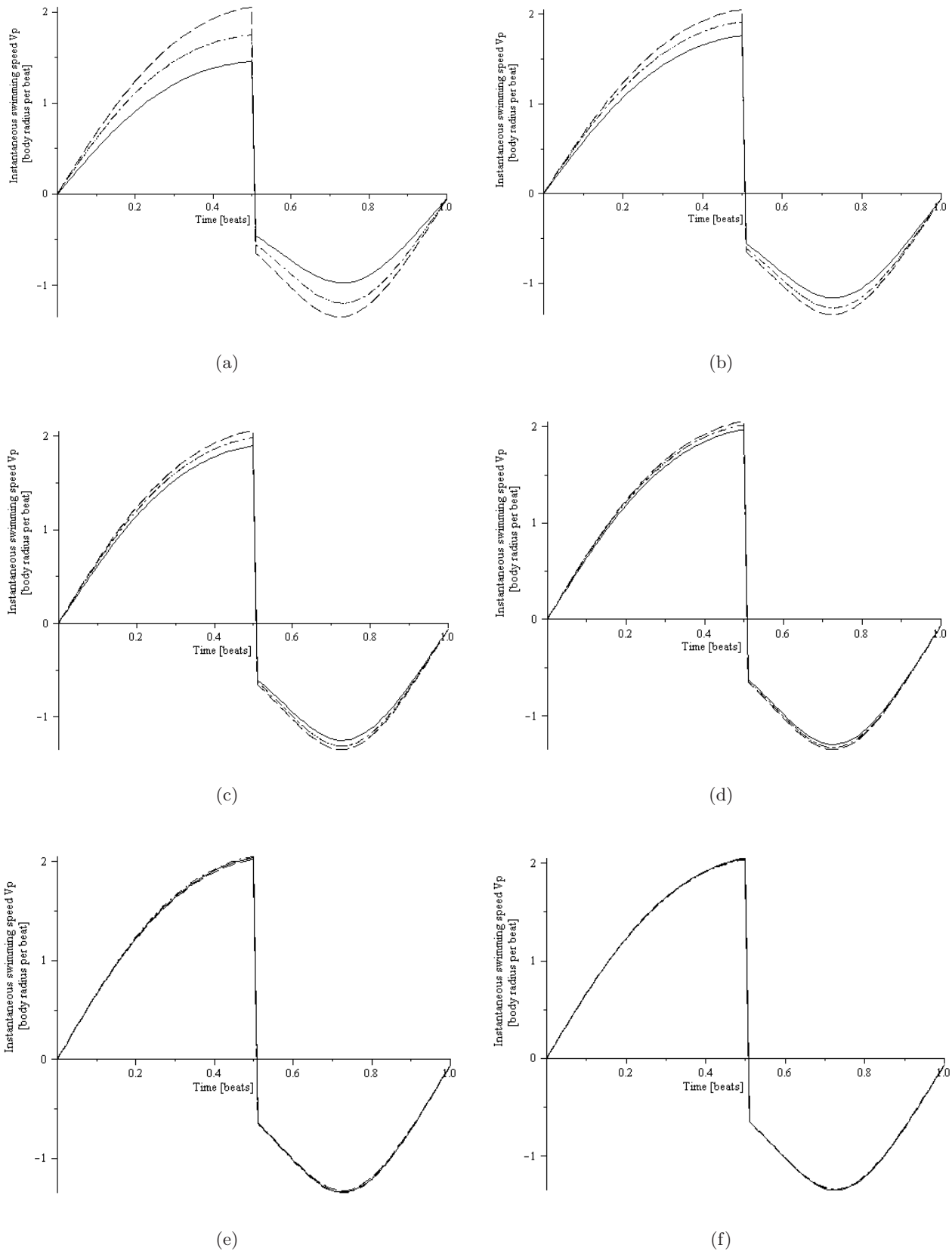


Figure 3.21: Variations of primary swimming speed v_p with the increase of h ((a)-(f), $h = 2, 5, 10, 20, 50, h = 100$) for one flagellar beat, when the cell is swimming parallel to the no-slip plane boundary. The dashed line represents the graph for unbounded case, dotted line for without Faxen's correction terms, dashdot line for without Faxen's correction and gravity contribution and solid line for bounded cell swimming.

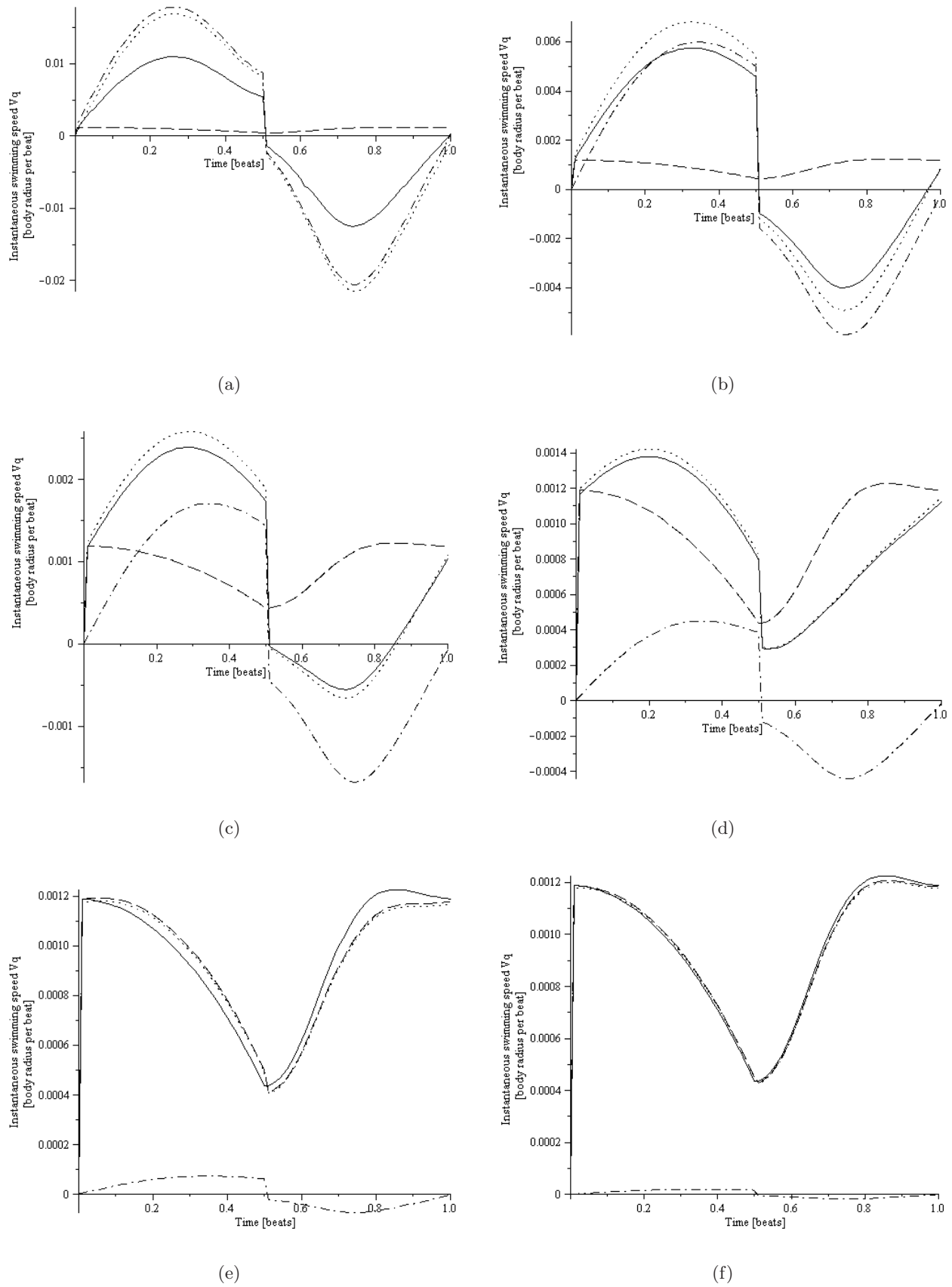


Figure 3.22: Variations of transverse swimming speed v_q with the increase of h ((a)-(f), $h = 2, 5, 10, 20, 50, h = 100$) for one flagellar beat, when the cell is swimming parallel to the no-slip plane boundary. The dashed line represents the graph for unbounded case, dotted line for without Faxen's correction terms, dashdot line for without Faxen's correction and gravity contribution and solid line for bounded cell swimming.

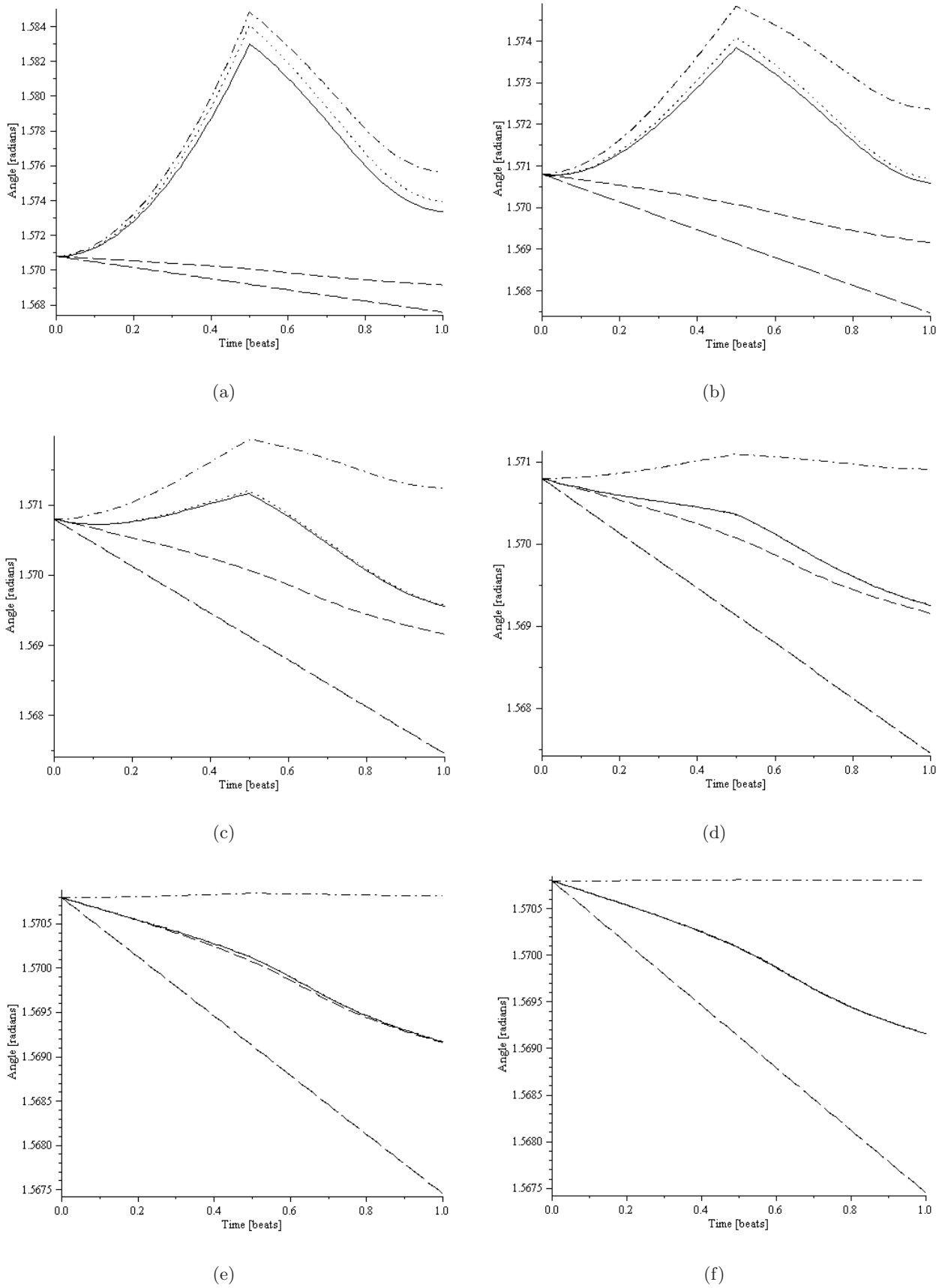


Figure 3.23: Variations of change in angle θ of biflagellate cell for one flagellar beat with the increase of h ((a)-(f), $h = 2, 5, 10, 20, 50, h = 100$), when the cell is swimming parallel to the boundary. The dashed line represents the graph for unbounded case, dotted line for without Faxen's correction terms, dashdot line for without Faxen's correction and gravity contribution, longdashed line for without flagella and solid line for bounded cell swimming.

to be exactly the same, which means that primary swimming speed does not depend on gravitational torque in general.

For the transverse swimming velocity v_q we have observed some noticeable contribution close to the boundary when the cell is swimming parallel to the plane boundary. The swimming velocity v_q increases by excluding the Faxen's correction terms whereas we found a decrease in v_q values while ignoring the gravity contributions when the biflagellate swims parallel to the plane boundary as shown in the graphs in Figure 3.22. This means that drift in the \mathbf{q} direction depends upon the gravitational torque, which may be due to the centre-of-gravity offset from the geometric centre or asymmetric distribution of the biflagellate cell contents.

Now the most important aspect of the biflagellate's swimming parallel to the plane boundary is to investigate the change in the angle during the flagella beat. This will provide the right estimates for the effective centre-of-gravity offset, cell eccentricity and gyrotactic reorientation time for one flagella beat. The results for the variations of angle θ for one flagella beat when biflagellate swimming parallel to the plane boundary are shown in graphs in Figure 3.23. It is clear from these graphs that the net change in swimming angle θ is positive very close to the plane boundary at $h = 2$ and as the biflagellate cell moves away or at a distance $h > 2$, we found the net change in angle θ to be negative. Far away from the plane boundary the value of net change in angle θ approaches the value for unbounded swimming of biflagellate cell, as clear from the Figure 3.24. It is also clear from the results that excluding the Faxen's correction causes some changes in the angular velocity close to the boundary but as the cell moves far away from boundary the results converge to those with Faxen's correction term results. On the other hand, in the absence of gravity torques, we have recorded some noticeable pattern in the change in swimming angle for one flagella beat. We have noticed the positive net change in angle close to the plane boundary, gradually goes to zero far away from the plane boundary as shown in the graphs in Figure 3.23. Since the biflagellate generally is bottom heavy, so we can expect the dependence of the angular velocity on the gravitational torques and conclude that in the absence of gravitational torques the angular velocity of biflagellate is zero far from the no-slip plane boundary as expected.

In order to investigate the contribution of the flagella while swimming parallel to the plane boundary we have computed the results for the angular velocity without the inclusion of the flagella. The result for the case of bounded biflagellate swimming after one flagella

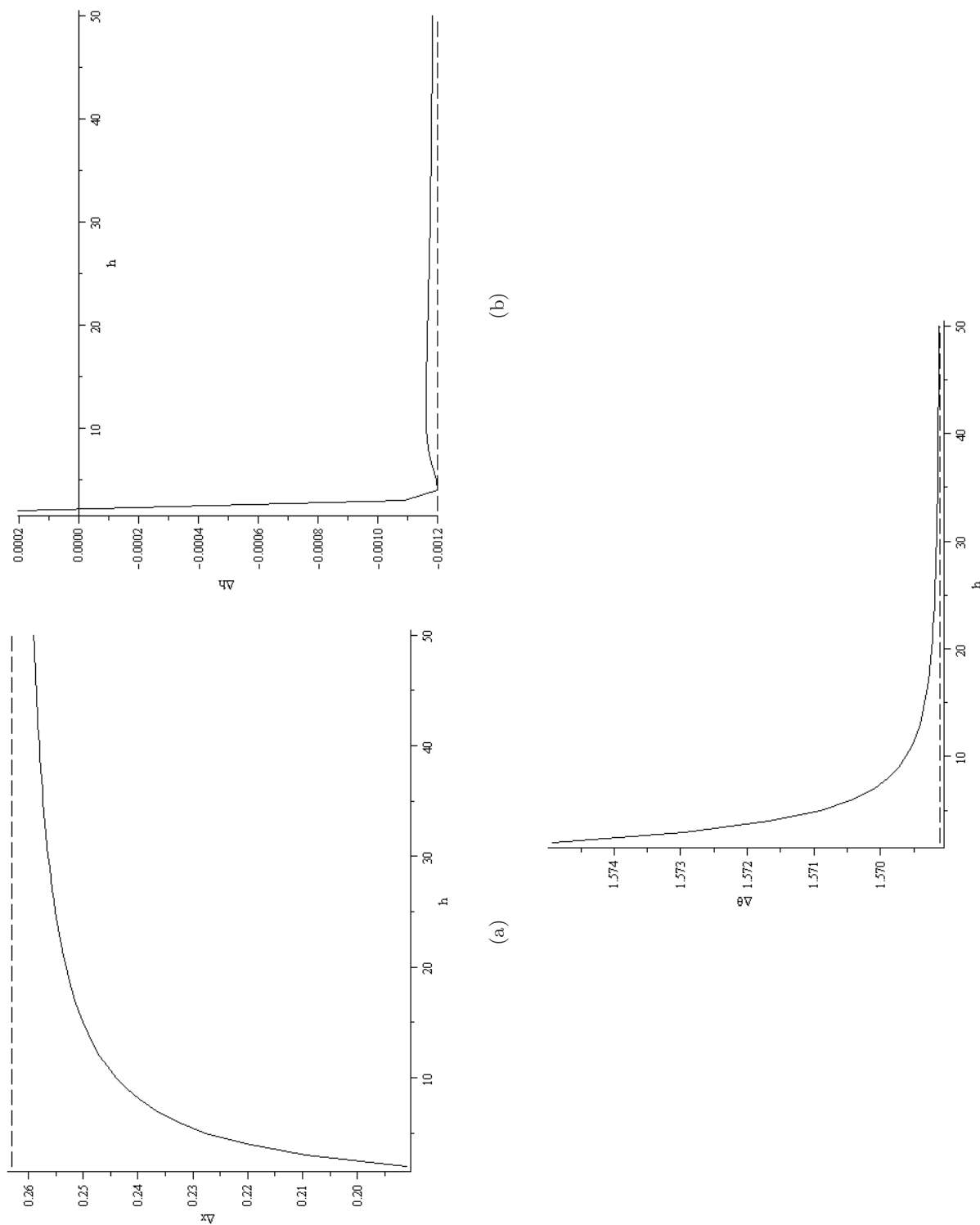


Figure 3.24: Variations of position and angle with the increase of h as the cell is swimming parallel to the no-slip plane boundary. The dashed line represents the graph for unbounded case whereas solid line for bounded cell swimming parallel to the boundary.

beat close to the boundary at $h = 2$ implies the change in angle from $\theta = 90^\circ$ to $\theta = 90.15^\circ$ whereas we have recorded the change of $\theta = 90^\circ$ to $\theta = 89.81^\circ$ for the case of biflagellate swimming without the contribution of flagella. This implies that angular velocity increases close to the boundary due to the right-hand flagellum facing the plane boundary within the fluid, whereas without flagella angular velocity decreases close to the boundary. On the other hand at far from the plane boundary $h = 100$ we have recorded the net change in angle of biflagellate cell in the presence of plane boundary as from $\theta = 90^\circ$ to $\theta = 89.91^\circ$ which is consistent with the change for unbounded swimming and has the same sign of $\Delta\theta$ as for without the flagella contribution case where θ changes from $\theta = 90^\circ$ to $\theta = 89.81^\circ$. This clearly shows that the inclusion of the beating flagella has a significant contribution for the calculation of the angular velocity for the case of biflagellate swimming in the vicinity of a plane boundary.

3.6 Conclusion

After successfully investigating biflagellate cells swimming in an unbounded domain using the generalized method and our Maple code discussed in chapter 2, we have extended the idea to apply to the more complex and practical situation of biflagellate swimming in the vicinity of a stationary no-slip plane boundary. In order to satisfy the no-slip plane boundary conditions we have added the contribution of the translational and rotating image cell body, as derived for a sphere by Blake and Chwang [16]. Now, again using the Resistive Force Theory (RFT) developed by Gray and Hancock [51] and employing Lighthill's resistance coefficients [95], we analytically model the problem following the same procedure discussed in chapter 2. For the calculation of results we implemented the problem in Maple and developed code to avoid cumbersome and laborious calculations.

In order to understand the bounded biflagellate swimming in detail, we have modelled different possible positions of the cell swimming in the vicinity of the no-slip plane boundary. In the first part, we have discussed the simple situations of a biflagellate swimming upwards away and towards a no-slip plane boundary. Here, we have noticed a regressed primary swimming speed v_p for both cases close to the boundary in comparison with the unbounded swimming speed for one flagella beat. The swimming speed in the transverse direction v_q and angular velocity $\dot{\theta}$ are equal to zero.

In the second part, we have modelled the general case of the biflagellate swimming

in the vicinity of a no-slip plane boundary. Here, we have calculated the results for the biflagellate swimming at an angle of $\theta = 40^\circ$ away from the stationary plane boundary. The primary swimming velocity results were found without any substantial change in the values and patterns from the previous case. Due to the geometry of the problem and contribution of the gravitational torques we have observed some non-zero contributions for v_q and $\dot{\theta}$ close to the plane boundary.

Finally, in the last section we have analyzed the biflagellate swimming parallel to the no-slip plane boundary, which is the most important situation in the context of laboratory experimental work. Here again we have observed a regressed swimming speed v_p close to the boundary as compared to the unbounded biflagellate swimming, and far from the boundary the two cases coincide. Due to the position of the cell the right-hand flagellum beats closer to the boundary than the left-hand flagellum and with the gravitational torques constitutes some non-zero components of the swimming velocity v_q and angular velocity $\dot{\theta}$. These components tend to the values of unbounded swimming case far from the plane boundary. Additionally, we have investigated the contributions of Faxen's correction terms by calculations of excluding them, and found higher values of the components of the velocity and angular velocity without the Faxen's correction terms. To analyze the effects of the gravitational torque, we have computed the results without incorporating them and found again higher values of the velocity and angular velocity close to the plane boundary. The values of velocity components approach the values for the unbounded swimming velocity components whereas angular velocity tends to zero far from the plane boundary.

Last but not least, we investigate the contribution of the flagella in the swimming of the biflagellate swimming parallel to the plane boundary by excluding the flagella and computing the velocity and angular velocity. Here, we have found higher values of the net change in the angle of the biflagellate without the flagella for one flagella beat near the plane boundary. This indicates that by including the flagella we will have lower value of the angular velocity in the vicinity of the plane boundary. This could modify the existing continuum model of Pedley and Kessler [114], which does not incorporate the flagellar contributions. It will also assist to modify the values of the centre-of-gravity offset, cell eccentricity, and gyrotactic reorientation time. As a first step this analysis gives some insight to understand the interaction phenomena of biflagellate with the wall or other geometries which can be extended to interaction with two or more biflagellates. This analysis will help to better understand and analyze bioconvection phenomena, suspension

behavior and may improve the efficiency and designs of hydrogen production and alga photo bio-reactors for biodiesel production accordingly.

The main results from this chapter are that the swimming speed of the biflagellated cell swimming towards or away from the no-slip stationary plane boundary are increasing or decreasing respectively. For the case of swimming parallel to the stationary no-slip plane boundary the cells are reoriented to swim away from the plane boundary.

Chapter 4

Experimental analysis of sheared bioconvection in a horizontal cylindrical tube

4.1 Synopsis

In this chapter, we have investigated the quantitative analysis of bioconvection patterns in a long horizontal tube. Aggregations of populations of swimming micro-organism in suspensions biased by environmental cues, are subject to instabilities generates interesting bioconvection patterns. To date, quantitative experimental studies of pattern formation experiments involved mostly in petri dishes by Bess and Hill [7], Czirók *et al.* [37] and Williams [147]. Here we have performed experiments to quantitatively explore the onset and long-time bioconvection of suspensions of biflagellate green algae *Chlamydomonas augustae* in long horizontal tubes. First we described the full details of the experimental procedures followed by an explanation of the image analysis techniques employed to collect the useful data. Initial pattern wavelength λ_i and long time onset patterns wavelength λ_f , by changing the concentration of the suspension using dilution procedure and by changing the horizontal tubes with different tube diameter was explored with no imposed flow. Additionally, changes in the wavelength was recorded and analyze for the weak poiseuille flow in the tube by varying the cell concentration and the flow rate using syringe pump. Initially vertical plumes of cells were observed to bend in the direction of the flow and progressively fragment into piecewise linear diagonal plumes for comparatively

increased shear rates. The nature of the patterns dynamics qualitatively and average angle measurement found nearly unchanged with the variations of concentrations. It is also observed that even at high imposed flow rates, bioconvection is not completely suppressed and perturbs the flow field. The main application of our investigations involve cell transport in tubular geometries used mostly in alga photo bioreactors. Literature survey reveals that this is the pioneering attempt to quantitatively investigate the changes in wavelength of bioconvection patterns by changing the concentration, tube diameter and varying flow rate in a long horizontal cylindrical tubes.

4.2 Introduction

This chapter includes the analysis of the experimental work which we have carried out in our departmental biofluids laboratory. Here we mostly focused our attention to the experiments related to the bioconvection phenomena of swimming micro-organism, the green algae in a thin long horizontal cylindrical tubes. The aim of this study is to endeavor quantify observations of pattern formation in thin horizontal tubes by the swimming micro-organism in a rational and reproducible manner. Micro-organisms are mostly motile and bias their motion (taxis) in response to environmental cues to seek conducive environment for their living. Many species of bacteria, (e.g. *Escherichia coli*) biasing their locomotion towards nutrients and away from toxic chemicals, termed as chemotactic (see Berg [12]). Green algae species *Chlamydomonas* and *Dunaliella* on average swim upward due to centre-of-gravity offset from the geometric centre to find the water surfaces named as gravitaxis. In addition to gravitaxis these species with in the fluid flow also display gyrotaxis which is due to the biasing in the swimming direction resulting from the balance of viscous and gravitational torques acting on them. A combination of these above defined taxis often generates spatially localized structures and patterns, such as bioconvection patterns observed in suspensions of *Chlamydomonas sp.* due to combination of gravitaxis and gyrotaxis (see Pedley and Kessler [114], Hill and Pedley [63]). These patterns formation occurs due to the instabilities within the suspensions of cell which are denser than the surrounding fluid (5% for *Chlamydomonas sp.*). These patterns appear as visually striking alterations of dark (high cell concentration) and light (low cell concentration) spots or strips. In this chapter we will explain in detail of the methods and techniques we have established for measuring the attributes of these patterns formed in suspensions

of green algae in thin horizontal tubes. The qualitative study of pattern formation have been reported earlier by the authors as Wager [144], Loeffler and Mefferd [98], Wille and Ehert [146], Kessler [80] and Durham *et al* [38].

The important development in the study of bioconvection was carried out by Bees and Hill [7], who conducted the set of 39 controlled experiments aimed at quantitatively cataloguing aspects of the bioconvection patterns of green algae *Chlamydomonas nivalis* in a petri dishes. The images of bioconvection patterns were captured for every 10 seconds and long time patterns were also captured after 5-10 minutes. Later images were analyzed in Interactive Data Language (IDL) using Fast Fourier Transform (FFT) to find a distribution of wavenumbers of different Fourier densities. Using double Gaussian curve was fitted to the Fourier spectra and finally extracted the most dominant wavenumber. They found initial instability and final pattern wavelength as a function of cell concentration of the suspension and depth of the petri dish and finally they compared the initial wavelength with the mathematical model predictions by their own model [9]. Later, Cziráková *et al.* [37] used the same procedure to investigate trends in initial pattern wavelength as a function of cell concentration and depth for the case of suspension of aerotactic bacteria *Bacillus subtilis*, by employing double logarithmic curve fit for the Fourier spectra. The same techniques were employed for studying chemoconvection pattern formation in the Methylene-Blue-Glucose system by Pons *et al.* [119]. Recently Williams in her PhD thesis [147] quantitatively investigated the changes in initial wavelength of bioconvection pattern as a function of light intensity and changes in concentration. She also formulated an automated mixing regime and using the same technique devised by Bees and Hill [7] found similarities while comparing her experimental results with the theoretical predictions.

The purpose of this study is to experimentally investigate bioconvection in a horizontal tube under conditions of no imposed flow and also in the presence of weak shear. Recently Lewis [93] showed that gyrotactic algae in a homogenous and isotropic turbulent flow field maintain their bias and only perturb the effective value of diffusivity of cell concentration due to turbulence. Literature survey reveals that this is the first study of bioconvection under shear, and first quantitative study of bioconvection in horizontal tubes. The only other experimental investigations of bioconvection in horizontal tubes were carried out by Wager [144] in which he placed the concentrated suspension of the alga *Euglena viridis* in tubes and discussed the aggregations of cells (pattern formation). Here we aim to inves-

tigate the transport of algae in a least perturb environment keeping in view of bioreactor geometry and following the motivation of Bees and Croze [11], and with a spirit of understanding the coupled cell and fluid dynamics in bioreactors. We investigated the effects of concentration and tube diameter on the initial and final pattern wavelength of the instability, formed during pattern formation of gravitactic *C. augustae* swimming cells suspension in the horizontal thin cylindrical long tube for the case of no flow experiments. However, for the case of flow experiments changes in the final pattern wavelength by varying the cell concentration and flow rate were investigated. Here again we have employed the same technique for image analysis used by Bees and Hill [7] and used the logarithmic curve fit for Fourier spectra as used by Cziráková *et al.* [37]. The first instability that occurs before any higher order, non-linear forms is most important for analysis as this is the only wavelength that can be compared with those obtained from the linear analysis of the mathematical models. We have repeated the experimental runs using the same cells suspension with different cell concentrations and three different tubes of variable diameter, which ensures the statistical measures of the standard deviation and standard error of the mean for cells under the same experimental parameters.

4.3 Breeding and concentration of green algae cells

4.3.1 Culturing of cells

To analyze the bioconvection phenomena of green algae, we first required to breed a homogeneous culture of cells which are fresh and in a actively motile phase of development. This needs to be taken care as these organisms exhibits numerous forms depending upon different environmental and laboratory conditions. Here we have carried out experiments on motile green alga species called *Chlamydomonas augustae*, strain CCAP (Culture Collection of Algae and Protozoa; 11/51B), delivered by Sciento, Manchester UK.

For culturing of algae there are different types of media researchers have used like Soil water medium, Fish meal media, Bolds basal medium (BBM) and Tri Acetate Phosphorous (TAP) medium. Out of these we mostly used BBM and recently modified (3N-BBM) Bolds basal medium with three fold Nitrogen in our lab because these are found much clearer, match the natural environmental conditions and are relatively easy to prepare in a standard laboratory conditions, whilst being easily adaptable (Bold and Wynne [18]). We used this medium in large Erlenmeyer or conical flasks of 1000ml or 500ml which not only even out



Figure 4.1: Cultures of green algae *Chlamydomonas augustae* in conical flasks.

the light source but also allow moderate growth of the cells. In addition to that, the long neck shape of these flasks is useful for the cell concentration process as defined in section 4.3.2. Later, the flasks were sealed with a cotton wool bung which was inserted within the long neck of the flask and covered with aluminium foil to avoid bacteria and any other contamination. We can stimulate the growth and motility of the cells by the addition of vitamin B12 into the medium, but this sometimes caused abnormal growth of cells when used repeatedly over a few months.

In general, we used modified 3N-BBM and cells were subcultured every four weeks. For experiments purpose we required fresh, healthy and active cultures of green algae of three to four weeks old. Since the cells are phototropic, so we illuminate the cultures using eight strip cool white, fluorescent tubes which give a maximum light intensity of 1900 lux measured just above the culture flask using a digital light meter. The lights are adjusted on a cycle of sixteen hours of light followed by eight hours of darkness. The light cycle was set to breed cells which are available in correct motile phase and do not effect their own diurnal cycles of breeding, dividing and feeding. Like human beings these cells do not behave actively during the first few hours of the light cycle and later at the middle of

No.	Stocks with symbol	Quantity per 500 ml	Final medium of 1 Liter
1.	Sodium Nitrate - $NaNO_3$	12.5 g	30.0 ml
2.	Magnesium Sulphate - $MgSO_4$	3.75 g	10.0 ml
3.	Sodium Chloride - $NaCl$	1.25 g	10.0 ml
4.	Potassium Phosphate dibasic - K_2HPO_4	3.75 g	10.0 ml
5.	Potassium dihydrogen Orthophosphate - KH_2PO_4	8.75 g	10.0 ml
6.	Calcium Chloride dihydrate - $CaCl_2 \cdot 2H_2O$	1.25 g	10.0 ml
7.	Trace elements solutions (see Table 4.2)	-	1.0 ml
8.	Boric Acid - H_3BO_3	5.7 g	1.0 ml
9.	Ethylenediaminetetraacetic acid - $EDTNa_2$ and Disodium salt dihydrate - KOH	25.0 g 15.5 g	1.0 ml
10.	Iron (II) Sulphate - $FeSO_4 \cdot 7H_2O$ and Concentrated Sulphuric acid - H_2SO_4	2.49 g 0.5 ml	1.0 ml

Table 4.1: Table of ingredients for 3N-BBM modified (nitrogen enriched Bold's basal medium; Schlösser 1997).

No.	Stocks with symbol	Quantity per 500 ml
a.	Zinc Sulphate - $ZnSO_4 \cdot 7H_2O$	4.41 g
b.	Manganese(II) Chloride - $MnCl_2 \cdot 4H_2O$	0.72 g
c.	Molybdenum trioxide - MoO_3	0.355 g
d.	Copper(II) Sulphate - $CuSO_4 \cdot 5H_2O$	0.785 g
e.	Cobalt(II) Nitrate - $Co(NO_3)_2 \cdot 6H_2O$	0.245 g

Table 4.2: Table of ingredients for Trace elements solutions used in 3N-BBM modified.

the day they behave best and swims effectively to generate most robust patterns, which is not always true. The cells stop dividing when the suspension is well mixed and breed maximum when the suspension is not agitated (see Thomson and Demets [141]).

Since cells are sensitive to sudden change of temperature, so we maintain the constant temperature ($24 \pm 2^\circ\text{C}$) within the laboratory during the process of culturing and breeding of the cells. To avoid contamination by bacteria and fungi all the laboratory equipment was washed with liquid soap and rinsed with distilled water. We sterilized the equipment and modified 3N-BBM recipe in flasks in an autoclave at 126°C for 10 minutes. Later, we left the sterilized, modified 3N-BBM flasks overnight to cool down to room temperature, then we did the mixing of modified 3N-BBM flasks with existing grown cultures flasks over a heat source using a sterile technique to avoid contamination. As contamination is irreversible in this case so we must ensure the cleanliness of the all required equipment used in the experiments.

4.3.2 Concentration of cells

Now after breeding and culturing we do the process of concentration of algae cells, which we require for our experiments to observe suitable bioconvection patterns. We have picked up the cultures of aged between two to four weeks for cells concentration procedure. Since *C. augustae* are negatively gravitactic or gyrotaxis which means they tend to swim upwards on average, this characteristic really facilitate us to concentrate them easily at the top of long neck of the same culture flask (see Kessler [80], Bees [6]). First we top up the conical flask with the culture from the other flask to fill up to the top of the neck and over that added some fresh media (to attract cells for nutrition). Secondly as we know cotton acts as a porous medium and cells can easily swim into, so we placed the sterilized piece of cotton wool at the top and cover the conical flask with the aluminium foil. The aluminium foil should not cover the long neck of the flask and acts as a lid of flask, because cells required light for swimming upward into cotton wool. The cells swim upward into the neck of flask and get stuck into the cotton wool and after three to five days when white cotton wool turns into green and clear fluid left within the rest of the flask, this indicates that concentrated suspension is ready at the top. This also ensures that the concentrated cells are healthy, motile and good swimmers at that stage. Here we avoid to keep this state for long time because cells will quickly run out of the nutrients and may get into non-motile state. Now the concentrated suspension can be extracted



(a) Initial stage of cells concentration procedure as initially no cells accumulation in white cotton wool bung held at the top of long neck of conical flask.



(b) Final stage of cells concentration procedure as the same conical flask after 4 days shows millions of cells trapped in cotton wool bung which turns green.

Figure 4.2: Snap shot of algae cells concentration procedure captured at our biofluids laboratory.

from the cotton wool held in long neck of the flask using Pasteur pipette (avoiding shear induced deflagellation) to either petri dish or any other container used for experiments. The initial and final stages of the cell concentration procedure are shown in the Figure 4.2.

4.3.3 Transfer of suspension of cells

After three to four days of concentration process we extracted the cells from the cotton held at the top neck of culture flasks using Pasteur pipette (avoiding shear induced deflagellation) gently, and transferred into clean new plastic bottle. The bottle was washed with distilled water before pouring in the suspension. Later, we mixed the suspension using magnetic stir mixer and measured the concentration. To record pattern formation, the suspension then transferred into horizontal tube held fixed using the controlled flow apparatus as mentioned earlier. To avoid sticking due to surfactant and chemicals used in apparatus material we first rinsed the apparatus with distilled water. The cylindrical glass tube washed with soap and rinsed with distilled water before the experiment as well. To minimize the sticking of cells for repeated run of experiments in glass tube we introduced double treatment of BSA (Bovine Serum Albumin) in our experiments, which limits adhesion in micro channels (see Weibel *et al.* [145]). First we have soaked the glass tube with 4.0% BSA with modified 3N-BBM medium over night, and secondly, we mixed 0.4% BSA in our suspension using magnetic stirrer before transferred into the tube for pattern formation. Repeated trial and experiments revealed that both of these procedures were not proved effective at this scale as it slightly changed the concentration of the suspension, and reduced the swimming speed which slightly suppressed the pattern as well. The decrease of the concentration by surface fouling was not significant on the experimental timescale (10 min). It is convincible that in the longer lasting experiments in the presence of flow, the flow itself helped prevent adhesion. Thus we finally dropped the idea of BSA treatment and stick to the distilled water treatment only to minimize the sticking of cells with the inner walls of the tube.

4.3.4 Measuring concentration of cells in suspension

After concentrating the suspension of green algae, we extracted it from flask and stored it in some container or clean plastic bottle. For our experiments a standard volume of cultures suspension of 30-40 mL was used unless otherwise stated. The cell concentration

was measured using spectrophotometer apparatus (WPA CO7500 spectrophotometer), which is an electronic device used for measuring the amount of light of a certain wavelength that can pass through the sample compared to a reference state, called as absorbance A . In our experiments, we mostly used the reference as 3.0 mL of modified 3N-BBM, and measured the absorbance of the concentrated cells only not the medium.

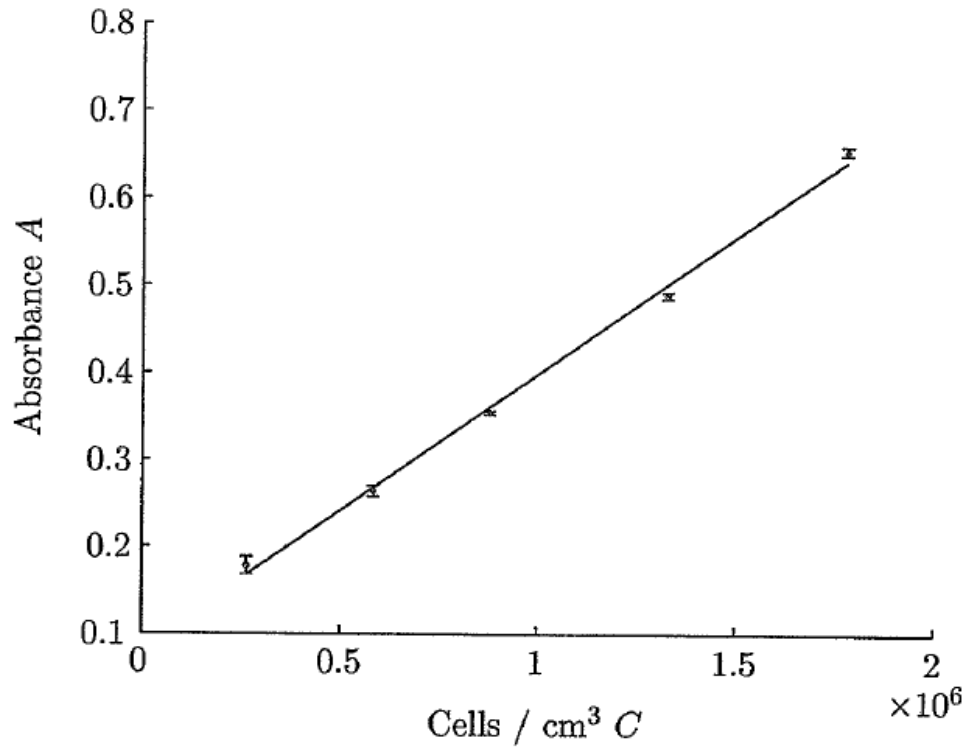


Figure 4.3: Calibration of A the absorbance measurement from the spectrophotometer readings with C cell concentration found using cell counting with hemocytometer reproduced from Williams [147].

The standard measuring concentration procedure involved first measuring the reference modified 3N-BBM of 3.0 mL in a cuvette using spectrophotometer. Later, we transferred the concentrated cells of 1.0 mL sample in another cuvette and diluted it with 2.0 mL of modified 3N-BBM, and mix it with the pipette before measuring the cell's concentration using spectrophotometer. For highly concentrated suspension we can dilute more with the modified 3N-BBM to get a reading that would be in the appropriate linear range of the spectrophotometer readings as shown in the graph in Figure 4.3. This process was repeated 4-5 times and the averaged measure of absorbance was then converted to a cell's

concentration of suspension using the relationship between absorbance and concentration from the hemocytometer as explained by Williams [147] i.e.

$$c = (3.187A - 0.2678) \times 10^6 \text{ cells cm}^{-3}. \quad (4.1)$$

The measurement of concentration process had to be completed before the start of the experiment and optionally can be done after the experiment for calibration. This process required culture to be removed from the suspension and due to dilution with modified 3N-BBM could not be suitable for use again for other experiments.

4.4 Environmental control and Methods

4.4.1 Light source control

As *C. augustae* cells are phototactic as well which means sensitive to light source (see Foster and Smyth [40]). They swim towards the light source and swim away from dark and high intensity light. Instead of using white light we used here low intensity BL1960 LED red light source (Advanced Illumination, Rochester, VT, USA) of wavelength of about 660 nm because these green algae do not respond phototactically (see Foster and Smyth [40]). We also made sure that all other lights in our lab switched off and even brightness of the computer monitors dimmed and directed in the opposite direction of the experiments apparatus. Additionally, our lab established at basement of the department and has no windows and even sunlight had no light effect on the experiments. Finally, we measured the light intensity using the digital light meter and ensure that the light intensity for the setup would not exceed 225 lux.

4.4.2 Mixing of suspension

In our experiments we have followed two different culture mixing protocols which we named as mixing outside the tube and mechanical mixing inside the tube. For the first case the mixing was performed with the magnetic stirrer after extraction of cells suspension from the concentrated flask as shown in Figure 4.2(b). The suspension was later poured into the tube. This ensures that cells are homogenously mixed when poured into the tube for recording of images of the bioconvection pattern formations in horizontal tubes.

On the other hand, the mechanical mixing inside the tube was indigenously developed procedure to mix the suspension homogenously even after pouring into the tube to record

multiple set of recordings. The evolution of this procedure involved different setups and we have tried different options like we have attached peristaltic pump with variable flow rate at one end of the tube, syringe at one end or both ends of the tube and many other setups to induce least shear prone homogenous mixing. All different setups and variable arrangements were have multiple issues and short comings like causing bubbles within the tube, sticking of cells with walls of tube, vibrations and violent shear. Finally after many trials, we have devised indigenous setup by attaching switch control to adjust air pressure at one end of the tube while on the other end we have attached flexible plastic tube of larger diameter with small container. Thus before pouring the suspension in the main tube we close the switch to stop the air to get in the tube and pour the suspension into the attached container then gently open the switch to get the suspension into the main glass tube. This will reduce the chances of bubble to establish into the suspension within the tube. For mixing we open the switch completely and pull the attached container gently up and then down, and repeat again then wait for few seconds than again pull up and down gently. This protocol worked better and ensure nearly homogenous mixing for repeated number of times.

Repeated experimental runs reveals that this indigenous mixing procedure resulted best for low and medium level cell suspension concentration whereas not very suitable for higher suspension concentration. This can be improved by more number of pulls up and down with rush which is not effective because of generation of violent shear which is not desired for these experiments. This mixing procedure also not suitable after two to three runs as repeated mixing caused shear which resulted in break away of flagella and sticking of cells with the walls of the tube.

4.4.3 Image recordings

Timelapse sequences of projected bioconvection patterns during our experiments were captured from side using a black and white CCD camera (Camtek CL-1014) and from above using an EOS digital camera (Canon SLR-350D) connected to frame grabber (Sensoray 611) controlled by customized SX11 C++ routines. To avoid any effects of vibrations on pattern formation we kept the experiment apparatus and adjoining PC on different work benches. For image recording we have used computer code written in C++ language in which we could control the frequency of image capture and the total number of images. Image recordings began at a specific time and images were taken every two seconds until

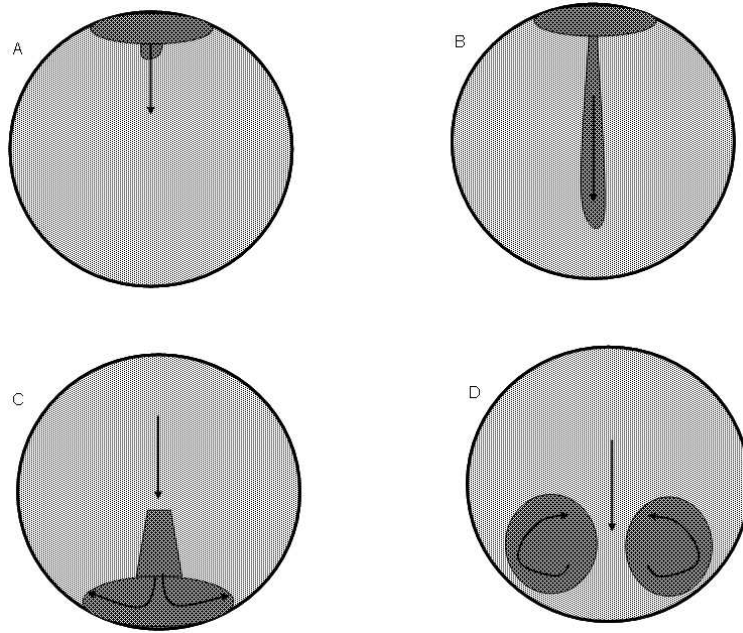


Figure 4.4: Illustration of the formation of the bioconvection pattern formation in a thin horizontal cylindrical tube as viewed from side.

the maximum number of images, typically 200 was reached. This arrangement of recordings can be altered by amending the computer code accordingly. The process of mixing in the tube or before pouring in the tube followed by image recordings is termed as a one experimental run. For different parameter values like diameter of the tube d , cell concentration c , n experimental runs were performed with the same cells, with approximately 50-60 seconds between each experimental run unless otherwise stated. However for the imposed flow experiments mixing was performed outside the tube before pouring in and images were recorded every second until 49 images for each flow rate. The process was repeated until we reached to obtain maximum flow rate typically $30\text{-}35\text{ ml h}^{-1}$ for different cell concentrations. All images recorded were 768×576 pixels.

4.4.4 Variation of cell concentration of suspension

During the experiments of the bioconvection pattern formation we varied the cell concentration and investigate the effect on the initial instability and final pattern wavelength. In all experiments we kept the lab conditions like temperature, light and tube diameter constant. we initially started with the maximum concentration, c_{max} , and conducted n experimental run. Later we took the suspension out of the tube and dilute it with the

Tube No.	Inner diameter (cm)	Outer diameter (cm)	length (cm)
tube A	1.1	1.35	30.0
tube B	0.8	1.03	28.5
tube C*	0.6	0.81	33.0
tube D	0.2	0.71	25.0

Table 4.3: Table of details of different cylindrical pyrex glass tubes used for bioconvection experiments whereas the tube C used is made of plastic material.

3N-BBM and measure the cell concentration using the spectrophotometer. Again we mix the suspension and poured into the tube and performed the n experimental run. This procedure was done without disturbing the tube and rest of apparatus, so that positioning and mixing conditions were identical for each concentration. Since our tube experiments required at least 30-40 ml of cell suspension for each experiment, which is well above than petri dish experiments. This minimum quantity of cell suspension required much more culture flasks for concentration process. So concentration limitations restricted us to carry out experiments involving suspensions with very high cell concentration.

4.4.5 Variation of tube diameter

As these experiments of pattern formation in horizontal long cylindrical tubes are one of the unique attempt so we have tried to investigate the effect of variation of tubes by using the cylindrical tubes of different diameters. Initially we have used four cylindrical tubes of different diameters, smallest with inner diameter of 0.25 cm and largest with inner diameter of 1.1 cm to analyze the bioconvection pattern formation. Repeated experiments revealed that nearly no pattern formation was observed in the smallest tube of inner diameter 0.25 cm and outer diameter 0.71 cm. This may be because of the effect of shear caused and close proximity of cylindrical boundary of the tube. Thus we performed detailed experiments on rest of three tubes i.e tube A, B made with pyrex glass and tube C made with plastic material excluding smallest glass tube D. For the case of imposed flow experiments we have used pyrex glass tube B of inner diameter 0.8 cm only. The details of the inner/outer diameters and length of tubes used are listed in Table 4.3.

4.4.6 Variation of Flow rate

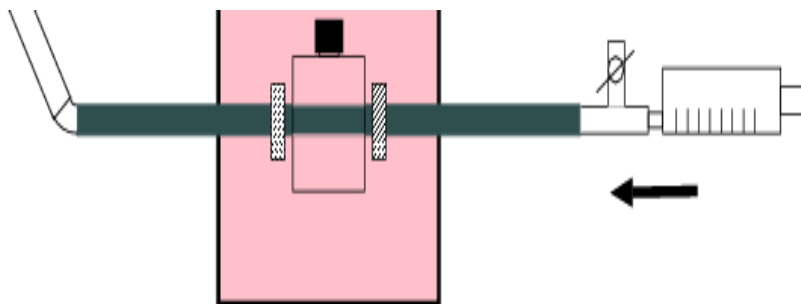
The most interesting aspect of our experiments of bioconvection patterns in horizontal cylindrical tubes was investigated by variation of the flow rate of suspension in the tubes. Here we have used the Graseby 3500 syringe pump (Graseby Medical Ltd., Watford, UK) attached at one end of the experimental setup to induced the pressure from one side which resulted in a weak poiseuille flow. We started with the zero or no flow, then initiate very small flow rate with gradually increasing the flow rate lead to relatively high flow rate and investigated the formation, distortion and breaking of pattern formation in the horizontal tube. Thus we repeated the process of variation of flow rate until we have obtained maximum flow rate typically 30-35 ml h⁻¹ for different cell concentrations for the case of tube B only.

4.4.7 Statistical Investigations

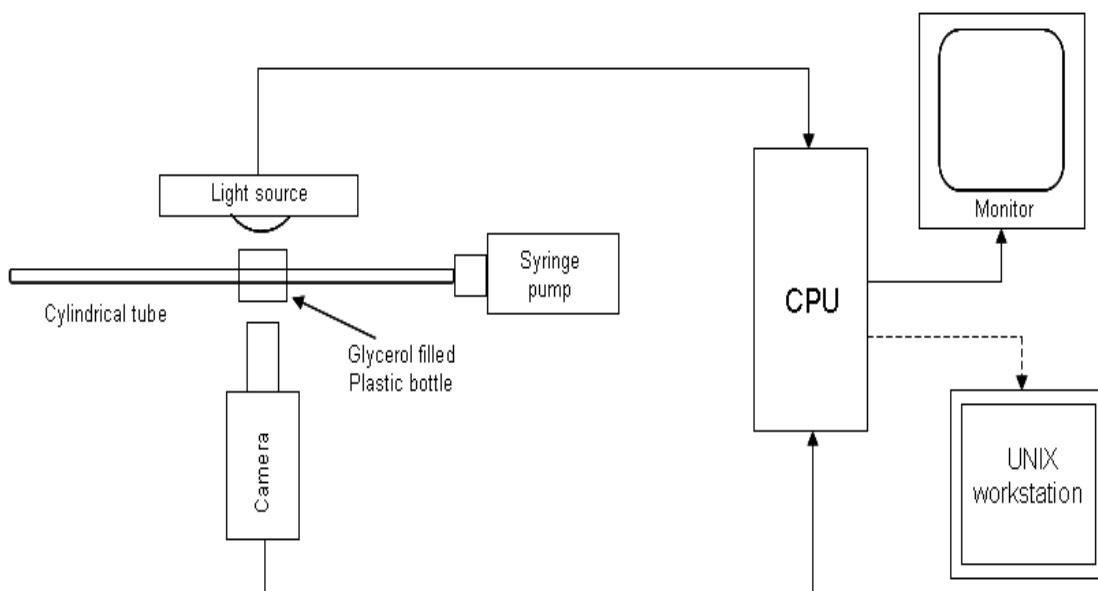
In order to investigate the patterns formation during the bioconvection in the horizontal tube as tube diameter and concentration change, we perform some basic statistical analysis on the data for initial instability wavelength λ_i of the bioconvection pattern and final pattern wavelength λ_f . Linear fitting was performed on data for initial instability wavelength and final pattern wavelength using gnuplot for each tube for the two different mixing procedures. Using these linear fits we try to analyze the trends in pattern formation using the gradients of the fits for the three different tubes. Asymptotic standard errors and root mean square of residuals were also recorded using the fit analysis. Similarly we have recorded Kolmogorov-Smirnov statistic error for the pattern wavelength for both cases of no flow and varying imposed flow experiments. To investigate the spread of data we have calculated the standard deviation as well.

4.5 Experimental setup

The experimental setup involves the main glass tube clumped with two stands to hold it horizontally balanced. The one end of the tube was attached with tube joints and T junction. Further one end of T junction was attached with switch to control the air and suspension flow into the tube, and other end was connected with syringe pump to initiate the imposed flow for the case of flow problems only. The other end of the main glass tube was attached with flexible plastic tube of higher diameter. This further attached



(a) Side-view of the experimental setup.



(b) Top-view of the experimental setup.

Figure 4.5: A schematic diagram of the experimental setup for recording images of bioconvection in a thin horizontal cylindrical tube. The tube is clumped at horizontal position and held fixed with two stands. The red LED light source was fixed behind the centre of the tube and camera was mounted on stand so that images could be recorded from the side of the cylindrical tube. Suspensions were loaded via a plastic tube affixed to the left of the bioconvection tube and flow was imposed using a syringe pump shown schematically on the right of the tube.

with small container which will be used as buffer and will served important role in our indigenously established mixing procedure within the tube. This further rested on the stand of exceeded hight to control the flow within the main glass tube.

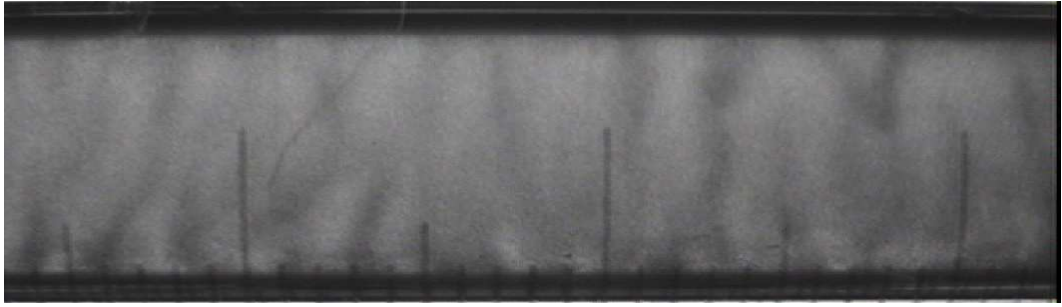
To improve the images visibility of the cell suspension within the tube and reduce the optical distortion or rarefaction effect we modify the tube setup by passing the tube with sealed glycerol filled perspex bottle. We ensured that this arrangement mounted at the centre of the tube, and we setup digital camera mounted on the stand right in front of the tube with glycerol filled perspex bottle setup. The red light held fixed behind the perspex bottle with tube and the whole apparatus was kept on working bench aligned and vibration free. The digital camera was further attached with the PC to record the images which are 200 images after every 2 seconds for no flow experiments and 49 images for every second for imposed flow problems. The schematic diagram of the experimental setup is shown in the Figure 4.5.

4.6 Cleaning and processing of images

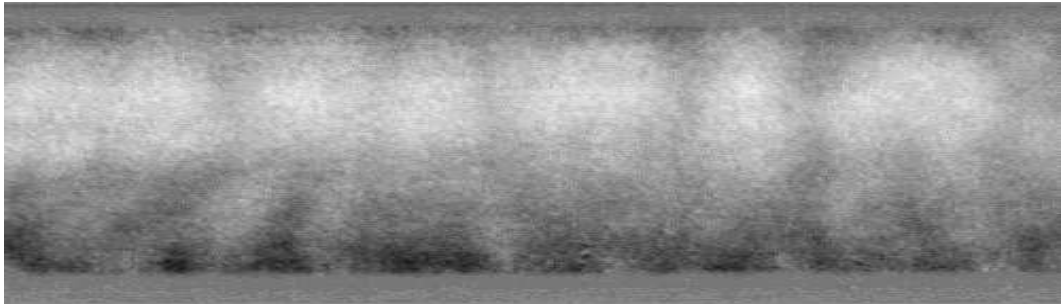
After setting up the apparatus we started recording the images and each image has 768×576 pixels. As mentioned earlier we have recorded 201 images for every 2 seconds for no flow experiments and 49 images for every second for imposed flow experiments. Here we follow the work of Bees and Hill [7] and Czirók *et al.* [37] to extract the dominant wavenumber from each of our recorded images. To analyze the recorded images we have used the digital image processing software IDL (RSI, Boulder, CO USA) which have been programmed to extract dominant wavenumber using the fast Fourier transform method.

The recorded images have some unwanted additional information like tube markings, labels, walls or surface of the tube etc. To get rid of all these unwanted information we clean the recorded images using the subtraction of recorded images either from the first homogenously mixed recorded image, or median of the recorded images. The first image subtraction cleaning was performed for the case of mixing outside the tube with no flow experiments whereas, for mixing inside the tube with no flow experiments we have subtracted the saved homogenously mixed image (mostly 1st) for cleaning. Additionally, we have cleaned the markings on the tubes by blanking markings on the tubes using the IDL. On the other hand, for the case of imposed flow experiments we have used subtraction from the median of the images for cleaning purpose. The cleaned image is

cropped to 512×512 pixels.



(a) Original captured image.



(b) Clean image using IDL.

Figure 4.6: A sample of cropped image from experiments recorded in tube A, where $c = 1.84 \times 10^6$ cells cm^{-3} . The mixing of cells suspension was performed outside the tube.

4.6.1 Fast Fourier Transform

Fast Fourier transform is a method to compute discrete Fourier transform in $O(N \log_2 N)$ operations with an algorithm. The first well known FFT algorithm was established by Cooley and Tukey [35] and details of the FFT method can be found in Press *et al.* [120]. Bees and Hill [7] and Williams [147] used the FFT algorithm on the cropped images and follow the same procedure as recorded image resolution good enough to use FFT algorithm. Similarly we have used Hahn windowing function to reduce the consequence of the brisk edges of the captured images. Hahn windowing function has property that it has maximum value at the centre and zero at the edges of the image as desired in our case. Additionally, it also help to take away oscillatory errors from the Fourier spectrum. The Hahn windowing function in two dimension is defined as

$$W_H(x, y) = \frac{1}{4} \left(1 - \cos \frac{2\pi x}{N}\right) \left(1 - \cos \frac{2\pi y}{N}\right), \quad (4.2)$$

where the size of the recorded image is $N \times N$.

After using the Hahn windowing function we used the FFT on cropped recorded images which convert the real, two dimensional image array into a complex array of the same size. The wavenumber information can be extracted from the data spread around the origin of the image which is actually the measurement of the distance of the data from origin. Additionally, this data enables us to specify the direction of the wave and extract the phase information. Later, we employ this useful data to plot a bar chart for every processed image and finally using appropriate fit we can extract the dominant wavenumber

4.6.2 Dominant wavenumber

The ultimate aim of the processing of the recorded images is to extract the dominant or most unstable wavenumber from each image. After obtaining the bar charts Bees and Hill [7] employed an un normalized double Gaussian distribution with the scheme that first fit for the noise and less unstable wavenumber whereas, second fit for the dominant wavenumber. Another approach introduced by Cziráok *et al.* [37] using double logarithmic fit which exhibit power law decay for both small and large wavenumber. The dominant wave number will extract using the fitting function defined as

$$\ln[I(k)] = \alpha |\ln(k) - \ln(k_0)| - \beta \ln(k) + c, \quad (4.3)$$

where k_0 is the peak of the fit or dominant wavenumber, α and β are the fitting parameters corresponds to different exponents for small and large wavenumber and c is a constant. Additionally they conclude that this is equivalent to separating the logarithms and rewrite as

$$I(k) \approx \begin{cases} k^{(-\alpha-\beta)} & \text{when } k < k_0, \\ k^{(\alpha-\beta)} & \text{when } k > k_0. \end{cases}$$

In our analysis we have used second approach of double logarithmic fit as it fits best mostly as compared to double Gaussian fit to extract the dominant wavenumber.

4.6.3 Error Analysis

As we know that both of the above fitting functions are approximate fits which definitely required to calculate the error while using fit. Following the error analysis by Bees [6] where he defined measure of error, the Kolmogorov-Smirnov statistic error ϵ_{KS} . This describes variations in the trends of cumulative data and measures only cumulative error not the total error sum of the data. He defined the Kolmogorov-Smirnov statistic

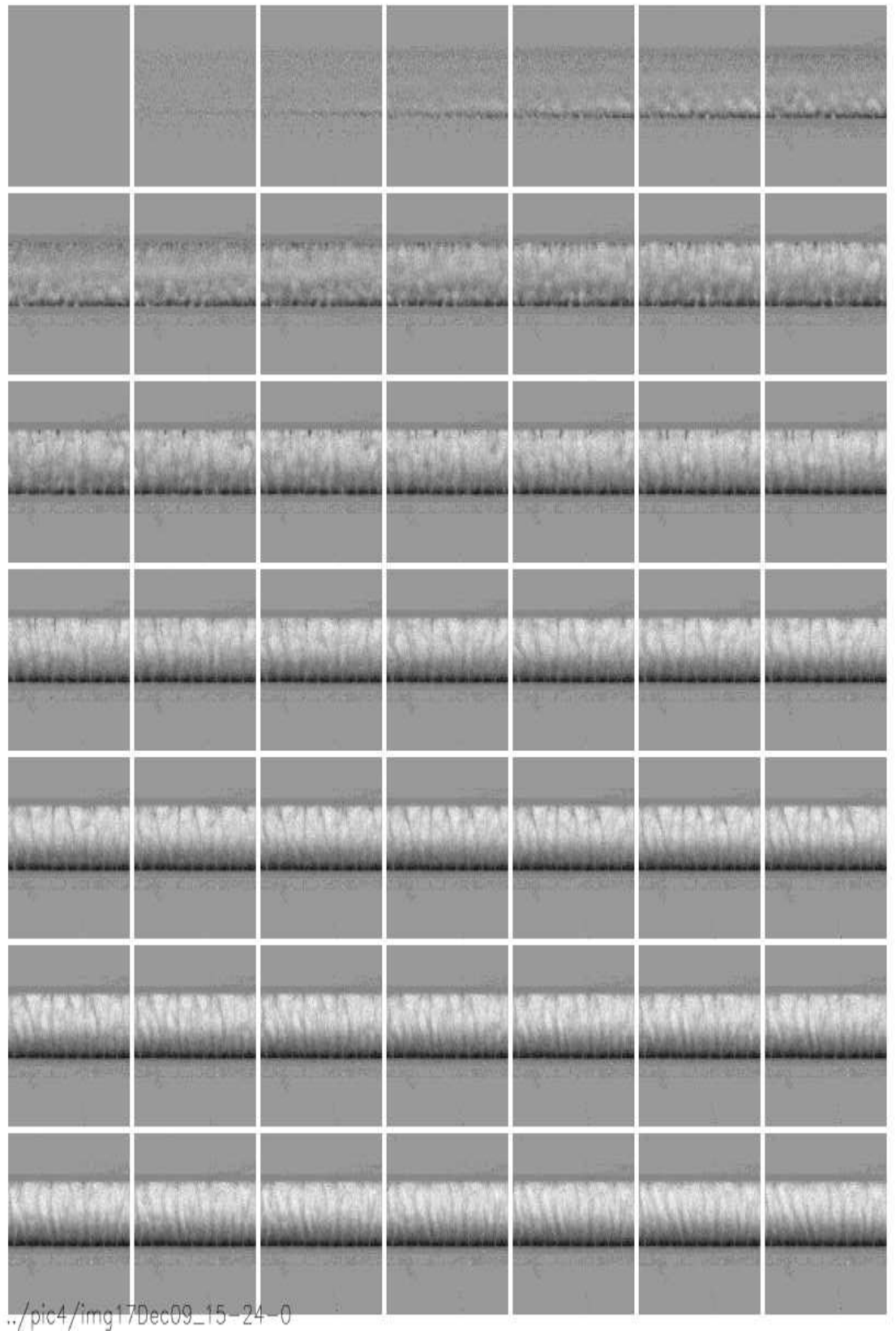


Figure 4.7: Sample of processed images from B0.42 experiment recorded in tube B where $c = 3.75 \times 10^6$ cells cm^{-3} . The images are captured every 2 seconds, where mixing was performed outside the tube.

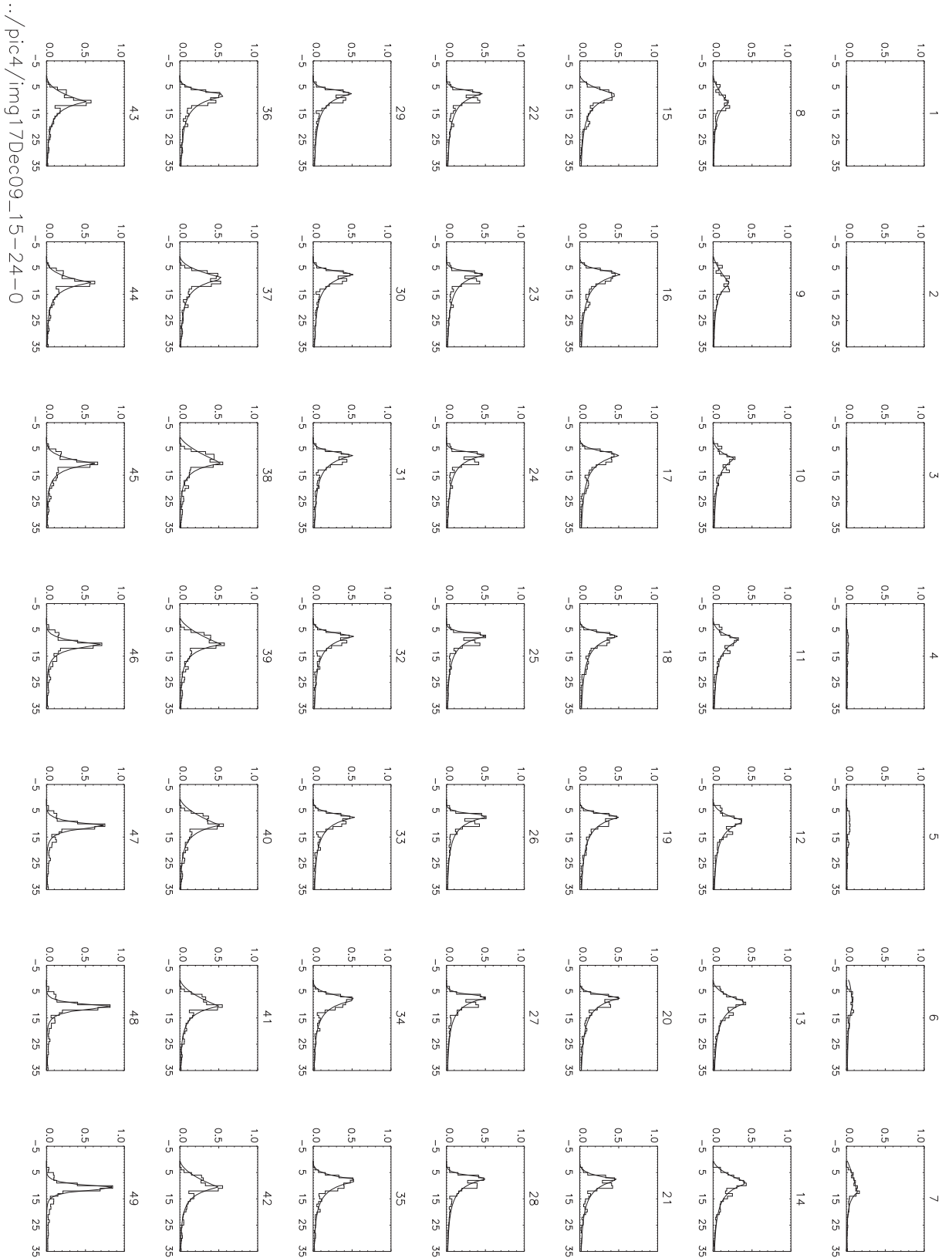


Figure 4.8: A sample fourier spectra from B0.42 experiment recorded in tube B where $c = 3.75 \times 10^6$ cells cm^{-3} . The images are captured every 2 seconds, where mixing was performed outside the tube. The horizontal axis is wavenumber and vertical axis is Fourier density. The logarithmic fitting function was used to fit the data.

error as

$$\epsilon_{KS} = \frac{1}{\sum_{n=0}^{N-1} \rho_n} \max_{n=0..N-1} \sum_{j=0}^{N-1} |\rho_n - \phi(X = n)|, \quad (4.4)$$

where ρ_n is the Fourier spectrum at wavenumber n and $\phi(X = n)$ is the fitting function distribution used for analysis like double logarithmic fit in our case. Higher values of ϵ_{KS} reveals that the trend of the fitting function ϕ used mostly deviates from the original data generally. Thus to get a more realistic fit the ϵ_{KS} values should be small enough as suggested by Bees [6] as well. Thus we have observed smaller error values for the case of double logarithmic fit as compared to double Gaussian, fit which confirms our preference of double logarithmic fit for data.

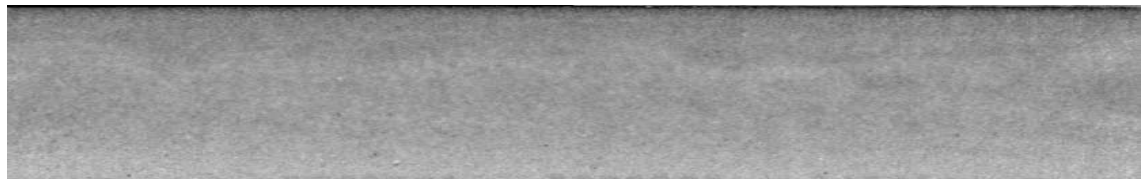
4.6.4 Dominant wavenumber analysis

Here we first homogenously mix the suspension before pouring into the tube and then slowly pour into the attached container with the tube. Later we allowed the suspension to flow into the tube from the container gently to avoid air or bubbles in the tube. After few minutes when cells have started making patterns we carried out our mixing regime to homogeneously mix the suspension. Here we have used the slow, least vigorous mixing setting to avoid any damage of either cells or cell's flagellum.

A perfect mixing of suspension is one that seems thoroughly mixed in which swirling has diminishes before the start of pattern formation. Thus after processing of the images we estimated the dominant wavenumber from each processed image. To give it some physical meaning we convert the wavenumber into wavelength. The relation between wavenumber k , and physical wavelength λ , is given by

$$\lambda = \frac{I_w}{k}, \quad (4.5)$$

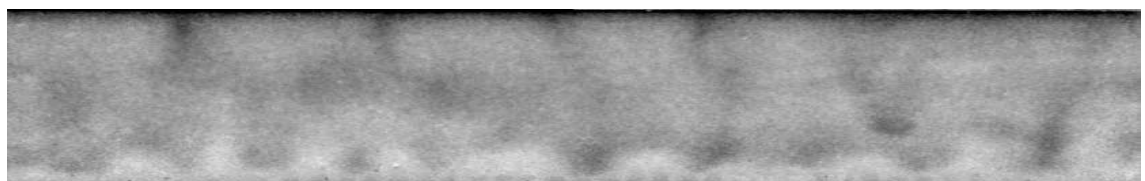
where I_w is the image width calculated using ImageJ 1.42q (Wayne Rasband NIH, USA) software and diameter of the tubes. The unit of diameter measured and image width is cm so the wavelength λ has units of cm as well. The image width was found different for three different tubes of variable diameter, and it slightly varies even for the single tube diameter because of the location, positioning of the camera and tube while recording images. The initial instability wavenumber and wavelength were denoted by k_i and λ_i whereas final pattern are denoted by k_f and λ_f respectively. It is always not easy to extract the exact dominant initial instability wavenumber, because of the noise produced after cleaning of the image which some times grow with the time. Thus we always picked



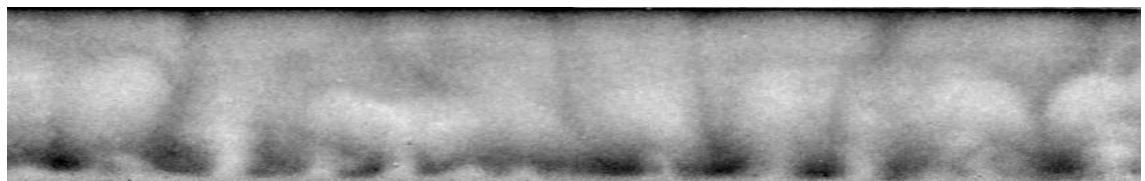
(a) 20 s



(b) 35 s



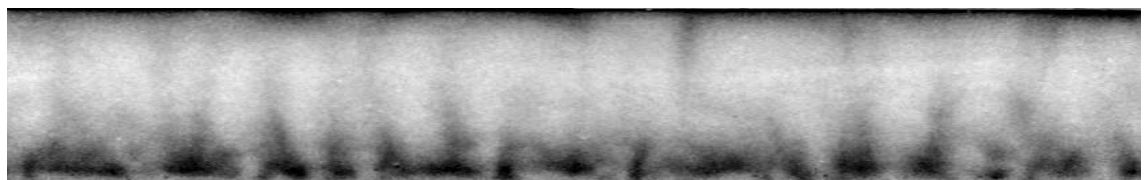
(c) 45 s



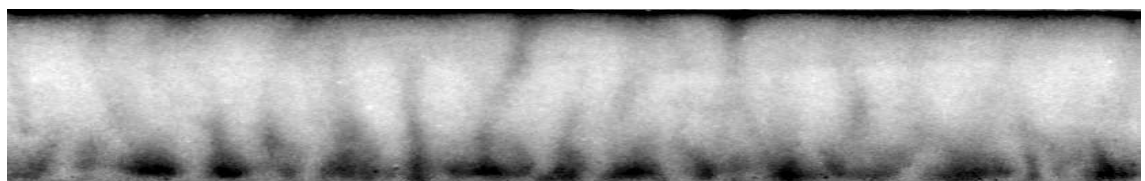
(d) 60 s



(e) 75 s



(f) 160 s



(g) 435 s

Figure 4.9: Snap shots of the processed image sequence (a-g) of a representative bioconvection pattern formation in tube A with varying time for cell concentration $1.84 \times 10^6 \text{ cells cm}^{-3}$ when mixing was performed outside of the tube.

../pic4/img02Dec09_15-57-0

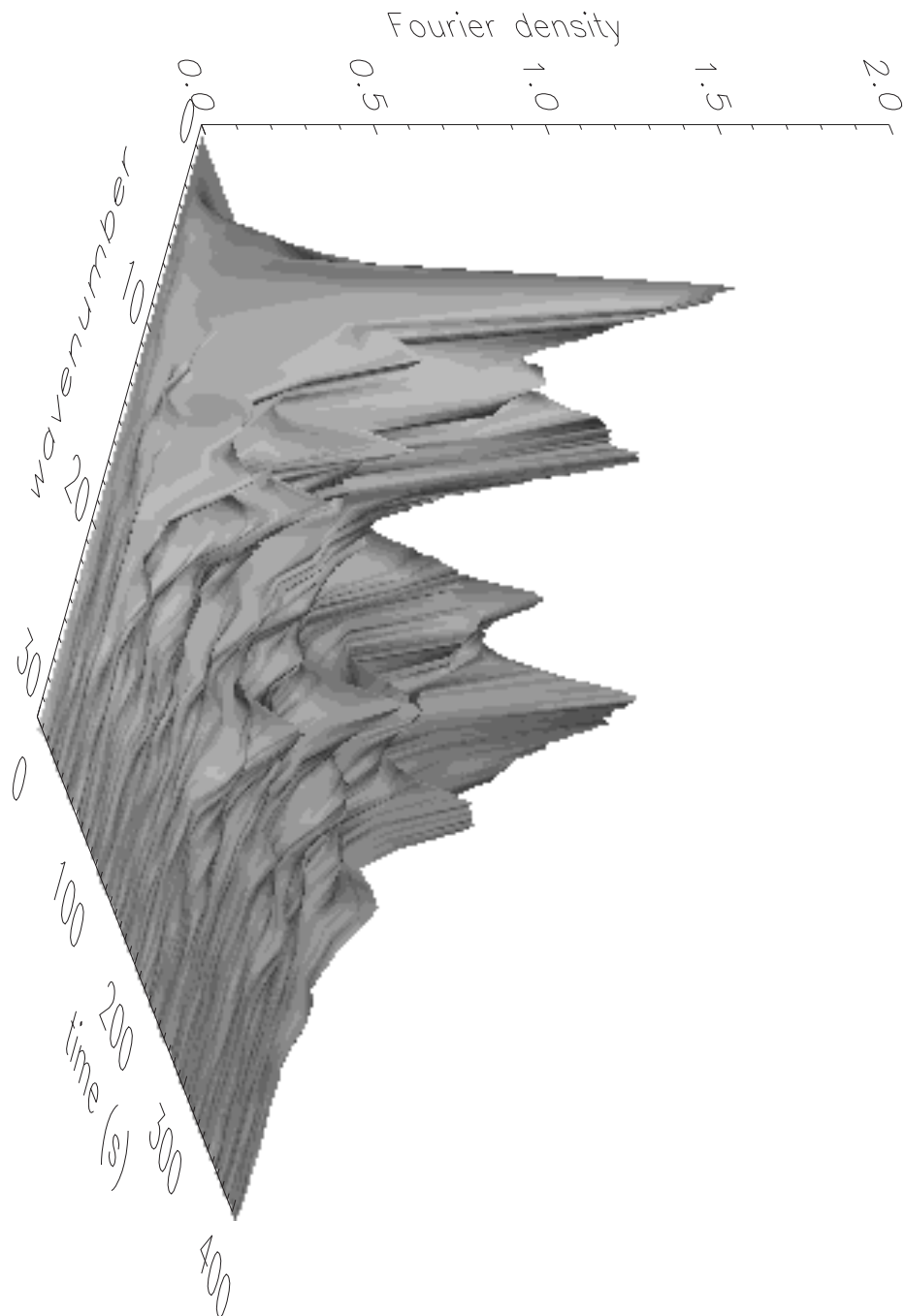
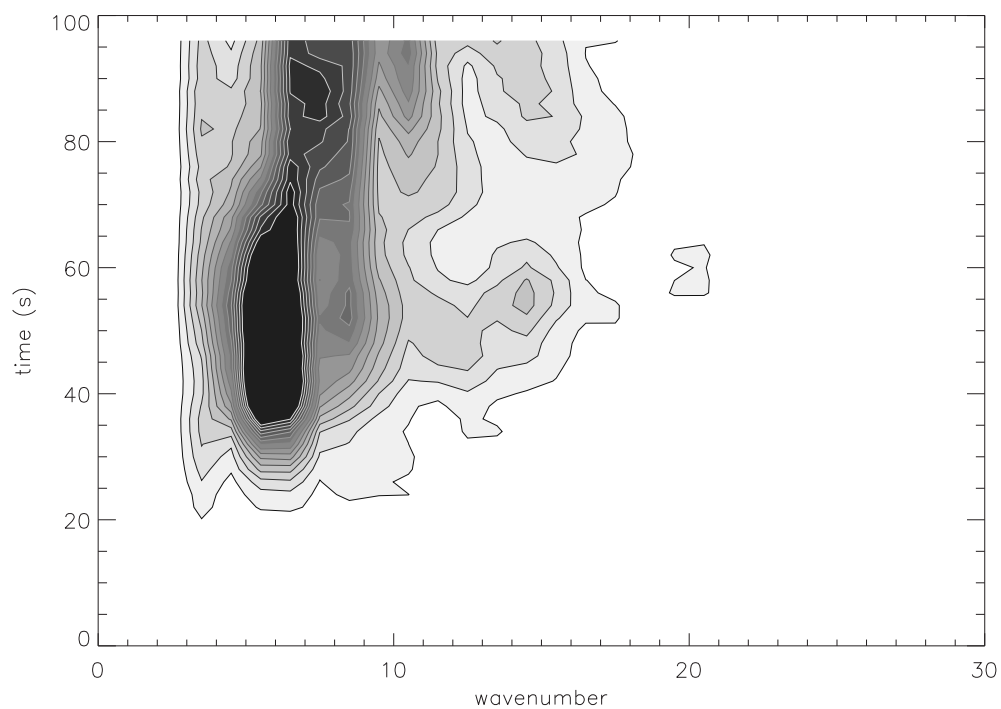
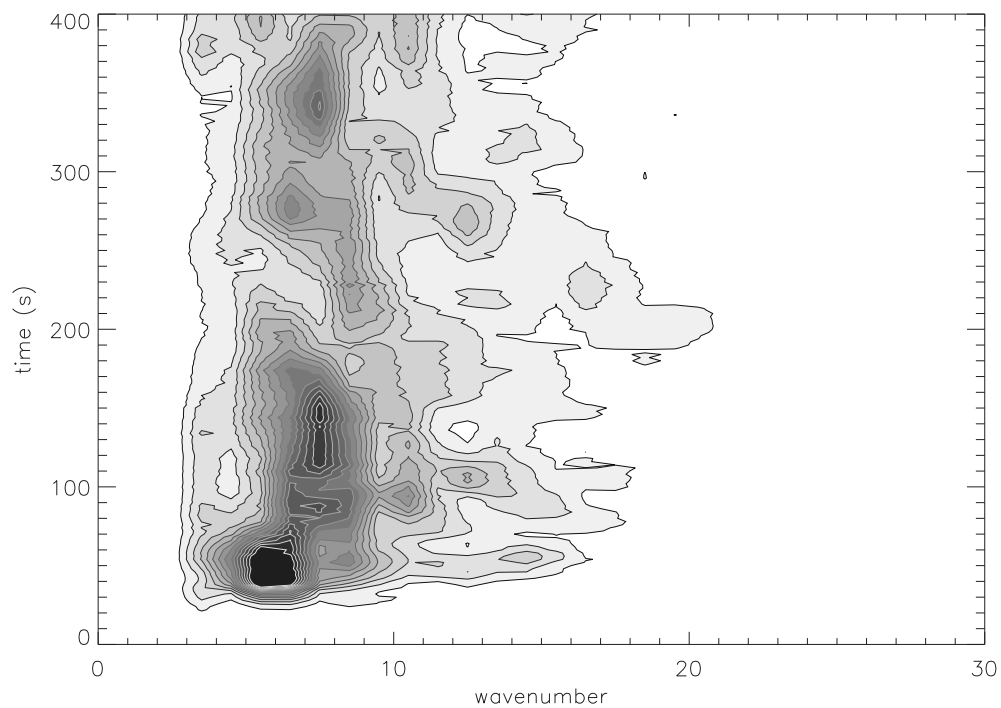


Figure 4.10: A sample 3d plot from experiment recorded in tube A, where $c = 1.84 \times 10^6$ cells cm^{-3} . The images are captured every 2 seconds, where mixing was performed outside the tube.



(a) Results for first 49 images.



(b) Results for complete 201 images.

Figure 4.11: A sample contour plot from experiment recorded in tube A, where $c = 1.84 \times 10^6$ cells cm^{-3} . The images are captured every 2 seconds, where mixing was performed outside the tube.

up the wavenumber when we have observed definite rise in the peak not because of mere noise only. Secondly, we must observed the Fourier spectrum density at that wavenumber increased with time which showed an evidence of development of pattern formation.

Thus using above defined procedure we analyzed the variations of initial instability wavelengths and final pattern wavelengths as a function of cell concentration, tube diameter, time and variable mixing procedures for the case of no flow and imposed flow experiments.

4.7 Experimental results for no flow problems

In this section we discussed the experimental results of bioconvection in horizontal tubes due to the variation of cell's concentration, tube diameter and time in the absence of flow. The calculated wavenumbers further normalized to the wavenumber per tube, as we have employed three different tubes of variable diameter. This normalization process will help us to compare the results for different tubes. This wavenumber further converted into wavelength by dividing the image width using equation (4.5). The image width I_w is not same for each case as it depends upon the tube diameter, position of the camera and tube used while recording the images.

Now we report the results of our observations and quantitative analysis of he bioconvection in horizontal tubes in the absence of flow. In the absence of flow, the pattern development was recorded after a cell suspension was mixed and poured into each tube. Experiments were carried out using tubes A, B and C, varying cell concentration, c , in the range $0.5 \times 10^6 - 4 \times 10^6$ cells cm^{-3} . The sequence in Figure 4.9(a)-(g) shows the evolution of a typical bioconvection pattern in tube A with $c=1.84 \times 10^6$ as viewed from the side. We observed that a well mixed suspension (homogeneous in the first frame) quickly becomes unstable, breaking up into a beautiful striated alterations of thin dark plumes (high cell concentration) and white bands (low cell concentration). The observed pattern is seen to sharpen in time, with plumes becoming spaced closer together which is consistent to the observations for the case of different geometries. Since the geometry in our case is cylindrical tubes of uniform diameter, statistically similar patterns are observed along the length of the tube. The above observations are usefully quantified by analysis of the dominant Fourier modes extracted from the images. Figure 4.11 shows the contour plots of the power spectrum of the image sequence whereas, Figure 4.9(a)-(g) demonstrating the

evolution of pattern wavenumber with time. The Fourier spectrum quantifies our observations: an initially homogeneous suspension quickly suffers an initial instability, with the wavenumber k_i (the first peak in Figure 4.11); the pattern then becomes unstable to other modes, evolving to a structure with an average final wavenumber k_f . The complex dynamics with which modes evolve from the initial instability is also clear in Figures 4.10 and 4.11. For clarity of the evolution of pattern formation, variations of pattern wave number with respect to time for different cell concentrations recorded in three different tubes in the absence of flow are plotted and shown in Figures 4.16 and 4.17. Here we explain the different results separately in different sections with details of trends found, observations with recommendations and comparisons with other relevant work where required.

4.7.1 Investigating the initial instability wavelength pattern

The one of the important aspect of our experimental analysis is to explore the initial instability wavelength of pattern formation before any non-linear fully developed pattern established, as these wavelength can be compared to the trends calculated during linear analysis of gyrotaxis models. It is really hard to exactly extract the initial instability wavenumber from the processed data due to noise and cleaning issues. Here we compared the processed images with the data obtained, contour plot drawn using data and bar plot with the fit, to exactly figure out the dominant initial instability wavenumber k_i . For comparison purpose we have calculated the initial instability wavenumber k_i per tube. Later, we converted it into wavelength λ_i for physical significance by dividing the width of the image I_w . The image width was found different for three different tubes depending upon the tube diameter, position of the camera and the tube during recording of the images.

Here we have employed two different mixing procedures to explore the trends in initial instability wavelength patterns. The first mixing procedure involved mixing of suspension with stirrer mixer outside the tube before pouring into the tube, and images were started recording just after pouring into the tube. The suspension was found homogeneously mixed initially and after few seconds instability started developing due to gyrotaxis and gravitaxis as discussed in section 4.4.2.

In the second mixing protocol, after pouring the suspension into the tube we waited for few minutes to establish patterns then we moved the attached container at one end up and down few times with certain routine and timings. This lead the suspension flow

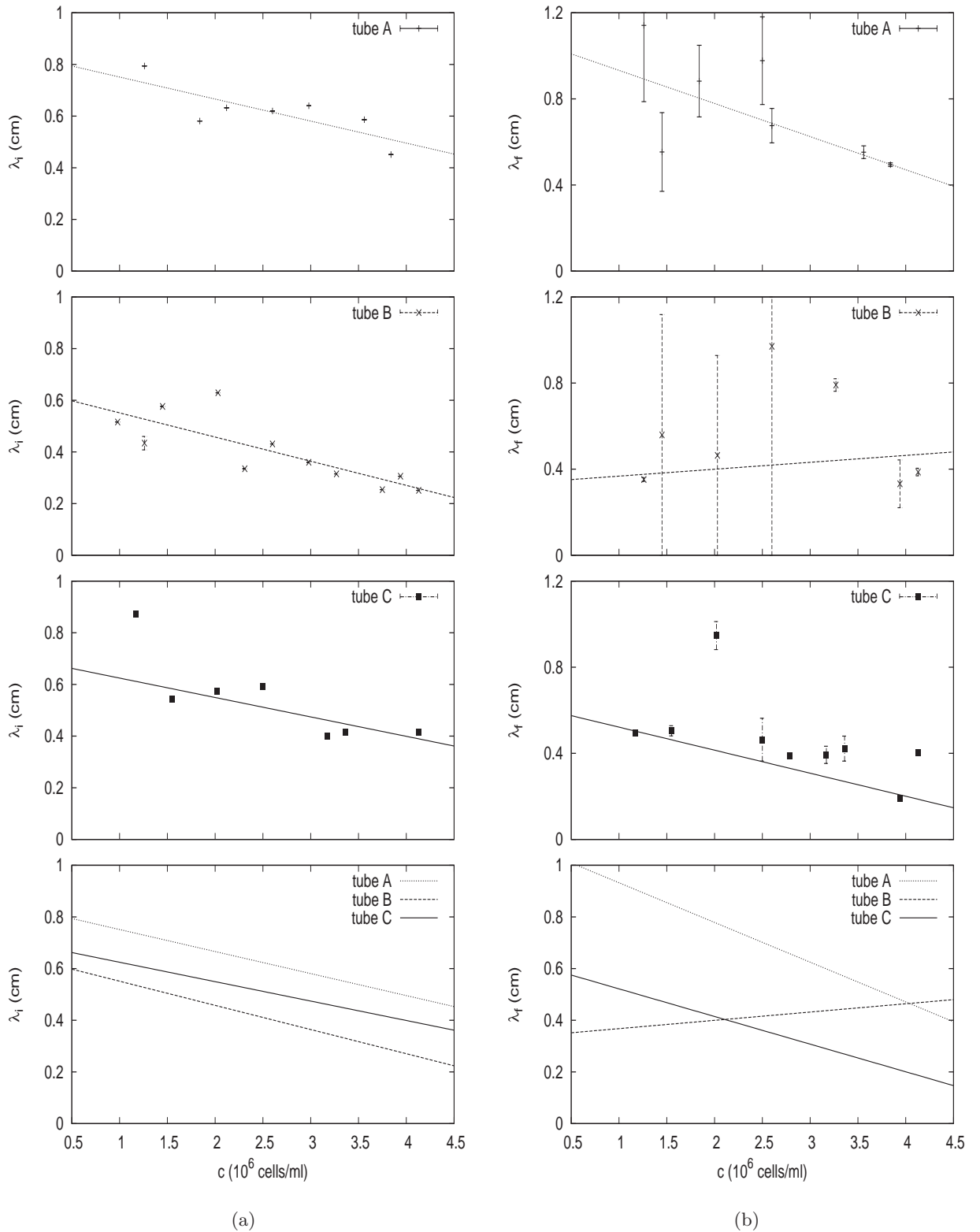


Figure 4.12: Experimental data for the initial dominant wavelength λ_i as function of concentration of tubes A, B and tube C (top three panels, as indicated) for the cases of (a) mixing outside, and (b) mixing inside the tube. Straight line fits to the data are shown (for tube C we only fitted for $c > 1.45 \times 10^6$ cell cm^{-3}). The last panel shows the fits without the data to allow a comparison of magnitudes. The error bars are standard deviations over a sample or the standard error in the mean over repeated experiments.

back and forth and mixed the suspension homogenously within the tube. During the mixing procedure we started again capturing the images and recorded the initial instability wavenumber k_i and time t_i to establish it. While during processing of images in the case of mechanical mixing we discard the first few images to remove the mixing of suspension effect.

Now to explore the trends in initial instability wavelength we fit the recorded data (≥ 1.45 million cells cm^{-3}) only, using the linear fit for the three different diameter tubes with two different mixing procedures. The low cell concentration data was neglected during fit procedure to avoid the non-linear effect. Later, we have plotted the fit with the data for the two different mixing procedures separately using gnuplot as shown the graphs in Figure 4.12.

As its clear from the gradients of fit in graphs, that wavelength decreases with the increase of suspension concentration for all the three tubes and both mixing procedures. This dependence was observed more phenomenal for the case of very low cell concentrations. Thus higher wavelength per tube implies broader plumes which means lower wavenumber per tube that leads to mathematically weakly non-linear problem. It is also observed that the trends vary for the two different mixing procedures significantly for low cell concentration and the disparity between the two graphs for two different mixing procedures was quite evident. This may be due the fact that the mechanical mixing within the tube was not proved efficient as for high concentrations the patterns were not completely vanished which restricted the complete or homogenous mixing of the suspension with in the tubes. Thus mixing outside of the tube was found more consistent and homogenous so naturally, we appreciate the data obtained using this mixing procedure in comparison to the mechanical mixing inside.

4.7.2 Investigating the final stable pattern wavelength

It is cumbersome to figure out when actually patterns get stable and how long they stayed. During the process of image recordings patterns formed due to gyrotaxis and gravitaxis instabilities, and plumes emerges and sometimes vanishes as time passes, and this process continues within the tube. In our experiments we have recorded 200 images for every two seconds for each concentration and both cases of mixing procedures. Later, for the case of mixing outside of the tube we have processed first 196 images to get 14×14 array using IDL as explained earlier. For the mechanical mixing inside the tube

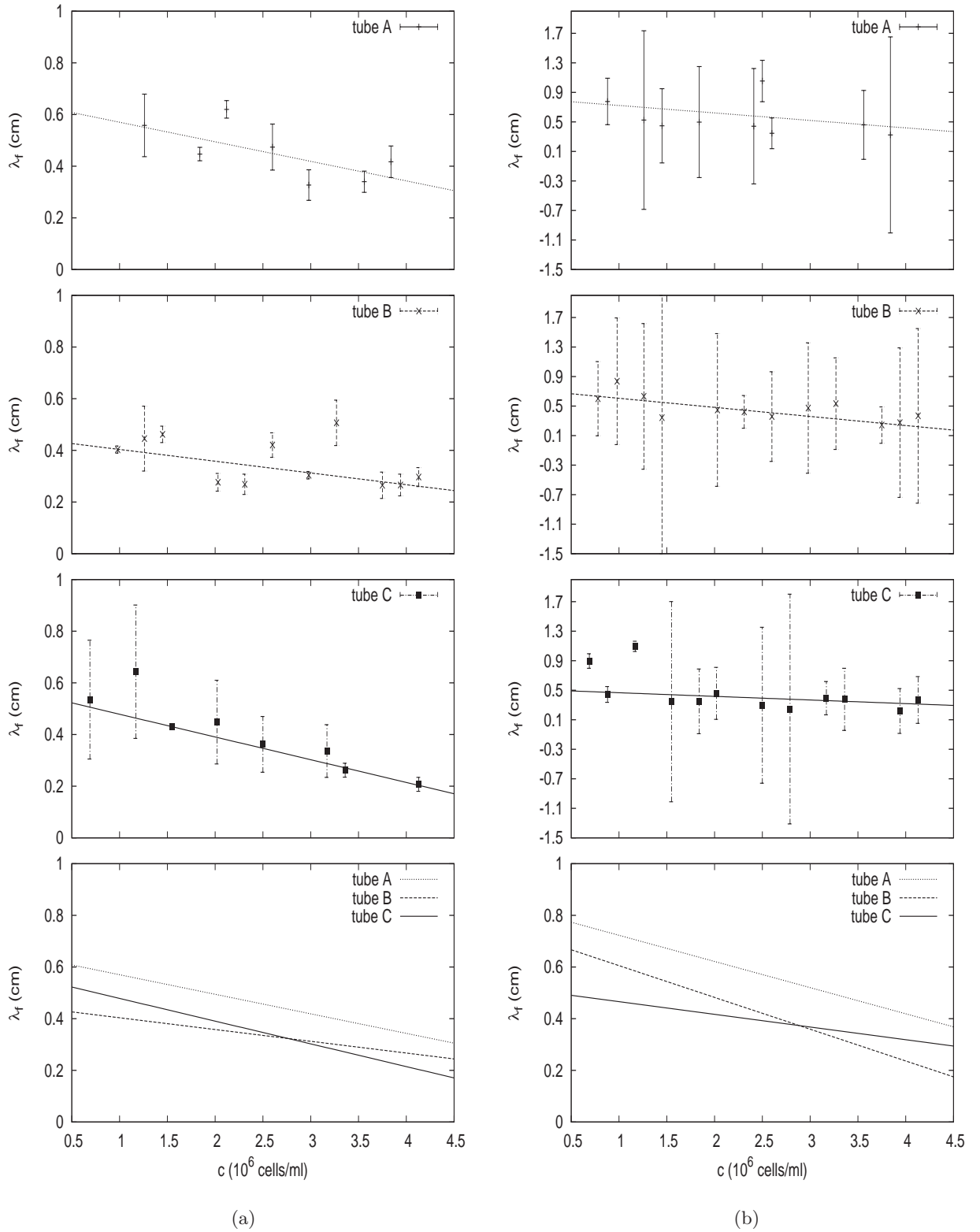


Figure 4.13: Experimental data for the final dominant wavelengths λ_f as function of concentration of tubes A, B and tube C (top three panels, as indicated) for the cases of (a) mixing outside, and (b) mixing inside the tube. Straight line fits to the data are shown. The last panel shows the fits without the data to allow a comparison of magnitudes. The error bars are standard deviations over a sample or the standard error in the mean over repeated experiments.

we have excluded first few images depending upon the cell concentrations (more images for higher suspension concentrations) again, to avoid images involved in mixing procedure and processed them using IDL. To get the final pattern wavenumber k_f we took the mean of the last 50 images wavenumbers and then converted into final pattern wavelength λ_f by dividing with image width I_w . Thus we have recorded all data extracted from all of our experiments, for variable cell concentrations with two different mixing protocols for three tubes of variable diameters.

The recorded data for final pattern wavelength λ_f for the three different tubes of variable diameter and two different mixing protocol, further fitted using the linear fit to investigate the trends. Here again for consistency with the previous case and to avoid non-linearity we have fitted data for cell concentration (≥ 1.45 million cells cm^{-3}) only. The data points with linear fit plot for the three tubes of variable diameter and two mixing procedures plotted, using gnuplot are shown in Figure 4.13.

In comparison to initial instability wavelength λ_i the above graphs showed less dependence on variations of cell concentrations for final pattern wavelength λ_f specially for tube A mixing outside the tube case. For the other tubes final pattern wavelength decreases with the increase of suspension concentration for the case of mixing outside the tubes. For mechanical mixing inside the tube the gradients of fits exhibits less dependence on suspension concentrations for the case of tube B and C whereas, final pattern wavelength λ_f decreases with the increase in suspension concentrations for the case of tube A.

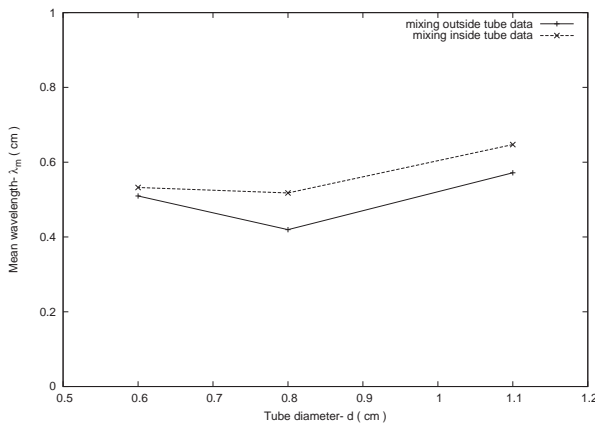
4.7.3 Investigating the dependence on variation of depth

Initially we have started recording pattern formation in four tubes of variable diameters ranging from tube D, 0.25 cm to tube A, 1.1 cm for variable cell concentrations. Repeated experiments revealed that, approximately no pattern observed in the tube D of smallest diameter. This may be due to large amount of shear and close proximity of the tube walls. Later, we have focused only rest of three tubes A, B and C. To analyze the pattern formation dependence on the depth or diameter of the tube, we have calculated the mean initial instability wavelength and final pattern wavelength of the data for each tube for the case of two different mixing protocol separately.

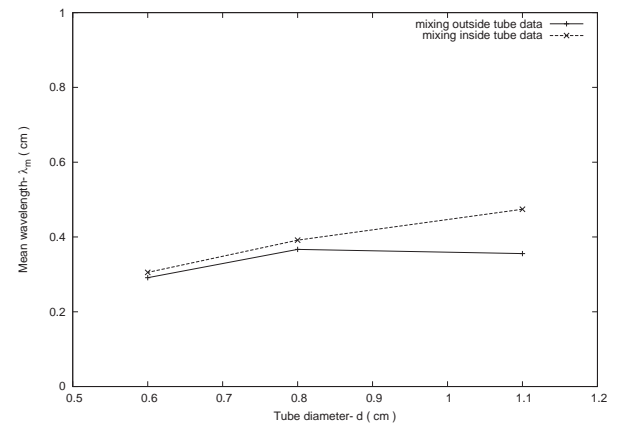
The plot of the data for initial instability mean wavelength for three tubes when mixing was performed inside the tubes, showed that tube B and C shared almost same values whereas tube A of largest diameter has higher initial instability mean wavelength. For the

case of mixing outside of the tube the order of dependence is changed slightly for the case of tube B, it showed less dependence as compared to tube A and C.

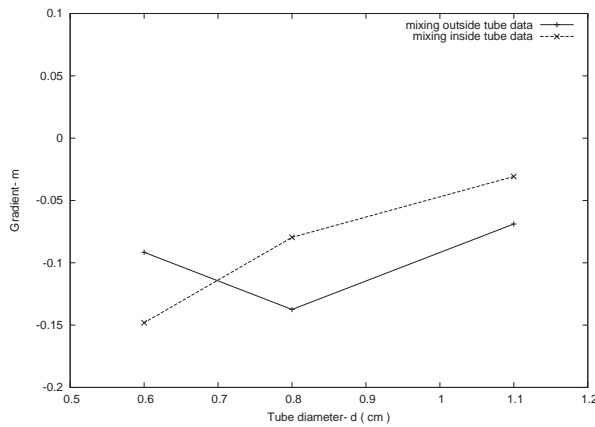
Similarly we have explored the depth dependence of final pattern wavelength by computing the mean pattern wavelength, for the three tubes with two different mixing procedures. In the case of mixing inside the tube the depth dependence varies in order, means varies with increasing the tube diameter. For mixing outside the tube case, tube A and B shared almost same value whereas lower final pattern wavelength value for small diameter tube C was observed as shown in the Figure 4.14. Within the uncertainties of our experiments, it is hard to ascertain any dependence of the wavelength on the tube diameter, but it would be reasonable to infer that both the initial and final wavelengths are in general larger for tube A than for tube B or C.



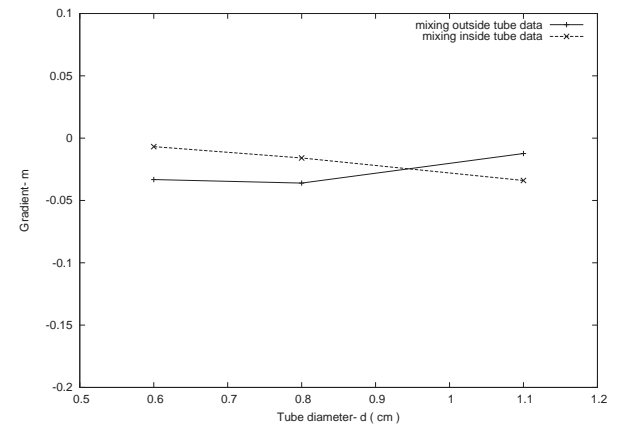
(a) Results for initial instability wavelength λ_i



(b) Results for final pattern wavelength λ_f



(c) Results for initial instability wavelength λ_i



(d) Results for final pattern wavelength λ_f

Figure 4.14: Experimental data plotted for mean pattern wavelength λ_m and gradient m for the three different diameter tubes for the initial instability and final pattern wavelength.

4.7.4 Investigating the dependence on variations of concentration

As our experiments involved tubes of variable diameters and maximum of tube A with inner diameter 1.1 cm which required minimum 30-40 ml of concentrated suspension for one experiment run. This minimum requirement really narrow down the liberty to record experiments for very high suspension concentrations. Thus we have managed at the most of 4.13 million cells cm^{-3} suspension concentration for three tubes. To explore the pattern formation dependence on the cell concentration, we have calculated the gradient of the linear fit of data for each tube for two different mixing procedures. This will enabled us to explore initial instability wavelength λ_i and final pattern wavelength λ_f dependence on the cell concentration for the three tubes with two different mixing procedures.

The gradient varies linearly with the increase of the tube diameter when mechanical mixing was performed inside the tube for the case of initial instability wavelength λ_i . The lower gradient value was obtained for initial instability wavelength λ_i for the tube B whereas, gradient increases with the increase of the tube diameter when mixing was performed outside the tube.

For the case of final pattern wavelength λ_f we have observed small variations of gradient with the variations of the tube diameters, which indicates the least dependence on suspension concentrations. We have observed almost same gradient for tube B and C and higher value for tube A when mixing was performed outside of the tube. On the other hand for the mechanical mixing inside the tube we have observed that gradient decreased slightly as the tube diameter increased.

4.7.5 Investigating the time for initiation of pattern formation

Another interesting aspect of our experiments is to explore the start time t_i of establishment of first dominant instability, during the process of pattern formation within the tube. This investigation can be best explored only in the case of mixing outside of the tube, as mechanical mixing inside the tube was not perfectly homogenous which leads inconsistent t_i data. We set the time $t_i = 0$ when we were pouring the suspension in, as the suspension was homogeneously mixed and just after pouring in it we started recordings for every two seconds. As explained earlier its not always easy to exactly figure out the initial instability wavenumber k_i and corresponding time t_i . Using the same procedure as defined for initial instability wavenumber k_i we have recorded the time t_i to establish initial instability.

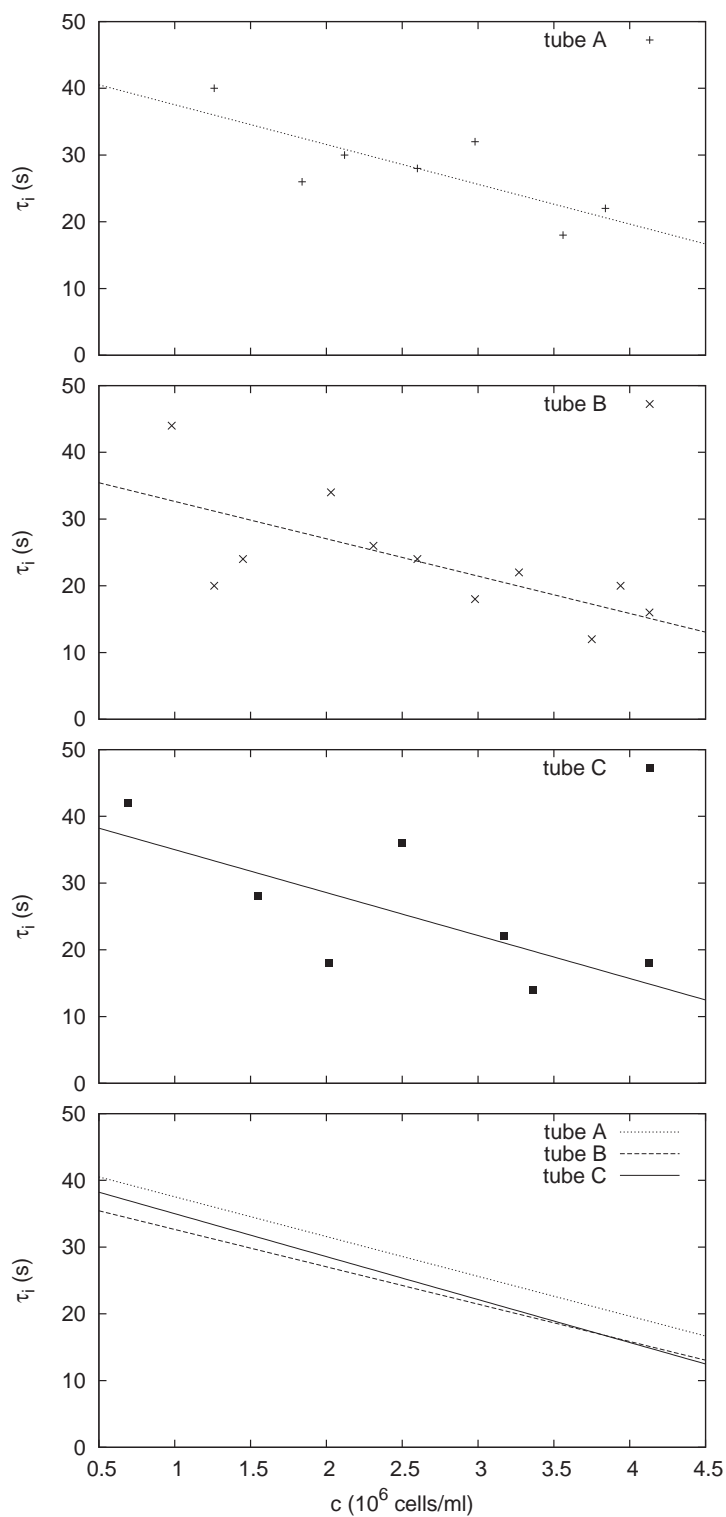


Figure 4.15: Experimental data for the variation of time to establish the initial instability for different cell concentrations for tubes A, B and C and bottom panel shows the comparison of linear fits to this variation.

Figure 4.15 shows the time t_i taken to establish the initial instability for the three different tubes of variable diameters as tubes A, B and C. Like λ_i , t_i falls linearly with concentration, but without any obvious sudden rise at low c for tube C. Now again using least square fit with a function of the form $t_i(c) = t_{0,i} + \gamma_i c$ (with $t_{0,i}$ and γ_i are fit parameters), we find $\gamma_i = -6.0 \pm 2.1$ s ml/cells and $t_{0,i} = 43 \pm 6$ s for the case of tube A, $\gamma_i = -5.6 \pm 1.9$ s ml/cells and $t_{0,i} = 38 \pm 5$ s for the case of tube B and $\gamma_i = -6.4 \pm 2.7$ s ml/cells and $t_{0,i} = 41 \pm 7$ s for the case of tube C. The analysis further reveals that dependence on the tube radius again is not strong for the case of bioconvection with no flow experiments.

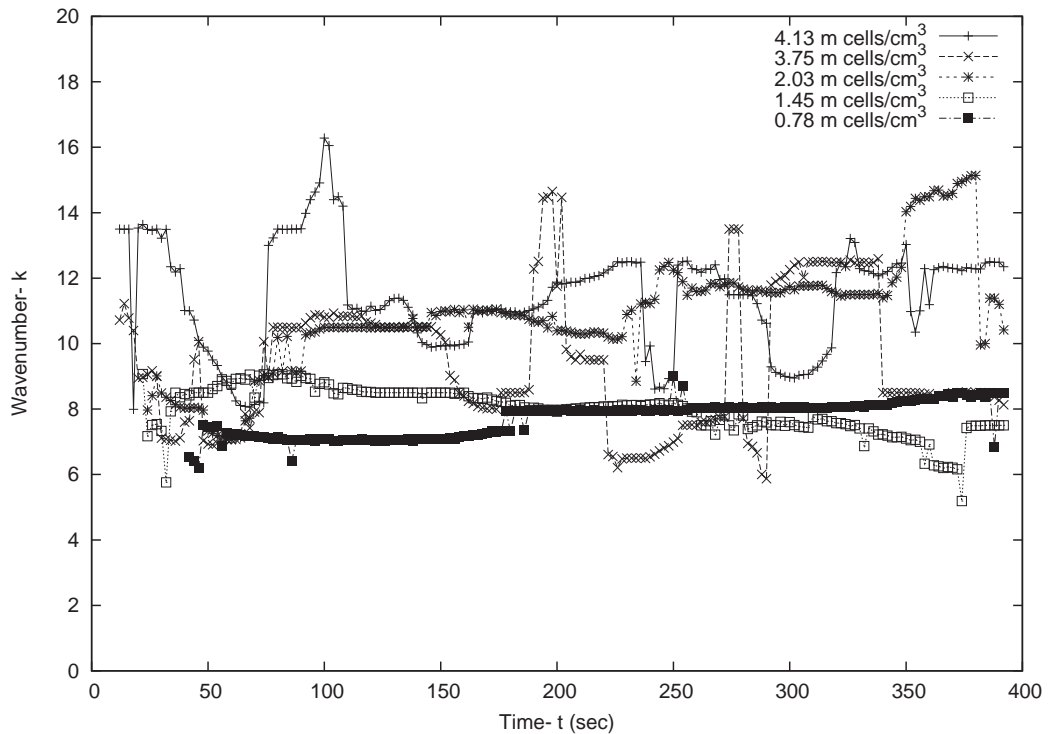
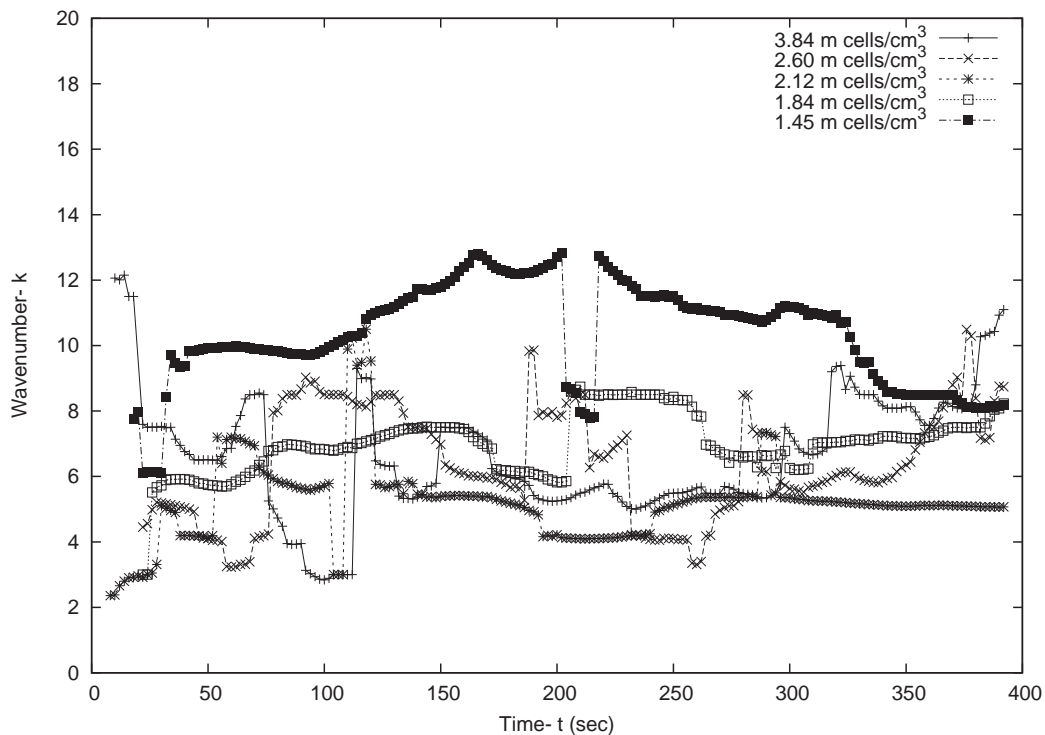
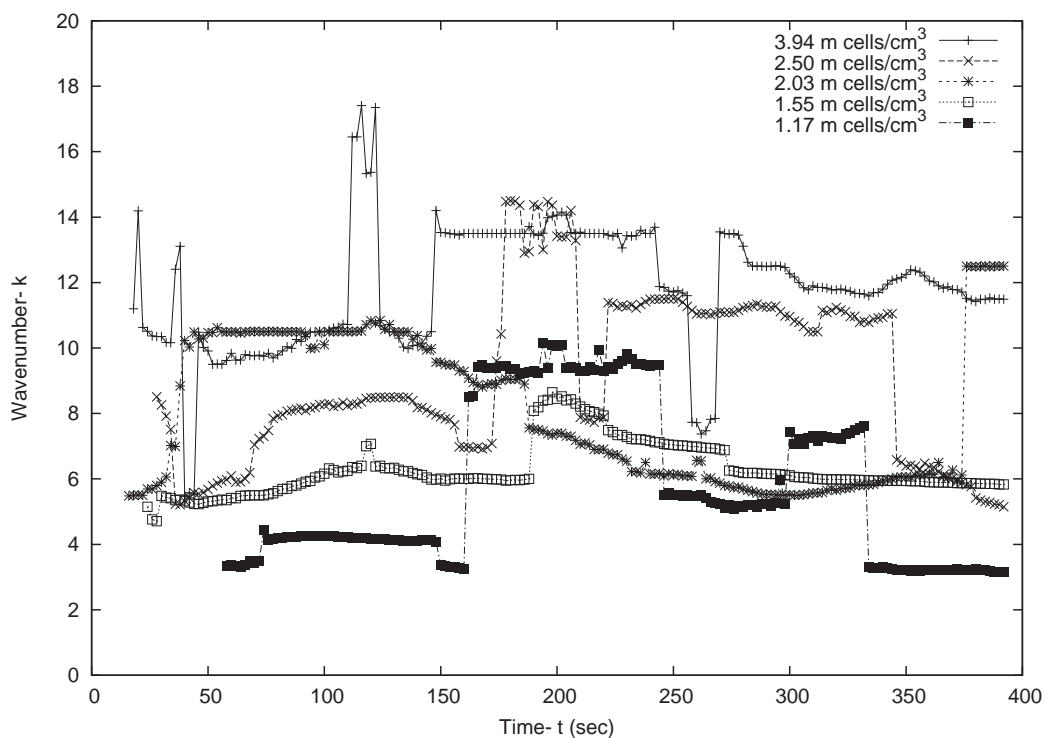


Figure 4.16: Variations of pattern wavenumber with respect to time for different cell concentrations recorded in tube B. The images were captured every two seconds, where mixing was performed outside the tube.



(a) Experimental results recorded in tube A



(b) Experimental results recorded in tube C

Figure 4.17: Variations of pattern wavenumber with respect to time for different cell concentrations. The images were captured every two seconds, where mixing was performed outside the tube.

4.8 Experimental results for imposed flow experiments

The most interesting aspect of our experimental work is to investigate the trends of pattern formation within the horizontal cylindrical tube with imposed flow. To impose the flow into the tube from one side we have used the syringe pump and ensured the sealed setup, which enabled us to induced continuous and controlled flow within the tube. Thus using the setup shown in the Figure 4.18, we have conducted 8 flow experiments runs for different cell concentrations in pyrex glass tube B only. Each experiment involved recordings for different imposed controlled flow rates ranging from no flow to maximum flow rate of $30 - 35 \text{ ml h}^{-1}$. For clarity of the evolution of pattern formation, variations of pattern wave number with respect to time for different flow rates recorded for different cell concentrations for tube B are plotted and shown in Figure 4.20.

In the presence of flow, patterns could be observed to be progressively distorted. The pattern formation in tube B for cell concentrations (a) $c=1.26 \times 10^6 \text{ cells cm}^{-3}$, (b) $c=2.22 \times 10^6 \text{ cells cm}^{-3}$, and (c) $c=5.18 \times 10^6 \text{ cells cm}^{-3}$ as the mean flow speed U_p is increased in steps of 2.8 cm s^{-1} from no flow to a maximum speed of 16.6 cm s^{-1} in the direction from right to the left as shown in the Figure 4.19. The qualitative behaviors observed is generally similar for different concentrations investigated. In the absence of flow or zero flow rate, the bioconvection plumes are parallel (on average) and slightly denser at the bottom. For small to moderate flow rates, most plumes still span the tube, but are seen to be curved so that the top and bottom of a plume are tilted at a characteristic angle to the vertical on average. The bowed plume shape is not symmetric for low concentrations, with plumes originating at the top stretching beyond the tube midpoint, before bending back at the bottom. The observation of the flowed pattern sequences reveals that plumes translate horizontally with the flow and that often high concentration pulses (blips) travel down a plume. As the flow rate is increased further, the pattern gets distorted more and more, with plumes tilting further away from the vertical at the top and bottom. The pattern appearance for increased flow rates is less orderly, many plumes break up, with less plumes spanning the tube. However, at higher flow rates, the plumes become more symmetric, linear bottom standing plumes stretch to the tube midpoint. Interestingly, the plumes maintain a constant average angle at the top and bottom of the tube, which increases with flow rate, as plumes are tilted by the flow due to nontrivial reasons as discussed in section 4.9.

It is also interesting to note that the plume behaviour discussed above is statistical,

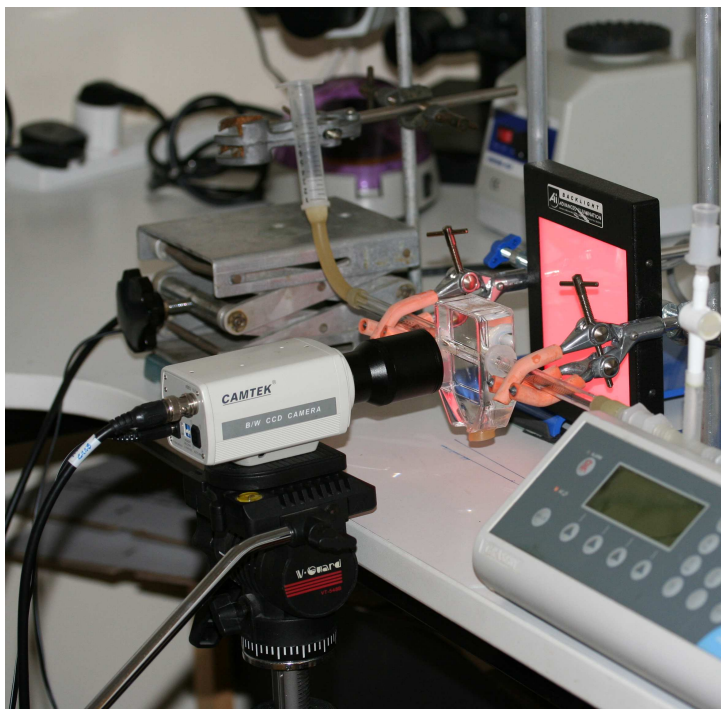


Figure 4.18: Snap shot of the experimental apparatus used for recording bioconvection pattern formation in a horizontal cylindrical tube with an imposed flow.

sequences show that individual plumes are not stable, meandering and either focusing or dispersing. For the maximum flow rates, all plumes fragment into very elongated structures making a large angle to the vertical and top and bottom plumes become fully symmetric about the tube midplane. Remarkably, as discussed above, the phenomenology described is qualitatively similar for all concentrations investigated, although there are quantitative differences.

4.8.1 Experiment protocol

Using the above defined setup we poured in homogenously mixed suspension into the tube and wait for three to five minutes so that patterns got established within the tube B. Here we are not interested in initial instability wavenumber and only record the final pattern wavenumber. After patterns established within the tube, we started recording the images after every second until 49 images to get an array of 7×7 images. This case may be termed as zero or no imposed flow case. Later, we switched on the syringe pump attached and initiate a small flow rate of 2.0 ml h^{-1} and waited for two minutes to allow flow fully established. After two minutes we started another run of 49 images captured

and then increased the flow rate to 4.0 ml h^{-1} . Again after waiting two minutes recorded 49 images and then increased the flow rate and kept recording the images. Initially we increased the flow rate by step size of 2 till 10 ml h^{-1} later, we increase by step of 5 till $30 - 35 \text{ ml h}^{-1}$ depending upon the cell concentrations and experimental setup.

4.8.2 Investigating the trends of wavelength

For each run we have recorded the wavenumber k of 49th image and then converted into wavelength λ for physical meaning using equation (4.5) again. This can be achieved by dividing with the image width I_w . The image width calculated using the tube diameter and again found slightly varied for different recordings depending upon the position of camera and tube while image captured. To investigate the trend of wavelength λ as a function of cell concentrations and imposed flow rates, we have plotted the recorded data as shown in the graphs in Figure 4.21.

A plot of dominant pattern wavelength λ as a function of the flow rate F shows a clear concentration dependence of the flowed pattern dynamics as shown in Figure 4.21(a). For all the concentration investigated, as the flow rate is increased, λ initially grows with the flow rate. However, there are critical concentrations around which this growth is interrupted by a sudden rise and fall of λ , which quantitatively demarcates a dynamical transition in the pattern. These transitions represent a statistical change in the dynamics which is not immediately obvious from the frame sequences; however, it is clear that these statistical changes in wavelength are associated with the rearrangements of the plumes as the flow rate is increased.

4.8.3 Investigating the first peak of wavelength

As we have noticed some interesting peaks while plotting the wavelengths λ against the varying flow rates F for different cell concentrations c . Out of them for different cell concentrations, we have tried to explore the trends for first peak found for different cell concentrations. The wavelength λ corresponding to first peak with error was recorded separately. Later, we have used linear fit to fit the first peak wavelength data and plotted it with the error bars as shown in the Figure 4.21(a).

The gradient of the linear fit graph shows less dependence of wavelength of first peak on suspension concentration. It also suggested that wavelength of the first peak increases with the increase of suspension concentration.

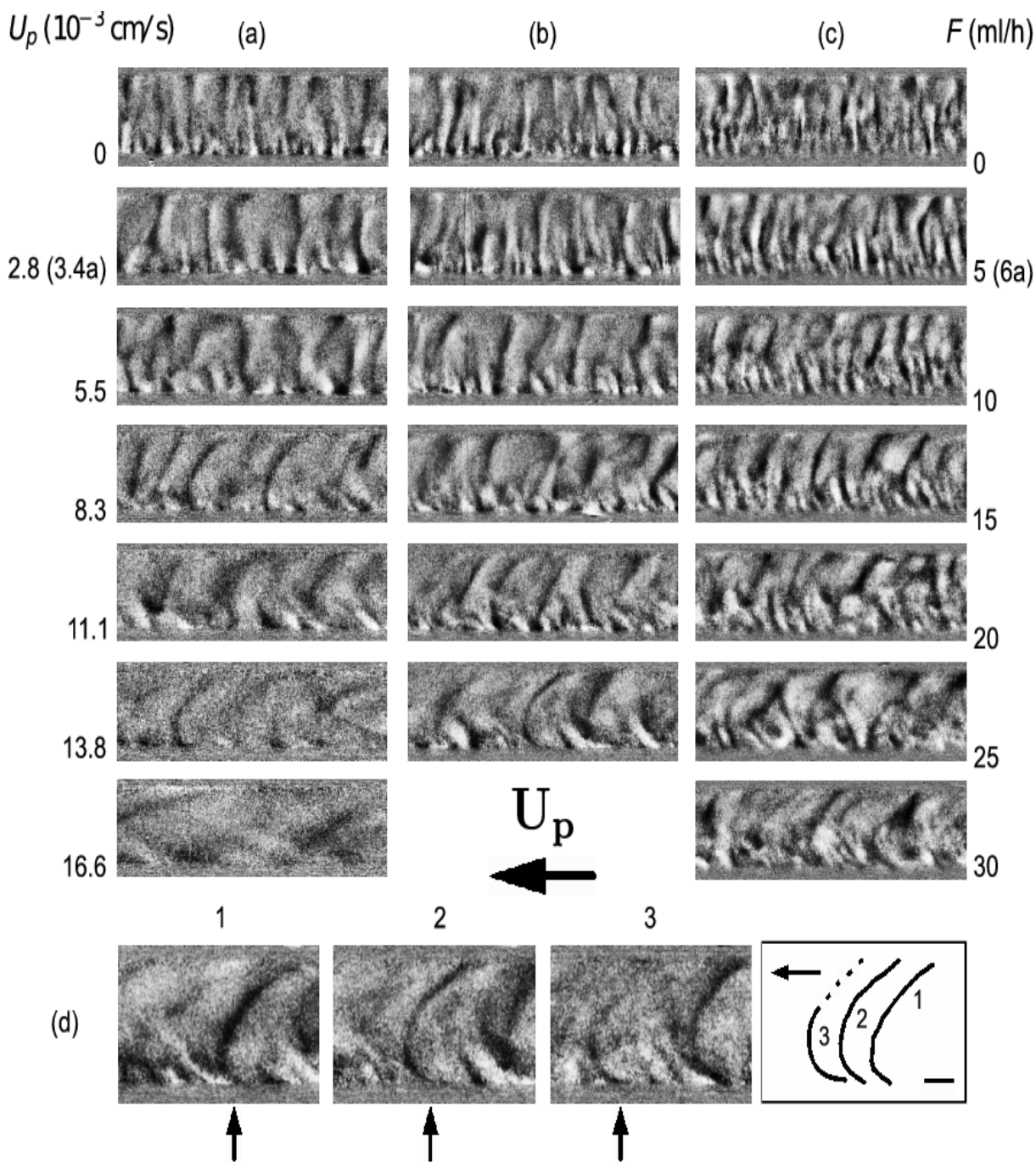
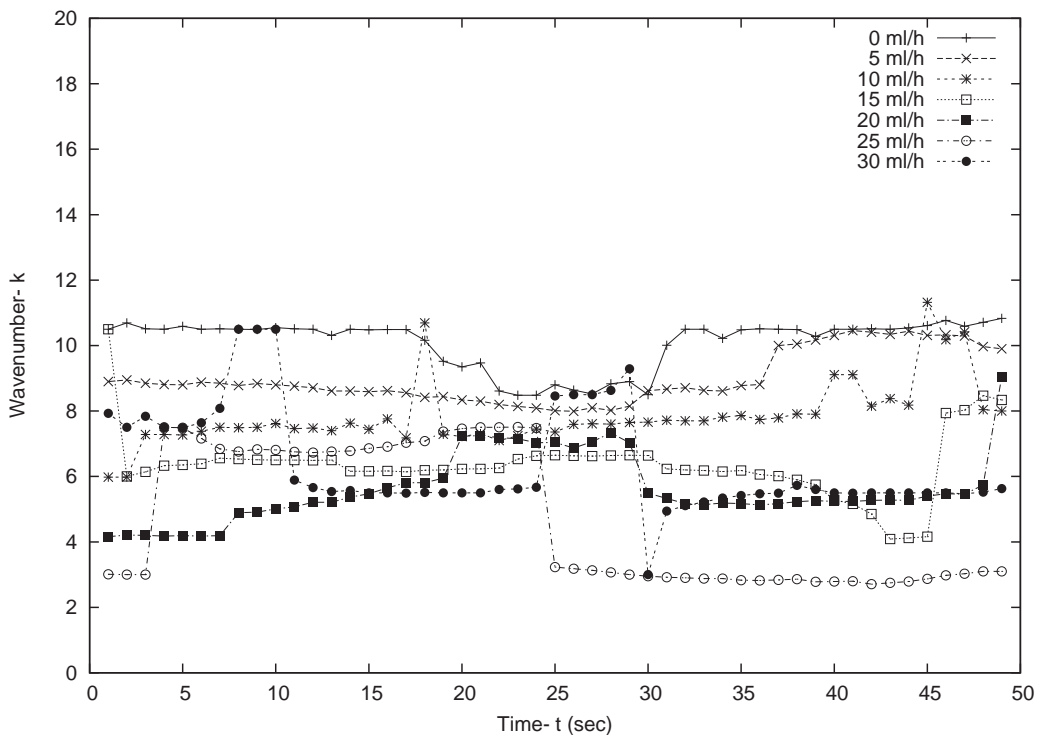
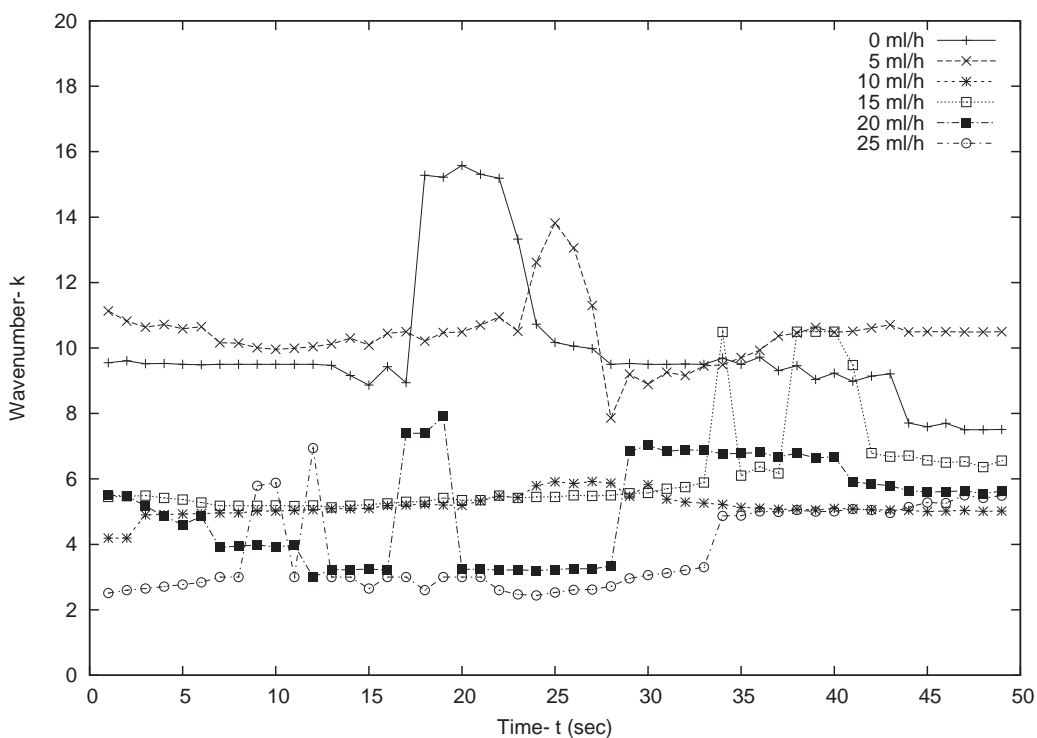


Figure 4.19: Bioconvection patterns recorded in tube B in the presence of imposed flow in the range $U_p = 0 - 16.6 \text{ cm s}^{-1}$ ($F = 0 - 35 \text{ ml h}^{-1}$) for cell concentrations (a) $c = 1.26 \times 10^6 \text{ cells cm}^{-3}$ and (c) $c = 5.18 \times 10^6 \text{ cells cm}^{-3}$. (As indicated, the second frame in (a) shows a frame for 3.4 cm s^{-1} rather than 2.8 cm s^{-1} .) (d) For $U_p = 13.8 \text{ cm s}^{-1}$ and concentration as in (b), we show three 5 s interval snapshots of the dynamics of a bowed plume (indicated by arrows). The figure to the right shows tracings of the plume with scale bar is 0.2 cm.



(a) Results for $c = 5.18 \times 10^6$ cells cm^3 .



(b) Results for $c = 2.22 \times 10^6$ cells cm^3 .

Figure 4.20: Variations of pattern wavenumber with respect to time for different flow rates, experiment recorded in tube B. The images were captured every second, where mixing was performed outside the tube.

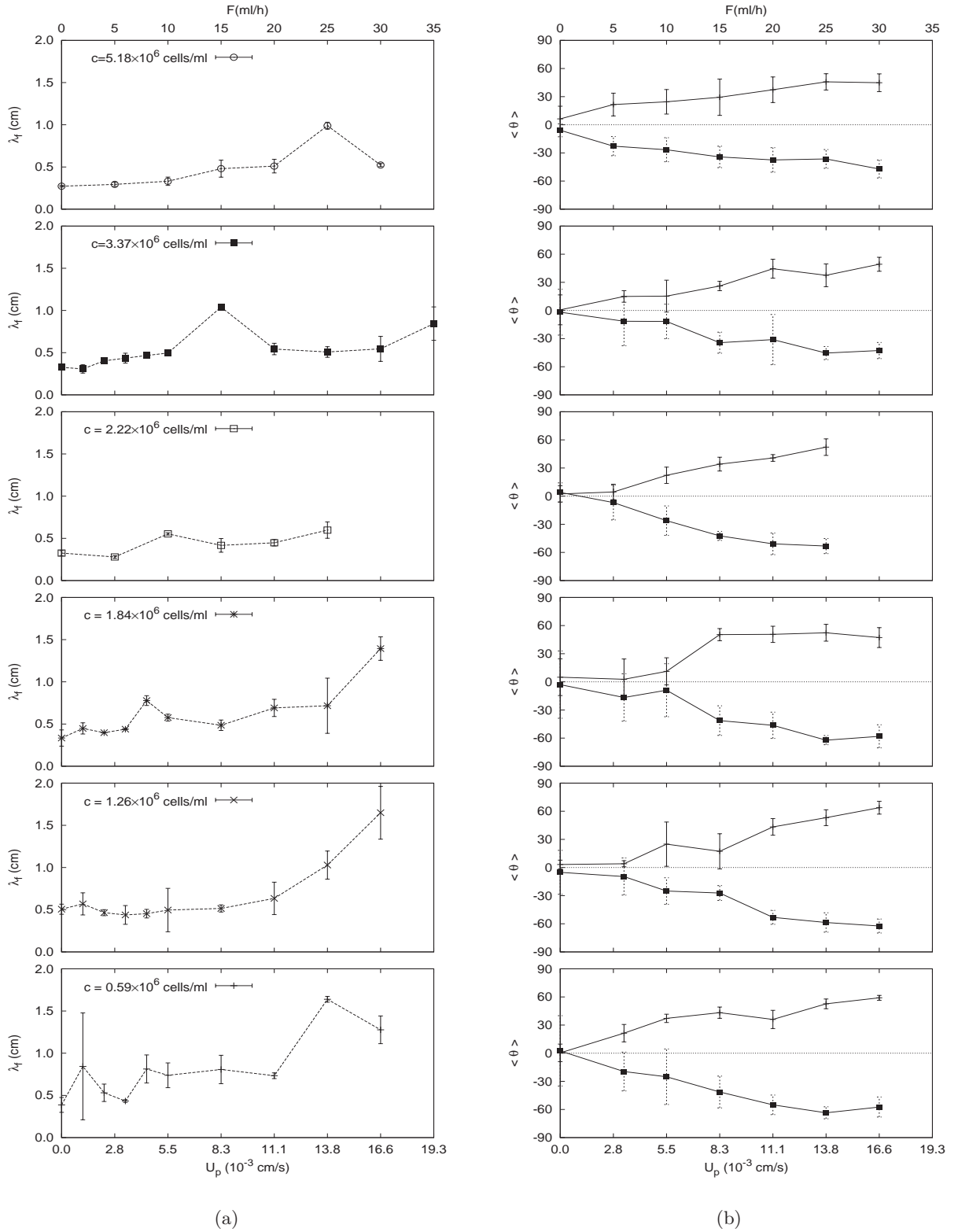


Figure 4.21: Plots of (a) final pattern wavelength and (b) average top (positive) and bottom (negative) plume angles to the vertical as a function of the flow rate F for concentrations in the range $0.59 \times 10^6 - 5.18 \times 10^6$ cells cm^{-3} , as indicated. The peaks in the wavelength around certain critical flow rates could be the signature of dynamic transitions in plume arrangement. The error bars indicates standard deviations..

4.8.4 Investigating the average angle and average drift speed

Now to quantify the inclination of plumes investigated, we measured the average angle $\langle\theta\rangle$, a plume makes to the vertical when measured from the top and bottom of the tube and average drift speed $\langle V\rangle$ of the plumes. For the case of top plumes, θ is defined as positive for tilt away from the vertical in the direction of flow, while for bottom plumes it is negative. It is evident from the Figure 4.22(b), that plume tilt does not seem to vary sensitively on concentration. The apparent independence of $\langle\theta\rangle$ on concentration can be made clearer by plotting all concentrations on the same graph, as shown in Figure 4.22(a), where the change in $\langle\theta\rangle$ with the flow rate F has been fitted with a linear trend constrained to go through origin. This is because as we expect $\langle\theta\rangle = 0$ for $F=0$ ml h⁻¹. The gradients obtained are very close in absolute value 3.65 ± 0.11 deg s cm⁻¹ for the top plumes.

The average drift speed $\langle V\rangle$ for all concentrations are plotted on the same graph as shown in Figure 4.22(b). It appears to increase linearly with the flow rate in a manner which appears generally independent of concentration. A constrained linear fit to data yields a value 1.30 ± 0.04 for the change in average plume speed with mean flow speed. Also shown in Figure 4.22(b) for comparison is the linear prediction for the maximum speed of the Poiseuille flow, $U_{poi} \equiv U = 2F/\pi a^2$, and for equivalent plug flow, $U_p = U/2$ (i.e. the mean Poiseuille speed), giving gradients of 2 and 1 respectively. The data appear to fall between these two limits but closer to plug flow. The significance of these results are discussed in the section 4.9 below.

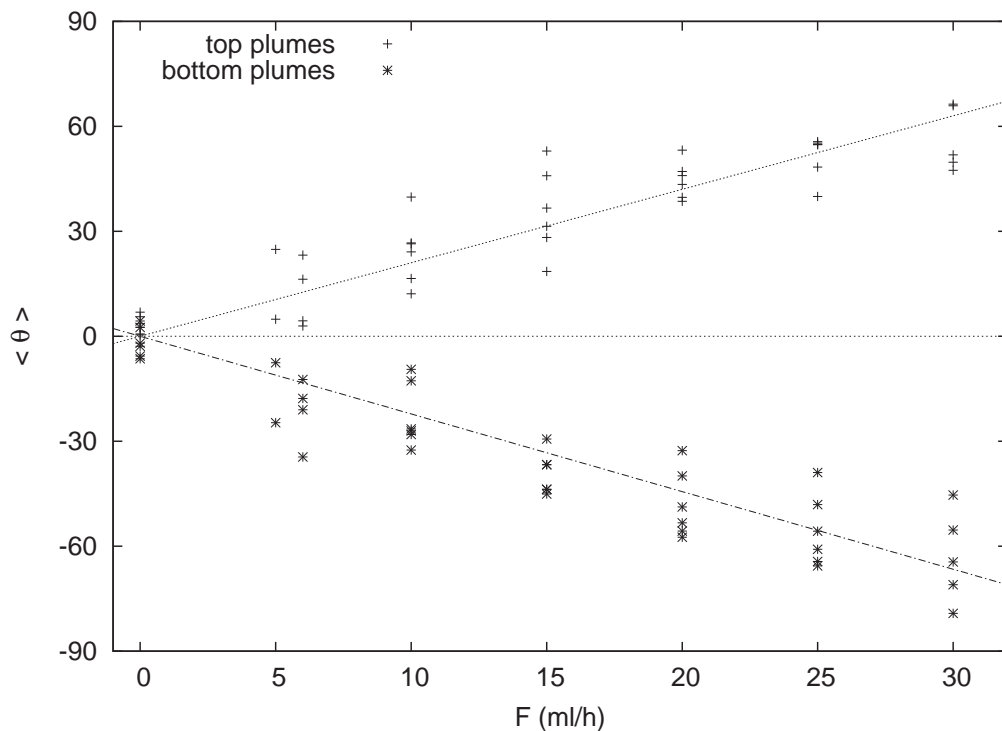
4.9 Discussion

In this chapter we have presented the quantitative analysis of the bioconvection patterns in thin long horizontal cylindrical tubes subject to imposed flow and without flow. A homogeneously mixed suspension of *C. augustae* becomes unstable to cell concentration fluctuations leading to a system of vertical plumes along the entire length of the tube. In the absence of the flow we have found that the pattern sharpens with time, and the plume spacing decreases, which is consistent with the observations by Wager [144]. After Fourier analysis of the images recorded from side we found that both initial and final dominant pattern wavelengths decrease slowly with concentration. This is consistent with the observations of Bees and Hill [7] for bioconvection in shallow layers. They also recorded that the initial wavelength increased linearly with depth, whereas the final wavelength found less

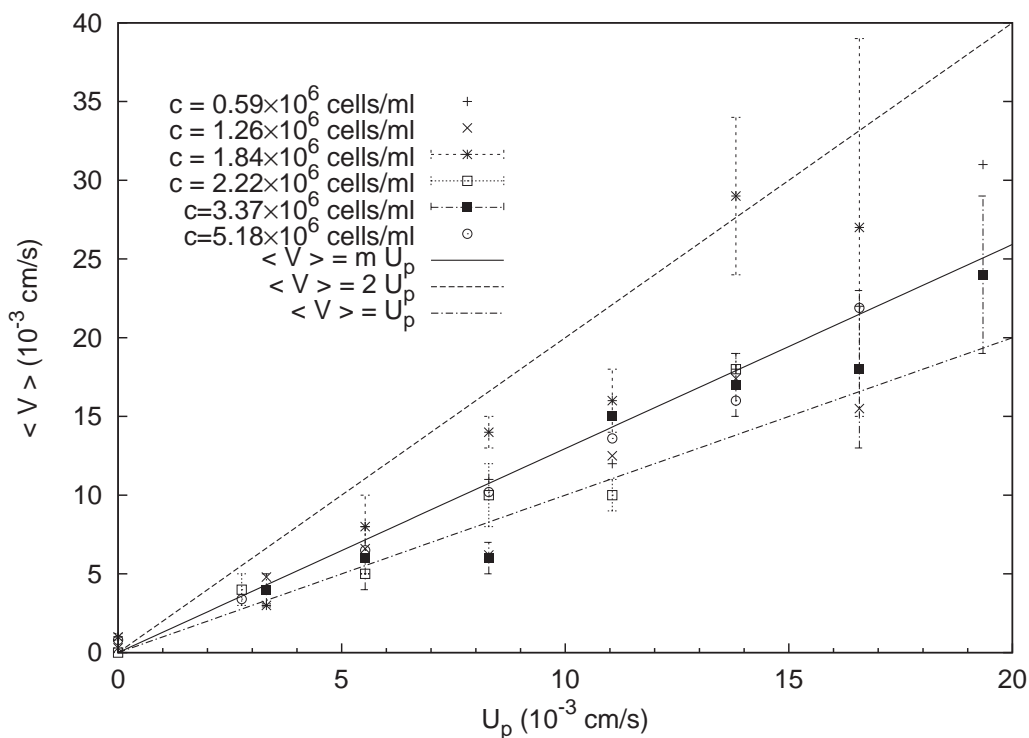
sensitive to it. We found here similar weak dependence on the tube radius for a fixed concentration, but this cannot be inferred with confidence. It would be interesting to perform experiments with greater range of tube diameters to explore these trends. Here we have also studied projections onto a vertical plane which are three dimensional patterns. The cross-sectional plume and flow structure may have an important role on the interpretations of the results.

We have investigated the experimental study of bioconvection subject to imposed flows. We find that plumes are simply distorted for weak flows and break for high flow rates. Thus the average plume drift speed $\langle V \rangle$ and inclination to the vertical $\langle \theta \rangle$, for a given flow rate, do not appear to depend appreciably on concentration in the range investigated. On the other hand, the plots of the final pattern wavelength as a function of the flow rate for different concentrations shows that transitions in the pattern dynamics occur at critical flow rates that are sensitive to concentration.

Now we discuss our results in the context of approximations of the recent model of bioconvection (see Pedley and Kessler [114]). For the case of no imposed flow, preliminary calculations (not listed) shows the existence of a steady-state profile in a horizontal tube, with most cells concentrated towards the top, consistent with the case of bioconvection between two horizontal sheets. This kind of distribution may lead to an overturning instability, as found by Hill *et al.* [64], Bees and Hill [9] for different geometries. Gyrotactic instabilities may also happen where the cells are focused into plumes as a result of self-driven flow. A question may arise that whether overturning or gyrotactic instabilities occur before the steady state has been achieved. It is worth to mention that in the presence of cells in the tube, fluid motion decay with a time scale, $\tau_v = a^2/\nu$, where a is the radius of the tube and ν is the kinematic viscosity. For the case of biggest tube diameter (tube A) $a = 0.55$ cm, and taking $\nu = 10^{-2}$ cm² s⁻¹, we compute $\tau_v = 30$ s. An unstable density profile will be established in the time it takes a cell to swim the lengthscale a , $\tau_0 = a/V_s$, where V_s is the cell swimming speed and as found for *Chlamydomonas* as $V_s = 10^{-2}$ cm s⁻¹, $\tau_0 = 55$ s. After comparing from the time for onset of initial instability $\tau_i = 30$ s (see Figure 4.15), we infer for the tube A that $\tau_v \simeq \tau_i < \tau_0$, the instability occurs approximately when mixing effects have decayed but a little before the steady-state profile has been established. Similarly we found $\tau_v \simeq \tau_i < \tau_0$ and $\tau_v < \tau_i \simeq \tau_0$ for tube B and tube C (the steady-state has been established before pattern onset with negligible mixing effects) respectively. Since patterns will likely be generated by an overturning instability



(a)



(b)

Figure 4.22: Plot of (a) the average angles and (b) average plume drift speed as functions of the mean flow speed for all concentrations. Neither of these measures appears to depend strongly on concentration. Linear fits to data for all concentrations are also shown, and in the case of (b) the plume drift speed, the fit (solid line) is compared with the prediction for the mean (dot-dashed) and maximum (dashed) flow speeds for the Poiseuille flow.

for lower concentration suspensions.

In the presence of the flow the evolution of patterns results from the coupling between the imposed suspension flux and bioconvection circulation. In this study flow is laminar for the flow rates investigated based on the maximum Poiseuille flow speed U is $O(1)$. The cells are advected horizontally, but the plumes of falling cells redistribute fluid, modifying the flow. In general, the secondary flows significantly alter the mean flow profile from its cell-less Poiseuille state, and the result suggest that the mean profiles are similar to plug flow sometimes. Since *C. augustae* are spherical shape so a balance between viscous and gravitational torques enables us to find the angle to the vertical, ψ at which these gyrotactic cells swim in a shear flow with vorticity ω . Bees *et al.* found that stable orientation requires $\omega \leq \omega_c = 1/B = 0.3 \text{ s}^{-1}$, where B is the gyrotactic reorientation time, otherwise cells tumble. The vorticity for the Poiseuille flow profile can be defined as $\omega(r) = 2Ur/a^2$, and for plug flow as $\omega(r) = 0$. If Poiseuille flow is assumed with the mean flow rates of $0.003 - 0.02 \text{ cm s}^{-1}$, the largest shear is smaller than ω_c , with $\omega_{\max} \equiv \omega(a) = 0.03 - 0.2 \text{ s}^{-1}$ and thus maximum inclinations ranging from 6° to 43° . Thus, we do not expect the formation of layers induced by gyrotactically trapped tumbling cells, as investigated by Durham *et al.* [38], except perhaps near the boundaries for flatter flow profiles.

The results of the investigation shows that for small to moderate flow rates, plume remain whole but are distorted by the flow, starting at the top of the tube, tilting from the vertical and then bending back at the bottom of the tube. This suggests that the circulation caused by descending plumes dominates that due to the imposed horizontal advection. An important aspect of the plumes is that they appear to translate horizontally at a fixed average speed $\langle V \rangle$, mostly preserving their shape during their lifetime. On the other hand, it is hard interpret the progressive ‘braking’ of curved plume structures into angled linear plumes as the flow rate is increased. It is also evident that stronger imposed flow disrupt bioconvection circulation to some degree. One hypothesis is that for small flows the bioconvective circulation cells adjust and translate with the mean flow profile speed, but when the flow becomes too strong the plumes stagger, splitting the large closed streamlines. The dynamical transitions highlighted from the measurements of the dominant pattern wavelength are intriguing. We conclude from the results shown in the Figure 4.21 that pattern transitions occur at higher flow rates for larger concentrations. This makes sense intuitively if we consider that for higher concentrations we expect a

stronger cell-induced circulation, which will be more stable to perturbations by the imposed flow. This further infer that patterns are affected at all non-zero flow rates, but are severely disrupted, with dramatic transitions in the plume dynamics, only beyond a concentration-dependent critical flow rate. The transition only affect the bioconvective circulation and so plume structure, which answer the question why the average plume speed $\langle V \rangle$ and average angle $\langle \theta \rangle$ do not depend on the concentration of the suspension.

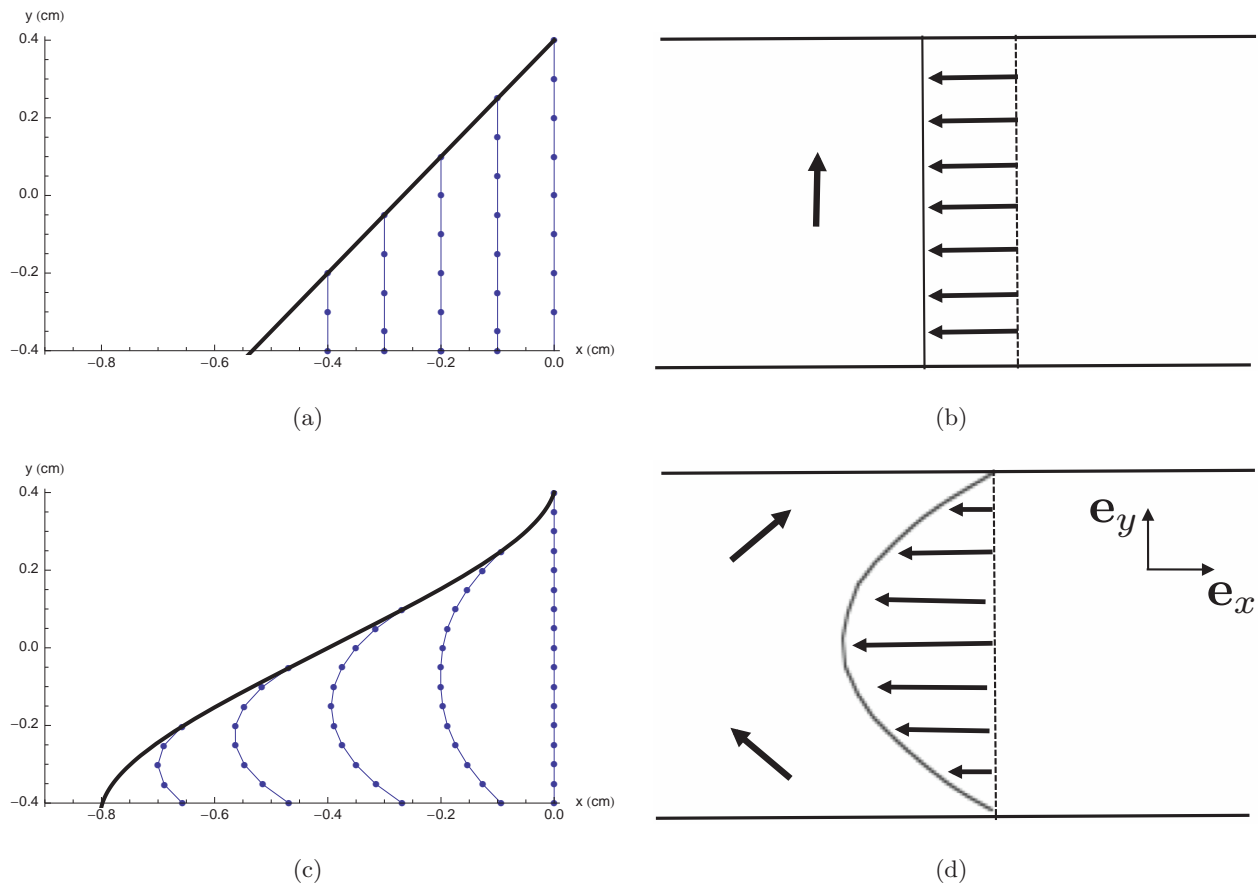


Figure 4.23: Evolution of cell positions for (a) Plug and (c) Poiseuille flows, according to the simplified description, a line of cells (thin lines) released at equally spaced positions across the tube collapses and deforms while advected for (c), while it collapses vertically in (a). The stages in evolution are 20 s apart. The upper envelope (thick line) is the trajectory of cells released at the top of the tube, for the above defined two flow situations.

To further understand the cell dynamics in flows, we consider the plume structure in a vertical plane at the centre of the tube, with two-dimensional (for simplicity) cartesian coordinates (x, y) as shown in the Figure 4.23. At its simplest, the position of a cell is subject to horizontal advection by the mean flow profile, $u(y)$, and vertical advection in

a plume, with constant speed V . Additionally, each cell swims at an angle to the vertical due to gyrotaxis with velocity

$$\mathbf{V}_c = V_s(-B\omega(y), \sqrt{1 - (B\omega(y))^2}),$$

such that

$$\dot{x}(t) = u(y) - V_s B\omega(y),$$

and

$$\dot{y}(t) = -V + V_s \sqrt{1 - B^2\omega(y)^2}. \quad (4.6)$$

The solution of the above equation (4.6) for the following initial conditions (x_0, y_0) , with $B = 3.4 \text{ s}$, $V = 0.0175 \text{ cm s}^{-1}$, $V_s = 0.01 \text{ cm s}^{-1}$, $a = 0.4 \text{ cm}$, and $U = 0.01 \text{ cm s}^{-1}$ are shown in the Figure 4.23. Here, the thick line shows the path of a cell released at the top of the tube $(0, a)$ which represents a plume that is fed from the top. It is also interesting to note from Figure 4.23 that in Poiseuille flow, the path is curved due to the flow profile and at the top and bottom shear induces diagonal gyrotactic reorientation (arrows). The cells on average move diagonally downwards but swim upwards in the case of plug flow. Additionally, the series of thin lines in Figure 4.23 shows the evolution of a vertical line of cells, initially across the tube, at time interval of 20 s. The line translates with the horizontal component of the swimming velocity at the bottom as it collapses and deforms for the case of Poiseuille flow whereas for plug flow the line remains vertical as it collapses and translates. Thus from this argument we infer that the behaviour of the plumes that we observe experimentally could result mean flow that is intermediate between Poiseuille and plug flow. In particular, the curved plumes are reminiscent of those for Poiseuille flow but the curved plumes translate with a fixed shape as though they were in plug flow. In addition to that Figure 4.22 illustrate the fact that plumes drift at a speed closer to plug flow than Poiseuille flow. Thus we conclude that gyrotactic reorientation by the imposed flow does not lead *per se* to focusing (convergent trajectories) because advection by the flow and gravity are not collinear as found in vertical tubes (see Kessler [80]), although locally cells drive the flow and will focus as a result.

The study and findings of transport of cells in tubes has enormous implications. For the case of vertical tubes, cells are subject to a modified Taylor-Aris dispersion and are transported within a plume parallel to the flow, with advective swimming and diffusive contributions (see Bees and Croze [11]). On the other hand, in our case of horizontal

tubes, results demonstrate different situation, with cells transported in numerous plumes translating at fixed speeds, $\langle V \rangle$.

4.10 Conclusion

In this chapter we have established the techniques and methodology, to quantitatively record the attributes of bioconvection pattern formation in a horizontal cylindrical tube. Here we have analyzed dominant initial instability and final pattern wavelength as a function of time, suspension concentration and tube diameter for the case of no flow problems. On the other hand, for the case of imposed flow problems we have explored the final pattern wavelength as a function of time, suspension concentration and rate of imposed flow. A consistent methodology of sub-culturing and cell concentration for young and motile cells was adopted to obtain repeatable and reproducible results for suspension cell concentrations. We have employed three cylindrical tubes of variable diameter for static experiments whereas tube B of diameter 0.8 cm was used only for imposed flow experiments. Two different automated mixing protocols were employed to control the initial concentration distribution from which pattern forms. The first mixing procedure was conducted outside the tube whereas the second method was performed mechanically inside the tube to get homogeneously mixed suspension. After recording the images following the method formulated by Bees and Hill [7] and using the double logarithm fit defined by Cziráková *et al.* [37] to the wavenumber, we have extracted the dominant wavenumber. The most important case for no flow experiments is initial instability wavenumber before any non-linear fully developed pattern, as these can be analyzed and compared with the linear analysis of the gyrotaxis models. Trends were found and investigated, for initial and final pattern wavelengths by varying the cell concentrations and tube diameters for the two different mixing procedures. For flow experiments trends were found for pattern wavelength as a function of cell concentrations and flow rate.

The results from experiments show that even very weak laminar flows are sufficient to perturb bioconvection patterns and complex structures persist in the flow for larger flow rates, rather than flow simply having a mixing effect. The inclusion of motile cells seems to modify the mean flow to be more like plug flow than Poiseuille flow. In future experiments should be conducted to measure the (mean) horizontal flows using particle tracking or PIV. Most of the bioreactors designs involved arrangements of horizontal,

vertical and/or inclined tubes in which cells can be transient turbulent or turbulent flow to maximize mixing and equalize light exposure (see Grima *et al.* [52], García-González *et al.* [42], Chisti [30]). It is important to establish the most efficient flow rates for maximum biomass production with minimal energy consumption, and how the optical properties of bioconvecting suspensions (transmittance) change with the flow and couple to growth. Thus, insights into the transition to turbulence in the presence of motile cells will be invaluable, as will an understanding of how cells are arranged within a developed turbulent pipe flow (see Lewis [93]). The experiments performed in this chapter represent a first step in this direction.

Advected bioconvection in horizontal tubes theoretically has not been solved in detail yet. The main challenge is to predict the average inclination and speed of plumes formed, as well as the flow transitions observed, as the function of concentration and tube diameter. However, an open challenge is how to predict the effective transport properties of swimming cells in laminar and turbulent regimes in tubes of arbitrary orientation.

Chapter 5

Linear analysis of advected gyrotactic bioconvection in a horizontal tube: derivations of linear stability equations and future research directions

5.1 Synopsis

In this chapter, we have analyzed the initiation of pattern formation due to the effect of imposed weak Poiseuille flow on a fluid of finite depth, for Pedley and Kessler's [113] model of bioconvection. Here, we have followed the Bees and Hill [9] technique by incorporating the cell's random swimming in a realistic geometry. The aim of the work is to compare the results using linear analysis for the pattern wavelength with the experimental observations and trends as discussed in chapter 4. The mathematical modelling of the problem with equilibrium solution is carried out whereas numerical analysis is need to be done for understanding and comparison with the experimental investigations mentioned above.

5.2 Introduction

Many micro-organisms such as green algae exhibits taxes or biased motion relative to external or local cues. *Chlamydomonas sp.* due to he centre-of-gravity offset from the geometric centre is gravitaxis (see Kessler [82]). Additionally, a balance between viscous and gravitational torque can bias these cells to swim towards the downwelling regions termed as gyrotactic instability. After a series of experiments Kessler [82], [83] found that for a suspension of gyrotactic *Chlamydomonas nivalis* in a vertical tube, cells focused at the centre for down flowing flow and scattered towards the edge for up flowing flow. For shallow containers such as petri dishes Bees and Hill [7] recorded intricate bioconvection patterns formation in just tens of seconds, with characteristic length scales of millimeters to centimeters. Recently, Bees and Croze [11] investigated the dispersion of the gyrotactic swimming of micro-organisms in a vertically aligned tube using Taylor-Aris dispersion theory. Literature survey reveals that bioconvection in horizontal tubes has not yet been tackled theoretically.

The main purpose of this chapter is to investigate the most unstable mode from the initial equilibrium solution for the suspension under an imposed weak poiseuille flow in a thin, long horizontal tube. The theoretical results later can be compared with the experimental observations discussed in chapter 4. Initially we derived an equilibrium solution of the full linear equations for finite depth between the two plates and later doing a small perturbation to investigate the effects of perturbation. Following the Bees and Hill [9] initially we solve Fokker-Planck equation to find the mean cell swimming speed and non-constant diffusion tensor. Bees and Hill [9] with minor corrections used the Pedley and Kessler [113] and found the full linear equations for their finite depth bioconvection model in petri dishes. Here we follow the same procedure and derived the full linear equations for the weak poiseuille flow between the two stationary horizontal plates.

5.3 Solution of the Fokker-Planck equation

In this section, the linear solution of the Fokker-Planck equation on a sphere can be found and used to calculate the mean cell swimming direction $\langle \mathbf{p} \rangle$ and diffusion tensor \mathbf{D} . The probability density function (p.d.f.) for cell swimming direction on the unit sphere can be written as $f(\mathbf{p})$, where

$$\mathbf{p} = (\sin \theta \cos \phi, \sin \theta \sin \phi, \cos \theta)^T, \quad (5.1)$$

and θ is the colatitude angle measured relative to \mathbf{k} . Then, the mean cell swimming direction for bottom heavy micro-organism can be defined as

$$\mathbf{q} = \langle \mathbf{p} \rangle = \int_S \mathbf{p} f(\mathbf{p}) dS, \quad (5.2)$$

where S is the surface of the unit sphere and cell diffusivity tensor \mathbf{D} can be defined as

$$\mathbf{D}(t) = \int_0^\infty \langle \mathbf{V}_r(t) \mathbf{V}_r(t-t') \rangle dt' \quad (5.3)$$

Here \mathbf{V}_r is the cell velocity relative to its mean velocity. Using the assumption that the cell's swimming direction changes less than a fixed assumed angle as discussed by Bees and Hill [9] and thus, we can write the diffusivity tensor as

$$\mathbf{D} \approx D^c \langle (\mathbf{p} - \mathbf{q})(\mathbf{p} - \mathbf{q}) \rangle, \quad (5.4)$$

where, $D^c = V_s^2 \tau$ is the characteristic diffusion scale, V_s is the mean cell swimming speed and τ is the direction correlation time scale.

The probability density function $f(\mathbf{p})$ defined above in equation (5.1) in spherical polar coordinates, satisfies the Fokker-Plank equation which can be written as

$$\frac{\partial f}{\partial t} + \nabla \cdot (\dot{\mathbf{p}} f) = D_r \nabla^2 f, \quad (5.5)$$

where $\dot{\mathbf{p}}$

$$\dot{\mathbf{p}} = \frac{1}{2B} [\mathbf{k} - (\mathbf{k} \cdot \mathbf{p}) \mathbf{p}] + \frac{1}{2} \boldsymbol{\Omega} \wedge \mathbf{p} + \alpha_0 \mathbf{E} \cdot \mathbf{p} \cdot [\mathbf{I} - \mathbf{p} \mathbf{p}], \quad (5.6)$$

with

$$B = \frac{\mu \alpha_\perp}{2hg\rho} \quad \text{and} \quad \alpha_0 = \frac{a^2 - b^2}{a^2 + b^2},$$

are the gyrotactic reorientation time scale and eccentricity of the cell respectively. Here, D_r is a constant rotational diffusivity associated with the rotational Brownian effects during the swimming of cells, h is the centre-of-mass offset from the geometric centre, a and b are the major and minor axis of the cell body respectively and α_\perp is the dimensionless resistance coefficient for rotation about an axis perpendicular to \mathbf{p} .

Following the method of solution by Bees and Hill [9], we assume the steady Fokker-Planck equation for orientation of bottom heavy gyrotactic swimming cells at (\mathbf{x}, t) as

$$\nabla \cdot (\dot{\mathbf{p}} f) = D_r \nabla^2 f, \quad (5.7)$$

Since $\boldsymbol{\Omega}$ is the local vorticity vector and \mathbf{E} is the rate of strain tensor. We non dimensionalize such that

$$\boldsymbol{\Omega} = \left(\frac{D^c}{H^2} \right) \boldsymbol{\omega} \quad \text{and} \quad \mathbf{E} = \left(\frac{D^c}{H^2} \right) \mathbf{e},$$

where, D^c is the characteristic diffusion scale and H is the depth of the suspension.

For spherical cell body shape we take cell eccentricity $\alpha_0 = 0$, then above steady Fokker-Planck equation (5.7) using (5.6) takes the form as

$$\mathbf{k} \cdot \nabla f - 2(\mathbf{k} \cdot \mathbf{p})f + \eta \boldsymbol{\omega} \cdot (\mathbf{p} \wedge \nabla f) = \lambda^{-1} \nabla^2 f, \quad (5.8)$$

where

$$\lambda = \frac{1}{2D_r B}, \quad \text{and} \quad \eta = \frac{BD_r}{H^2}. \quad (5.9)$$

Here η is known as the non-dimensional gyrotaxis parameter. The expressions for mean cell swimming direction (5.2) and diffusion tensor (5.4) can be obtained for all values of $\boldsymbol{\omega}$ by expanding equation (5.8) in spherical harmonics. Following the procedures used by Bees and Hill [9] and to avoid the repetitions of the detailed calculations we can use the expressions directly. In particular for vorticity $\boldsymbol{\omega} = \omega \mathbf{j}$, we shall write

$$\mathbf{q}(\mathbf{x}, t) = \langle \mathbf{p} \rangle = \int_S \begin{bmatrix} \sin \theta \cos \phi \\ \sin \theta \sin \phi \\ \cos \theta \end{bmatrix} f(\theta, \phi) dS = \begin{bmatrix} \frac{4\pi}{3} A_1^1 \\ 0 \\ \frac{4\pi}{3} A_1^0 \end{bmatrix} = \begin{bmatrix} q_1(\zeta(\mathbf{x}, t)) \\ 0 \\ q_3(\zeta(\mathbf{x}, t)) \end{bmatrix},$$

and

$$\begin{aligned} \mathbf{D} &= D^c [\langle \mathbf{p}\mathbf{p} \rangle - \langle \mathbf{p} \rangle^2] \\ &= \aleph D^c \begin{bmatrix} \frac{4\pi}{3} A_0^0 - \frac{4\pi}{15} A_2^0 + \frac{8\pi}{5} A_2^2 - \frac{16\pi^2}{9\aleph} (A_1^1)^2 & 0 & \frac{4\pi}{5} A_2^1 - \frac{16\pi^2}{9\aleph} A_1^1 A_1^0 \\ 0 & \frac{4\pi}{3} A_0^0 - \frac{4\pi}{15} A_2^0 - \frac{8\pi}{5} A_2^2 & 0 \\ \frac{4\pi}{5} A_2^1 - \frac{16\pi^2}{9\aleph} A_1^1 A_1^0 & 0 & \frac{8\pi}{15} A_2^0 + \frac{4\pi}{3} A_0^0 - \frac{16\pi^2}{9\aleph} (A_1^0)^2 \end{bmatrix}, \\ &= D^c \begin{bmatrix} D_{11}(\zeta(\mathbf{x}, t)) & 0 & D_{13}(\zeta(\mathbf{x}, t)) \\ 0 & D_{22}(\zeta(\mathbf{x}, t)) & 0 \\ D_{31}(\zeta(\mathbf{x}, t)) & 0 & D_{33}(\zeta(\mathbf{x}, t)) \end{bmatrix}, \end{aligned}$$

where, $q_i(\zeta(\mathbf{x}, t))$ and $D_{ij}(\zeta(\mathbf{x}, t))$ are the expressions for unknown functions in the spherical harmonic expansion. Following Bees and Hill [9] and solving equations for second order approximation results in the expressions as

$$\begin{aligned} A_0^0 &= \frac{1}{4\pi}, \\ A_1^0 &= \frac{825(5589 + 2420\zeta^2)}{4\pi(1098075\zeta^4 + 2363735\zeta^2 + 2772144)}, \\ A_1^1 &= \frac{1815(1887\zeta + 1210\zeta^3)}{4\pi(1098075\zeta^4 + 2363735\zeta^2 + 2772144)}, \end{aligned}$$

$$A_2^0 = \frac{605(11178 + 4235\zeta^2)}{8\pi(1098075\zeta^4 + 2363735\zeta^2 + 2772144)},$$

$$A_2^1 = \frac{2495625\zeta}{4\pi(1098075\zeta^4 + 2363735\zeta^2 + 2772144)},$$

$$A_2^2 = \frac{1830125\zeta^2}{16\pi(1098075\zeta^4 + 2363735\zeta^2 + 2772144)},$$

where ratio $\aleph = \frac{\langle V^2 \rangle}{V_s^2}$ and $\zeta(\mathbf{x}, t) = \eta\boldsymbol{\omega}$ and $\boldsymbol{\omega}$ represents the vorticity.

5.4 Modelling the linear bioconvection equations

Following Pedley and Kessler [113], we assume that the suspension is incompressible, then the equation of continuity takes the form as

$$\nabla \cdot \mathbf{u} = 0, \quad (5.10)$$

and the equation of momentum for dilute suspension of swimming cells, using the Boussinesq approximation, takes the form

$$\rho \frac{D\mathbf{u}}{Dt} = \rho \left[\frac{\partial \mathbf{u}}{\partial t} + (\mathbf{u} \cdot \nabla) \mathbf{u} \right] = -\nabla P_e + \mu \nabla^2 \mathbf{u} + nv \Delta \rho \mathbf{g}. \quad (5.11)$$

where $\mathbf{u}(\mathbf{x})$ is the velocity of the suspension of swimming cells, $n(\mathbf{x})$ is the local cell concentration, μ is the fluid viscosity, $p_e(\mathbf{x})$ is the excess pressure over hydrostatic, v is the mean volume of cell and $\Delta \rho$ is the difference between the cell density and fluid density.

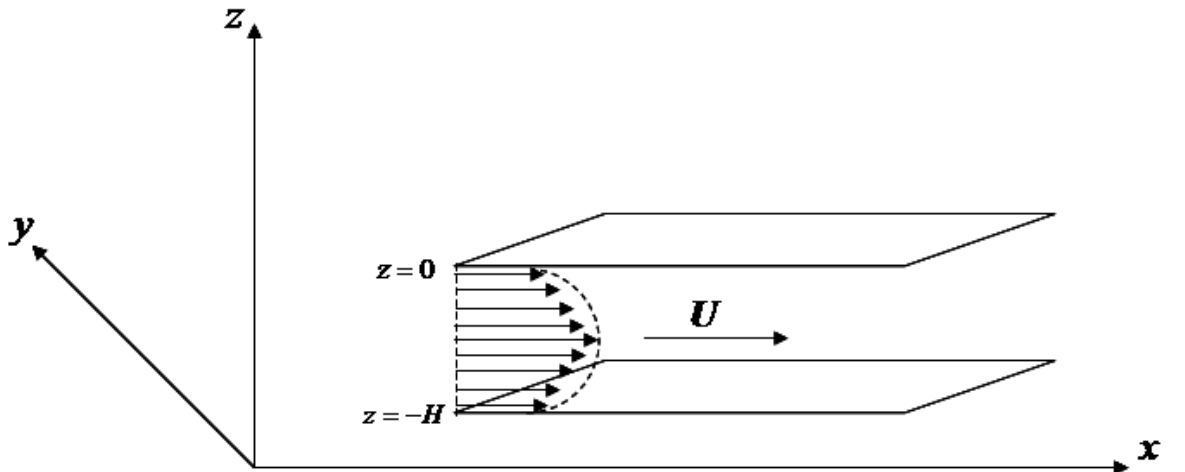


Figure 5.1: Linear bioconvection subject to weak poiseuille flow between two plates.

Name with dimensions	Dimensionless form
Length - $[L]$	$\mathbf{x} = H \tilde{\mathbf{x}}$
Velocity - $[L S^{-1}]$	$\mathbf{u} = \left(\frac{D^c}{H}\right) \tilde{\mathbf{u}}$
Time - $[S]$	$t = \left(\frac{H^2}{D^c}\right) \tilde{t}$
Cell concentration	$n = N \tilde{n}$
Diffusion	$\mathbf{D} = D^c \tilde{\mathbf{D}}$
Peclet number	$P_e = \left(\frac{\mu D^c}{H^2}\right) \tilde{P}_e$

Table 5.1: Table of non-dimensionalisation.

The cell conservation equation can be defined as

$$-\nabla \cdot [n(\mathbf{u} + V_s \mathbf{q}) - \mathbf{D} \cdot \nabla n] = \frac{\partial n}{\partial t}, \quad (5.12)$$

where $\mathbf{q}(\mathbf{x}) = \langle \mathbf{p}(\mathbf{x}) \rangle$ is the mean cell swimming direction, V_s is the mean cell swimming speed and $\mathbf{D}(\mathbf{x})$ is the cell diffusion tensor.

The no-slip boundary conditions for the suspension enclosed between the two rigid horizontal stationary plates, can be defined as

$$\mathbf{u} = \mathbf{0}, \quad \text{at } z = -H, 0, \quad (5.13)$$

and zero cell flux perpendicular to the plates wall gives,

$$\mathbf{k} \cdot [n(\mathbf{u} + V_s \mathbf{q}) - \mathbf{D} \cdot \nabla n] = 0, \quad \text{at } z = -H, 0. \quad (5.14)$$

where \mathbf{k} is a unit vector directed vertically upwards.

Now using the above non-dimensional terms given in the Table (5.1) and after dropping the tildes we can write the system of equations again in non-dimensionalized form as

$$\nabla \cdot \mathbf{u} = 0, \quad (5.15)$$

$$S_c^{-1} \frac{D\mathbf{u}}{Dt} = -\nabla P_e - \gamma n \mathbf{k} + \nabla^2 \mathbf{u}, \quad (5.16)$$

and

$$\frac{\partial n}{\partial t} = -\nabla \cdot [n(\mathbf{u} + \beta \mathbf{q}) - \mathbf{D} \cdot \nabla n], \quad (5.17)$$

where

$$\beta = \frac{H V_s}{D^c}, \quad \text{and} \quad S_c = \frac{\nu}{D^c},$$

are the swimming Peclet number and Schmidt number respectively. The Rayleigh number is defined as

$$r = \gamma d = \frac{Nvg\Delta\rho H^3}{\nu\rho D^c}, \quad (5.18)$$

which is based on the depth of the whole layer not on the sub-layer depth as explained in Bees and Hill [9]. The non-dimensionalized form of the boundary conditions can be rewritten as

$$\mathbf{u} = \mathbf{0}, \quad \text{at } z = 0, -1 \quad (5.19)$$

and

$$\mathbf{k} \cdot [n(\mathbf{u} + \beta\mathbf{q}) - \mathbf{D} \cdot \nabla n] = 0, \quad \text{at } z = 0, -1. \quad (5.20)$$

Now for the weak Poiseuille flow between the two stationary parallel plates, we can define the velocity of the suspension as

$$\mathbf{u} = u^0(z)\mathbf{i} = -\frac{4U}{H^2}(z+H)z\mathbf{i}, \quad (5.21)$$

which satisfy the equation of continuity (5.15) and U is the maximum flow speed observed at the centre of the two stationary plates as shown in the Figure (5.1). The mean speed of the suspension can be calculated as

$$\bar{\mathbf{u}} = \frac{1}{H} \int_{-H}^0 u^0(z) dz = \frac{2U}{3}, \quad (5.22)$$

which can further simplifies to give

$$u^0(z) = \frac{6\bar{u}}{H^2}(z+H)z. \quad (5.23)$$

Thus using the Table (5.1) and dropping the tildes we can rewrite the velocity of the suspension for the weak poiseuille flow between the two rigid parallel plates in non-dimensional form as

$$\mathbf{u} = u^0(z)\mathbf{i} = -\frac{4UH}{D^c}(z+1)z\mathbf{i}, \quad (5.24)$$

similarly, mean speed can be calculated in non-dimensional form as

$$\bar{\mathbf{u}} = \frac{D^c}{H} \int_{-1}^0 u^0(z) dz = \frac{2}{3} \frac{uH}{D^c}, \quad (5.25)$$

which further can be written as

$$u^0(z) = -\frac{6\bar{u}H}{D^c}(z+1)z. \quad (5.26)$$

Thus finally, velocity of the weak poiseuille flow between the two stationary parallel plates using (5.26), can be defined as

$$\mathbf{u} = u^0(z)\mathbf{i} = -6P_e(z+1)z\mathbf{i}, \quad (5.27)$$

where

$$P_e = \frac{\bar{U}H}{D^c}$$

is the Peclet number. The solutions of this form can exist that are partially uncoupled from the cell problem. Thus using the velocity of the suspension for weak poiseuille flow (5.27), Navier-Stokes equations (5.16) takes the form as

$$0 = -\partial_x p_e + \partial_z^2[-6P_e(z+1)z], \quad (5.28)$$

$$0 = -\partial_y p_e,$$

$$0 = -\partial_z p_e - \gamma n,$$

which further simplifies after integration to give

$$p_e = -12P_e x - \int \gamma n(z) dz + \text{constant}. \quad (5.29)$$

Now we define the vorticity for the weak poiseuille flow between the two rigid parallel plates as

$$\boldsymbol{\omega} = \nabla \wedge \mathbf{u} = -6P_e(2z+1)\mathbf{j},$$

then equation (5.17) for cell conservation takes the form as

$$0 = -\partial_z[\beta n^0 q_3 - D_{33}\partial_z n^0], \quad (5.30)$$

which is the flux in the \mathbf{k} direction and is zero at $z = 0, -1$ using the boundary condition.

Hence we solve the above equation to get

$$\beta n^0(z)q_3 = D_{33}\partial_z n^0(z) = D_{33}\frac{d}{dz}n^0,$$

$$\frac{\beta q_3}{D_{33}} = \frac{1}{n^0(z)}\frac{d}{dz}n^0(z),$$

$$[\ln n^0(z)]_0^z = \int_0^z \frac{\beta q_3}{D_{33}} dz,$$

which further simplifies to give the equilibrium solution

$$n^0(z) = n(0) \exp\left[\int_0^z \frac{\beta q_3}{D_{33}} dz\right]. \quad (5.31)$$

Here if we substitute $n(0) =: 1$ then we have non-dimensional cell concentration with the dimensional cell concentration at the upper surface ($N =: \text{dim } n(0)$). Also for no flow equilibrium state we substitute $Pe = 0$, in equation (5.27) which implies $\mathbf{u} = \mathbf{0}$, then we have found $q_3 = k_1$ and $D_{33} = k_2$ both constants as found by Pedley and Kessler [113]. Now using above values in equilibrium solution (5.31) we can rewrite as

$$n^0(z) = \exp\left[\beta \frac{k_1}{k_2} z\right], \quad (5.32)$$

which is exactly the same equilibrium solution as found by Bees and Hill [9] with different notations. In general for non-zero flow situation i.e. $Pe \neq 0$, and $\mathbf{u} \neq 0$, we need to calculate equilibrium solution from equation (5.31) using the already known solutions for the values of $q_3(\boldsymbol{\omega})$ and $D_{33}(\boldsymbol{\omega})$ from Bees *et al.* [8].

5.4.1 Stability analysis

After discussing the equilibrium solution now we consider a perturbation from this equilibrium solution by substituting

$$\begin{aligned} \mathbf{u} &= \mathbf{u}^0(z) + \epsilon \mathbf{u}^1(x, z, t), \\ n &= n^0(z) + \epsilon n^1(x, z, t), \\ pe &= pe^0(z) + \epsilon pe^1(x, z, t), \\ \mathbf{q} &= \mathbf{q}^0(z) + \epsilon \mathbf{q}^1(x, z, t), \\ \mathbf{D} &= \mathbf{D}^0(z) + \epsilon \mathbf{D}^1(x, z, t). \end{aligned} \quad (5.33)$$

Also vorticity perturbation can be defined as

$$\boldsymbol{\omega} = \nabla \wedge u^0(z) + \epsilon \nabla \wedge u^1(x, z, t) = -6Pe(2z + 1)\mathbf{j} + \epsilon \nabla \wedge u^1(x, z, t),$$

where $u^0(z)$ and $n^0(z)$ are equilibrium solutions obtained in equations (5.27) and (5.31) respectively.

For $O(\epsilon)$, the governing system of equations takes the form as

$$\nabla \cdot \mathbf{u}^1 = 0, \quad (5.34)$$

$$S_c^{-1} \frac{\partial \mathbf{u}^1}{\partial t} = -\nabla pe^1 - \gamma n^1 \mathbf{k} + \nabla^2 \mathbf{u}^1, \quad (5.35)$$

and

$$\frac{\partial n^1}{\partial t} = -\nabla \cdot [n^1 \mathbf{u}^0 + n^0 \mathbf{u}^1 + \beta n^1 \mathbf{q}^0 + \beta n^0 \mathbf{q}^1 - \mathbf{D}^1 \cdot \nabla n^0 - \mathbf{D}^0 \cdot \nabla n^1]. \quad (5.36)$$

Now to find the solution of the above five p.d.e's in five unknowns we try to reduce them into two p.d.e.'s in two unknowns. As a first step we take the divergence of the equation (5.34) which gives

$$0 = -\nabla^2 p e^1 - \gamma \partial_3 n^1, \quad (5.37)$$

and secondly, we take the Laplacian of the third component of the equation (5.35) which leads to

$$S_c^{-1} \partial_t (\nabla^2 u_3^1) = -\partial_3 (\nabla^2 p e^1) - \gamma \nabla^2 n^1 + \nabla^2 \nabla^2 \mathbf{u}_3^1,$$

which further simplifies by using equation (5.37) into

$$S_c^{-1} \partial_t (\nabla^2 u_3^1) = -\gamma \partial_3 \partial_3 n^1 - \gamma \nabla^2 n^1 + \nabla^4 \mathbf{u}_3^1. \quad (5.38)$$

For the solution of the equation (5.36), we require an understanding of the \mathbf{q}^0 , \mathbf{q}^1 , \mathbf{D}^0 , and \mathbf{D}^1 . These are the functions of the vorticity $\boldsymbol{\omega}$. As we know that

$$\mathbf{u} = \mathbf{u}^0(z) + \epsilon \mathbf{u}^1(x, z, t),$$

then, we can define

$$\boldsymbol{\omega} = \omega^0(z) \mathbf{j} + \epsilon \omega^1(x, z, t) \mathbf{j}, \quad (5.39)$$

with

$$\omega^0 = -6Pe(2z + 1), \quad \text{and} \quad \omega^1 = \partial_z u_1^1 = \partial_z u_3^1.$$

Also

$$\mathbf{q} = \begin{bmatrix} q_1 \\ 0 \\ q_3 \end{bmatrix} (\eta \boldsymbol{\omega}), \quad (5.40)$$

now, using the Taylor expansion we can write as

$$q_i^0 + \epsilon q_i^1 + O(\epsilon^2) = q_i[\eta(\omega^0 + \epsilon \omega^1)] = q_i(\eta \omega^0) + \epsilon \eta \omega^1 q_i'(\eta \omega^0) + O(\epsilon^2),$$

which further implies

$$q_i^0 = q_i(\eta \omega^0), \quad \text{and} \quad q_i^1 = \eta \omega^1 q_i'(\eta \omega^0).$$

Hence equation (5.36) takes the form as

$$\frac{\partial n^1}{\partial t} = -\nabla \cdot [n^1 \mathbf{u}^0 + n^0 \mathbf{u}^1 + \beta n^1 q_i(\eta \omega^0) + \beta n^0 \eta \omega^1 q_i'(\eta \omega^0) - \eta \omega^1 \mathbf{D}'(\eta \omega^0) \cdot \nabla n^0 - \mathbf{D}(\eta \omega^0) \cdot \nabla n^1]. \quad (5.41)$$

From now on words, the dependence of \mathbf{q} and \mathbf{D} on $(\eta\omega^0)$ is implied. Also

$$\omega^0 = -6Pe(2z + 1), \quad \text{and} \quad \partial_3\omega^0 = -12Pe.$$

Using equation (5.34) we can rewrite equation (5.41) as

$$\begin{aligned} \frac{\partial n^1}{\partial t} = & -\mathbf{u}^0 \cdot \nabla n^1 - u_3^1 \partial_3 n^0 - \beta \mathbf{q} \cdot \nabla n^1 - \beta \eta n^1 q_i' \partial_i \omega^0 - \beta \eta q_i' \omega^1 \partial_i n^0 \\ & - \beta \eta q_i' n^0 \partial_i \omega^1 - \beta \eta^2 n^0 \omega^1 q_i'' \partial_i \omega^0 + \eta \partial_i (\omega^1 D'_{i3} \partial_3 n^0) + \partial_i (D_{ij} \partial_j n^1), \end{aligned} \quad (5.42)$$

which can be rearranged and takes the form as

$$\begin{aligned} [\partial t + u_1^0 \partial_1 + \beta q_i \partial_i - 12Pe\beta\eta q_3' + 12Pe\eta D'_{3j} \partial_j - D_{ij} \partial_i \partial_j] n^1 = & \quad (5.43) \\ -(\partial_3 n^0) u_3^1 + [-\beta \eta q_3' \partial_3 n^0 - \eta \partial_i D'_{i3} \partial_3 n^0 - 12Pe\beta \eta^2 n^0 q_3'' \\ + \eta D''_{33} \partial_3 \partial_3 n^0 + \eta \partial_3 n^0 D'_{i3} \partial_i - 12Pe \partial_3 n^0 D''_{33}] \omega^1, \end{aligned}$$

since

$$\omega^1 = \partial_z u_1^1 - \partial_x u_3^1 = \partial_3 u_1^1 - \partial_1 u_3^1.$$

Thus we have now reduced from five to two p.d.e.'s (5.38) and (5.43), in terms of the independent variables u_1^1 , u_3^1 and n^1 .

Now we introduce a horizontal platform and an exponential component in t . The particular choices of normal modes can be defined as

$$u_1^1 = U(z)e^{ikx+\sigma t}, \quad (5.44)$$

$$u_3^1 = W(z)e^{ikx+\sigma t}, \quad (5.45)$$

and

$$n^1 = \Phi(z)e^{ikx+\sigma t}, \quad (5.46)$$

then equation (5.34) takes the form as

$$ikU(z) + W'(z) = 0, \quad (5.47)$$

since

$$\omega^1 = \partial_z u_1^1 - \partial_x u_3^1 = U'(z)e^{ikx+\sigma t} - ikW(z)e^{ikx+\sigma t},$$

using equation (5.47) we can write as

$$\omega^1 = \left[-\frac{W''(z)}{ik} - ikW \right] e^{ikx+\sigma t} = \frac{i}{k} [W''(z) - k^2 W(z)] e^{ikx+\sigma t},$$

then equation (5.35) becomes

$$\left[S_c^{-1}\sigma + k^2 - \frac{d^2}{dz^2}\right]\left(k^2 - \frac{d^2}{dz^2}\right)W(z) = -\gamma k^2 \Phi(z). \quad (5.48)$$

Now substituting the above equations into equation (5.41) gives

$$\begin{aligned} \left[D_{33}\frac{d^2}{dz^2} - (\beta q_3 + 12Pe\eta D'_{33} - 2ikD_{13})\frac{d}{dz}D_{11}k^2 - \sigma + \{-ik(u_1^0 + \beta q_1 \right. \\ \left. + 12Pe\eta D'_{31}) + 12Pe\eta\beta q'_3\}\right]\Phi(z) = [n^{0'} - \eta H_2\frac{d^3}{dz^3} - \eta H_1\frac{d^2}{dz^2} \\ + \eta H_2k^2\frac{d}{dz} + \eta H_1k^2]W(z), \end{aligned} \quad (5.49)$$

where

$$\begin{aligned} H_1 &= -\beta(q'_3n^{0'} + n^0q'_1ik - \eta n^0q''_312Pe)\frac{i}{k} + (D'_{33}n^{0''} + n^{0'}D'_{13}ik \\ &\quad - \eta n^{0'}D'_{33}12Pe)\frac{i}{k}, \\ H_2 &= (q'_3n^0q'_3 + n^{0'}D'_{33})\frac{i}{k}. \end{aligned} \quad (5.50)$$

Now for the case of no Poiseuille flow i.e. $\mathbf{u} = 0$, we can find that $q'_3 = 0$ and $D'_{33} = 0$ then equation (5.50) takes the form as

$$\begin{aligned} H_1 &= -\beta n^0q'_1 + n^{0'}D'_{13} = de^{dz}\left[J_1\frac{k_2}{k_1} + J_1k_1 - J_2\right], \\ H_2 &= 0, \end{aligned} \quad (5.51)$$

where

$$d = \frac{\beta k_1}{k_2},$$

which is exactly same as found by Bees and Hill [9] for the equilibrium solution.

The equations (5.48) and (5.49) need to be solved subject to the boundary conditions

$$\mathbf{u} = \mathbf{0}, \quad \text{on } z = 0, -1,$$

and

$$\mathbf{k} \cdot [n(\mathbf{u} + \beta\mathbf{q}) - \mathbf{D} \cdot \nabla n] = 0, \quad \text{on } z = 0, -1, \quad (5.52)$$

which can be written as

$$W(z) = \frac{d}{dz}W(z) = 0, \quad \text{at } z = 0, -1,$$

and

$$n_0W(z) + \beta n q_3(\omega\eta) - D_{13}\partial_1 n - D_{33}\partial_3 n = 0, \quad \text{at } z = 0, -1, \quad (5.53)$$

since $W(z) = 0$ at $z = 0, -1$ at $O(\epsilon)$ we can get

$$\beta n^1 q_3^0 + \beta n^0 q_3^1 - D_{13}^0 \partial_1 n^1 - D_{33}^0 \partial_3 n^1 - D_{13}^0 \partial_1 n^1 - D_{33}^1 \partial_3 n^0 = 0, \quad \text{at } z = 0, -1, \quad (5.54)$$

and now adopting the q and D notations we have used earlier and noting that

$$\omega^1 = \frac{i}{k} [W''(z) - k^2 W(z)] = \frac{i}{k} W''(z), \quad \text{on } z = 0, -1,$$

we can write

$$(\beta q_3 - D_{33} \frac{d}{dz}) \Phi - D_{13} i k \Phi + \frac{i}{k} \eta (\beta n^0 q_3' - D_{33}' n^{0'}) \frac{d^2}{dz^2} W(z) = 0, \quad \text{on } z = 0, -1, \quad (5.55)$$

with

$$\Phi = \Phi_r + i \Phi_i, \quad \text{and } W = W_r + i W_i.$$

Now we define the equations for the neutral curve such that

$$\text{Re } \sigma = 0, \quad \text{and } \sigma = i \sigma_i,$$

then equation (5.48) takes the form as

$$-S_c^{-1} \sigma_i (k^2 - \frac{d^2}{dz^2}) W_i + (k^2 - \frac{d^2}{dz^2})^2 W_r = -\gamma k^2 \Phi_r,$$

and

$$-S_c^{-1} \sigma_i (k^2 - \frac{d^2}{dz^2}) W_r + (k^2 - \frac{d^2}{dz^2}) W_i = -\gamma k^2 \Phi_i. \quad (5.56)$$

Also equation (5.49) takes the form as

$$\begin{aligned} & [D_{33} \frac{d^2}{dz^2} - A_3^r \frac{d}{dz} - D_{11} k^2 + A_4^r] \Phi_r - [-A_3^i \frac{d}{dz} - \sigma_i + A_4^i] \Phi_i = \\ & [n^{0'} - \eta A_1^r \frac{d^2}{dz^2} + \eta A_1^r k^2] W_r - [n^{0'} - \eta A_2^i \frac{d^3}{dz^3} - \eta A_1^i \frac{d^2}{dz^2} + \eta A_2^i k^2 \frac{d}{dz} + \eta A_1^i k^2] W_i, \end{aligned}$$

and

$$\begin{aligned} & [D_{33} \frac{d^2}{dz^2} - A_3^r \frac{d}{dz} - D_{11} k^2 + A_4^r] \Phi_i - [-A_3^i \frac{d}{dz} - \sigma_i + A_4^i] \Phi_r = \\ & [n^{0'} - \eta A_1^r \frac{d^2}{dz^2} + \eta A_1^r k^2] W_i + [n^{0'} - \eta A_2^i \frac{d^3}{dz^3} - \eta A_1^i \frac{d^2}{dz^2} + \eta A_2^i k^2 \frac{d}{dz} + \eta A_1^i k^2] W_r, \end{aligned} \quad (5.57)$$

where

$$\begin{aligned} A_1^r &= \beta n^0 q_1' - n^{0'} D_{13}', \\ A_1^i &= -\frac{\beta}{k} (q_3' n^{0'} - \eta n^0 q_3'' 12Pe) + \frac{1}{k} (D_{33}' n^{0''} - \eta n^{0'} D_{33}' 12Pe), \\ A_2^r &= 0, \end{aligned}$$

$$A_2^i = \frac{1}{k}(\beta n^0 q_3' + n^{0'} D_{33}'),$$

$$A_3^r = \beta q_3 + 12Pe\eta D_{33}',$$

$$A_3^i = -2kD_{13},$$

$$A_4^r = 12Pe\eta\beta q_3',$$

$$A_4^i = -k(u_1^0 + \beta q_1 + 12Pe\eta D_{13}'),$$

whereas the boundary conditions (5.53) can be written as

$$W_i = W_r = 0, \quad \text{on } z = 0, -1,$$

and

$$\frac{d}{dz}W_i = \frac{d}{dz}W(r) = 0, \quad \text{on } z = 0, -1, \quad (5.58)$$

also equation (5.55) takes the form

$$(\beta q_3 - D_{33} \frac{d}{dz})\Phi_r - D_{13}k\Phi_i - \frac{\eta}{k}(\beta n^0 q_3' - D_{33}'n^{0'}) \frac{d^2}{dz^2}W_i = 0, \quad \text{on } z = 0, -1,$$

and

$$(\beta q_3 - D_{33} \frac{d}{dz})\Phi_i - D_{13}k\Phi_r + \frac{\eta}{k}(\beta n^0 q_3' - D_{33}'n^{0'}) \frac{d^2}{dz^2}W_r = 0, \quad \text{on } z = 0, -1, \quad (5.59)$$

5.5 Numerical analysis

In this section we will define the method for numerical solution of the full linear equations derived earlier in section 5.4 by following the methodology by Bees and Hill [9]. Here we will incorporate a numerical scheme devised by Cash and Moore [25] and provided by Dr. D. R. Moore, named "NRK", which is a fourth order finite difference scheme that iterates using the Newton-Raphson-Kantorovich algorithm. The program is written in FORTRAN77 and following the Bees and Hill [9] routines can be rewritten which enable the program to search for the neutral curves of the equations given initial guesses for the concentration and velocity fields, Φ and W , and Rayleigh number r . The procedure involves substitution of an initial value of the wavenumber k and subsequent trial solutions were guessed until a solution is found.

As the above solution formed the basis so in the next step we can use it to find the next solution estimate for the higher value of k . Using the same methodology with small steps in k we can trace the neutral curve with an efficient number of iterations. In this process

guessing a reasonable initial value of r and the form of mesh used in the z direction are really significant. Here we will use up to eighty-one grid points to find convergent solution but this is not always true. In addition an accuracy of six significant figures is tried to obtain for convergence.

The above defined numerical technique was devised by Bees and Hill [9] for the investigations of bioconvection pattern formation in petri dishes, which worked very well. This gives motivation to employ the the same numerical technique for the tube or two plates geometry, which is the case under considerations.

After doing numerical analysis we would be in a better position to compare and verify the experimental results discussed in chapter 4.

5.6 Discussion

We have developed the linear model for the finite depth stochastic gyrotactic bioconvection pattern formation between the two fixed stationary plates geometry in the presence of the flow. At the initial stage Fokker-Planck equations were solved to calculate the mean cell swimming direction and diffusion tensor following Bees and Hill [9]. An equilibrium solution of the full linear equations for finite depth and zero flow is found. Later, a small perturbation is made which causes a weak ambient flow between the two fixed horizontal plates.

For stochastic gyrotactic bioconvection pattern formation Bees and Hill [9] using linear analysis found the possibility of obtaining a zero most unstable wavenumber or a non-zero most unstable wavenumber. They found dependency of this on the values of the gyrotactic orientation parameter α_0 and variance of the cell swimming speed. They also showed that modelling the organism's swimming in a stochastic fashion rather than deterministic is paramount important for the shape of the neutral curves. Bees and Hill [9] found that a non-zero most unstable wavenumber will always exists for the large values of gyrotactic orientation parameter.

Thus keeping in view of the method used and results of the investigations by Bees and Hill [9], we will carry out the numerical analysis of the model to get the better understanding of the experimental results of the investigations discussed in chapter 4. The challenges include prediction of a particular most unstable mode from the initial equilibrium solution, prediction of average inclination and speed of plumes and last but

not least the flow transitions observed.

The main results of this chapter is that for the first time we have derived the linear stability equations for bioconvection pattern formation in a flow between two stationary horizontal plates.

Chapter 6

Conclusions and future work

6.1 Concluding remarks

The recent price hikes of fossil fuels and biofuels extracted from edible crops forced the researchers to explore other possible options of feed stocks for biofuels. The one of the tremendous option available is using microorganisms for biofuels. Initially scientists and researchers used microorganisms in photobioreactors for biofuels and water treatment plants and treated them as mere collides or inert chemicals instead of living organisms. This motivates us to study and investigate the locomotion and orientation of an individual flagellated microorganism and collective phenomena of bioconvection and cell dispersion in closed or bounded geometries. Information of the forces and moments that are acting on or produced by the flagellated microorganisms can help us to understand the cell swimming trajectories and internal mechanism of the flagellum. The Individual microorganism modelling can explain how an organism benefits from the proximity of the barrier for either feeding or locomotion. In the presence of boundary or cell-cell interactions modelling can aid in understanding how they influence one another and surrounding fluid and how one organism feed, mate another. Additionally, on a larger scale, precise single microorganism models are in demand for further investigations of bottom standing plumes or bioconvection patterns, population dynamics, plankton bloom models, clogging in closed geometries etc. To optimize light and nutrient uptake for growth, many microorganisms swim in directions biased by environmental cues termed as taxis. These taxes inevitably lead to accumulations of microorganisms can induce hydrodynamic instabilities due to the density difference from the surrounding fluid. The large scale or bulk fluid flow and interesting patterns that arise are known as bioconvection. The affect of bioconvection on the

transport properties of microorganisms suspension within the closed or tubular geometries is still a matter to be investigated.

In this thesis we have model the single spherical shaped biflagellated bottom heavy microorganism named as *Chlamydomonas augustae* swimming within a shear flow in the absence and presence of the no-slip plane boundary. In addition to that we have investigated the attributes of the bioconvection pattern formation within the thin long horizontal tubes without and with the imposed flow.

Chapter 2 includes the details of the idealized model for biflagellated swimming cell after generalization of the beat pattern proposed by Jones *et al.* [76] using Resistive Force Theory (RFT). The model is uniplanar in which the flow field, gravity and entire flagellar beat all coincide. This generalization makes the model simple to employ and θ dependent which enables computation of the trajectory of the swimming cell. We employed software Maple for tedious computations to rectify the potential drawback of complexity of the time dependent beat coefficients as mentioned by Jones [77]. Our method of generalization and simplifications showed good agreement with the results found in Jones *et al.* [76] and predicts the realistic swimming speed. The model shows handsome qualitative agreement with the experimental observations for the cell's swimming velocity and angular velocity in an unbounded domain. Results reveals that the torque due to the flagella has an important contribution in the calculations of the cell's angular velocity, which was not incorporated previously for continuum models. It is also verified that increased gyrotactic re-orientation time scale B was recorded due to the flagellar torque which slows down the angular velocity of the microorganism. The revised or increased values of B and cell's eccentricity α_0 due to the presence of flagella were recorded which are the characteristics of single swimming cell for the purpose of bioconvection modelling.

In chapter 3, we have model the biflagellate swimming cell in the vicinity of the stationary no-slip plane boundary. To satisfy the no-slip plane boundary conditions we have incorporated the contributions of the translational and rotational motion for image cell's body as discussed by Blake and Chawang [16]. Again using the RFT and our simplified beat pattern with Maple programming we modelled and calculated the cell's swimming and angular velocity near the plane boundary. For clarity we modelled all possible position of the swimming cell in the vicinity of the plane boundary. For the simple situation of biflagellate upward swimming away from the boundary we found regressed swimming speed and nearly equal to zero angular velocity close to the boundary after one flagella

beat in comparison to the unbounded swimming. For the case of swimming parallel to the boundary we again observed the regressed swimming speed and non zero angular velocity close to the boundary and at far from the boundary the results overlap to the unbounded swimming velocity and angular velocity. The results were computed with and without the inclusion of flagella close to the boundary to investigate the net change. The results indicate that including the flagella will have lower angular velocity close to the boundary which subsequently changes the values of centre-of-gravity offset H , eccentricity α_0 and gyrotactic re-orientation time B . These changes will have to be incorporated while modelling the bioconvection or suspension behavior in the bounded or closed domains as previously were not entertained.

Chapter 4 deals with the experimental investigations of the bioconvection pattern formation in thin horizontal tubes in the absence and presence of the imposed flow. This is the first experimental study to quantify the patterns due to the suspension of the gravitactic and gyrotactic biflagellate green algae *Chlamydomonas augustae* in horizontal tubes subject to imposed flow. The dependence of the dominant pattern wavelength at pattern onset on cell concentration is found for the three tubes of different diameters for the case of no flow. In the presence of small imposed flows, the vertical plumes of cells are observed merely to bow in the direction of the flow. The plumes progressively fragment into piecewise linear diagonal plumes, inclined at constant angles and translating with fixed speed for the sufficiently high flow rates. In general, pattern wavelength grows with flow rate, with transition at critical rates that depend on suspension concentration. It is also found that bioconvection is not wholly suppressed and perturb the flow field even at high imposed flow rates. The results also conclude that even very weak laminar flows are sufficient to perturb bioconvection patterns and complex structures persists in the flow for higher flow rates, rather than mere mixing effect. The presence of the motile microorganisms appears to modify the mean flow to be more like plug flow than Poiseuille flow.

In chapter 5 we have carried out the linear analysis of the stochastic, gyrotactic bioconvection model in a suspension layer in horizontal tubes. Since theoretically bioconvection in tubes has not yet been attempted before. Here we tried to first model the problem to predict the average inclination and speed of plumes and flow transitions as the function of concentration and tube diameter which were found in the experimental results of chapter 4. As a first step we tried to mathematically model the real problem by incorporating

the cylindrical geometry but due to cumbersome calculations the aim was not achieved. Later, for simplicity we model the problem by following Bees and Hill [9] for two horizontal plates to investigate the most unstable mode from the initial equilibrium solution for the suspension in the presence of weak Poiseuille flow. Initially we derived the equilibrium solution of the full linear equations for the finite depth between the two plates and later by doing a small perturbation investigated the pertaining effects using numerical techniques similar to Bees and Hill [9]. At this stage project is incomplete as linearization of the model equations and equilibrium solution have been found and more inputs are required to complete the numerical or asymptotic analysis to compare the results with the experimental investigations.

6.2 Future work

As research is never ending passion and in this section i will record the shortcoming and outline the possible research directions from this thesis.

In the first step i will complete the linear analysis project to get the mathematical results using numerical and asymptotic analysis. This will help to compare and better understand of the experimental results discussed in chapter 4. Additionally, instead of two plates, a real cylindrical geometry for the mathematical modelling can be attempted using appropriate numerical techniques.

For the case of swimming cell problem a useful extension is to model an organism with a prolate spheroidal body to get a realistic feeling of the *Chlamydomonas augustae* cell. However, it is hard to define the flow field around the cell body due to the difficulty in construction of the straining motion of a spheroid in Stokes flow. More accurate hydrodynamic method or computer intensive method can be incorporated to investigate the inclusion of the interaction between the flagella, non planar beat pattern, rotation around axis and realistic beat pattern as discussed by Ruffer and Nultsch [128]. In our model flagellum does not directly interact with the plane boundary. To incorporate the image flagellum contribution one may require more image singularities to satisfy the no-slip boundary conditions which makes the model tedious and may be solved with appropriate numerical techniques. Instead of plane boundary, tubular and other geometries can also be investigated as majority of the alga bioreactors consists of arrangement of horizontal, vertical and inclined tubes.

In this thesis we have considered the swimming algae to be in the Newtonian fluids, and this is perfectly reasonable as the algae's natural environment is mostly water or similar fluids and suspensions are dilute. However, it might be interesting to also consider non-Newtonian fluids as is important for the case of spermatozoa or bacteria locomotion (see Smith *et al.* [135], [136]). Turbulence is ignored throughout the analysis for ease of calculations, but it is important to investigate the turbulence effects as most of the time we have observed turbulent flow instead of laminar flow in alga photo bioreactors.

For the case of future experimental investigations, one should measure the horizontal or mean flows of the suspension in tubes using particle tracking or PIV. Since in tubular bioreactors the cells suspension in tubes can be in transient turbulent or turbulent flow to maximize mixing and equalize light exposure. Therefore for the optimum efficiency, it is important to establish the most efficient flow rates for maximum biomass production with minimal energy consumption. Additionally to understand how the optical properties of bioconvecting suspension or transmittance changes with the flow and couple to growth. Thus understanding of the transition to turbulence in the presence of motile cells is really important similar to understanding of how cells are arranged within a developed turbulent pipe flow. Another challenge is to predict the effective transport properties of swimming cells in laminar and turbulent flows in tubes of arbitrary orientation.

Appendix A

A.1 Time dependent beat coefficients α_{ij}

Jones [77] defined the time dependent beat coefficients α_{ij} separately for effective and recovery stroke. Since we have modified the method by redefining the single position vector for the three different sections of the flagella beat so this motivate us to define now single expressions for the beat coefficients α_{ij} as:

Beat coefficients due to the forces

$$\begin{aligned} \bar{\alpha}_{11} = & K_n \left[-\sin^2 \chi \left(I_1 - \frac{3}{4} I_2 - \frac{1}{4} I_3 \right) + \frac{3}{4} \cos \chi \sin \chi r_n (J_3 - J_4) + \frac{3}{4} \sin^2 \chi r_n^2 \right. \\ & (I_3 - I_4) \left. \right] + K_t \left[-\cos^2 \chi \left(I_1 - \frac{3}{4} I_2 - \frac{1}{4} I_3 \right) + \frac{3}{4} \sin \chi \cos \chi r_n (J_3 - J_4) \right. \\ & \left. + \frac{3}{4} \cos^2 \chi (I_7 - I_8) \right], \end{aligned} \quad (\text{A.1})$$

$$\begin{aligned} \alpha_{12} = & K_n \left[\cos \chi \sin \chi \left(I_1 - \frac{3}{4} I_2 - \frac{1}{4} I_3 \right) + \frac{3}{4} \sin^2 \chi r_n (J_3 - J_4) - \frac{3}{4} \sin \chi \cos \chi r_n^2 \right. \\ & (I_3 - I_4) \left. \right] + K_t \left[-\cos \chi \cos \chi \left(I_1 - \frac{3}{4} I_2 - \frac{1}{4} I_3 \right) - \frac{3}{4} \cos^2 \chi r_n (J_3 - J_4) \right. \\ & \left. + \frac{3}{4} \cos \chi \sin \chi (I_7 - I_8) \right], \end{aligned} \quad (\text{A.2})$$

$$\begin{aligned} \alpha_{21} = & K_n \left[-\sin \chi \cos \chi \left(I_1 - \frac{3}{4} I_2 - \frac{1}{4} I_3 \right) - \frac{3}{4} \cos^2 \chi r_n (J_3 - J_4) - \frac{3}{4} \sin \chi \sin \chi r_n^2 \right. \\ & (I_3 - I_4) \left. \right] + K_t \left[-\cos \chi \cos \chi \left(I_1 - \frac{3}{4} I_2 - \frac{1}{4} I_3 \right) + \frac{3}{4} \sin^2 \chi r_n (J_3 - J_4) \right. \\ & \left. + \frac{3}{4} \cos \chi \sin \chi (I_7 - I_8) \right], \end{aligned} \quad (\text{A.3})$$

$$\begin{aligned} \bar{\alpha}_{22} = & K_n \left[-\cos^2 \chi \left(I_1 - \frac{3}{4} I_2 - \frac{1}{4} I_3 \right) - \frac{3}{4} \cos \chi \sin \chi r_n (J_3 - J_4) + \frac{3}{4} \cos^2 \chi r_n^2 \right. \\ & (I_3 - I_4) \left. \right] + K_t \left[-\sin^2 \chi \left(I_1 - \frac{3}{4} I_2 - \frac{1}{4} I_3 \right) - \frac{3}{4} \sin \chi \cos \chi r_n (J_3 - J_4) \right. \\ & \left. + \frac{3}{4} \sin^2 \chi (I_7 - I_8) \right], \end{aligned} \quad (\text{A.4})$$

$$\begin{aligned} \alpha_{61} = & K_n \left[\sin\chi \left(J_1 - \frac{3}{4}J_2 - \frac{1}{4}J_3 \right) - \frac{3}{4} \sin\chi r_n^2 (J_3 - J_4) - \frac{3}{4} \cos\chi r_n \right. \\ & (I_7 - I_8) \left. \right] + K_t \left[-\cos\chi \left(I_1 - \frac{3}{4}I_2 - \frac{1}{4}I_3 \right) + \frac{3}{4} \sin\chi r_n^2 (J_3 - J_4) \right. \\ & \left. + \frac{3}{4} \cos\chi r_n (I_7 - I_8) \right], \end{aligned} \quad (\text{A.5})$$

$$\begin{aligned} \alpha_{62} = & K_n \left[-\cos\chi \left(J_1 - \frac{3}{4}J_2 - \frac{1}{4}J_3 \right) + \frac{3}{4} \cos\chi r_n^2 (J_3 - J_4) - \frac{3}{4} \sin\chi r_n \right. \\ & (I_7 - I_8) \left. \right] + K_t \left[-\sin\chi \left(I_1 - \frac{3}{4}I_2 - \frac{1}{4}I_3 \right) - \frac{3}{4} \cos\chi r_n^2 (J_3 - J_4) \right. \\ & \left. + \frac{3}{4} \sin\chi r_n (I_7 - I_8) \right]. \end{aligned} \quad (\text{A.6})$$

Beat coefficients due to the torques

$$\alpha_{16} = K_n \left[\sin\chi (J_1 - J_3) \right] + K_t \left[-\cos\chi r_n (I_1 - I_3) \right], \quad (\text{A.7})$$

$$\alpha_{26} = K_n \left[-\cos\chi (J_1 - J_3) \right] + K_t \left[-\sin\chi r_n (I_1 - I_3) \right], \quad (\text{A.8})$$

$$\bar{\alpha}_{66} = K_n \left[I_7 - I_6 \right] + K_t \left[-r_n^2 (I_1 - I_3) \right]. \quad (\text{A.9})$$

A.2 Time dependent beat coefficients h_{ij}

These beat coefficients correspond to the straining motion which we have neglected in our study. Following Jones [77] the values are reproduced for clarity of the readers. Here again due to the generalization of the method we will have single expressions of h_{ij} for different parts of the flagella beat which are defined as

Beat coefficients due to the forces

$$\begin{aligned} h_{11} = & K_n \left[\sin^3\chi r_n (I_1 - I_4) + \cos^2\chi \sin\chi (J_1 - J_4) - \frac{5}{2} \sin^3\chi r_n^3 (I_4 - I_5) + 5 \sin^2\chi \cos\chi r_n^2 \right. \\ & (J_4 - J_5) - \frac{5}{2} \cos^2\chi \sin\chi r_n (I_8 - I_9) \left. \right] + K_t \left[-\cos^2\chi \sin\chi r_n (I_1 - I_4) + \cos^3\chi (J_1 - J_4) \right. \\ & \left. - \frac{5}{2} \sin^2\chi \cos\chi r_n^2 (J_4 - J_5) + 5 \cos^2\chi \sin\chi r_n (I_8 - I_9) - \frac{5}{2} \cos^3\chi (J_6 - J_7) \right], \end{aligned} \quad (\text{A.10})$$

$$\begin{aligned} h_{13} = & K_n \left[\cos^2\chi \sin\chi r_n (I_1 - I_4) + \cos\chi \sin^2\chi (J_1 - J_4) - \frac{5}{2} \sin\chi \cos^2\chi r_n^3 (I_4 - I_5) - 5 \sin^2\chi \right. \\ & \left. \cos\chi r_n^2 (J_4 - J_5) - \frac{5}{2} \sin^3\chi r_n (I_8 - I_9) \right] + K_t \left[\cos^2\chi \sin\chi r_n (I_1 - I_4) + \cos\chi \sin^2\chi (J_1 - J_4) \right. \\ & \left. - \frac{5}{2} \cos^3\chi r_n^2 (J_4 - J_5) - 5 \cos^2\chi \sin\chi r_n (I_8 - I_9) - \frac{5}{2} \sin^2\chi \cos\chi (J_6 - J_7) \right], \end{aligned} \quad (\text{A.11})$$

$$\begin{aligned} h_{22} = & K_n \left[-2 \sin\chi \cos^2\chi r_n (I_1 - I_4) + (\sin^2\chi - \cos^2\chi) \cos\chi (J_1 - J_4) - 5 \cos^2\chi \sin\chi r_n^3 (I_4 - I_5) \right. \\ & \left. - 5 (\sin^2\chi - \cos^2\chi) \cos\chi r_n^2 (J_4 - J_5) + 5 \cos^2\chi \sin\chi r_n (I_8 - I_9) \right] + K_t \left[(\sin^2\chi - \cos^2\chi) \right. \\ & \left. \sin\chi r_n (I_1 - I_4) - 2 \cos\chi \sin^2\chi (J_1 - J_4) - 5 \sin^2\chi \cos\chi r_n^2 (J_4 - J_5) \right. \\ & \left. - 5 (\sin^2\chi - \cos^2\chi) \sin\chi r_n (I_8 - I_9) + 5 \sin^2\chi \cos\chi (J_6 - J_7) \right], \end{aligned} \quad (\text{A.12})$$

Beat coefficients due to the torques

$$\begin{aligned}
h_{62} = & K_n \left[-2 \cos \chi \sin \chi r_n (J_1 - J_4) - (\sin^2 \chi - \cos^2 \chi) (I_6 - I_8) \right] + K_t \left[(\sin^2 \chi - \cos^2 \chi) r_n^2 \right. \\
& (I_1 - I_4) - 2 \sin \chi \cos \chi r_n (J_1 - J_4) \left. \right] - \frac{5}{2} (K_t - K_n) \left[2 \cos \chi \sin \chi r_n^3 (J_4 - J_5) \right. \\
& \left. + 2 (\sin^2 \chi - \cos^2 \chi) r_n^2 (I_8 - I_9) - 2 \cos \chi \sin \chi (J_6 - J_7) \right], \tag{A.13}
\end{aligned}$$

A.3 Core integrals involved in beat coefficients α_{ij}

Following the calculations of Jones *et al.* [76], we have calculated the core integrals for three different sections of the beat namely effective stroke, straight section of the recovery stroke and angled section of the recovery stroke are calculated below.

$$ds = \frac{r dr}{r_t},$$

which is also valid for the angled section of the recovery stroke whereas for the straight section of the recovery stroke transformation becomes

$$ds = dr.$$

Lower limit $s = b = a$ and Upper limit $s = c = [(l + \cos \chi)^2 + \sin^2 \chi]^{\frac{1}{2}}$.

For the straight section of the recovery stroke, $i = st$, $r_{n,st} = 0$ and the limits of integration are calculated as

Lower limit $r = 1$ and Upper limit $r = 1 + \omega t$.

The normal distance from the flagellum during the angled section of the recovery stroke, $i = ag$, $r_{n,ag} = (1 + \omega t) \sin \chi$ and the limits of integration found as

Lower limit $r = 1 + \omega t$ and

Upper limit $r = \left[(l - \omega t + (1 + \omega t) \cos \chi)^2 + ((1 + \omega t) \sin \chi)^2 \right]^{\frac{1}{2}}$.

The integrals $I_{j,i}$ involve integration of powers of r_t^2 and r and defined as following

$$I_{1,i} = \int ds = \begin{cases} l & \text{for } i = ef \\ \omega t & \text{for } i = st \\ l - \omega t & \text{for } i = ag \end{cases}$$

$$I_{2,i} = \int \frac{ds}{r} = \int \frac{dr}{r_t} = \begin{cases} \ln r & \text{for } r_{n,i} = 0 \\ \ln \left| \frac{r + \sqrt{r^2 - r_{n,i}^2}}{r_{n,i}} \right| & \text{for } r_{n,i} \neq 0 \end{cases}$$

$$I_{3,i} = \int \frac{ds}{r^3} = \int \frac{dr}{r^2 r_t} = \begin{cases} -\frac{1}{2r^2} & \text{for } r_{n,i} = 0 \\ \frac{1}{r_{n,i}^2} \left(\frac{\sqrt{r^2 - r_{n,i}^2}}{r} \right) & \text{for } r_{n,i} \neq 0 \end{cases}$$

$$I_{4,i} = \int \frac{ds}{r^5} = \int \frac{dr}{r^4 r_t} = \begin{cases} -\frac{1}{4r^4} & \text{for } r_{n,i} = 0 \\ \frac{1}{r_{n,i}^4} \left[\frac{\sqrt{r^2 - r_{n,i}^2}}{r} - \frac{1}{3} \left(\frac{\sqrt{r^2 - r_{n,i}^2}}{r} \right)^3 \right] & \text{for } r_{n,i} \neq 0 \end{cases}$$

$$I_{5,i} = \int \frac{ds}{r^7} = \int \frac{dr}{r^6 r_t} = \begin{cases} -\frac{1}{6r^6} & \text{for } r_{n,i} = 0 \\ \frac{1}{r_{n,i}^6} \left[\frac{\sqrt{r^2 - r_{n,i}^2}}{r} - \frac{2}{3} \left(\frac{\sqrt{r^2 - r_{n,i}^2}}{r} \right)^3 + \frac{1}{5} \left(\frac{\sqrt{r^2 - r_{n,i}^2}}{r} \right)^5 \right] & \text{for } r_{n,i} \neq 0 \end{cases}$$

$$I_{6,i} = \int r_t^2 ds = \begin{cases} \frac{l^3}{3} + l^2 \cos \chi + l \cos^2 \chi & \text{for } i = ef \\ \frac{(\omega t)^3}{3} + (\omega t)^2 + \omega t & \text{for } i = st \\ \frac{(l - \omega t)^3}{3} + (l - \omega t)^2 (1 + \omega t) \cos \chi + (l - \omega t)(1 + \omega t)^2 \cos^2 \chi & \text{for } i = ag \end{cases}$$

$$I_{7,i} = \int \frac{r_t^2 ds}{r^3} = \int (r^2 - r_{n,i}^2) \frac{dr}{r^2 r_t} = I_{2,i} - r_{n,i}^2 I_{3,i}$$

$$I_{8,i} = \int \frac{r_t^2 ds}{r^5} = \int (r^2 - r_{n,i}^2) \frac{dr}{r^4 r_t} = I_{3,i} - r_{n,i}^2 I_{4,i}$$

$$I_{9,i} = \int \frac{r_t^2 ds}{r^7} = \int (r^2 - r_{n,i}^2) \frac{dr}{r^6 r_t} = I_{4,i} - r_{n,i}^2 I_{5,i}$$

The integrals $J_{j,i}$ involve integration of r_t , r_t^3 and powers of r and defined as following

$$J_{1,i} = \int r_t ds = \begin{cases} \frac{l}{2} + l \cos \chi & \text{for } i = ef \\ \frac{(\omega t)^2}{2} + \omega t & \text{for } i = st \\ \frac{(l - \omega t)^2}{2} + (l - \omega t)(1 + \omega t) \cos \chi & \text{for } i = ag \end{cases}$$

$$J_{2,i} = \int \frac{r_t ds}{r} = \int dr = r$$

$$J_{3,i} = \int \frac{r_t ds}{r^3} = \int \frac{dr}{r^2} = -\frac{1}{r}$$

$$J_{4,i} = \int \frac{r_t ds}{r^5} = \int \frac{dr}{r^4} = -\frac{1}{3r^3}$$

$$J_{5,i} = \int \frac{r_t ds}{r^7} = \int \frac{dr}{r^6} = -\frac{1}{5r^5}$$

$$J_{6,i} = \int \frac{r_t^3 ds}{r^5} = \int (r^2 - r_{n,i}^2) \frac{dr}{r^4} = J_{3,i} - r_{n,i}^2 J_{4,i}$$

$$J_{7,i} = \int \frac{r_t^3 ds}{r^7} = \int (r^2 - r_{n,i}^2) \frac{dr}{r^6} = J_{4,i} - r_{n,i}^2 J_{5,i}$$

A.4 Core integrals involved in beat coefficients α_{ij}

Similarly we can define the integrals involved in the beat coefficients α_{ij} . Using the generalized form of the flagella beat the expression for the position vector for the image sphere takes the form as

$$\mathbf{R}^F(s, t) = [b \sin \chi + 2h \sin(\chi + \theta)] \mathbf{n} + [(s - b) + b \cos \chi + 2h \cos(\chi + \theta)] \mathbf{t},$$

which is valid for the three different sections of the beat.

During the effective stroke the distance from the flagellum in the normal direction is calculated as $R_n = b \sin \chi + 2h \sin(\chi + \theta)$ and the limits of integrations for effective stroke, are given by

$$\text{Lower limit } s = b = a \quad \text{and} \quad \text{Upper limit } s = b + c = a + l.$$

For the straight section of the recovery stroke, $R_n = 0$ and the limits of integration are calculated as

$$\text{Lower limit } s = b = a \quad \text{and} \quad \text{Upper limit } s = b + c = a + wt.$$

The normal distance from the flagellum during the angled section of the recovery stroke, $R_n = b \sin \chi$ and the limits of integration found as

$$\text{Lower limit } s = b = a + wt \quad \text{and} \quad \text{Upper limit } s = b + c = a + l - wt.$$

The integrals II_i involve integration of powers of R_t^2 and R which are defined and calculated using the above defined limits of integrations as

$$II_1 = \int ds = \begin{cases} wt & \text{for } R_n = 0 \\ l & \text{for } R_n \neq 0 \end{cases}$$

$$II_2 = \int \frac{ds}{R} = \begin{cases} \ln |wt| & \text{for } R_n = 0 \\ \ln |l| & \text{for } R_n \neq 0 \end{cases}$$

$$II_3 = \int \frac{ds}{R^3} = \begin{cases} -\frac{1}{2(wt)^2} & \text{for } R_n = 0 \\ -\frac{1}{2l^2} & \text{for } R_n \neq 0 \end{cases}$$

$$II_4 = \int \frac{ds}{R^5} = \begin{cases} -\frac{1}{4(wt)^4} & \text{for } R_n = 0 \\ -\frac{1}{4l^4} & \text{for } R_n \neq 0 \end{cases}$$

$$II_5 = \int \frac{ds}{R^7} = \begin{cases} -\frac{1}{6(wt)^6} & \text{for } R_n = 0 \\ -\frac{1}{6l^6} & \text{for } R_n \neq 0 \end{cases}$$

$$II_6 = \int R_t^2 ds = \begin{cases} \frac{(wt)^3}{3} + (wt)^2 + wt & \text{for } R_n = 0 \\ \frac{l^3}{3} + l^2 \cos\chi + l \cos^2\chi & \text{for } R_n \neq 0 \end{cases}$$

$$II_7 = \int \frac{R_t^2}{R^3} ds = \int (R^2 - R_n^2) \frac{ds}{R^3} = II_2 - R_n^2 II_3,$$

$$II_8 = \int \frac{R_t^2}{R^5} ds = \int (R^2 - R_n^2) \frac{ds}{R^4} = II_3 - R_n^2 II_4,$$

$$II_9 = \int \frac{R_t^2}{R^7} ds = \int (R^2 - R_n^2) \frac{ds}{R^6} = II_4 - R_n^2 II_5,$$

where

$$R = \left[R_t^2 + R_n^2 \right]^{\frac{1}{2}} = \left[(s - b + b \cos \chi + 2h \cos(\chi + \theta))^2 + (b \sin \chi + 2h \sin(\chi + \theta))^2 \right]^{\frac{1}{2}}.$$

The integrals JJ_i involve integration of R_t , R_t^3 and powers of R , which are defined and calculated using the limits of integrations for effective and recovery strokes as

$$JJ_1 = \int R_t ds = \begin{cases} \frac{(wt)^2}{2} + wt & \text{for } R_n = 0 \\ \frac{l^2}{2} + l \cos\chi & \text{for } R_n \neq 0 \end{cases}$$

$$JJ_2 = \int \frac{R_t}{R} ds = \begin{cases} wt & \text{for } R_n = 0 \\ l & \text{for } R_n \neq 0 \end{cases}$$

$$JJ_3 = \int \frac{R_t}{R^3} ds = \begin{cases} -\frac{1}{wt} & \text{for } R_n = 0 \\ -\frac{1}{l} & \text{for } R_n \neq 0 \end{cases}$$

$$JJ_4 = \int \frac{R_t}{R^5} ds = \begin{cases} -\frac{1}{3(wt)^3} & \text{for } R_n = 0 \\ -\frac{1}{l^3} & \text{for } R_n \neq 0 \end{cases}$$

$$JJ_5 = \int \frac{R_t}{R^7} ds = \begin{cases} -\frac{1}{5(\omega t)^5} & \text{for } R_n = 0 \\ -\frac{1}{5l^5} & \text{for } R_n \neq 0 \end{cases}$$

$$JJ_6 = \int \frac{R_t^3}{R^5} ds = \int (R^2 - R_n^2) \frac{ds}{R^4} = JJ_3 - R_n^2 JJ_4$$

$$JJ_7 = \int \frac{R_t^3}{R^7} ds = \int (R^2 - R_n^2) \frac{ds}{R^6} = JJ_4 - R_n^2 JJ_5$$

A.4.1 Special integrals when point Q lies on the flagellum

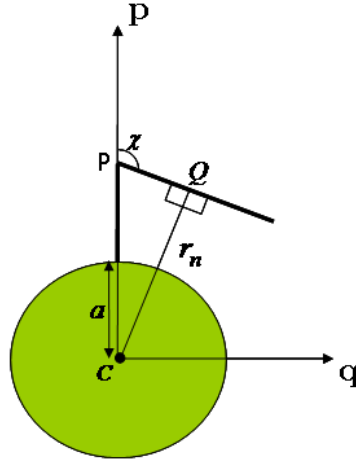


Figure A.1: Difference in length of r during angled section of recovery stroke.

Jones *et al.* [76] observed during the angled section of the recovery stroke that the length r started decreasing with increasing s instead of increasing away from the fixed point P until a point Q. Thereafter, r started increasing again with s as shown in the figure (A.1). This shortest distance from point Q will be of length $r_{n,i}$ so point Q lies on the flagellum at $r = r_{n,i}$.

We need to find the time at which the point Q no longer lies on the flagellum during the recovery stroke. This will occur after the time when

$$r_{n,i} = (1 + \omega t) \sin \chi = \left[(l - \omega t + (1 + \omega t) \cos \chi)^2 + ((1 + \omega t) \sin \chi)^2 \right]^{\frac{1}{2}}.$$

After rearrangement we can rewrite this as

$$\cos \chi = \frac{\omega t - l}{1 + \omega t}, \quad (\text{A.14})$$

where, χ is a function of t only. Now to calculate the value of t which solves the above equation we will use the value of angle χ for zero-moment angular rotation calculated earlier as

$$\chi = 2 \arctan \left(1 - \frac{\omega t}{l} \right),$$

which can be rewritten as

$$\cos \chi = \frac{(l - \omega t)^3 - l^3}{l^3 + (l - \omega t)^3}. \quad (\text{A.15})$$

Substituting equation (A.15) into (A.14) gives the cubic equation

$$(\omega t)^3 - 3l(\omega t)^2 + \left[\frac{(5l + 3)l^2}{1 + l} \right] (\omega t) - \frac{2l^4}{1 + l} = 0, \quad (\text{A.16})$$

which will determine the time after which point Q no longer lies on the flagellum during the recovery stroke. Using the method for solution for cubic equation (see Murray's [105]) we find

$$T_Q = \frac{1}{\omega} \lambda + T_e. \quad (\text{A.17})$$

$$\lambda = -2(-\alpha)^{\frac{1}{2}} \sinh \Theta - a = -2l \left[\frac{2l}{3(1 + 2h)} \right]^{\frac{1}{2}} \sinh \Theta + l. \quad (\text{A.18})$$

$$\Theta = \frac{1}{3} \sinh^{-1} \left(\frac{\beta}{2(-\alpha)^{\frac{3}{2}}} \right) = \frac{1}{3} \sinh^{-1} \left(\frac{1}{2} \left[\frac{2l}{3(1 + l)} \right]^{-\frac{3}{2}} \right), \quad (\text{A.19})$$

which further gives

$$a = -l \quad b = \frac{(5l + 3)l^2}{3(1 + l)} \quad \alpha = \frac{-2l^3}{3(1 + l)} \quad \text{and} \quad \beta = l^3,$$

Thus using above values of Θ and λ we have found the time T_Q after which point Q disappears from the flagellum during the recovery stroke as

Hence, the limits of integrals have to be amended when point Q lies on the flagellum during the angled section of the recovery stroke as

$$\begin{aligned} \int_{\omega t}^l f(r) ds &= \int_{\omega t}^Q f(r) ds + \int_Q^l f(r) ds, \\ &= - \int_{1+\omega t}^{r_{n,i}} f(r) \frac{r dr}{r_t} + \int_{r_{n,i}}^L f(r) \frac{r dr}{r_t}, \end{aligned} \quad (\text{A.20})$$

where $L = \left[(l - \omega t + (1 + \omega t) \cos \chi)^2 + ((1 + \omega t) \sin \chi)^2 \right]^{\frac{1}{2}}$. However when point Q disappears from the flagellum during the angled section of the recovery stroke the limits of integration again become simple, such that

$$\int_{\omega t}^l f(r) ds = - \int_{1+\omega t}^L f(r) \frac{r dr}{r_t}. \quad (\text{A.21})$$

Appendix B

B.1 Maple11 programming

After solving analytically and reviewing the calculations of Jones *et al.* [76] we realized that method involves lengthy and laborious calculations. The method also involves tedious integrals, leaving much room for analytical error. To minimize the chance of error we have employed software Maple11 for the symbolic manipulation.

Thus we have established a code which exactly solves the same problem and have obtained the same results for the swimming velocity and angular velocity of the cell in an unbounded fluid flow problem as shown in the sections below.

B.1.1 Instruction flow and code details

The aim of the program is to calculate the components of the swimming velocity and angular velocity of the micro-organism during one flagellar beat. A flagella beat consist of effective stroke during which micro-organism gain some ground and the recovery stroke, during which ground is lost. The different steps and the flow chart of the Maple code is shown below.

Input parameters

The input parameters are read into the code as a first step. The different inputs to be specified and variable names are summarized below:

cell's (sphere) radius: a

cell's mass: m

Time to complete one flagella beat: T

centre of mass offset: h

Gravity: g

Bending waves constant velocity: w

Resistance coefficients acting in the tangential and normal direction: K_t, K_n

Rotation matrix from fixed space ($\mathbf{i}, \mathbf{j}, \mathbf{k}$) to body coordinates ($\mathbf{p}, \mathbf{q}, \mathbf{r}$) system: R_{SB}

Rotation matrix from body ($\mathbf{p}, \mathbf{q}, \mathbf{r}$) to flagella coordinates ($\mathbf{t}, \mathbf{n}, \mathbf{b}$) system: R_{BF}

Position vector on any element of flagellum from the centre of the cell's body in flagella coordinates: r_f

Velocity vector field due to the translating motion of the cell (sphere) in flagella coordinates system: U_f

Dot product of force component in tangent direction with \mathbf{t} and in normal direction with \mathbf{n} : U_t, U_n

Torque vector field due to the translating motion of the cell (sphere) in flagella coordinates system: L_f

Dot product of torque component in binormal direction with \mathbf{b} and in normal direction with \mathbf{n} : L_b

Velocity vector field due to the rotational motion of the cell (sphere) in flagella coordinates system: $U1_f$

Dot product of force component in tangent direction with \mathbf{t} and in normal direction with \mathbf{n} : $U1_t, U1_n$

Torque vector field due to the rotational motion of the cell (sphere) in flagella coordinates system: $L1_f$

Dot product of torque component in binormal direction with \mathbf{b} and in normal direction with \mathbf{n} : $L1_b$.

Resistive Force Theory (RFT)

Now we calculate the forces and torques action on an element of the flagellum due to the translational and rotational motion of the cell (sphere) using RFT as

$$dF = [(K_t U_t dS), (K_n U_n dS), 0]$$

Forces acting on element of flagellum due to translational and rotational motion of cell: $dF, d1F$

Torques acting on element of flagellum due to translational and rotational motion of cell: $dL, d1L$

Total forces due to translational and rotational motion of cell acting on one flagellum by integrating along the length of flagellum: $F, F1$

Total torques due to translational and rotational motion of cell acting on one flagellum by integrating along the length of flagellum: $L, L1$.

Time dependent beat coefficients α_{ij}

Using the equations of total forces and total torques acting on one flagellum we can calculate time dependent beat coefficients α_{ij} as

Total forces acting on the flagellum in body coordinates system: $Fb, F1b$

Total torques acting on the flagellum in body coordinates system: $Lb, L1b$

Dot product of Fb with p gives α_{11} and α_{12}

Dot product of Fb with q gives α_{21} and α_{22}

Dot product of Lb with r gives α_{61} and α_{62}

Dot product of $F1b$ with p gives α_{16}

Dot product of $F1b$ with q gives α_{26}

Dot product of $L1b$ with r gives α_{66}

Later we defined the core integrals and substitute back into the beat coefficients α_{ij} . Also we defined the initial conditions like time t , angle θ .

Effective stroke

Now we define angle χ , and f_{1E} velocity of the flagellum for effective stroke. Using the initial conditions we calculate the beat coefficients α_{ij} for different values of time t for effective stroke. Later using the do loop we calculate the v_p, v_q velocity components and $\dot{\theta}$ angular velocity of the cell during the effective stroke.

Recovery stroke

Similarly we define angle χ and f_{1R} velocity of the flagellum for recovery stroke. Using the same procedure for effective stroke we will find the v_p, v_q velocity components and $\dot{\theta}$ angular velocity of the cell during the recovery stroke.

Plotting

Finally we plot the graphs of v_p primary direction velocity component and v_q velocity component versus time for effective and recovery stroke. Additionally we plot the graph of variation of angle θ from initial angle during the effective and recovery stroke.

B.1.2 Programming code

Here we have listed down the actual Maple code established to calculate the swimming and angular velocity of the micro-organism in an unbounded domain. Here we have used editor Kwrite and compiled the program in the software Maple11. To avoid repetitions and lengthy details of the code we have not listed the bounded swimming code.

```

`Program to calculate velocity and angular velocity of the swimming C. nivalis cell`;

with(LinearAlgebra): with(plots):
assume( t>=0, t<=1, b>=a, b<=a+l, c>=0, c<=l, chi>=-Pi, chi<=Pi );

`Constant values involved in alpha11 & Tq`;
#Kn := 3.7: #Kt := 2.2:
a := 1: T := 1: Te := T/2: m := .00525:
dt := T/500: l := 2*a: w := l/(T-Te): H := 0.02: g := 800:
print(`KN` = Kn, `KT` = Kt, `Length of flagellum` = l, `Time complete one beat` = T );
print(`bending waves constant velocity` = w, `Euler angle theta` = theta, `radius of cell`
= a );
print(`mass of cell` = m, `center of mass offset` = H, `gravity` = g );
`Rotations Matrices`;
`Fixed space coordinates to body coordinate system`;
Rsb := Matrix( [[sin(theta), 0, cos(theta)], [cos(theta), 0, -sin(theta)], [0, 1, 0]] );
`Body coordinates to flagella coordinate system`;
Rbf := Matrix( [[cos(chi), sin(chi), 0], [-sin(chi), cos(chi), 0], [0, 0, 1]] );

#####
`Main program structure`;
`Rr- position vector`;
Rr[s] := Vector(3): r[s] := Vector(3): rf[f] := Vector(3):

Rr[s][1] := b*sin(theta) + (s-b)*sin(theta + chi): Rr[s][3] := b*cos(theta) + (s-
b)*cos(theta + chi): Rr[s] := Rr[s];
Rr[b] := `.`(Rsb, Rr[s]): Rr[f] := `.`(Rbf, Rr[b]):
`Angular velocity vector Omega`;
Omega[s] := Vector(3):
Omega[s][1] := 0: Omega[s][2] := Omega[2]: Omega[s][3] := 0: Omega[s] :=
Omega[s]:
r[s][1] := r[1]: r[s][2] := 0: r[s][3] := r[3]: r[s] := r[s]:
rf[f][1] := x[t]: rf[f][2] := x[n]: rf[f][3] := 0: rf[f] := rf[f]:
print(`r flag jones` = rf[f], `r space jones` = r[s], `Omega space` = Omega[s]);

#####
`Defining translating velocity field vector U(tran) acting on element of flagellum in
flagella coordinate system- cell's frame of reference`;
U[s] := Vector(3): U[f] := Vector(3):
U[s][1] := -V[1]*( 1 - 3/(4*r) - 1/(4*r^3) ) + 3*( V[3]*r[1]*r[3] + V[1]*r[1]^2 )*( 1 -
1/r^2)/(4*r^3):
U[s][3] := -V[3]*( 1 - 3/(4*r) - 1/(4*r^3) ) + 3*( V[1]*r[3]*r[1] + V[3]*r[3]^2 )*( 1 -
1/r^2)/(4*r^3):
U[s][2] := 0: U[s] := U[s];
U[b] := `.`(Rsb, U[s]): U[f] := `.`(Rbf, U[b]):
`Defining torue vector L(tran) due to translating velocity field vector U(tran) in flagella
coordinate system- cell's frame of reference`;
L[s] := Vector(3): L[f] := Vector(3):

```

```

L[s] := CrossProduct( r[s], U[s] );
L[b] := `.`(Rsb, L[s]);      L[f] := `.`(Rbf, L[b]);
`Defining Rotational velocity field vector U1(rotational velocity) in flagella coordinate
system- cell's frame of reference`;
U1[s] := Vector(3);          U1[f] := Vector(3);
U1[s][1] := -Omega[2]*r[3]*( 1 - 1/r^3 );
U1[s][3] := Omega[2]*r[1]*( 1 - 1/r^3 );
U1[s][2] := 0;              U1[s] := U1[s];
U1[b] := `.`(Rsb, U1[s]);    U1[f] := `.`(Rbf, U1[b]);
`Defining torue vector L1(rot) due to rotational velocity field vector U(rotational) in
flagella coordinate system- cell's frame of reference`;
L1[s] := Vector(3);          L1[f] := Vector(3);
L1[s] := CrossProduct( r[s], U1[s] );
L1[b] := `.`(Rsb, L1[s]);    L1[f] := `.`(Rbf, L1[b]);
U[ff] := subs( { V[1] = V[t]*sin(chi+theta) + V[n]*cos(chi+theta), V[3] =
V[t]*cos(chi+theta) - V[n]*sin(chi+theta),
r[1] = x[t]*sin(chi+theta) + x[n]*cos(chi+theta), r[3] = x[n]*sin(chi+theta) -
x[t]*cos(chi+theta) }, U[f] );
Ut := expand( U[ff][1] );     Un := expand( U[ff][2] );
U1[ff] := subs( { V[1] = V[t]*sin(chi+theta) + V[n]*cos(chi+theta), V[3] =
V[t]*cos(chi+theta) - V[n]*sin(chi+theta),
r[1] = x[t]*sin(chi+theta) + x[n]*cos(chi+theta), r[3] = x[n]*sin(chi+theta) -
x[t]*cos(chi+theta), Omega[2] = Omega[b] }, U1[f] );
U1t := expand( U1[ff][1] );   U1n := expand( U1[ff][2] );
`Dot product of Ut (velocity component in tangent direction) with t`;
Ut := expand(Ut);
`Dot product of Un (velocity component in normal direction) with n`;
Un := expand(Un);
`Dot product of Lb (trans torque component in binormal direction) with b`;
Lb := Kt*x[n]*Ut - Kn*x[t]*Un :    Lb := expand ( Lb );
`Dot product of U1t (rotational velocity component in tangent direction) with t`;
U1t := expand(U1t);
`Dot product of U1n (rotational velocity component in normal direction) with n`;
U1n := expand(U1n);
`Dot product of L1b ( rotational torque component in binormal direction ) with b`;
L1b := Kt*x[n]*U1t - Kn*x[t]*U1n:    L1b := expand(L1b);

#####
`Resistive Force Theory equation (RFT)- force/torque on an element of a flagellum`;
dF := Vector(3);      dL := Vector(3);      d1F := Vector(3);      d1L := Vector(3);
dF[1] := expand(dS*Ut*Kt);    dF[2] := expand(dS*Un*Kn);    dF[3] := 0;
dF := dF;
dL[1] := 0;              dL[2] := 0;              dL[3] := expand(dS*Lb);
dL := dL;
d1F[1] := expand(dS*U1t*Kt);    d1F[2] := expand(dS*U1n*Kn);    d1F[3] := 0;
d1F := d1F;
d1L[1] := 0;              d1L[2] := 0;              d1L[3] := expand(dS*L1b);
d1L := d1L;

```

`Total force (trans. comp.) acting on one flagella is obtained by integrating along the length of flagellum`;

```
F := Vector(3):          L := Vector(3):
FF1 := algsubs( dS*x[t]/r^5 = JJ[4], algsubs( dS*x[t]^2/r^3 = II[7], algsubs(
dS*x[t]^2/r^5 = II[8], dF ) ) ):
F := algsubs( dS = II[1], algsubs( dS/r = II[2], algsubs( dS/r^3 = II[3], algsubs( dS/r^5 =
II[4], algsubs( dS*x[t]/r^3 = JJ[3], FF1 ) ) ) ) ):
```

```
L1 := expand( dL[3] ):
L2 := expand( algsubs( dS*x[t]/r^5 = JJ[4], algsubs( dS*x[t]^2/r^3 = II[7], algsubs(
dS*x[t]^3/r^5 = II[9], L1 ) ) ) ):
L3 := algsubs( dS = II[1], algsubs( dS/r = II[2], algsubs( dS/r^3 = II[3], algsubs( dS/r^5 =
II[4], algsubs( dS*x[t]/r^3 = JJ[3], L2 ) ) ) ) ):
L4 := algsubs( II[1]*x[t] = JJ[1], L3 ):  L4 := expand( L4 ):
L5 := algsubs( II[2]*x[t] = JJ[2], L4 ):  L5 := expand( L5 ):
L[1] := 0:      L[2] := 0:      L[3] := expand(L5):
L := L;
```

`Total force (rot. comp.) acting on one flagella is obtained by integrating along the length of flagellum`;

```
F1 := Vector(3):          L1 := Vector(3):
F2 := expand( algsubs( dS*x[t]/r^3 = JJ[3], d1F ) ):
F3 := algsubs( dS = II[1], algsubs( dS/r^3 = II[3], F2 ) ):
F4 := algsubs( II[1]*x[t] = JJ[1], F3 ):  F4 := expand( F4 ):
```

```
F1 := expand(F4):
L2 := expand( algsubs( dS*x[t]^2/r^3 = II[7], d1L ) ):
L3 := algsubs( dS = II[1], algsubs( dS/r^3 = II[3], L2 ) ):
L4 := algsubs( II[1]*x[t]^2 = II[6], L3 ):  L4 := expand( L4 ):
L1 := expand(L4);
```

```
#####
```

`Total force acting on one flagella in body coordinates system (p, q, r)`;

```
Fb := simplify( `.(MatrixInverse(Rbf), F ) ):
F1b := simplify( `.(MatrixInverse(Rbf), F1) ):
Lb := simplify( `.(MatrixInverse(Rbf), L ) ):
L1b := simplify( `.(MatrixInverse(Rbf), L1) ):
```

`Conversion matrix for velocity components from flagella (t, n, b) to body coordinates system (p, q, r)`;

```
Vb := Vector(3):          Omegab := Vector(3):
Vb[1] := vp:      Vb[2] := vq:      Vb[3] := 0:          Vb := Vb:
Vf := expand( `.(Rbf, Vb) ):
Omegab[1] := 0:      Omegab[2] := 0:      Omegab[3] := Omega[r]:      Omegab
:= Omegab:
Omega[f] := `.(Rbf, Omegab):
```

```
#####
```

```

`Dot product of force F with p & q (force due to trans. velocity in body coordinates
system)`;
FB := subs( { V[t] = Vf[1], V[n] = Vf[2] }, Fb );
FB := simplify(FB);
`Dot product of force F1 with r (force due to rot. velocity in body coordinates system)`;
F1B := subs( Omega[b] = Omega[f][3], F1b );
`Dot product of torque L with p & q (torque due to trans. velocity in body coordinates
system)`;
LB := subs( { V[t] = Vf[1], V[n] = Vf[2] }, Lb );
LB := simplify(LB);
`Dot product of torque L1 with r (torque due to rot. velocity in body coordinates
system)`;
L1B := subs( Omega[b] = Omega[f][3], L1b );

` Time dependent beat coefficient alphaij `;
beta11 := expand( subs( { vp = 1, vq = 0, vr = 0, x[n] = b*sin(chi) }, FB[1] ) );
beta22 := expand( subs( { vp = 0, vq = 1, vr = 0, x[n] = b*sin(chi) }, FB[2] ) );
beta26 := expand( subs( { Omega[p] = 0, Omega[q] = 0, Omega[r] = 1, x[n] =
b*sin(chi) }, F1B[2] ) );
beta62 := expand( subs( { vp = 0, vq = 1, vr = 0, x[n] = b*sin(chi) }, LB[3] ) );
beta66 := expand( subs( { Omega[p] = 0, Omega[q] = 0, Omega[r] = 1, x[n] =
b*sin(chi) }, L1B[3] ) );

#####

`Core integrals involved in alphaij for effective & recovery stroke`;
rr := sqrt( ( (s-b)+b*cos(chi) )^2 + ( b*sin(chi) )^2 );   rt := (s-b)+b*cos(chi);   m :=
b*sin(chi);
`Core integrals`;
intgs := expand( simplify( { II[8] = int(1/(rr)^3, s = b .. b+c)-( (m)^2 )*(int(1/(rr)^5, s =
b .. b+c) ), II[7] = int(1/rr, s = b .. b+c)-( (m)^2 )*(int(1/(rr)^3, s = b .. b+c) ), II[1] = int(1,
s = b .. b+c), II[2] = int(1/rr, s = b .. b+c), II[3] = int(1/(rr)^3, s = b .. b+c), II[4] =
int(1/(rr)^5, s = b .. b+c), II[5] = int(1/(rr)^7, s = b .. b+c), II[6] = int((rt)^2, s = b .. b+c),
JJ[1] = int( rt, s = b .. b+c ), JJ[2] = int( rt/rr, s = b .. b+c ), JJ[3] = int(rt/(rr)^3, s = b ..
b+c), JJ[4] = int(rt/(rr)^5, s = b .. b+c) } ) ) assuming ( chi::RealRange(-Pi, Pi),
t::RealRange(0, 1), c::RealRange(0,l), b::RealRange(1,l+a));
`Core integrals- straight section`;
intgs1 := expand( simplify( { II[8] = int(1/(s)^3, s = b .. b+c), II[7] = int(1/s, s = b ..
b+c), II[1] = int(1, s = b .. b+c), II[2] = int(1/s, s = b .. b+c), II[3] = int(1/(s)^3, s = b ..
b+c), II[4] = int(1/(s)^5, s = b .. b+c), II[5] = int(1/(s)^7, s = b .. b+c), II[6] = int((s)^2, s
= b .. b+c), JJ[1] = int( s, s = b .. b+c ), JJ[2] = int( s/s, s = b .. b+c ), JJ[3] =
int(s/(s)^3, s = b .. b+c), JJ[4] = int(s/(s)^5, s = b .. b+c) } ) ) assuming (
chi::RealRange(-Pi, Pi), t::RealRange(0, 1), c::RealRange(0,l), b::RealRange(1,l+a));

#####

`Substitution of integrals into alphaij for effective & recovery strokes`;
alpha11 := subs( intgs, beta11 );
alpha22 := subs( intgs, beta22 );
alpha26 := subs( intgs, beta26 );

```

```

alpha62 := subs( integs, beta62 );
alpha66 := subs( integs, beta66 );

alpha11s := subs( integs1, beta11 );
alpha22s := subs( integs1, beta22 );
alpha26s := subs( integs1, beta26 );
alpha62s := subs( integs1, beta62 );
alpha66s := subs( integs1, beta66 );

#####
count := 0;
th[0] := evalf( 40*evalf(Pi)/180 );          thi := [seq(i, i = 0 .. 1, dt)];
tte := [seq(i, i = 0 .. Te, dt)];          tt1 := [seq(i, i = Te .. T, dt)];
VPE[0] := 0:      VQE[0] := 0:      V1[0] := 0:      V3[0] := 0:      ThetadotE[0] :=
0:
VPR := 'VPR':      VQR := 'VQR':      V33 := 'V33':      V11 := 'V11':      ThetadotR
:= 'ThetadotR':

`Effective stroke`;
for tt from dt by dt to Te do
  t1:=tt;
  ctemp := evalf( evalf(Pi)*t1/(2.0*Te) ):      chidot := evalf(evalf(Pi)/(2.0*Te)):
  ctempl := evalf( - evalf(Pi)*t1/(2.0*Te) ):      chidotl := evalf( - evalf(Pi)/(2.0*Te) ):
  f1E := - (Kn*(l^2)*chidot*sin(ctemp)/(2.0) + Kn*(l^2)*chidotl*sin(ctempl)/(2.0)):

  alphaeff11 := evalf( subs( { chi=ctemp, theta=th[count], b=a, c=l, t=t1 }, alpha11 ) ) +
evalf( subs( { chi=ctempl, theta=th[count], b=a, c=l, t=t1 }, alpha11 ) );
  alphaeff22 := evalf( subs( { chi=ctemp, theta=th[count], b=a, c=l, t=t1 }, alpha22 ) )
+ evalf( subs( { chi=ctempl, theta=th[count], b=a, c=l, t=t1 }, alpha22 ) ):
  alphaeff26 := evalf( subs( { chi=ctemp, theta=th[count], b=a, c=l, t=t1 }, alpha26 ) )
+ evalf( subs( { chi=ctempl, theta=th[count], b=a, c=l, t=t1 }, alpha26 ) ):
  alphaeff62 := evalf( subs( { chi=ctemp, theta=th[count], b=a, c=l, t=t1 }, alpha62 ) )
+ evalf( subs( { chi=ctempl, theta=th[count], b=a, c=l, t=t1 }, alpha62 ) ):
  alphaeff66 := evalf( subs( { chi=ctemp, theta=th[count], b=a, c=l, t=t1 }, alpha66 ) )
+ evalf( subs( { chi=ctempl, theta=th[count], b=a, c=l, t=t1 }, alpha66 ) ):

  count := count + 1;
  `For pure Vertical Up-swimming, the Force-Torque balance equation reduces to`;
  VPE[count] := evalf( 0.5*( f1E/( alphaeff11-6.0*evalf(Pi) ) ) ):
  VQE[count] := evalf( 0.5*( ( alphaeff26 / ( alphaeff26*alphaeff62 - (alphaeff22-
6.0*evalf(Pi))*(alphaeff66-8.0*evalf(Pi)) ) ) *m*g*H*sin( th[count-1] ) ) ):
  ThetadotE[count] := evalf(-( alphaeff22-6.0*evalf(Pi) ) / ( alphaeff26*alphaeff62 -
(alphaeff22-6.0*evalf(Pi))*(alphaeff66-8.0*evalf(Pi)) ) ) *m*g*H*sin( th[count-1] ) ):

  V1[count] := ( sin(th[count-1])*VPE[count] + cos(th[count-1])*VQE[count] ):
  V3[count] := ( cos(th[count-1])*VPE[count] - sin(th[count-1])*VQE[count] ):
  th[count] := th[count-1] + (dt)*( ThetadotE[count] );
end do;

```

```

vpe := convert( VPE, list );      pointse := convert( linalg[transpose]([tte, vpe]), listlist );
vqe := convert( VQE, list );      pointse1 := convert( linalg[transpose]([tte, vqe]), listlist );
vpe2 := convert( V3, list );      pointse2 := convert( linalg[transpose]([tte, vpe2]), listlist );
):
vqe2 := convert( V1, list );      pointse22 := convert( linalg[transpose]([tte, vqe2]), listlist );
):

```

```

VPR[count] := VPE[count];      VQR[count] := VQE[count];      VPR1[count] :=
VPE[count];
V11[count] := V1[count];      V33[count] := V3[count];      ThetadotR[count] :=
ThetadotE[count];

```

```
#####
```

```
`Recovery stroke- Zero moment case- (Recovery 1) `;
```

```
for tt from Te by dt to T-dt do
```

```
  t1 := tt-Te:
```

```
  ctemp := evalf( 2.0*arctan( 1/( 1-w*t1/l )^(3/2) ) );  chidot :=
evalf(3.0*w*sin(ctemp)/(2.0*(l-w*t1))):
```

```
  ctempl := evalf( -( 2.0*arctan( 1/( 1-w*t1/l )^(3/2) ) ) );  chidotl := evalf(
3.0*w*sin(ctempl)/(2.0*(l-w*t1)) ):
```

```
  f1R := Kn*(w*sin(ctemp)*(l-w*t1)-(1/2)*(l-w*t1)^2*chidot)*sin(ctemp) +
Kt*w*(cos(ctemp)-1)*(l-w*t1)*cos(ctemp) + Kn*(w*sin(ctempl)*(l-w*t1)-(1/2)*(l-
w*t1)^2*chidotl)*sin(ctempl) + Kt*w*(cos(ctempl)-1)*(l-w*t1)*cos(ctempl);
```

```
  alphastr11 := evalf( subs( { chi=0, theta=th[count], b=a, c=w*t1, t=t1 }, alpha11s ) ) +
evalf( subs( { chi=0, theta=th[count], b=a, c=w*t1, t=t1 }, alpha11s ) ):
```

```
  alphastr22 := evalf( subs( { chi=0, theta=th[count], b=a, c=w*t1, t=t1 }, alpha22s ) ) +
evalf( subs( { chi=0, theta=th[count], b=a, c=w*t1, t=t1 }, alpha22s ) ):
```

```
  alphastr26 := evalf( subs( { chi=0, theta=th[count], b=a, c=w*t1, t=t1 }, alpha26s ) ) +
evalf( subs( { chi=0, theta=th[count], b=a, c=w*t1, t=t1 }, alpha26s ) ):
```

```
  alphastr62 := evalf( subs( { chi=0, theta=th[count], b=a, c=w*t1, t=t1 }, alpha62s ) ) +
evalf( subs( { chi=0, theta=th[count], b=a, c=w*t1, t=t1 }, alpha62s ) ):
```

```
  alphastr66 := evalf( subs( { chi=0, theta=th[count], b=a, c=w*t1, t=t1 }, alpha66s ) ) +
evalf( subs( { chi=0, theta=th[count], b=a, c=w*t1, t=t1 }, alpha66s ) ):
```

```
  alphaang11 := evalf( subs( { chi=ctemp, theta=th[count], b=a+w*t1, c=l-w*t1, t=t1 },
alpha11 ) ) + evalf( subs( { chi=ctempl, theta=th[count], b=a+w*t1, c=l-w*t1, t=t1 },
alpha11 ) ):
```

```
  alphaang22 := evalf( subs( { chi=ctemp, theta=th[count], b=a+w*t1, c=l-w*t1, t=t1 },
alpha22 ) ) + evalf( subs( { chi=ctempl, theta=th[count], b=a+w*t1, c=l-w*t1, t=t1 },
alpha22 ) ):
```

```
  alphaang26 := evalf( subs( { chi=ctemp, theta=th[count], b=a+w*t1, c=l-w*t1, t=t1 },
alpha26 ) ) + evalf( subs( { chi=ctempl, theta=th[count], b=a+w*t1, c=l-w*t1, t=t1 },
alpha26 ) ):
```

```
  alphaang62 := evalf( subs( { chi=ctemp, theta=th[count], b=a+w*t1, c=l-w*t1, t=t1 },
alpha62 ) ) + evalf( subs( { chi=ctempl, theta=th[count], b=a+w*t1, c=l-w*t1, t=t1 },
alpha62 ) ):
```

```

alphaang66 := evalf( subs( { chi=ctemp, theta=th[count], b=a+w*t1, c=l-w*t1, t=t1 },
alpha66 ) ) + evalf( subs( { chi=ctempl, theta=th[count], b=a+w*t1, c=l-w*t1, t=t1 },
alpha66 ) );

```

```

alpharec11 := alphaang11 + alphastr11:

```

```

alpharec22 := alphaang22 + alphastr22:

```

```

alpharec26 := alphaang26 + alphastr26:

```

```

alpharec62 := alphaang62 + alphastr62:

```

```

alpharec66 := alphaang66 + alphastr66:

```

```

count := count + 1;

```

```

`For pure Vertical Up-swimming, the Force-Torque balance equation reduces to`

```

```

VPR[count] := evalf( 0.5*( f1R/( alpharec11-6.0*evalf(Pi) ) ) );

```

```

VQR[count] := evalf( 0.5*( ( alpharec26 / ( alpharec26*alpharec62 - (alpharec22-
6.0*evalf(Pi))*(alpharec66-8.0*evalf(Pi)) ) ) *m*g*H*sin( th[count-1] ) );

```

```

ThetadotR[count] := evalf(- ( alpharec22-6.0*evalf(Pi) ) / ( alpharec26*alpharec62 -
(alpharec22-6.0*evalf(Pi))*(alpharec66-8.0*evalf(Pi)) ) ) *m*g*H*sin( th[count-1] ) );

```

```

V11[count] := ( sin(th[count-1])*VPR[count] + cos(th[count-1])*VQR[count] );

```

```

V33[count] := ( cos(th[count-1])*VPR[count] - sin(th[count-1])*VQR[count] );

```

```

th[count] := th[count-1] + (dt)*( ThetadotR[count] );

```

```

end do:

```

```

vpr := convert( VPR, list );           pointsr := convert( linalg[transpose]([tt1, vpr]), listlist );

```

```

vqr := convert( VQR, list );           pointsr1 := convert( linalg[transpose]([tt1, vqr]),
listlist );

```

```

vpr2 := convert( V33, list );          pointsr2 := convert( linalg[transpose]([tt1, vpr2]),
listlist );

```

```

vqr22 := convert( V11, list );         pointsr22 := convert( linalg[transpose]([tt1, vqr22]),
listlist );

```

```

#####

```

```

`constant angular velocity case- (Recovery 2)`;

```

```

for tt from Te by dt to T-dt do

```

```

  t1 := tt-Te:

```

```

  ctemp1 := evalf( evalf(Pi)/(2.0)+evalf(Pi)*w*t1/(2.0*I)):  chidot1 := evalf(
evalf(Pi)*w/(2.0*I) );

```

```

  ctemp1l := evalf( - evalf(Pi)/(2.0) - evalf(Pi)*w*t1/(2.0*I)):  chidot1l := evalf( -
evalf(Pi)*w/(2.0*I) );

```

```

  f1R1 := Kn*(w*sin(ctemp1)*(l-w*t1)-(1/2)*(l-w*t1)^2*chidot1)*sin(ctemp1) +
Kt*w*(cos(ctemp1)-1)*(l-w*t1)*cos(ctemp1) + Kn*(w*sin(ctemp1l)*(l-w*t1l)-(1/2)*(l-
w*t1l)^2*chidot1l)*sin(ctemp1l) + Kt*w*(cos(ctemp1l)-1)*(l-w*t1l)*cos(ctemp1l);

```

```

  alpha1str11 := evalf( subs( { chi=0, b=a, c=w*t1, t=t1 }, alpha11s ) ) + evalf( subs( {
chi=0, b=a, c=w*t1, t=t1 }, alpha11s ) );

```

```

  alpha1ang11 := evalf( subs( { chi=ctemp1, b=a+w*t1, c=l-w*t1, t=t1 }, alpha11 ) ) +
evalf( subs( { chi=ctemp1l, b=a+w*t1, c=l-w*t1, t=t1 }, alpha11 ) );

```

```

  alpha1rec11 := alpha1str11 + alpha1ang11:

```

```

alpha1rec11 := alpha1str11 + alpha1ang11:
count := count + 1;
`For pure Vertical Up-swimming, the Force-Torque balance equation reduces to`;
  VPR1[count] := evalf( 0.5*( f1R1/( alpha1rec11-6.0*evalf(Pi) ) ) );
end do;

```

```

vpr1 := convert( VPR1, list ):    pointsr3 := convert( linalg[transpose]([tt1, vpr1]),
listlist ):

```

```

#####

```

```

thdotr := convert( th, list ):    points11 := convert( linalg[transpose]([thi, thdotr]),
listlist ):

```

```

points := [ op(pointse), op(pointsr)]:    points2 := [ op(pointse), op(pointsr3)]:
points22 := [ op(pointse2), op(pointsr2)]:    points1 := [ op(pointse1), op(pointsr1)]:
points222 := [ op(pointse22), op(pointsr22)]:

```

```

plot( { points, points2 }, title = "Graph for vp ( swimming velocity in the primary
direction ) during effective & recovery stroke " );
plot( points22, title = "Graph for V3 ( swimming velocity in the k- direction ) during
effective & recovery stroke " );
plot( points222, title = "Graph for V1 ( swimming velocity in the i- direction ) during
effective & recovery stroke " );
plot( points11, title = "Graph for change in thata swimming angular velocity during
effective & recovery stroke ");

```

References

- [1] Arfken G., *Mathematical methods for physicist*, Academic Press Inc. London, 3rd edition, 1985.
- [2] Barta E., Liron N., Slender body interactions for low Reynolds numbers-part I: Body wall interactions, *SIAM Journal of Applied Math*, 1988; **48**: 992-1008.
- [3] Barta E., Liron N., Slender body interactions for low Reynolds numbers-part II: Body wall interactions, *SIAM Journal of Applied Math*, 1988; **48**: 1262-1280.
- [4] Batchelor G. K., Stress system in a suspension of force-free particles, *J. Fluid Mech.*, 1970; **41**: 545-570.
- [5] Bearon R. N., and Grübaum D., Bioconvection in a stratified environment: Experiments and theory, *Phys. of Fluids*, 2006; **18**: 1-14.
- [6] Bees M. A., Non-linear pattern generation in suspensions of swimming micro-organism, PhD thesis, Univ. of Leeds, 1996.
- [7] Bees M. A., Hill N. A., Wavelengths of bioconvection patterns, *J. of Exp. Biology*, 1997; **200(10)**: 1515-1526.
- [8] Bees M. A., Hill N. A. and Pedley T. J., Analytical approximations for the orientation distribution of small dipolar particles in steady shear flows, *J. of Math. Biology*, 1998; **36**: 269-298.
- [9] Bees M. A., Hill N. A., Linear bioconvection in a suspension of randomly swimming, gyrotactic micro-organisms, *physics of fluids*, 1998; **10(8)**: 1864-1881.
- [10] Bees M. A., Hill N. A., Non-linear bioconvection in a deep suspension of gyrotactic swimming micro-organisms, *J. of Math. Biology*, 1999 **168**: 38-135.

- [11] Bees M. A. and Croze O. A., Dispersion of biased swimming micro-organism in a fluid flowing through a tube, *Proc. of the Royal Society A*, 2010; **10**: 1-21.
- [12] Berg H. C., *E. Coli* in motion, *Springer*, 2004.
- [13] Binous H. and Phillips J. R., The effect of sphere-wall interactions on particle motion in a viscoelastic suspension of FENE dumbbells, *J. Non-Newtonian Fluid Mech.*, 1999; **85**: 63-92.
- [14] Blake J. R., A note on the image system for a stokeslet in a no-slip boundary., *Proc. Camb. Phil. Soc.*, 1971; **70**: 303-310.
- [15] Blake J. R., Chwang A. T., Fundamental singularities of viscous flow, *J. of Engg. Math.*, 1974; **8**: 23-29.
- [16] Blake J. R., Chwang A. T., Fundamental singularities of viscous flow PartI: The image systems in the vicinity of a stationary no-slip boundary., *J. of Engg. Math.*, 1974; **8**: 23-29.
- [17] Blake J. R., Otto S. R., Ciliary propulsion, chaotic filtration and a 'blinking' stokeslet., *J. of Engg. Math.*, 1996; **30**: 151-168.
- [18] Bold H. C. and Wynne M. J., Introduction to the algae. Structure and Reproduction. Englewood Cliffs, NJ: Prentice-Hall. 1978.
- [19] Brennen C., Winet H., Fluid mechanics of propulsion by cilia and flagella, *Ann. Rev. Fluid Mech.*, 1977; **9**: 339-398.
- [20] Brokaw C. J., Non-sinusoidal bending waves in sperm flagella, *J. of Exp. Biology*, 1965; **43**: 155-169.
- [21] Brokaw C. J., Computer simulation of flagellar movement I. Demonstration of stable bend propagation and bend initiation by a sliding filament model, *Biophys. J.*, 1972; **12**: 564-586.
- [22] Brokaw C. J., Computer simulation of flagellar movement VI. Simple curvature-controlled models are incompletely specified, *Cell Motil. Cytoskel.*, 1985; **48**: 633-642.
- [23] Brokaw C. J., Computer simulation of flagellar movement VII. Coordination of dynein by local curvature control can generate helical bending waves, *Cell Motil. Cytoskel.*, 2002; **53**: 102-124.

- [24] Brokaw C. J., Luck D. J. L., Bending patterns of Chlamydomonas flagella I: Wild type bending patterns, *Cell Motility*, 1983; **3**: 131-150.
- [25] Cash J. R., and Moore D. R., A high order method for the numerical solution of two-point boundary value problems, *BIT*, 1980; **20**: 44.
- [26] Chandrasekar S., *Hydrodynamic and Hydromagnetic Stability*, Oxford, 1961.
- [27] Childress S., *Mechanics of swimming and flying*, Cambridge Univ. Press, New York.
- [28] Childress S., and Spiegel E. A., Pattern formation in a suspension of swimming micro-organism: non-linear aspects. In D. Givoli, M. J. Grote, and G. P. Papanicoulaou, editors, *A Celebration of Mathematical Modelling: The Joseph B. Keller Anniversary Volume*, 2004 (based on the previous version from 1978).
- [29] Childress S., Levandowsky M., Spiegel E. A., Pattern formation in a suspension of swimming micro-organism: equations and stability theory, *J. of Fluid Mechanics*, 1975 **69(3)**: 591-613.
- [30] Chisti Y., Biodiesel from microalgae beats bioethanol, *Biotechnol. Adv.*, 2007; **25**: 126-131.
- [31] Chwang A. T., and Wu T. Y., A note on the helical movement of micro-organisms, *Proc. R. Soc. Lond. Ser. B*, 1971; **178**: 327-346.
- [32] Chwang A. T., and Wu T. Y., Hydrodynamics of low Reynolds number flow: Part 1 Rotation of axisymmetric prolate bodies, *J. Fluid Mech.*, 1974; **63**: 607-622.
- [33] Chwang A. T., and Wu T. Y., Hydrodynamics of low Reynolds number flow: Part 2 Singularity method for Stokes flow, *J. Fluid Mech.*, 1975; **67**: 787-815.
- [34] Clarke R. J., Jensen O. E., Billingham J., and Williams P. M., Three dimensional flow due to a microcantilever oscillating near a wall: an unsteady slender body analysis, *Proc. R. Soc. Lond. Ser. A*, 2006; **462**: 913-933.
- [35] Cooley J. W., Tukey J. W., An algorithm for the machine calculation of complex Fourier series, *Mathematics of Computation*, 1965 **19(90)**: 297-301.
- [36] Cox R. G., The motion of long slender bodies in a viscous fluid: Part 1 General theory, *J. Fluid Mech.*, 1970; **44**: 791.

- [37] Cziráok A., Jánosi M., Kessler J. O., Bioconvection dynamics: dependence on organism behaviour, *J. of Exp. Biology*, 2000; **203(21)**: 3345-3354.
- [38] Durham W. M., Kessler J. O., and Stocker R., Disruption of vertical motility by shear triggers formation of thin phytoplankton layers, *Science*, 2009; **323**: 1067-1070.
- [39] Faxen H., Arkiv. Mat. Astrom. Fys., 1923; **17(1)**.
- [40] Foster K. W., and Smyth R. D., Light antennas in phototactic algae, *Microbiology and Molecular Biology Reviews*, 1980 **44(4)**: 572-630.
- [41] Fulford G. R., Katz D. F., and Powell R. L., Swimming of spermatozoa in a linear viscoelastic fluid, *Biorheology*, 1998 **35(4-5)**: 295-309.
- [42] García-González M., Moreno J., Manzano J. C., Florencio F. J., and Guerrero M. G., Production of dunaliella salina biomass rich in 9-*cis*- β -carotene and lutein in a closed tubular bioreactor, *J. Biotechnol.*, 2005; **115**: 81-90.
- [43] Ghirardi M. L., Dubini A., Yu J., and Maness P. -C., Photobiological hydrogen producing system, *Chemical Society Review*, 2009; **38**: 52-61.
- [44] Ghorai S., and Hill N. A., Development of stability of gyrotactic plumes in bioconvection, *J. of Fluid Mechanics*, 1999 **400**: 1-31.
- [45] Ghorai S., and Hill N. A., Periodic arrays of gyrotactic plumes in bioconvection, *Physics of Fluids*, 2000 **12(1)**: 5-22.
- [46] Ghorai S., and Hill N. A., Axisymmetric bioconvection in a cylinder, *J. of Theoretical Biology*, 2002 **219(2)**: 137-152.
- [47] Ghorai S., and Hill N. A., Gyrotactic bioconvection in three dimensions, *Physics of Fluids*, 2007 **19(5)**: 054107.
- [48] Goldman A. J., Cox R. G., and Brenner H., Slow viscous motion of a sphere parallel to plane wall-I Motion through a quiescent fluid, *Chemical Engineering Science*, 1967; **22**: 637-651.
- [49] Goldman A. J., Cox R. G., and Brenner H., Slow viscous motion of a sphere parallel to plane wall-II Couette flow, *Chemical Engineering Science*, 1967; **22**: 653-660.

- [50] Goodess C. M., and Palutikof J. P., The development of regional climate scenarios and ecological impact of green house gas warming. In F. I. Woodward, editor, *The Ecological consequences of global climate change*, 1992; **22**: 33-62.
- [51] Gray J., Hancock C. J., The propulsion of sea-urchin spermatozoa, *J. of Exp. Biology*, 1955; **32**: 802-814.
- [52] Grima E. M., Belarbi E. H., Fernández F. G. A., Medina A. R., and Chisti Y., Recovery of microalgal biomass and metabolites: process options and economics, *Biotechnol. Adv.*, 2003; **20**: 491.
- [53] Gröbba D., Peter principle packs a peck of phytoplankton, *Science*, 2009; **323**: 1022-1023.
- [54] Gueron S., and Levit-Gurevich K., A three dimensional model for ciliary motion based on the internal 9+2 structure, *Proc. R. Soc. Lond. ser B*, 2001; **268**: 599-607.
- [55] Gueron S., and Liron N., Ciliary motion modelling, and dynamic multicilia interactions, *Biophysics Journal*, 1992; **63**: 1045-1058.
- [56] Hancock G. J., The self propulsion of microscopic organism through liquids, *Proc. R. Soc. London*, 1953; **217**: 96-121.
- [57] Harkes G., Dankert J., and Feijen J., Bacterial migrations along solid surfaces, *Appl. Environ. Microbiol.*, 1992; **58**: 1500-1505.
- [58] Hasimoto H., Sphere theorem for the stokes flow, *Physics of Fluids*, 1997; **9**: 1838-1840.
- [59] Hasimoto H., Sano O., Stokeslet and eddies in creeping flow, *Ann. Rev. Fluid Mech.*, 1980; **12**: 335-363.
- [60] Hawkes F. R., Dinsdale R., Hawkes D. L., and Hussy I., Sustainable fermentative hydrogen production: challenges for process optimisation, *International Journal of Hydrogen Energy*, 2002; **27(11-12)**: 1339-1347.
- [61] Higdon J. J. L., The hydrodynamics of flagellar propulsion: helical waves, *J. of Fluid Mech.*, 1979; **94(2)**: 331-351.
- [62] Hill N. A. and Bees M. A., Taylor dispersion of gyrotactic swimming micro-organisms in a linear flow, *Physics of Fluids*, 2002; **14(8)**: 2598-2605.

- [63] Hill N. A. and Pedley T. J., Bioconvection, *Fluid Dynamic Research*, 2005; **37**: 1-20.
- [64] Hill N. A., Pedley T. J., and Kessler J. O., Growth of bioconvection patterns in a suspension of gyrotactic micro-organisms in a layer of finite depth, *J. of Fluid Mechanics*, 1989; **208**: 509-543.
- [65] Hinch E. J., and Leal L. G., Note on the rheology of dilute suspension of dipolar spheres with weak brownian couples, *J. of Fluid Mechanics*, 1972; **56(4)**: 803-813.
- [66] Holmes S., Henderson's dictionary of biological terms, Longmans, London and New York, 9th edition, 1985.
- [67] Holwill M. E. J., 'Dynamics of flagellar movement', *In symposia of the society for experimental biology: Prokaryotic and eukaryotic flagella*, 1982; **35**: 289-312.
- [68] Holwill M. E. J., and Miles C. A., Hydrodynamic analysis of non-uniform flagellar undulations, *J. of Theoretical Biology*, 1971; **31**: 25-42.
- [69] Holwill M. E. J., and Sleigh M. A., Propulsion of hispid flagella, *J. Exp. Biology*, 1967; **47**: 267-276.
- [70] Hyams J. S., Borissy G. G., Isolated flagellar apparatus of *Chlamydomonas*: Characterization of forward swimming and alteration of waveform and reversal of motion by calcium ions in vitro, *J. Cell Sci.*, 1978; **33**: 235-253.
- [71] Ishikawa T., and Pedley T. J., The rheology of a semi-dilute suspension of swimming model micro-organism, *J. of Fluid Mech.*, 2007; **588**: 399-435.
- [72] Jánosi I. M., Kessler J. O., and Horváth V. K., Onset of bioconvection in suspensions of *Bacillus subtilis*, *Phys. Rev. E*, 1998; **58**: 4793-4800.
- [73] Jeffery G. B., The motion of ellipsoidal particles immersed in a viscous fluid, *Proc. R. Soc. Lond. A*, 1922; **102**: 161-179.
- [74] Johnson R. E., Slender body theory for stokes flow and flagellar hydrodynamics. PhD thesis, California Institute of Technology, 1977.
- [75] Johnson R. E., Brokaw C. J., Flagellar hydrodynamics: A comparison between resistive-force theory and slender-body theory, *Biophys. J.*, 1979; **25**: 113-127.

- [76] Jones M. S., Baron L. L., Pedley T. J., Biflagellate gyrotaxis in a shear flow, *J. of Fluid Mech.*, 1994; **281**: 137-158.
- [77] Jones M. S., Hydrodynamics of biflagellated locomotion, PhD thesis, University of Leeds, 1995.
- [78] Katz D. F., Blake J. R. and Paveri-Fontana S. L., On the movement of slender bodies near plane boundaries at low Reynolds number, *J. Fluid Mech.*, 1975; **72(3)**: 529-540.
- [79] Kessler J. O., Gyrotactic buoyant convection and spontaneous pattern formation in algal cell cultures. In M. G. Velarde, editor, *Non-equilibrium cooperative phenomena in physics and related fields*, New York: Plenum 1984; 241-248.
- [80] Kessler J. O., Co-operative and concentrative phenomena of swimming micro-organisms. *Contemporary Physics*, 1985; **26(2)**: 147-166.
- [81] Kessler J. O., Hydrodynamic focusing of motile algal cells. *Nature*, 1985; **313**: 218-220.
- [82] Kessler J. O., The external dynamics of swimming micro-organisms. *Progress in Physiological Research*, 1986; **4**: 257-307.
- [83] Kessler J. O., Individual and collective dynamics of swimming cells, *J. of Fluid Mech.*, 1986; **173**: 191-205.
- [84] Kessler J. O., Path and pattern - the mutual dynamics of swimming cells and their environment, *Comments in Theoretical Biology*, 1989; **1**: 85-108.
- [85] Kessler J. O., Individual and collective dynamics of swimming cells, *Advanced space research*, 1992; **12**: 33-42.
- [86] Kessler J. O., Hill N. A., Hader D. P., Orientation of swimming flagellates by simultaneously acting external factors, *J. Phycology*, 1992; **28**: 816-822.
- [87] Kim S., Karrila J. S., *Microhydrodynamics: Principles and selected applications*, Butterworth-Heinemann, 1991.
- [88] Kinukawa M., Ohmuro J., Baba S. A., Murashige S., Okuno M., Nagata M., and Aoki F., Analysis of flagellar bending in hamster spermatozoa: characterisation of an effective stroke, *Biol. Repord.* **73(6)**, 1269-1274.

- [89] Lauga E., Diluzio W. R., Whitesides G. M., and Stone H. A., Swimming in circles: motion of bacteria near solid boundaries, *Biophys. J.*, 2007; **90(2)**: 400-412.
- [90] Lauga E., and Powers T. R., The hydrodynamics of swimming microorganisms, *Rep. Proc. Phys.*, 2009; **72**: 1-36.
- [91] Levandowsky M., Childress W. S., Spiegel E. A., and Hunter S. H., A mathematical model of pattern formation by swimming micro-organisms, *J. of Eukaryotic Microbiology*, 1975; **22(2)**: 296-306.
- [92] Leal L. G., Laminar flow and convective transport processes, *J. Fluid Mech.*, 1970; **41**: 545-570.
- [93] Lewis D. M., The orientation of gyrotactic spheroidal micro-organisms in a homogeneous isotropic turbulent flow, *Proc. R. Soc. A*, 2003; **459**: 12935-1323.
- [94] Lighthill M. J., Flagellar Hydrodynamics, *SIAM Review*, 1976; **18**: 161-230.
- [95] Lighthill J. S., Reinterpreting the basic theorem of flagellar hydrodynamics, *J. of Engg. Math.*, 1996; **30**: 25-34.
- [96] Liron Nadav, The Lighthill-Gueron-Liron theorem-historical perspective and critique, *Mathematical Methods in the Applied Sciences*, 2001; **24**: 1533-1540.
- [97] Lighthill J. S., Helical distribution of stokeslet, *J. of Engg. Math.*, 1996; **30**: 35-78.
- [98] Loeffler J. B., Mefferd R. B., Concerning pattern formation by free swimming micro-organisms. *The American Naturalist*, 1952 **86(830)**: 325-329.
- [99] Lorentz H. A., Eene algemeene stelling omtrent de beweging eener vloeistof met wrijving en eenige daaruit afgeleide gevolgen. *Zittingsverslag Koninkl. Akad. van Wetensch. Amsterdam*, 1896; **5**: 168-175.
- [100] Madigan T. M., Martinko M. J., Parker J., Brock biology of micro-organisms, Prentice Hall International, 10th edition, 2003.
- [101] Manela A., and Frankel I., Generalized Taylor dispersion in suspension of gyrotactic swimming micro-organisms, *J. Fluid Mechanics*, 2003; 490-499.
- [102] Maul C., Kim S., Image of a point force in a spherical container and its connection to the Lorentz reflection formula., *J. of Engg. Math.*, 1996; **30**: 119-130.

- [103] Melis A., Green alga hydrogen production: progress, challenges and prospects, *Int. J. of Hydrogen Energy*, 2002; **27**: 1217-1228.
- [104] Melis A., and Happe T., Hydrogen production: green algae as a source of energy, *Plant Physiol.*, 2001; **127**: 740-748.
- [105] Muarray J. D., *Mathematical biology*, Springer-Verlag, New York.
- [106] Nultsch W., and Hoff E., Investigations on pattern formation in Euglenae, *Archive für Protistenk*, 1973; **115**: 336-352.
- [107] Oseen C. W., *Hydrodynamik*. Leipzig: Teubner, 1927: 337 pp.
- [108] Palaniappan D., Nigam S. D., Amarnath T., Lamb's solution of Stokes's equations: A sphere theorem., *Q. J. Mech. appl. Math.*, 1992; **45**: 47-56.
- [109] Pasol L., Chaoui M., Yahiaoui S. and Feuillebois F., Analytical solutions for a spherical particle near a wall in axisymmetrical polynomial creeping flow, *Physics of Fluids*, 2005; **17**: 1-13.
- [110] Pasol L., Sellier A., Feuillebois F., A sphere in a second degree polynomial creeping flow parallel to a wall., *Q. J. Mech. Appl. Math.*, 2006; **59**: 587-614.
- [111] Pedley T. J., Kessler J. O., The orientation of spheroidal micro-organisms swimming in a flow field, *Proc. R. Soc. Lond.*, 1987; **B231**: 47-70.
- [112] Pedley T. J., Hill N. A., Kessler J. O., The growth of bioconvection patterns in a uniform suspension of gyrotactic micro-organisms, *J. of Fluid Mech.* B, 1988; **195**: 223-237.
- [113] Pedley T. J., Kessler J. O., A new continuum model for suspensions of gyrotactic micro-organisms, *J. Fluid Mech.*, 1990; **212**: 155-182.
- [114] Pedley T. J. and Kessler J. O., Hydrodynamic phenomena in suspension of swimming microorganisms, *Annu. Rev. Fluid Mech.*, 1992; **24**: 313-358.
- [115] Pironneau O. and Katz D. F., Optimal swimming of flagellated micro-organisms, *J. Fluid Mech.*, 1974; **66**: 391-415.
- [116] Platt J. R., "Bioconvection patterns" in cultures of free swimming organisms, *Science*, 1961; **133**: 1766-1767.

- [117] Plesset M. S., and Winet H., Bioconvection patterns in swimming microorganisms cultures as an example of Rayleigh-Taylor instability, *Nature*, 1974; **248**: 441-443.
- [118] Polin M., Tuval I., Drescher K., Gollub J. P., and Goldstien R. E., *Chlamydomonas* swims with two 'gears' in a eukaryotic version of run-and-tumble locomotion, *Science*, 2009 **325(5939)**: 487-490.
- [119] Pons A. J., Sagues F., Bees M. A., and Sorensen P. G., Quantitative analysis of chemoconvection patterns in the methylene-blue-glucose system, *The J. of Physical Chemistry B*, 2002 **106(29)**: 7252-7259.
- [120] Press W. H., Tenkolsky S. A., Flannery B. P., and Vetterling W. T., Numerical Recipes in FORTRAN: The art of scientific computing. Cambridge University press, second edition, 1992.
- [121] Purcell E. M., Life at low Reynold number, *American J. of Phycics*, 1977; **45(1)**: 3-11.
- [122] Rallison J. M., The effects of brownian rotations in a dilute suspension of rigid particles of arbitrary shape, *J. of Fluid Mechanics*, 1978; **828**: 237-263.
- [123] Ramia M., Tullock D. L., Phan-Thien N., The role of hydrodynamic interaction in the locomotion of micro-organism, *Biophys. J.*, 1993; **65**: 755-778.
- [124] Ringo D. L., Flagellar motion and fine structures of the flagellar apparatus in *Chlamydomonas.*, *J. Cell Biol.*, 1967; **33**: 543-571.
- [125] Roberts A. M., The external dynamics of swimming micro-organisms, *Nature*, 1970; **828**: 375-376.
- [126] Roberts A. M., Geotaxis in motile micro-organisms, *J. of Exp. biology*, 1970; **53(3)**: 687-699.
- [127] Roberts A. M., Mechanics of gravitaxis in *Chlamydomonas*, *Biology Bulletin*, 2006; **210**: 78-80.
- [128] Ruffer U., Nultsch W., High speed cinematographic analysis of the movement of *chlamydomonas*, *Cell Motility*, 1985; **5**: 251-263.
- [129] Ruffer U., Nultsch W., Comparison of beating of *cis*- and *trans*-flagella of *chlamydomonas* held on micropipettes, *Cell Motility and cytoskeleton*, 1987; **7**: 87-93.

- [130] Ruffer U., Nultsch W., Flagellar photoresponses of *chlamydomonas* cells held on micropipettes: III. Shock responses, *Botanica Acta*, 1995; **108**: 255-265.
- [131] Ruffer U., Nultsch W., Flagellar photoresponses of *ptx1*, a nonphototactic mutant of *chlamydomonas*, *Cell Motility and cytoskeleton*, 1997; **37(2)**: 111-119.
- [132] Ruffer U., Nultsch W., Flagellar coordination in *chlamydomonas* cells held on micropipettes, *Cell Motility and cytoskeleton*, 1998; **41(44)**: 297-307.
- [133] Shack W. J., Fray C. S., and Lardner T. J., Observations on the hydrodynamics and swimming motions of mammalian spermatozoa, *Bulletin of Mathematical Biology*, 1974; **36**: 555-565.
- [134] Smith D. J., Modelling muco-ciliary transport in the lung, PhD thesis, University of Birmingham, 2005.
- [135] Smith D. J., Gaffney E. A., Blake J. R., Discrete cilia modelling with singularity distributions: Application to the embryonic nose and the airway surface liquid, *Bulletin of Mathematical Biology*, 2007; **69**: 1477-1510.
- [136] Smith D. J., Gaffney E. A., Blake J. R. and Kirkman-Brown J. C., Human sperm accumulation near surfaces: a simulation study, *J. Fluid Mech.*, 2009; **621**: 289-320.
- [137] Silvester N. R., and Holwill M. E. J., An analysis of hypothetical flagellar waveforms, *J. of Theoretical Biology*, 1972; **35**: 505-523.
- [138] Taylor G. I., Analysis of swimming of microscopic organisms, *Proc. R. Soc. Lond. Ser. A*, 1951; **209**: 447-461.
- [139] Taylor C. C., Dryden I. L., and Farnoosh R., The K function for nearly regular point processes, *Biometrics*, 2001; **57(1)**: 224-231.
- [140] Tillett J. P. K., Axial and transverse Stokes flow past slender axisymmetric bodies, *J. of Fluid Mech.*, 1970; **44**: 401-417.
- [141] Tomson A. M., Demets R., Sexual communication in the green alga *Chlamydomonas eugametos*, PhD thesis, University of Amsterdam, 1989.
- [142] Vladimirov V. A., Wu M. S. C., Pedley T. J., Denissenko P. V., and Zakhidova S. G., Measurement of cell velocity distributions in populations of motile algae, *The J. of Exp. Biology.*, 2004; **207**: 1203-1216.

- [143] Vincent R. V., Mathematical modelling of phototaxis in motile micro-organisms, PhD thesis, University of Leeds. 1995.
- [144] Wager I. I., On the effect of gravity upon the movements and aggregation of *Euglena viridis*, Ehrb., and other micro-organism, *Philosophical Transactions of the Royal society of London. Series B*, 1911 **201**: 333-390.
- [145] Weibel D. B., Garstecki P., Ryan D., DiLuzio W. R., Mayer M., Seto J. E., and Whitesides G. M., Microoxen: microorganisms to move microscale loads, *Proc Natl Acad Sci USA*, 2005 **102**: 11963.
- [146] Wille J. J. and Ehret C. F., Circadian rhythm of pattern formation in populations of a free-swimming organism, *Tetrahymena. J. Protozool* 1968 **15**: 789-792.
- [147] William R. C., Bioconvection and hydrogen production in a suspension of swimming microorganism, Phd thesis, Univ. of Glasgow, 2009.
- [148] Witman G., Chlamydomonas phototaxis, *Trends in Cell Biology*, 1993; **3**: 403-408.
- [149] Yoshimura K., Matsuo Y., and Kamiya R., Gravitaxis in *Chlamydomonas reinhardtii* studied with novel mutant, *Plant Cell phisol.*, 2003; **44(10)**: 1112-1118.
- [150] Zhang L., Happe T., and Melis A., Biochemical and morphological characterization of sulphur-deprived and H_2 -producing *Chlamydomonas reinhardtii*, *Planta*, 2002; **214(4)**: 552-561.
- [151] Zhang L., and Melis A., Probing green algal hydrogen production, *Philosophical Transactions of the Royal Society of London B: Biological Sciences*, 2002; **357(1426)**: 1499-1507.